NATIONAL AERONAUTICS AND SPACE ADMINISTRATION

Space Programs Summary 37-47, Vol. I

Flight Projects

For the Period July 1 to August 31, 1967

RECEIVED
DEC 27 1967
DEPT. OF AERONAUTICAL AND
ASTRONAUTICAL ENGINEERING
THE OHIO STATE UNIVERSITY

JET PROPULSION LABORATORY
CALIFORNIA INSTITUTE OF TECHNOLOGY
PASADENA, CALIFORNIA

September 30, 1967

JET PROPULSION LABORATORY *California Institute of Technology • 4800 Oak Grove Drive, Pasadena, California 91103*

September 30, 1967

ANNOUNCEMENT

SPACE PROGRAMS SUMMARY (SPS)

REORGANIZATION

Since mid-1962 (beginning with SPS 37-15), the SPS series has consisted of six volumes. Beginning with this issue (SPS 37-47), the SPS reporting structure has been modified to consist of four volumes, as explained in the Preface appearing on p. iii of this volume. Adjustments have been made to the SPS distribution lists to ensure that SPS recipients will receive equivalent information under the new reporting structure.

Equivalent information will be distributed during the same months as previously, with one exception: Since the reporting period of the new Vol. IV begins one month later than that of the new Vol. I, the specifically classified flight project material appearing in Vol. IV will be reported one month later than the specifically unclassified flight project material appearing in Vol. I. Under the former SPS structure, all flight project material was contained in one volume and thus covered the same reporting period.

Telephone 354-4321 *Twx 213-449-2451*

NATIONAL AERONAUTICS AND SPACE ADMINISTRATION

Space Programs Summary 37-47, Vol. I

Flight Projects

For the Period July 1 to August 31, 1967

JET PROPULSION LABORATORY
CALIFORNIA INSTITUTE OF TECHNOLOGY
PASADENA, CALIFORNIA

September 30, 1967

SPACE PROGRAMS SUMMARY 37-47, VOL. I

Copyright © 1967
Jet Propulsion Laboratory
California Institute of Technology

Prepared Under Contract No. NAS 7-100
National Aeronautics & Space Administration

Preface

The Space Programs Summary is a bimonthly publication that presents a review of engineering and scientific work performed, or managed, by the Jet Propulsion Laboratory for the National Aeronautics and Space Administration during a two-month period.

Beginning with this current 37-47 series, the Space Programs Summary is composed of four volumes. The titles of all volumes of the Space Programs Summary are:

Vol. I. *Flight Projects* (Unclassified)

Vol. II. *The Deep Space Network* (Unclassified)

Vol. III. *Supporting Research and Advanced Development* (Unclassified)

Vol. IV. *Flight Projects and Supporting Research and Advanced Development* (Confidential)

All *specifically unclassified* reporting previously included in the former Vol. I, *The Lunar Program* (Confidential), and the former Vol. II, *The Planetary–Interplanetary Program* (Confidential), will be presented in the new Vol. I. The *specifically classified* reporting previously included in the former Vols. I and II plus all reporting included in the former Vol. V, *Supporting Research and Advanced Development* (Confidential), will be presented in the new Vol. IV. The former Vol. III, *The Deep Space Network* (Unclassified), and the former Vol. IV, *Supporting Research and Advanced Development* (Unclassified) have been renumbered Vols. II and III, respectively. Because all specifically unclassified reports on space exploration programs and space sciences will now be published in an unclassified volume (Vol. I), the former Vol. VI, *Space Exploration Programs and Space Sciences* (Unclassified), has been discontinued.

Approved by:

W. H. Pickering, *Director*
Jet Propulsion Laboratory

Page intentionally left blank

Contents

PLANETARY-INTERPLANETARY PROGRAM

I. *Mariner IV* Project 1

A. Introduction 1

B. Telecommunications 2

II. *Mariner* Venus 67 Project 4

A. Introduction 4

B. Systems 5

C. Telecommunications 9

III. *Mariner* Mars 1969 Project 23

A. Introduction 23

B. Systems 24

C. Project Engineering 48

D. Guidance and Control 49

E. Telecommunications 50

F. Space Sciences 60

IV. *Voyager* Project 79

A. Introduction 79

B. Project Engineering 80

C. Propulsion 82

D. Telecommunications 88

References 92

LUNAR PROGRAM

V. *Surveyor* Project 95

A. Introduction 95

B. Power Systems 96

C. Flight Control Subsystem 105

D. Telecommunications 107

E. Radar Altimeter and Doppler Velocity Sensor 107

Contents (contd)

F. Thermal Engineering 107
G. Structures, Mechanisms, and Spacecraft Integration 108
H. Systems Analysis 115
I. Systems Engineering 123
J. Propulsion 125
K. Deep Space Network Test, Operations, and Training 131
L. Payload 131
M. Flight Spacecraft Testing 135
N. Space Flight Operations Facility Support Equipment 139
O. Special Deep Space Station Test, Operations, and Training . . . 139
P. Ground Support Equipment 141
Q. Operational Ground Equipment 141
Reference 145

I. *Mariner IV* Project

PLANETARY—INTERPLANETARY PROGRAM

A. Introduction

The *Mariner IV* Project is under the administrative cognizance of the *Mariner* 1967 Project Office, which also directs the *Mariner* Venus 67 Project and the residual activity of the *Mariner* Mars 1964 Project. Residual activity of the *Mariner* Mars 1964 Project consists primarily of continuing analysis of tracking data, publication of results by the principal investigators, and preparation of final reports. However, periodic detection, recording, and commanding activities involving the *Mariner IV* spacecraft have been assigned to the Deep Space Network. Elements of the experimental facilities at Goldstone Station (Venus and Mars Deep Space Stations) have been used to successfully communicate with the spacecraft. The DSN results will be published periodically in Vol. II of future Space Programs Summaries. *Mariner* Venus 67 Project activities are reported in the following Section II.

The objectives, authorized in December 1965, simultaneously with those for the Venus flight, have been established as:

> *The primary objective of the Mariner IV Project is to obtain scientific information on the interplanetary environment in a region of space further from the sun than the orbit of earth during a period of increasing solar activity in 1967, using the Mariner IV spacecraft still operating in orbit around the sun.*
>
> *The secondary objectives are to obtain additional engineering knowledge about the consequences of extended exposure of spacecraft equipment in the interplanetary space environment and to acquire experience in the operation of a planetary spacecraft after a prolonged lifetime in deep space.*

Performance of the *Mariner IV* spacecraft during the July–August reporting period continues to be satisfactory. During the period August 12 through August 21 the *Mariner IV* and *Mariner V* spacecraft were tracked on a 24 h/day basis to accommodate what may be called a "radial" configuration. In this configuration, *Mariner IV*, *Mariner V*, and the earth are in a nearly straight line. The phenomena of interest were the solar wind and the magnetic field lines embedded in it. The data obtained during this intensive combined tracking period are being analyzed.

Telemetry recordings were obtained by the Mars Deep Space Station (DSS 14) during passes on June 15 and 26. The first acquisition, using a special antenna and receiver configuration[1] at the Johannesburg Deep Space Station (DSS 51), was attempted on July 3. The data recorded will be processed at a later date. Additional data were obtained during subsequent DSS 51 tracking on July 8, 17, 18, and 19.

---

[1]Refer to SPS 37-45, Vol. III, p. 65.

During the month of August, *Mariner IV* was primarily tracked from the Pioneer and Johannesburg Deep Space Stations.

B. Telecommunications

1. *Mariner IV* Radio Subsystem Switch From TWT to Cavity Amplifier

After the Mars encounter and playback of TV picture data, the *Mariner IV* spacecraft was switched to the transmit low-gain/receive low-gain mode and left on the TWT amplifier for the cruise around the solar system. When the spacecraft had completed its pass around the sun and again approached the earth, it was possible to resume communications at the Mars Deep Space Station (DSS 14), Goldstone, California. Data received from the spacecraft through March 2, 1967 indicated that it was still transmitting on the TWT amplifier and operating in a normal manner.

No tracking of *Mariner IV* was accomplished between March 2 and May 8 due to work being done on the station. An attempt was made to acquire the spacecraft RF signal on May 8 at the predicted frequency and power level. Past history of frequency data normally enables the DSN to predict the acquisition frequency accurately, resulting in a minimum acquisition time.

It required approximately twenty minutes to obtain one-way lock, at which time the acquisition frequency was nearly 2500 Hz higher than predicted, and the received signal level was about 2 dB lower than predicted. The ground telemetry demodulator could not be locked up at this signal level, so no real-time telemetry data were available for analysis. A possible failure model was constructed, based on the above data, which suggested that the spacecraft radio subsystem had switched from the TWT amplifier to the cavity amplifier.

a. Radio back-up switching. The radio subsystem has several automatic failure mode switching capabilities. These capabilities are generated within the spacecraft, utilizing the control unit in the radio subsystem and the cyclic pulses originating in the central computer and sequencer (CC&S) subsystem. In the event the RF power output of the power amplifier in use drops below a preset reference level of + 35 dBmW ±1 dB, the next CY-1 pulse from the CC&S will cause the radio subsystem to switch to the redundant power amplifier.

b. Telemetry data. Tape recordings of the composite telemetry subcarrier from the May 8 pass were brought to the Laboratory in Pasadena, and some telemetry data were obtained by using the digital demodulation program in the SFOF. Evaluation of the radio subsystem and RF tracking data indicated that switching of the power amplifiers had occurred and that the radio subsystem was transmitting on the triode cavity amplifier. At that time it was assumed that the power amplifier switched sometime between March 2 and May 8, 1967. Since no data were available during this period, it was not possible to determine the time the failure occurred.

However, since May 8 more data have been received from the spacecraft and it is now possible to construct a curve of the cavity output power versus time (Fig. 1). Life test data on RH7-C tubes, the type used in the *Mariner IV* cavity, indicate that the expected degradation is approximately 0.6 dB per 1000 h when operating with a filament voltage of 5.1 V, the voltage at which the cavity in question is operating. The amount of degradation seen at the present time on the cavity is approximately 0.55 dB per 1000 h. By extrapolating from this curve, it appears that the power amplifier switched somewhere around March 21, 1967.

At present it is not possible to determine definitely why the switching of power amplifiers took place, or if the TWT or associated power supply actually did fail. There are several possible reasons for the occurrence:

(1) The TWT power supply failed due to a short circuit, causing the power supply fuse to open.

(2) The TWT tube failed.

(3) A power transient in the spacecraft occurred, thereby causing the control unit, which is susceptible to transients, to switch power amplifiers.

c. Summary. It is apparent that the radio subsystem did switch from TWT to cavity power amplifier for some unknown reason. Though the output of the cavity is lower than the last time the cavity was observed to be operating, the degradation agrees well with the predicted. If no attempt is made to switch back to TWT, the back-up radio switching should switch back to the TWT around November 14, 1967, ±66 days. At this time the output of the cavity should have decreased to 35.0 dBmW, and perhaps more will be learned about the reason for the switch.

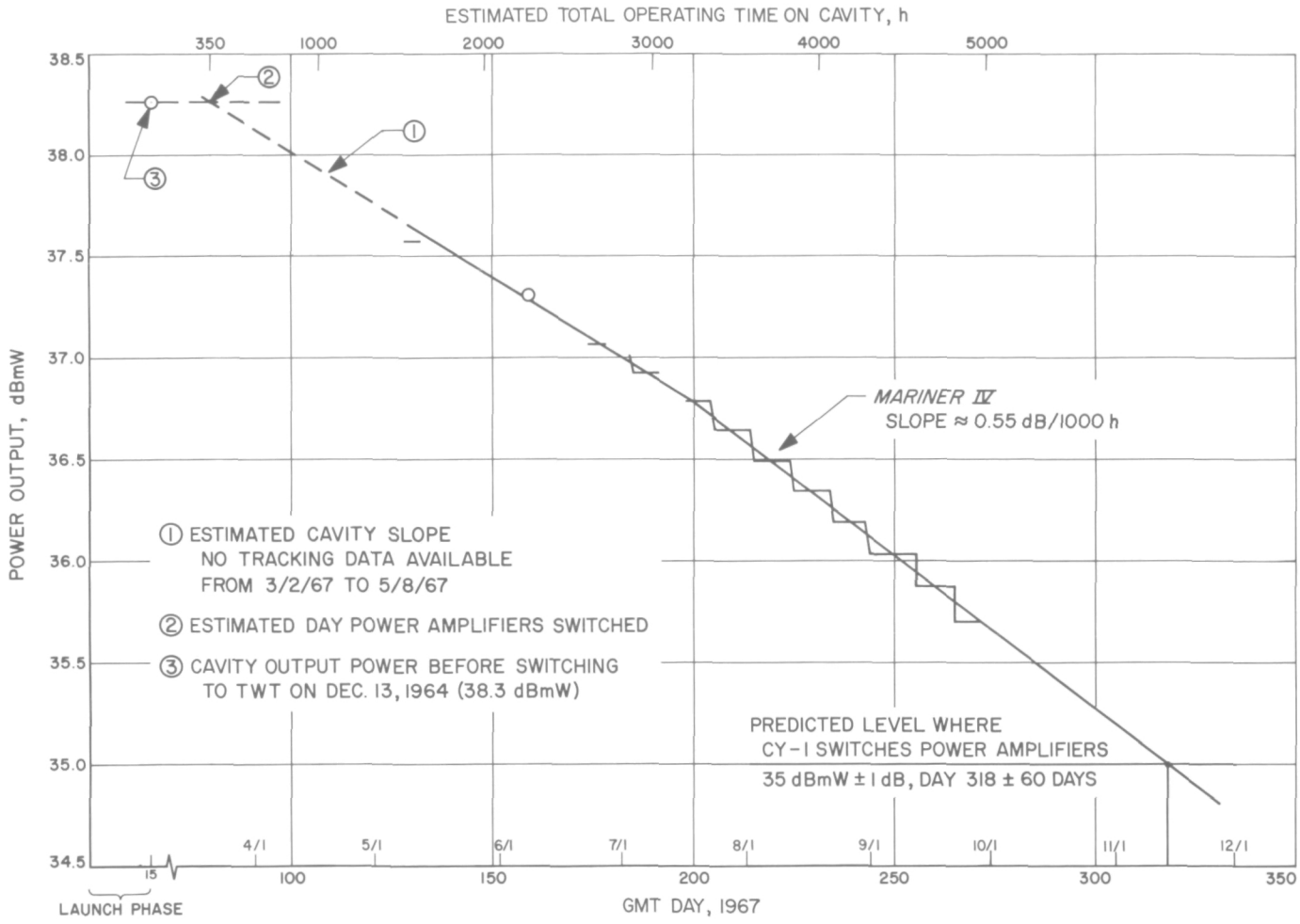

Fig. 1. *Mariner IV* cavity amplifier degradation versus time

II. *Mariner* Venus 67 Project

PLANETARY—INTERPLANETARY PROGRAM

A. Introduction

The *Mariner* Venus 67 Project is under the administrative cognizance of the *Mariner* 1967 Project Office, which is also responsible for the *Mariner* Mars 1964 Project and the *Mariner IV* Project (see Section I).

1. *Mariner* Venus 67 Project

The major task of the *Mariner* 1967 Project is the Venus flyby mission, named the *Mariner* Venus 67 Project. The following mission objectives have been established:

> *The primary objective of the Mariner Venus 67 Project is to conduct a flyby mission to Venus in 1967 in order to obtain scientific information which will complement and extend the results obtained by Mariner II relevant to determining the origin and nature of Venus and its environment.*
>
> *Secondary objectives are to acquire engineering experience in converting and operating a spacecraft designed for flight to Mars into one flown to Venus, and to obtain information on the interplanetary environment during a period of increasing solar activity.*

With the authorizing of this project late in December of 1965, and the launch opportunity occurring in June 1967, the period available to the *Mariner* Venus 67 Project for planning, design, test, and other flight preparation was 18 mo.

The single flight spacecraft, designated M67-2, was prepared by converting the spare spacecraft (MC-4) that was built for the *Mariner* Mars 1964 Project. An *Atlas-Agena D* launch vehicle was used to inject the spacecraft into a 127-day transit trajectory.

Seven scientific experiments were approved for the *Mariner* Venus 67 mission:

Experiment	Principal investigator
S-band radio occultation	Arvydas J. Kliore, Jet Propulsion Laboratory
Ultraviolet photometer	Charles A. Barth, University of Colorado
Dual-frequency radio propagation	Von R. Eshleman, Stanford University
Helium magnetometer	Edward J. Smith, Jet Propulsion Laboratory
Solar plasma	Herbert S. Bridge, Massachusetts Institute of Technology
Trapped radiation	James A. Van Allen, State University of Iowa
Celestial mechanics	John D. Anderson, Jet Propulsion Laboratory

The first experiment requires the use of only the RF transmission subsystem on the spacecraft, and the last one utilizes only the tracking doppler data received from the RF carrier. Of the remaining five experiments, four are to be accomplished with the existing instrumentation, with

only minor modifications. Only the dual-frequency radio propagation experiment of Stanford University requires the incorporation of a new scientific instrument into the payload.

Other changes to the basic spacecraft design were necessitated by the fact that the spacecraft will travel toward, rather than away from, the sun and also because conversions must be made to accommodate revised encounter sequencing and science payload. In particular, modifications were needed in the following areas:

(1) Scientific data automation system.

(2) Antenna pattern and orientation.

(3) Thermal control.

(4) Solar panel configuration.

(5) Planetary sensors.

2. *Mariner V*

Mariner V was successfully launched from the AFETR at 02:01 EDT June 14, 1967.

During the July–August reporting period, the *Mariner V* spacecraft continued to operate satisfactorily. Although the sensitivity of the ultraviolet photometer apparently degraded shortly after the midcourse correction maneuver, the instrument continues to operate in an apparently normal manner. No firm conclusions have yet been reached as to the nature of the change.

The spacecraft temperature control subsystem is performing as predicted. From June 28 to August 8, the solar intensity increased from 127 to 153 W/ft^2; solar intensity at Venus encounter is expected to be 248 W/ft^2.

Based on calculations thus far completed, it appears that all spacecraft assemblies will remain within their respective allowable temperature limits throughout the flight. Although the temperature of sun-exposed hardware increased 30°F and shaded hardware increased 10°F, the average bay temperature has increased only 2.1°F.

B. Systems

1. Space Flight Operations: Spacecraft Performance From Launch Through Midcourse (June 14 Through June 23, 1967)

a. Radio subsystem. The radio subsystem performed normally during this period. The cavity amplifier supplied spacecraft transmission power, and the spacecraft low-gain antenna was used for transmitting and receiving. Spacecraft RF power-up occurred normally at spacecraft separation. The radio subsystem data were consistent with preflight predictions.

Shortly after RF power-up, channel 214 (cavity power output to the low-gain antenna) began to decrease from an initial data number (DN) of 75. After the radio subsystem temperatures stabilized, channel 214 stabilized at a DN of 70 to 71. Based upon space simulator data, the cavity amplifier responded normally. The observed change was attributed to a decreasing temperature in Bay VI and to the time required for the cavity amplifier power output to stabilize. Channel 300 (cavity amplifier cathode current) also responded normally.

Predictions of Deep Space Instrumentation Facility (DSIF) acquisition frequencies for both uplink and downlink were based upon predicted spacecraft temperatures and curves of spacecraft transmitter and receiver frequencies versus temperature. The actual observed frequencies agreed with predictions.

During the midcourse maneuver, the radio subsystem temperatures increased by 8°F (within the predicted range). The spacecraft power switched from the solar panels to the battery during the pitch turn. While using battery power, channels 214 and 300 decreased by 1 DN. This decrease was a result of a slight drop of the cavity amplifier power supply voltage because of a lower primary input voltage from the spacecraft battery. After sun acquisition, channels 300 and 214 returned to their normal DN readings.

During the three rolls performed for calibration of the ultraviolet photometer, additional data were acquired pertaining to the antenna interferometer pattern. These data are presently being analyzed and will be used with data previously obtained to try to pinpoint the locations of the peaks and nulls in the spacecraft low-gain antenna pattern.

A DC-V9 command was transmitted to the spacecraft to turn on the ranging receiver (the first time a ranging receiver has been employed in a *Mariner*-type spacecraft). The following channels had changes in DN values to indicate that ranging was on:

(1) Channel 424 (spacecraft receiver VCO temperature) increased by 1 to 2 DN. This increase was attributed to the increased power (0.7 W) dissipated in the ranging phase detector module when ranging is on.

(2) Channels 203, 205, 225, and 227 (spacecraft power subsystem current monitors) increased by 1 DN. An increase in these channels reflects the additional 0.7 W of power drawn when ranging is on.

b. Command subsystem. Telemetry data of the subsystems to which the commands were sent indicated that all commands were detected and decoded properly.

c. Tape recorder subsystem. Nineteen tape passes were accumulated during the launch phase. The tape recorder was turned off approximately 5⅓ s after *Agena*/spacecraft separation (it will not be turned on again until Venus encounter).

d. Data encoder subsystem. One deck skip was observed at spacecraft separation (normal deck skip).

e. Attitude-control subsystem.

Gas subsystem. The spacecraft was launched with 5.18 lb of attitude control gas (2.58 lb in the $+x/-y$ tank, and 2.60 lb in the $-x/+y$ tank). Gas consumption during the launch through midcourse phase appeared to be normal. A longer period of operation will be required to establish the rate of consumption because so little gas was actually used.

Inertial sensors. Performance of the gyros was normal. The launch caused saturation of all three axes. While the separation rates cannot be easily measured, they were no smaller than +7.0 mrad/s (0.4 deg/s cw) in pitch, −15 mrad/s (0.86 deg/s ccw) in yaw, and −2.65 mrad/s (0.15 deg/s ccw) in roll. The decrease in angular velocity as the solar panels deployed was clearly visible at the time of the separation-initiated timer (SIT) event. The panels were deployed in less than 12.6 s; the angular velocity decreased by 1.4 mrad/s in pitch, 1.5 mrad/s in yaw, and 0.3 mrad/s in roll. Although conservation of momentum considerations would predict an increase in angular velocity in pitch and yaw at solar panel deployment, the increase of the moment arm of the gas jets (of approximately 1 to 8 ft) more than offsets the corresponding increase in angular velocity by acting to decrease the acquisition rates. The magnetometer calibrate spin rate was 78 DN or −3.72 mrad/s (12.8 deg/min). The search rate was 73 DN or −2.13 mrad/s (7.32 deg/min) based upon telemetry prior to acquisition. After earth acquisition, the spin rate was again 73 DN. However, after acquisition and subsequent deacquisition of the moon, the spin rate dropped to 71 DN or −1.86 mrad/s (6.4 deg/min) until Canopus acquisition.

After the gyros were turned on prior to the midcourse maneuver, the first gyro telemetry data indicated readings of 63 DN in pitch, 65 DN in yaw, and 64 DN in roll. Since the pitch, yaw, and roll DN readings did not change when the gyros were turned on, it was concluded that the turn-on transient was minimal.

The pitch and roll turn rates for the midcourse maneuver were in accord with those predicted. The data received following the turns indicated that the turns were accurate, and that they were performed according to the specified polarity and duration.

After the midcourse maneuver and the reacquisition of Canopus, a DC-V21 roll override command was sent to commence a ccw roll search; three roll searches were performed to provide further scientific data.

Celestial sensors. After emerging from the earth's shadow, all indications were that the earth sensor was apparently looking at the sun. Earth-sensor outputs were obtained during the magnetometer calibrate phase. Analysis of the apparent motion of the earth and its size will enable a very accurate measurement of the spin rate. In addition, an earth sensor output was obtained during the roll search, verifying the search rate and aiding identification of the objects acquired by the Canopus sensor.

The sun sensor initially showed saturated outputs. The spacecraft was driven cw in pitch and ccw in yaw to acquire the sun, but earthlight on the secondary sun sensors biased the electrical null approximately 78 mrad (4.5 deg) off the probe-sun line. The attitude control subsystem had acquired the false null in yaw and was limit-cycling about it; however, the null also had to be acquired in pitch to trigger the sun gate, because the sun gate field of view is about 5.1 deg.

The Canopus sensor was turned on for the first time at L-3. The acquisition of the earth was achieved. The maximum brightness noted was 30 DN, which corresponds to about 2.5 times that of Canopus; a brightness of about 0.75 × Canopus had been predicted. After the acquisition of the earth, two DC-V21's were transmitted to the spacecraft to override earth acquisition. The first DC-V21 was sent to the spacecraft to override acquisition on the earth's first stable null. The second DC-V21 was timed to arrive at the spacecraft shortly after the earth's second stable null was reached and before the gyros were turned off. The second command caused the spacecraft to roll off of the earth and, subsequently, acquire the moon. (A limit cycle was not established because the moon apparently

did not have a stable null.) The sensor moved off of the moon in the search (ccw) direction indicating a low gate dropout of between 48 and 49 DN (0.22 to 0.19 ×). The maximum observed brightness of the moon was 34 DN, about 1.6 × Canopus.

Roll search then continued until Canopus acquisition. The Canopus, sun, and earth sensors performed normally during the cruise and maneuver periods. During the roll searches after the midcourse maneuver, a star map was made by the Canopus sensor. This map was correlative to the a priori map produced by the Star Identification Program (*Mariner*) [SIPM] program. Several celestial objects were seen and identified in real-time. The earth sensor viewed the earth during these roll searches and during the initial Canopus reacquisition. An accurate analysis of the search rates and of the spacecraft clock angle at given times during the search is currently in process.

Control system. During the motor burn, the autopilot performed its function of maintaining the thrust vector orientation of the spacecraft. The results were inferred from the post-midcourse analysis of the pitch and roll turns. A detailed analysis of the attitude control subsystem indicated large deflections of the jet vanes during the motor burn of the midcourse maneuver. These deflections occurred in a manner such as to correct an apparent torque about the thrust axis. The deflections produced a drag which decreased the velocity increment of the motor burn. A tentative estimate, resulting from an investigation undertaken to determine the magnitude of error that this drag contributed to the total ΔV error of 4.5%, indicated that the deflections of the jet vanes produced a drag which possibly contributed a nominal error of 4.3%, a best case error of 2.8%, or a worst case error of as high as 6.3%. This investigation is continuing, and the results will be published at a later date.

f. Central Computer and Sequencer (CC&S) subsystem. All launch and maneuver events occurred as planned. The CC&S clock error at the time of the midcourse maneuver was −0.0014% at a case VII temperature of 55°F and was consistent with prelaunch predictions. The CC&S timing of events in telemetry channel 220 gave the correct number of overflows and the expected final readings for each of the turns and for the motor burn. The resolution of this channel is twice the word sync time (±0.42 s).

g. Power subsystem. A total of 4.3 Ah was consumed from the battery during launch and 0.6 Ah during the test period A-7 to A = 0. A total of 50.7 Ah was available at sun acquisition, indicating that an assumed nominal of 55.0 Ah was available at T-7. By 21:00 GMT on June 18, 1967 4.1 Ah had been returned to the battery. Because of the much lower charge rate used on the flight charger, a greater capacity will be returned to the battery than existed at launch. This is expected because the operational support equipment (OSE) charger cannot fully top off the battery at the constant current 1.9-A rate.

During the midcourse maneuver, a total of 2.33 Ah was consumed from the battery. A total of 53.17 Ah was available at sun reacquisition. A calculated total of 55.5 Ah was available prior to the midcourse maneuver. The battery supplied somewhat more power during the maneuver than was originally estimated but was within tolerance.

The shading of the solar panels by the spacecraft bus occurred as expected during the maneuver.

h. Temperature-control subsystem. Very little change was observed in the spacecraft temperatures during ascent and parking orbit. Temperatures at sun acquisition were within expected tolerances. The cooling of external items occurred during boost because of the gas expansion under the shroud. Further cooling occurred while the spacecraft was in the earth's shadow. Based upon the near-normal temperatures, it can be clearly inferred that the sun shade has properly deployed.

When the spacecraft entered the near-earth cruise configuration, the temperatures remained within design limits. The average spacecraft temperature was 2°F above the predicted level during pre-Canopus acquisition, and 1°F above the predicted level after Canopus acquisition. There were no bus temperatures that were more than 4°F from prediction during pre-Canopus acquisition, nor more than 2°F from predicted post-Canopus acquisition. As was expected, temperatures of equipment external to the bus show larger deviations from those predicted.

During the midcourse maneuver, the bay II primary sun sensor reached a maximum temperature of about 98°F (12°F lower than predicted). The difference between the predicted and actual ΔT is almost wholly attributed to considerably less severe "soakback" from the motor burn than had been expected. The majority of the temperature rise was attributed to solar heating. The thermal analysis which constrains the pitch angle for near-sun maneuvers considered only this heat factor;

therefore, the constraints generated prior to launch appear to be realistic.

After the post-midcourse sun acquisition, an apparent anomaly in the $-y$ pitch jet temperature (channel 425) was observed. A temperature of $-21°F$ was observed 2 min before sun acquisition was completed. At 41 min after sun acquisition, a 1-DN decrease in temperature to $-23°F$ was observed. There had been solar heating and a conduction heat input to the assembly for 40 min prior to the anomalous reading; therefore, such a decrease in temperature was very unexpected. The results of analysis suggested two possible explanations: (1) The pitch jets continued to release a considerable amount of N_2 at the time of the anomaly which caused cooling of the assembly because of gas expansion, and (2) At the time of sun acquisition, the gas valves were subcooled approximately 10°F (because of gas expansion during acquisition) below the manifold temperature. If (1) was a valid assumption, the average temperature of the assembly would have increased because of increased solar heating, while the measured temperature would be decreasing because of heat losses to the cooler valves. The latter theory is more plausible, but both the test data and the flight data are insufficient to permit a positive conclusion.

During this reporting period, the structural and mechanical devices, and the temperature control references performed as follows:

Structural and mechanical devices. The nominal spacecraft performance indicated that the spacecraft structure performed adequately through the critical launch and boost environments. The pyrotechnics arming switch (PAS) actuated normally, and the SIT squib-firing current event occurred normally, allowing for a maximum of seven seconds deployment time for solar panels. The corresponding SIT actuation time was 170 to 175 s (corresponds to a SIT temperature of 74 ±4°F). This temperature range nearly agrees with the predicted value of 80°F; therefore, it can be concluded that the SIT operation was normal.

Temperature control references (TCR). Temperature control reference data were obtained approximately ½ h after sun acquisition. All values were within predicted tolerances. A subsequent decrease in DN value of channels 413 and 432 over the following 3 h indicated a thermal input from the earth early in the mission. (There was a similar effect on the solar panels.) The lower equilibrium temperatures, apparently beyond earth influence, were still within tolerance.

The changes on the white TCR's (412, 432) have permitted resolution of change in solar absorptance (change only, not absolute value) of white coatings to an order of magnitude better than is possible in the laboratory.

The results recorded during the second week of flight indicated that the temperature control coatings on the TCR's performed differently in space than during laboratory tests, which further supports the results of the first week of flight. White S-13M continued to darken at a faster rate than expected, black continued to bleach at a faster rate than expected, and the white S-13 degraded faster than predicted.

i. Postinjection propulsion subsystem. The telemetry data indicated that the propulsion subsystem maintained a normal condition during launch. The thrust chamber pressure dropped to zero as the shroud cavity pressure dropped, as expected, during the boost phase. After injection, the propulsion subsystem ΔV capability was about 92.1 m/s.

Following injection, propulsion subsystem temperatures decreased to within 2°F of the predicted values. As the temperatures decreased, the pressures decreased according to predictions. During this dynamic period from launch through injection, the propulsion subsystem remained leak-tight.

Data analysis indicated that thermal equilibrium of the postinjection propulsion subsystem occurred during cruise by day 169 (June 18, 1967). The temperature and pressure parameters were:

Parameter	Postlaunch	Cruise equilibrium
Thrust chamber pressure	0 psia	0 psia
Fuel tank pressure	293 psia	277 psia
Fuel tank temperature	71°F	56°F
Nitrogen tank pressure	2961 psia	2870 psia
Oxidizer pressure	398 psia	390 psia
Terminator sensor excitation	off	off
Nitrogen tank temperature	67°F	52°F
ΔV capability	92.1 m/s	91.9 m/s

All parameters were in agreement with the tolerances of prelaunch predictions.

The propulsion subsystem performance during the motor burn of the midcourse maneuver appeared normal in all respects. There were deviations of 2 or 3 DN from the predicted chamber pressure. Based on previous experience, such small deviations from predictions were considered acceptable and not necessarily indicative of nonstandard subsystem performance.

After the midcourse motor burn, temperatures during "soakback" were not excessive. When cruise conditions were established following the maneuver, temperatures returned to within 1°F of premaneuver values. There were no indications of any leaks during or following the midcourse maneuver. The telemetered propulsion parameters during and immediately following the motor burn were:

Parameter	DN	Engineering unit
Thrust chamber pressure (during steady state)	79-80	185-187 psia
Propellant tank pressure (during steady state)	79	306 psia
Propellant tank temperature	37	59°F
Nitrogen tank pressure (at end of motor burn)	79	2438 psia
Oxidizer pressure (at end of motor burn)	93	362 psia
Nitrogen tank temperature	47	69°F

Postmaneuver tracking data indicated that the velocity increment imparted to the spacecraft during the maneuver was approximately 4.5% less than planned. An extensive investigation was initiated in an attempt to determine if the cause of the deviation from the predicted trajectory was attributable to an error in the velocity increment provided by the motor burn.

j. Pyrotechnics subsystem. All pyrotechnic subsystem parameters remained normal during and subsequent to launch. Pyro was armed by the PAS at separation and the event was recorded in register 3. Solar panel pinpullers were fired by the SIT at 06:30:19 GMT, and events were recorded in registers 1 and 3. No additional events were recorded when the CC&S L1 (solar panel deployment) occurred. The terminator sensor excitation remained off as expected.

During the midcourse maneuver, pyrotechnic events were recorded in registers 1 and 3 for both motor burn start and motor burn stop. It can be concluded from the telemetry data that both pyro units discharged, and that all squibs probably fired when commanded.

The terminator sensor excitation remained off as expected.

k. Science subsystem. All science instruments maintained their normal condition during launch. Following spacecraft separation, the plasma probe high-voltage inhibit was removed; the magnetometer was saturated on all axes; and the magnetometer ignition backup, UV photometer calibration and drift check, dual frequency receiver (DFR) calibration, and data automation system functions were normal.

The trapped radiation detector observed the Van Allen belts, as expected. The magnetometer roll calibrate was normal. The Stanford University antenna began sending signals to the DFR shortly after *Mariner V* first rose over the Stanford horizon. The DFR responded properly. After the midcourse maneuver, two anomalies were observed in the science data. Both anomalies occurred in the ultraviolet photometer data. The ultraviolet photometer calibrate and drift-check sequence changed during the telemetry mode 1 period. Additionally, the ultraviolet photometer C-tube readings decreased from approximately 20 DN before the midcourse maneuver to approximately 6 DN after the midcourse maneuver and Canopus acquisition. Both anomalies are being evaluated.

C. Telecommunications

1. Spacecraft Antennas

a. Introduction. Two antenna subsystems in use on the *Mariner V* spacecraft—the S-band and the dual-frequency receiver (DFR)—are discussed here. The S-band antennas are the same as were used on *Mariner IV*. The antennas are for telemetry, RF tracking, and command coverage. In addition, the S-band high-gain antenna will be utilized in the performance of the S-band radio occultation experiment. The DFR antennas were designed, fabricated, and implemented by JPL to provide coverage for the Stanford dual-frequency radio propagation experiment. The DFR antenna subsystem is new for *Mariner V*, and this article will include the design evolution and

special problems associated with the antennas, as well as their description. In the case of the S-band antennas, changes required from those used on the *Mariner IV* spacecraft are emphasized. Figure 1 shows the various *Mariner V* antennas.

b. S-Band antenna subsystem.

Low-gain antenna. The look angles to earth relative to the low-gain antenna during its period of primary use (first 100 days) for a Venus-bound spacecraft with its sun axis reversed are somewhat similar to those for Mars in 1964. Hence, the *Mariner IV* spare low-gain antennas could be used as is for the Venus 67 mission.

High-gain antenna. However, after the first 100 days, the two mission trajectories are quite dissimilar. In particular the look angles in the case of Venus '67 continue away from the low-gain peak, while those of Mars in 1964 reversed and retraced themselves with very little angular change during the last half of the mission. This was the primary reason for being able to use a fixed high-gain antenna in the Mars 1964 mission.

Moreover, since the quality occultation experiment is highly dependent on the high-gain antenna performance, the experiment's requirements strongly influenced the antenna's design. As the spacecraft passes behind the planet, the RF signals from the high-gain antenna pass through the dense Venus atmosphere, which not only attenuates the signal but bends it in the direction of the planet's curvature. Hence, the apparent direction of earth moves back along the trajectory track as the spacecraft goes behind the planet and reappears ahead of the earth track as it emerges from behind the planet.

After extensive study of the problem of optimizing the antenna's performance to allow for the deepest penetration of the Venus atmosphere, it was determined that the *Mariner IV* high-gain antenna with two pointing directions was more advantageous. The antenna is launched in a position such that it optimizes coverage going into planetary occultation. After loss of signal due to occultation while the spacecraft is behind the planet, the antenna is stepped to a second position which optimizes coverage as the spacecraft emerges from behind the planet.

The changes to the antenna to accommodate the two positions included the addition of a new mounting interface structure and revision of the coaxial cabling between the antenna and the electronics case.

Environmental testing. The environmental requirements for a Venus mission were different from those for a Mars mission. Primarily, the Venus mission exposed the antennas to low temperatures; whereas the Mars mission involved high temperatures.

Thermal-vacuum and magnetic field testing were the only type-approval (TA) level tests performed on the low-gain antennas. Unit level flight-acceptance (FA) vibration testing was accomplished for each flight antenna to determine if impedance changes occurred for any of the antennas as a result of the launch environment. This was necessary because the mismatch was tuned for a certain impedance range. The performance could, therefore, be degraded by excessive changes in antenna impedance. Measurements made before and after vibration indicated that no changes occurred.

In the case of the high-gain antenna, unit-level TA thermal-vacuum testing (required because of the different temperature environment on Venus) and unit-level vibration testing (required because of the change in mounting from that on *Mariner IV*) were performed. Unit-level FA vibration and thermal vacuum testing were also performed on each flight high-gain antenna. Also low-temperature deployment testing of the high-gain antenna was accomplished with the mounting superstructure, deployment mechanism, pyrotechnics, antenna, and associated cabling in a vacuum chamber where it was oriented to simulate a zero gravity condition. RF energy was transmitted through the coaxial cable to the antenna to simulate the minimum power anticipated in flight. Difficulty in obtaining proper low-temperature deployment was overcome after rearrangement of the cable routing.

Full-scale spacecraft model measurements. A full-scale antenna test model (ATM) spacecraft was used early in the mission analysis, as was used for *Mariner IV,* to determine the adequacy of the high-gain and low-gain antenna patterns. The ATM spacecraft was a sheet metal and window screen mock-up of the flight spacecraft and did not include any flight parts. Pattern data obtained on the ATM spacecraft indicated that no performance degradation would occur as a result of the *Mariner V* configuration changes.

A full-scale developmental test model (DTM) spacecraft which used many flight-type parts and was dimensionally accurate, was used for the final antenna patterns. These patterns were recorded on magnetic tape prior to launch as an estimate of the actual performance in flight. The primary purpose of recording final flight patterns

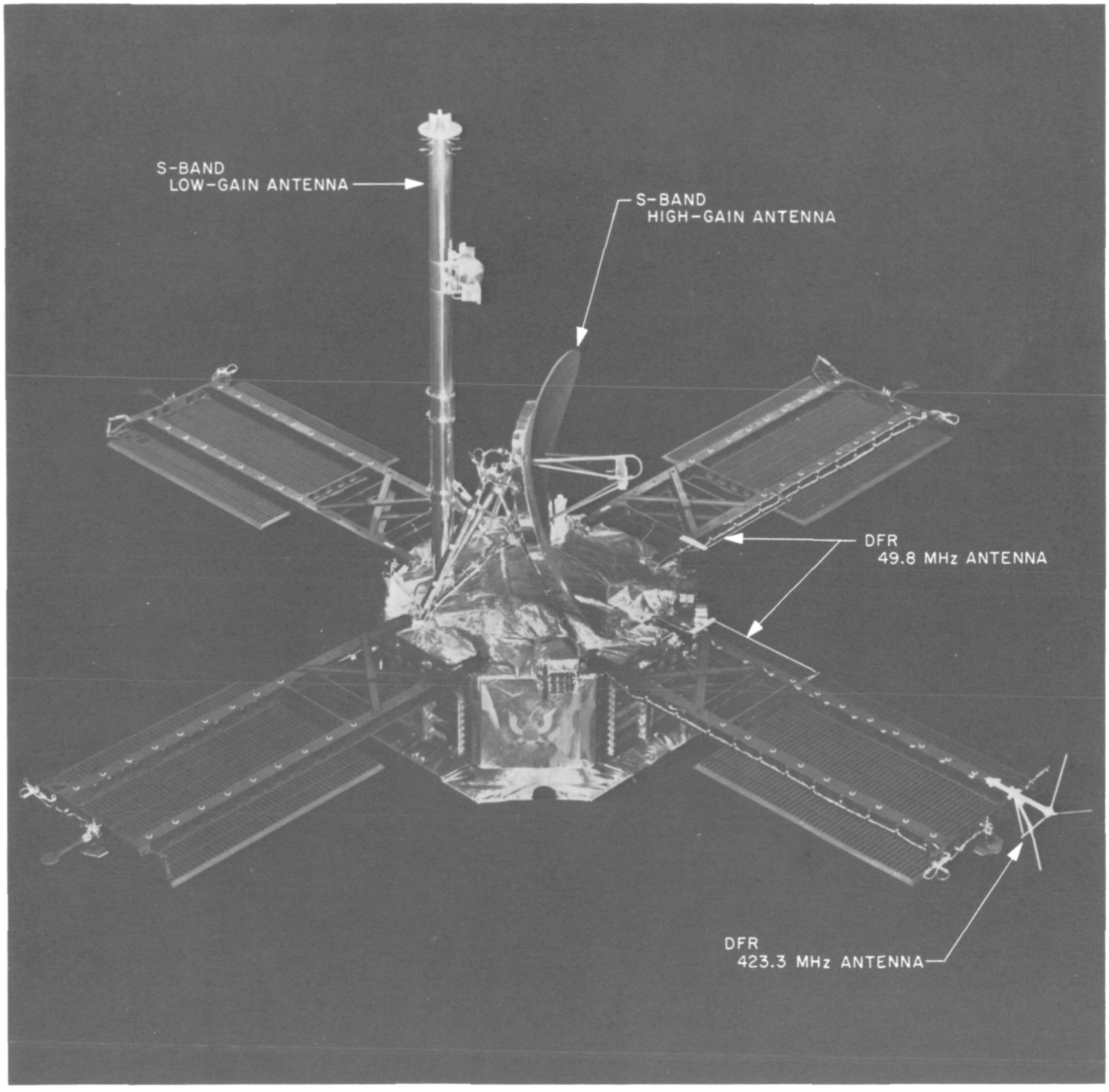

Fig. 1. *Mariner V* with S-band and DFR antennas

on a full-scale spacecraft model was to include the diffraction and multipath distortion effects which would be seen in flight due to the spacecraft structure.

c. Dual-frequency receiver antenna subsystem.

Subsystem description. The DFR antenna subsystem was implemented on *Mariner V* for the reception of signals at 49.8 and 423.3 MHz transmitted from earth to the Stanford dual-frequency radio propagation experiment on the spacecraft. The subsystem consists of an antenna, transmission lines, and a filter for each frequency.

The 49.8-MHz antenna consists of shunt feeding the two adjacent spars of the spacecraft Bay I and Bay III solar panels simultaneously through a power divider "T" element. The Bay III feed unit consists of a series-variable matching capacitor mounted on a terminal board bracket, with a conductor wire which extends between the terminal board bracket and a parallel-mounted shunt feed bracket 19 in. farther out on the solar panel spar. The Bay I and Bay III feed units are identical except that Bay III has a series tuning capacitor on the terminal board. Each feed unit is fixed relative to the respective solar panel, and the antenna is therefore deployed with the panels. The tuning of the antenna is determined by the relative coaxial line lengths connecting the "T" element to the feed units and adjustment of the series capacitor on the Bay III solar panel feed unit. The maximum antenna gain at 49.8 MHz was most nearly in the direction of earth at encounter. This direction is 104.0 and 102.5 deg in spacecraft cone and clock angle, respectively. From the "T" element the antenna is connected to the DFR through two lengths of flexible coaxial cable and a bandpass filter.

The 423.3-MHz antenna consists of a quarter wavelength stub radiator with two reflector elements over four ground plane radials. The ground plane radials are at 90-deg angles to each other and form a 120-deg conic angle with the stub. The reflector elements are each mounted on a radial and are parallel to the stub. The antenna is mounted on a mast at the tip of the Bay III solar panel spar. The entire antenna assemblage remains in a fixed position relative to the solar panel and is therefore deployed with the panel. The mast consists of aluminum tubing with an inner conductor, which connects the coaxial cable center conductor to the antenna stub. The antenna is implemented such that the maximum gain at 423.3 MHz is most nearly in the direction of earth at encounter. The received 423.3-MHz antenna signal is passed from the solar panel across the panel hinge and then through a low-pass filter to the DFR.

The final electrical parameters of the 49.8- and 423.3-MHz antennas are listed in Table 1. These data were based on the combined results of all data collected during the design development of the antennas in the following descriptions.

Design. The performance requirements specified by Stanford for the DFR antenna subsystem are summarized as follows:

(1) Gain (in the direction of earth at encounter, relative to linear isotropic):
49.8 MHz antenna ≥ 0 dB.
423.3 MHz antenna $\geq +4$ dB.

(2) The primary pattern coverage requirement for each antenna is the minimum gain at encounter specified above. The antenna pattern should contain no rapid variations or nulls within the envelope of expected look angles predicted for the period one month after launch to encounter.

(3) Impedance
49.8 MHz antenna. VSWR $\leq 2.0{:}1$ over a bandwidth of at least 2%.
423.3 MHz antenna. VSWR $\leq 1.5{:}1$ over a bandwidth of at least 2%.

(4) Each antenna will be used for receiving only.

(5) The S-band power at the terminals of either DFR antenna should not exceed +20 dBmW.

Table 1. DFR antenna parameters

Parameters	49.8-MHz antenna	423.3-MHz antenna
Gain (in direction of earth at encounter relative to linear isotropic)	+0.5 dB	+5.5 dB
VSWR (at center frequency)	1.15 to 1	1.13 to 1
Bandwidth (2:1 VSWR)	0.95 MHz	21.0 MHz
Cabling insertion loss (from gain measurement point to receiver, including filters)	0.8 dB	0.95 dB
Polarization	Linear	Linear
Mutual coupling (Minimum isolation between antenna terminals)		
At 2297.6 MHz from high gain	57 dB	62 dB
At 2115.7 MHz from high gain	56 dB	54 dB
At 423.3 MHz from high gain	—	79 dB
At 49.8 MHz from high gain	70 dB	—

The experiment includes operation during occultation, which involves the change in the apparent direction of received signals due to refraction by the planet atmosphere. It is desired that signals incident at the spacecraft from both sides of the planet be received at the DFR. Since the change in direction will be of opposite polarity for signals incident from opposite sides of the planet, a very broad pattern is required. Further, since bending due to refraction is greater at 49.8 than at 423.3 MHz, the pattern for the 49.8-MHz antenna must be broader than that for the 423.3-MHz antenna.

A further constraint was that implementation of the DFR antennas could not degrade the spacecraft system in any way. This included consideration of S-band antenna operation as well as maintenance of clear fields of view for the spacecraft attitude-control and instrument sensors.

Development. In general, the measurement of the effects of the spacecraft structure are of great concern in the case of spacecraft antennas. This is especially true for the DFR 49.8-MHz antenna, since part of the spacecraft serves as the antenna. Therefore all antenna measurements were performed in a simulated spacecraft environment by use of either scaled or full-scale models.

(1) Scaled Model Measurements. During the initial phase, a 1:8.5-scale model spacecraft was used. Later a 1:5-scale model spacecraft was used for additional development and for comparison of results with those of the 1:8.5-scale model. The design of the full-scale test antennas was accomplished according to results obtained from the scaled model antenna patterns. The models are shown in Fig. 2.

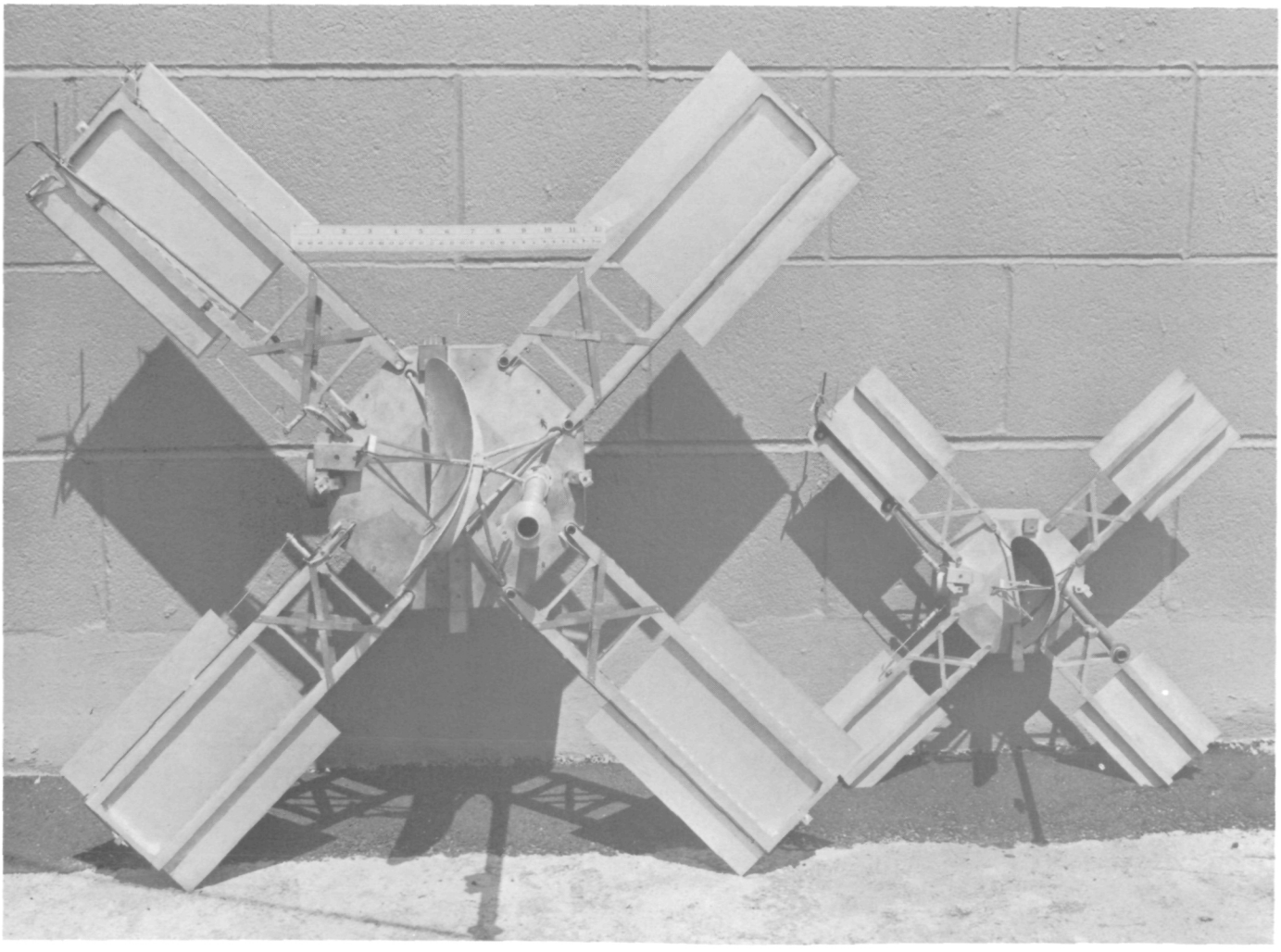

Fig. 2. Scale models (1:5 and 1:8.5) of *Mariner V*

(2) Preliminary Full-Scale Model Measurements. Beginning the final stages of the design development, measurements were made using a full-scale antenna test model (ATM) spacecraft. Verification of scale-model results and refinement of the scale-model design were accomplished during this phase as well as selection of coaxial cabling. Measurements of the isolation between the S-band and DFR antennas were also made at the antenna range on the ATM spacecraft. The results of these measurements are recorded in Table 1 and indicate that the S-band power at the input terminals of the DFR antennas will be less than the required maximum of +20 dBmW.

Final full-scale measurements. Following antenna fabrication and completion of the required environmental tests, the flight-type antennas were measured on the DTM spacecraft. The DTM was a full-scale spacecraft with flight-type parts, except that the electronics were removed from the bays, the solar cells were omitted from the solar panels, and the flight sensors were mocked-up.

VSWR, gain, and pattern data were recorded for each set of 49.8-MHz flight antenna feeds on the DTM spacecraft. The patterns were recorded with linearly polarized illumination and were recorded over only a sector. These patterns showed that the peak of the beam was properly pointed and that there were no deep nulls in the vicinity of the encounter angles. Figures 3 and 4 show the antenna's radiation patterns.

VSWR, gain, and pattern data were recorded for each of four 423.3-MHz flight antennas on the DTM spacecraft. Gain and pattern measurements were in good agreement with the other model results. Patterns were recorded with circularly polarized illumination to represent accurately the flight condition. Figures 5 and 6 show the 423.3-MHz antenna's radiation patterns. The flight data recorded in Table 1 were determined from the measurements on the DTM spacecraft.

Special tests. Several residual problem areas existed following delivery of the flight-qualified antennas. These problem areas included verification of the proper tuning of the 49.8-MHz antenna on the flight spacecraft, and verification of proper operation of both the 49.8-MHz and 423.3-MHz antennas on the flight spacecraft. Special investigation and testing are discussed below.

Tuning of 49.8-MHz Antenna on Flight Spacecraft. The method of exciting the spacecraft structure created the problem of obtaining performance repeatability between the scaled models and the flight spacecraft. This further involved the problem of obtaining sufficiently accurate and repeatable measurements for verification of the performance. The full-scale gain, VSWR, and pattern measurements for the ATM and DTM spacecraft provided a relative comparison between test model feeds on a rough spacecraft (ATM) and the flight feeds on a more flight-like spacecraft (DTM). In particular, the method of tuning to place the peak of the beam in the proper direction was verified. This also indicated that performance obtained on the full-scale spacecraft model would be repeatable on the flight spacecraft. Therefore, it was planned that the flight feeds were to be installed on the flight spacecraft after being tuned on the DTM spacecraft at the antenna range.

The problem remaining after the flight feeds were tuned at the antenna range was to verify that the flight feeds remained tuned without adjustment when mounted on the flight spacecraft. Since the flight spacecraft could not be taken to the antenna range, it was questioned if a valid VSWR measurement at 49.8 MHz could be made in the spacecraft assembly facility (SAF). A set of test feeds were tuned on the DTM spacecraft at the antenna range and then installed on the flight spacecraft in the SAF. The VSWR measurements were made in the SAF with the flight spacecraft on its dolly and suspended 15 ft above the floor by nylon ropes. The VSWR bandwidth was monitored on a scope with the reflectometry setup. The VSWR in all cases remained the same as that measured at the antenna range.

Final Verification. VSWR and radiative coupling measurements were made at Cape Kennedy for the 49.8-MHz antenna to verify that the feeds and cables were properly connected and that the tuning had not changed. VSWR and radiative coupling measurements were also recorded for the 423.3-MHz antenna at Cape Kennedy to verify proper cable connections and operation. The coupling measurements were performed by radiating 49.8- and 423.3-MHz signals at varying levels to the appropriate spacecraft antenna from a test antenna located close by the spacecraft. The received signals were translated to data numbers and retrieved from the spacecraft via the S-band telemetry link for evaluation.

2. *Mariner V* Radio

a. Introduction. The *Mariner V* radio subsystem is basically the same as the system used on *Mariner IV*.

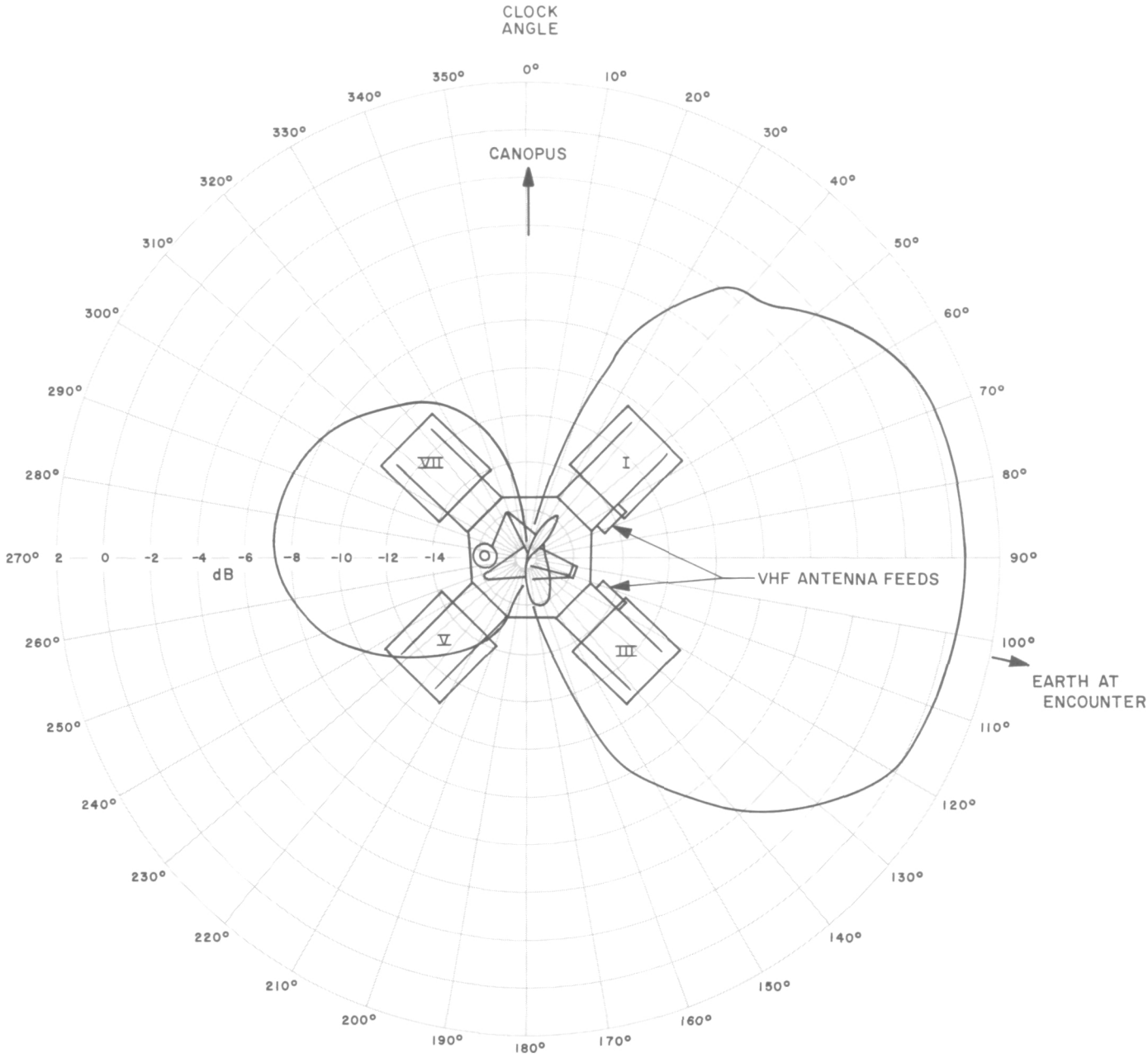

f = 49.8 MHz
RIGHT-HAND CIRCULAR ILLUMINATION

Fig. 3. 49.8-MHz antenna radiation pattern in the x-y plane of the spacecraft

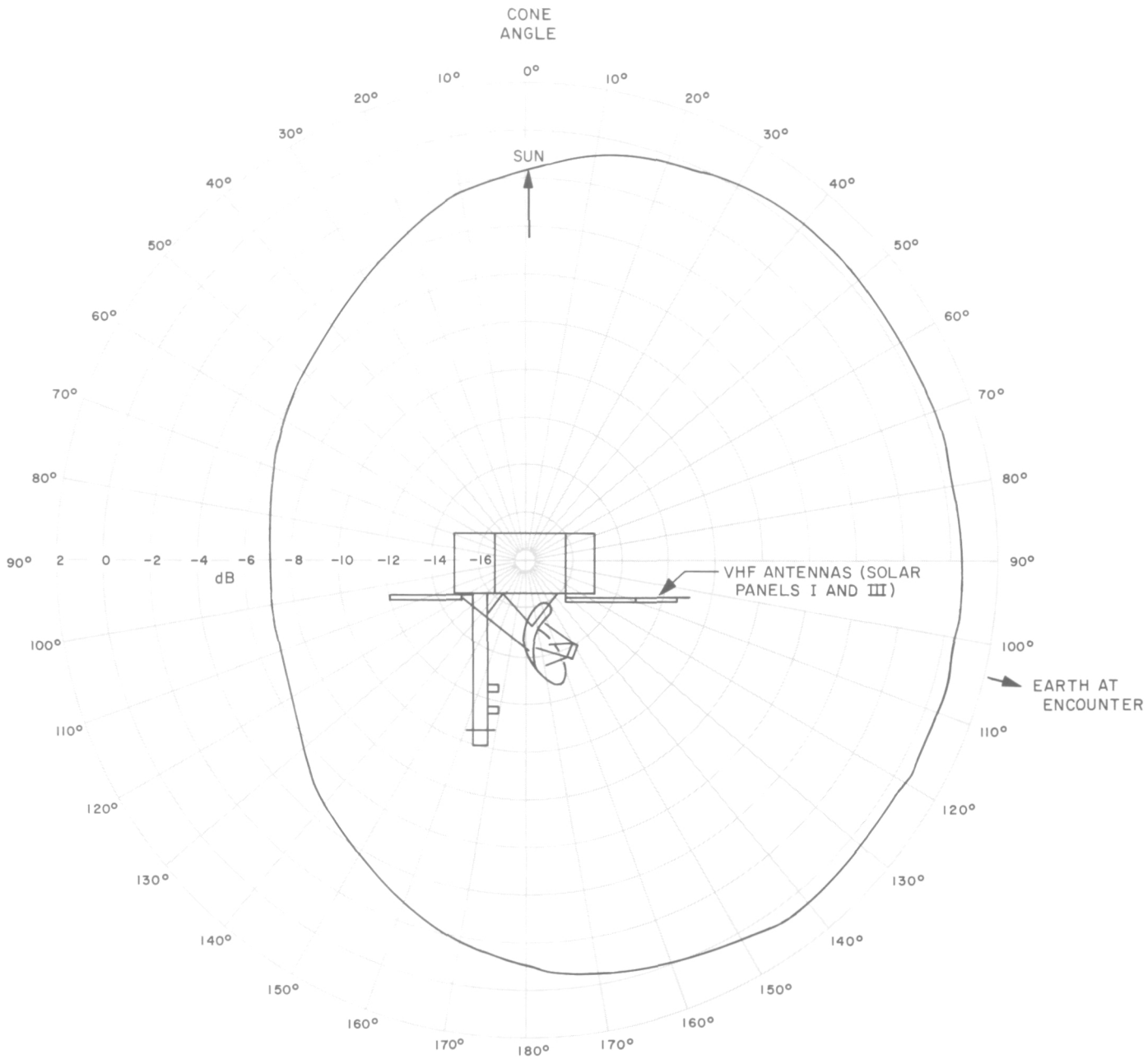

f = 49.8 MHz
RIGHT-HAND CIRCULAR ILLUMINATION

Fig. 4. 49.8-MHz antenna radiation pattern in earth-sun plane at encounter

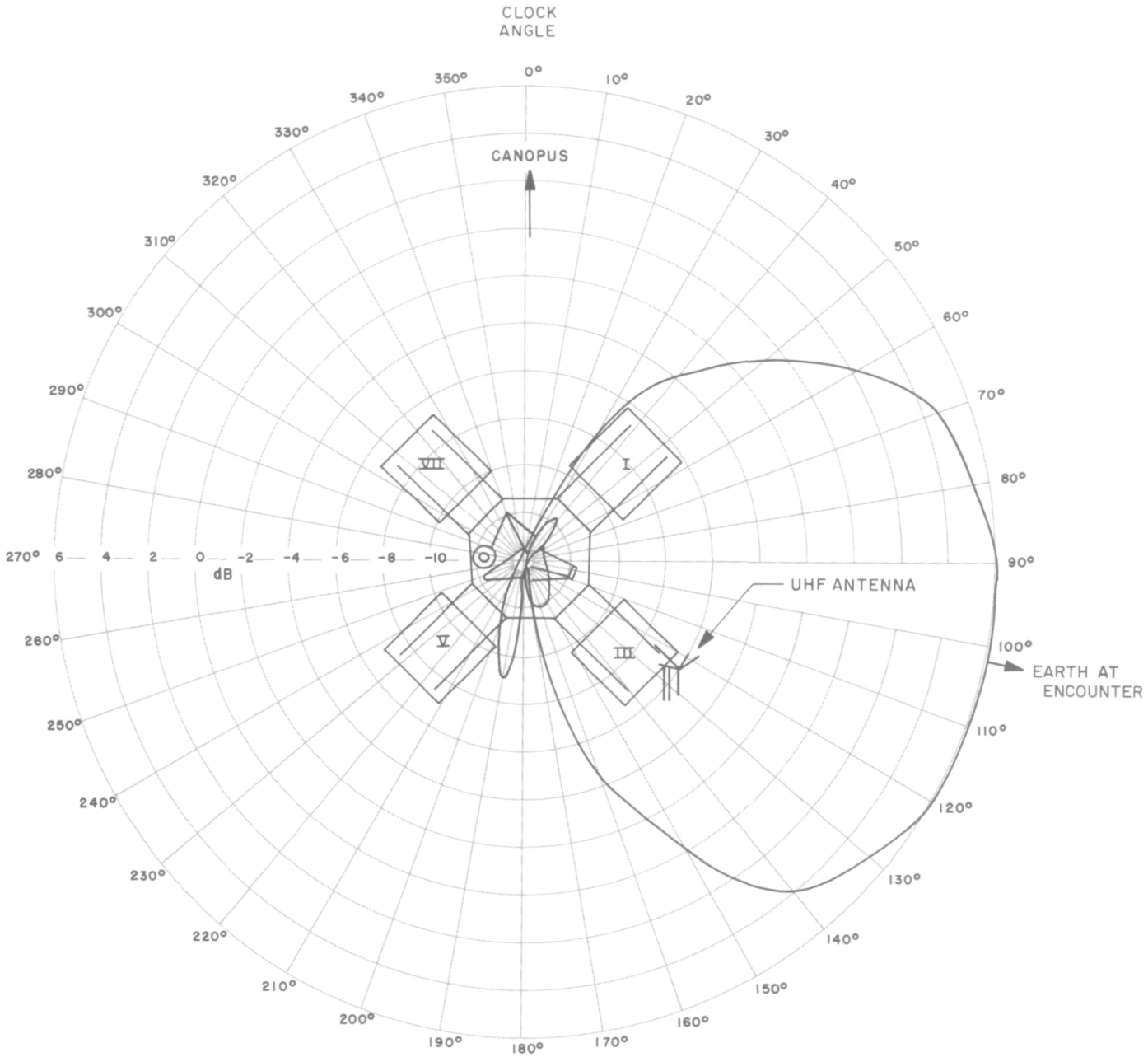

f = 423.3 MHz
RIGHT-HAND CIRCULAR ILLUMINATION

Fig. 5. 423.3-MHz antenna radiation pattern in the x-y plane of the spacecraft

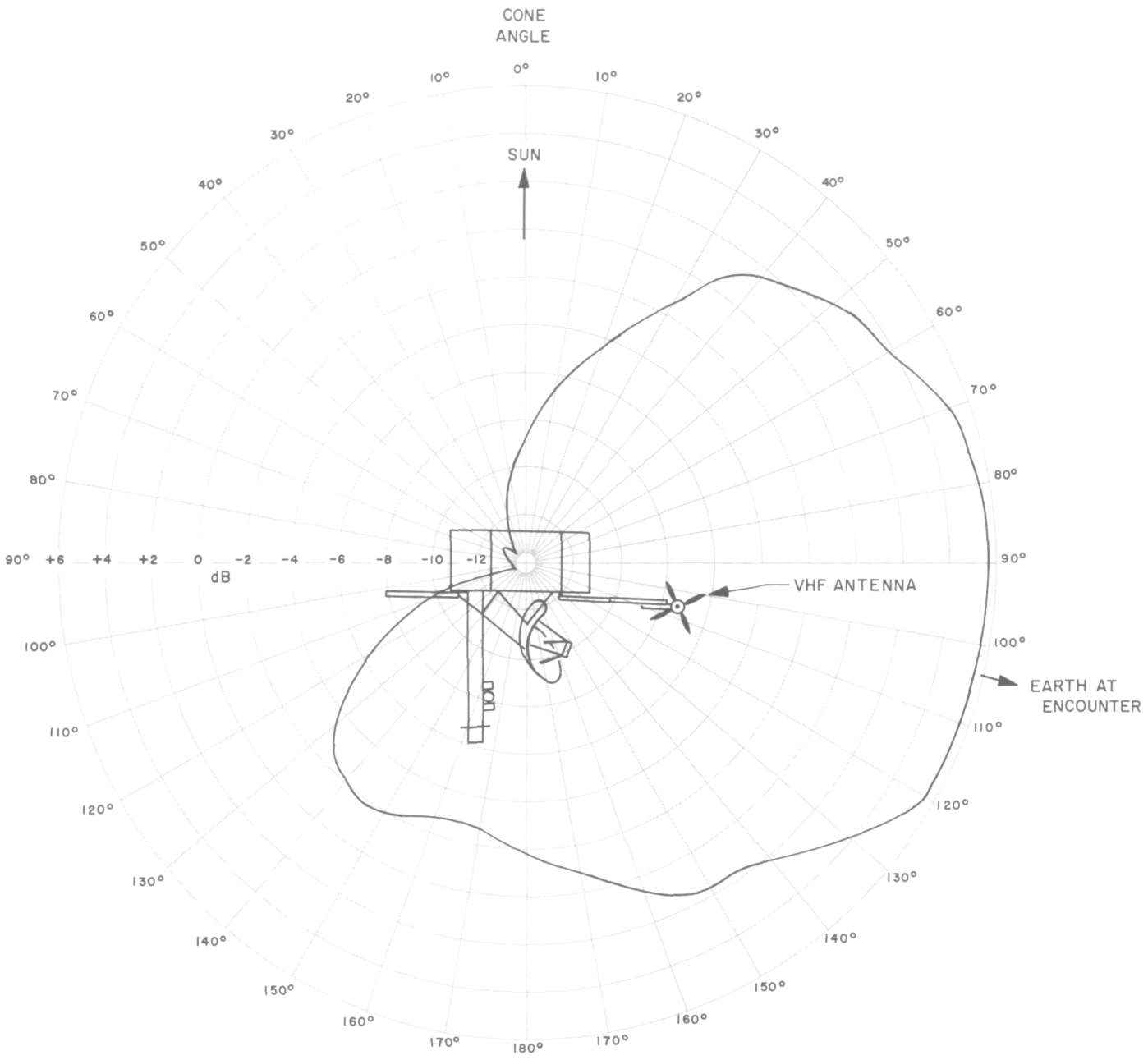

f = 423.3 MHz
RIGHT-HAND CIRCULAR ILLUMINATION

Fig. 6. 423.3-MHz antenna radiation pattern in earth-sun plane at encounter

There have been some modifications to the *Mariner* Mars 1964 design to make it compatible to the *Mariner* Venus 67 mission requirements. However, these changes did not greatly change the design or functional requirements of the radio subsystem. In the block diagram of the *Mariner V* radio subsystem (Fig. 7) the shaded areas indicate the changes made. Some other changes were required in the circuit to reduce the probability of self-lock occurring to the receiver. Self-lock was a potential problem on *Mariner IV* which could only be prevented by leaving the transponder ranging channel off. When ranging was on, there was a strong possibility of the receiver acquiring phase lock to an internally generated spurious signal. Since the receiver responds only to signals to which it is phase-locked, the occurrence of self-lock could have effectively failed the transponder two-way tracking capability and prevented the receiver demodulation of ground transmitted direct commands. Some minor circuit modifications in both the receiver and exciter either eliminated or reduced the probability of certain known self-generated spurious signals. However, to provide even greater assurance against self-lock, the filters described below were added to greatly attenuate any possible spurious signals in the self-lock frequency region. The additions were a low-pass filter at the input of the receiver and a bandpass/low-pass filter at the output of the exciters. The notch filter at the output of the TWT was retained to reduce the effect of broad-band noise and possible spurious signals at the receiver input. The notch filter was removed from the cavity input because the bandpass/low-pass filter accomplished the same function. The interferometer fix, denoted as the tuned mismatch in Fig. 7, was added to reduce the effect of the interferometer at the critical planetary encounter phase of the mission. Without the fix, command capability to the spacecraft near encounter would not be reliable because of the periodic nulls produced by the simultaneous reception of the uplink signal over both the low-gain and high-gain antennas due to the leakage inherent in the antenna switch design. Other changes noted on the block diagram were required for the change in transponder operating frequency, telemetry additions and changes, and for system reliability.

b. Radio description. The *Mariner V* radio design met the same general requirements as the *Mariner IV* due to their close similarity. The duration of operation was, of course, relaxed to a period of about five months. The radio is contained in Bays V and VI of the spacecraft. Bay V contains the receiver and its transformer–rectifier type of power supply, while Bay VI contains the transmitter–exciter, the RF power amplifiers, the control unit, all RF components, and all the associated power supplies. The radio can: (1) receive and demodulate command signals, (2) modulate and transmit spacecraft telemetry, (3) receive and retransmit the turnaround ranging code, and (4) provide a coherent signal for tracking. A functional block diagram of the radio is presented in Fig. 7.

Receiver. The receiver is a double superheterodyne phase-lock unit utilizing all solid-state circuitry. The reception frequency is nominally 2115.7 MHz, and the receiver has a dynamic signal strength range of −70 to −150 dBmW (threshold). The high sensitivity is achieved by using high-gain amplifiers in conjunction with an active bandpass filter which tracks the received signal while restricting the noise bandwidth, thereby improving the signal-to-noise ratio. The receiver in Bay V is connected to the rest of the radio in Bay VI by three coaxial cables. The three associated signals are: (1) received signal from the antennas, (2) VCO output from the receiver VCO to drive the exciters, and (3) demodulated ranging code from the receiver to the exciter modulator.

Exciter. The exciter is a phase-modulated, crystal-controlled unit operating at a nominal frequency of 2297.6 MHz with a power output of about ½ W. It is all solid state and has total redundancy, i.e., there are two separate, identical exciters, each with a separate power supply. Selection is by ground command or spacecraft failure-mode switching. If the power output of the operating exciter falls below a preset value, the other unit is switched on to replace the failed one. The exciter is constantly modulated with telemetry data from the spacecraft and may also be modulated with the ranging code under certain conditions. When no signal is present at the receiver, the exciter provides its own 19⅛-MHz signal source. When the receiver is phase-locked to an uplink signal, the receiver VCO provides the signal source for the exciter; hence, the uplink and downlink RF signals are phase-coherent.

Power amplifiers. The radio features a pair of dissimilar redundant power amplifiers—one traveling wave tube (TWT) amplifier and one cavity tuned triode amplifier, each powered by a separate supply. The TWT is capable of about 11.2 W output, while the cavity amplifier is rated at about 7.1 W. Selection is by direct command or by automatic logic which monitors the power and switches to the inactive unit should the power output of the active unit fall below some predetermined

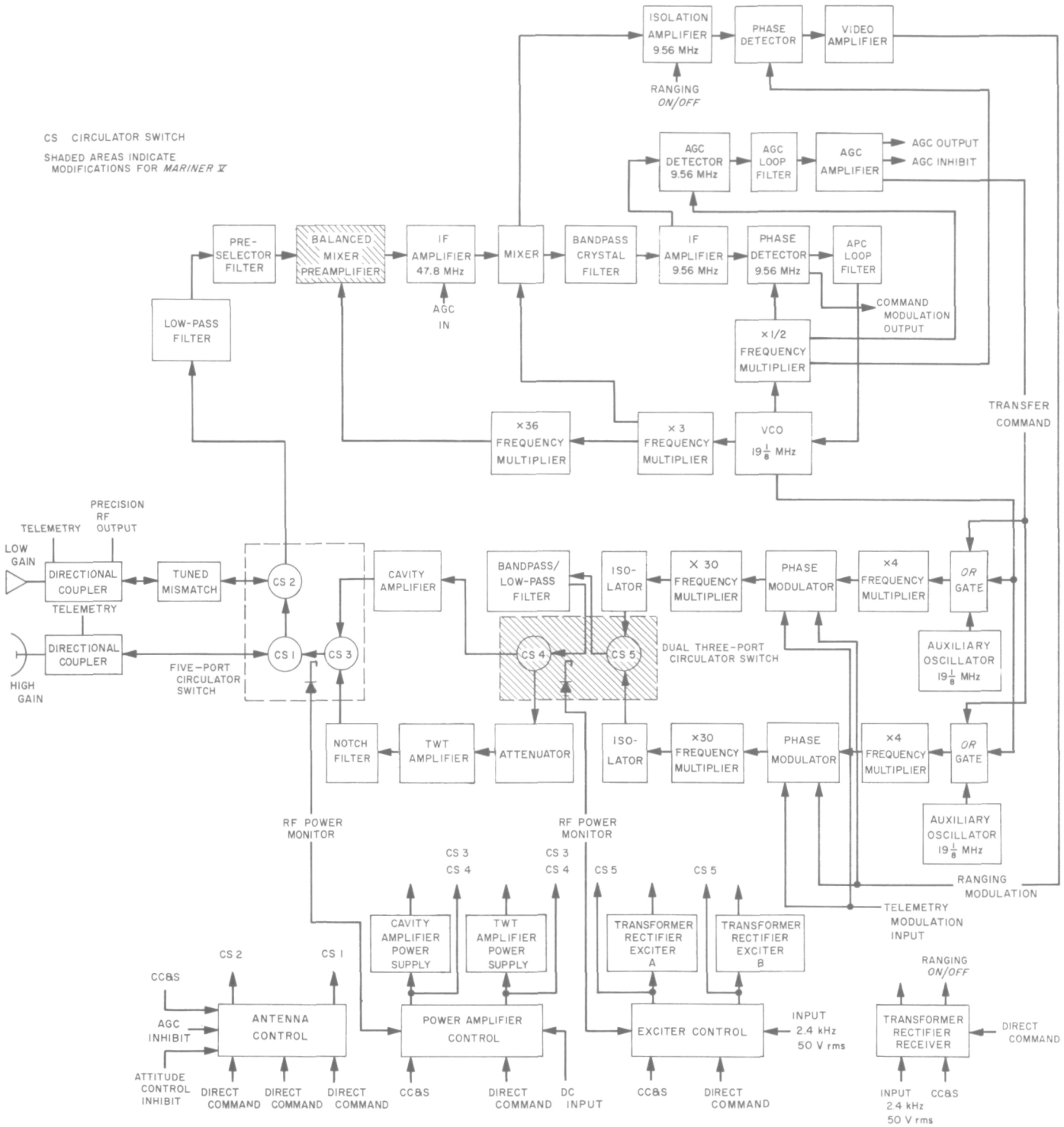

Fig. 7. Radio subsystem functional block diagram

value. The cavity amplifier also has a low-power reduced-plate voltage mode. This is used only during launch when the spacecraft passes through a critical pressure region for the higher voltages associated with high power output. When the launch vehicle separates from the spacecraft, the cavity amplifier is permanently switched into the high power mode.

Low-pass filter. The low-pass filter is placed between the antenna and the receiver preselector filter. The low-pass filter, in conjunction with the preselector filter, prevents any spurious RF energy in the self-lock frequency region from entering the spacecraft receiver. The receiver preselector filter is a bandpass filter at the receiver frequency which does not provide rejection to signals above 3750 MHz in the self-lock region. This unexpected characteristic is caused by a waveguide-mode type of leakage between the preselector input and output cavities. The low-pass filter design stop-band response is from 3600 to 10,000 MHz with a rejection of greater than 60 dB. Hence, the low-pass filter greatly attenuates possible self-lock signals entering the receiver.

Low-pass/bandpass filter. A bandpass/low-pass filter is placed in the common RF line between the two circulator switches used for exciter/power amplifier switching. Its purpose is to prevent any spurious exciter outputs in the self-lock frequency region from reaching the power amplifier. The bandpass/low-pass filter is a composite design consisting of a five-cavity bandpass filter and a coaxial low-pass filter in series and packaged as a single unit. The stop-band extends from dc to over 7000 MHz with a narrow pass-band centered at 2298 MHz.

Notch filter. A five-cavity 2116-MHz stop-band notch filter is connected to the output of the TWT power amplifier. The notch filter prevents any spurious TWT output signals and/or broad-band noise in the receiver's frequency pass-band from reaching the receiver input.

Dual three-port circulator switch. A dual three-port voltage-controlled ferrite circulator switch is provided to select which exciter is to be connected to which power amplifier. This switch was changed from the *Mariner IV* four-port design to accommodate the bandpass/low-pass filter. The switch consists of two identical, three-port circulator switches. Two additional TNC connectors were provided between the two switch sections so that the external bandpass/low-pass filter could be installed in the common RF line connecting the two circulator switches. A directional coupler type of power monitor samples exciter power in the common leg of the output switch.

Five-port circulator switch. The five-port switch provides the means of connecting and selecting the two power amplifiers and the high- and low-gain antennas. The five-port switch consists of three Y-junction circulators. Each of the junctions is driven by a voltage whose polarity determines the direction of circulation. By connecting the two common branch lines internally, two external cables are eliminated. A loop-type coupler monitors the power output from the amplifiers into the antennas. No changes were made in this unit for *Mariner V*.

Tuned mismatch. The low-gain antenna system has a tuned RF mismatch located between the five-port switch and the low-gain antenna directional coupler. This was required to reduce the depth of the nulls which result from the interferometer effect when the look angles to earth intersect the peak of the high-gain antenna and the receiver is on the low-gain antenna. The interferometer pattern was caused by insufficient isolation between the high-gain and low-gain antennas, which was due to internal RF leakage in the antenna-switching system. In or near the direction of earth at encounter, without the tuned mismatch the contributing signals from each antenna at the receiver would be of approximately equal amplitude. Deep nulls result from the rapidly changing phase relationship between the two antenna signals as a function of spacecraft look angle. In order to reduce the depth of the nulls at 2116 MHz, the isolation between the low-gain and high-gain antennas was decreased even further. This was done by inserting a $\frac{3}{4}$-λ short-circuited coaxial stub at the low-gain antenna port of the five-port circulator switch. The resulting VSWR looking at the low-gain antenna was increased at 2116 MHz. However, the $\frac{3}{4}$-λ stub was tuned such that the VSWR of the low gain antenna system at 2298 MHz was not significantly altered.

Directional couplers. In each of the antenna RF paths, there is a directional coupler with a power monitor, the purpose of which is to provide power output information to be telemetered to earth. In addition, the low-gain directional coupler has a precision RF output available for ground testing via the umbilical cable.

Control unit. The control unit, unchanged from the *Mariner IV* design, contains the input and output switching logic required to change the operating mode of the radio subsystem. It acts upon ground-transmitted direct command to select the exciter, the power amplifier, the transmitting antenna, and the receiving antenna. By monitoring the exciter and power amplifier output power, the

unit will automatically switch from a failed or degraded unit when the periodic 66⅔-h CC&S-derived CY-1 is received. The mission programmed MT-5 output from CC&S switches the transmitter output to the high-gain antenna. Also, in the event of a loss of celestial reference the receiver is automatically switched to the low-gain antenna via an attitude control output command or by internally timed logic via two CY-1's. The unit also conditions the exciter output power level and antenna drive levels for telemetry outputs.

Power supplies. The two transformer–rectifier (T–R) supplies convert 50-V 2.4-kHz input power to the required regulated dc output voltages. The receiver T–R supply also controls the ranging channel *on/off* state. A change in the *Mariner IV* design allowed ranging to be turned off, if on, with the CY-1 cyclic. The exciter T–R unit contains an individual supply for each exciter and, except for two telemetry biasing resistors, is unchanged. Another T–R supply is built into the control unit and provides the logic circuitry and control output voltages required. The separate cavity and TWT power supplies are dc to dc converters which convert the input unregulated 25-50 Vdc to regulated output voltages. The cavity supply, which provides for the cavity high- and low-power states, and the TWT supply are unchanged from the *Mariner IV* design except for a filter capacitor type of change required for increased reliability.

III. *Mariner* Mars 1969 Project

PLANETARY—INTERPLANETARY PROGRAM

A. Introduction

The *Mariner* Mars 1969 Project was initiated in late December 1965 and formally tasked on February 1, 1966. The primary objective is to conduct two Mars flyby missions in 1969 to make exploratory investigations of the planet which will set the basis for future experiments—particularly those relevant to the search for extraterrestrial life. The secondary objective is to develop Mars mission technology.

The spacecraft design concept will be based on the configuration of the successful *Mariner IV* spacecraft, with considerable modifications to meet the 1969 mission requirements and to enhance mission reliability.

The launch vehicle will be the *Atlas/Centaur* SLV-3C as used for *Surveyor* missions. This vehicle, developed under contract for and direction by the Lewis Research Center by General Dynamics/Convair, has a single- or double-burn capability in its second stage and a considerably increased performance rating over the *Atlas D/Agena D* used in the *Mariner IV* mission.

Mariner Mars 1969 missions will be supported by the Eastern Test Range launch facilities at Cape Kennedy, the tracking and data acquisition facilities of the Deep Space Network, and other NASA facilities.

Six planetary-science experiments have been selected by NASA for the *Mariner* Mars 1969 missions; they are listed in Table 1.

The launch period available for 1969 Mars launches, using planar and dog-leg direct-ascent trajectories, runs from the middle of February to the beginning of April. Arrival is planned to occur between August 1 and 10, 1969; two separate aiming points will be chosen.

During this reporting period the Mission Operations and Tracking and Data Acquisition Systems' functional designs were reviewed. The Spacecraft/Mission Operations and Spacecraft/DSIF Telecommunications interface control documents were released. Progress continued toward completing the Software and Operational Support Equipment Design Books and updating the Spacecraft Design Book.

Table 1. *Mariner* Mars 1969 scientific investigations

Experiment	Scientific investigator	Affiliation
Television	R. B. Leighton[a]	California Institute of Technology (CIT)
	B. C. Murray	CIT
	R. P. Sharp	CIT
	N. H. Horowitz	CIT
	J. D. Allen	Jet Propulsion Laboratory (JPL)
	A. G. Herriman	JPL
	R. K. Sloan	JPL
	L. R. Malling	Massachusetts Institute of Technology
	M. E. Davies	Rand Corporation
	C. Leovy	Rand Corporation
Infrared spectrometer	G. C. Pimentel[a]	University of California, Berkeley (UCB)
	K. C. Herr	UCB
Ultraviolet airglow spectrometer	C. A. Barth[a]	University of Colorado
	W. G. Fastie	Johns Hopkins University
Infrared radiometer	G. Neugebauer[a]	CIT
	G. Munch	CIT
	S. C. Chase	Santa Barbara Research Center
S-band occultation	A. J. Kliore[a]	JPL
	D. L. Cain	JPL
	G. S. Levy	JPL
Celestial mechanics	J. D. Anderson[a]	JPL

[a] Principal investigator.

Development and fabrication of the various spacecraft subsystems are being carried out by industrial contractors with contracting efforts currently in process to cover fabrication under 14 Phase II contracts. The approach guidance subsystem on the spacecraft has been deleted due to fiscal considerations. The subsystem final design review series, begun in the previous period, continued during July and August, and is nearly complete. The Sixth Quarterly Project Review has been scheduled for early October.

B. Systems

1. Introduction

The Systems Division's current technological activities in direct support of the *Mariner* Mars 1969 Project include:

(1) Mission design, analysis, and evaluation.

(2) Trajectory and maneuver design and analysis; radio guidance, including orbit determination and accuracy analysis.

(3) Intersystem analysis and integration involving launch vehicle, tracking and data acquisition, space flight operations, and spacecraft systems.

(4) Planning and direction of space flight operations, including the gathering of tracking, engineering, and scientific data; the design of software system and flight operations programming; the processing and display of information; and the command and control of the spacecraft.

(5) The design of the System Test Complex Data System used for science data processing and spacecraft operations testing; and the design of other data handling and processing systems as required.

2. Trajectory Design

a. Selected trajectory information. Figure 1 is a photograph of a Mars-centered trajectory scale model designed by C. E. Kohlhase and D. A. Tito of JPL. The model may be used as a tool to aid the trajectory design engineering in examining either orbiter or flyby trajectory missions. In Fig. 1, the model has been configured to depict the southerly of the two nominal flyby trajectories to be used in 1969. The nominal trajectory has a closest approach altitude of 3,000 km, and the plane of the trajectory is inclined approximately 60 deg to the Mars equator in order to pass 5 deg below the edge of the southern polar cap. As can be seen in Fig. 1, the scientific instruments start gathering data in the near-encounter phase at approximately 17 to 18 min prior to encounter (closest approach). All experiments continue taking data through dark limb crossing except for the TV, which stops taking pictures shortly after terminator crossing. The total data gathering time is 24 min for all instruments except the TV, which takes pictures for a total of 18 min. The model also shows the time of entrance and exit of the earth occultation zone. For the nominal trajectory, entrance occurs at about 10 min after encounter and exit occurs at 40 min after encounter.

Figure 2 illustrates the less southerly of the two nominal flyby trajectories and depicts the same type of information described above for the more southerly pass. Whereas the Fig. 1 pass is designed to collect data in the vicinity of the polar cap edge, the Fig. 2 pass is designed to view the large number of light and dark surface features contained between about 30°S lat and 10°N lat. The nominal

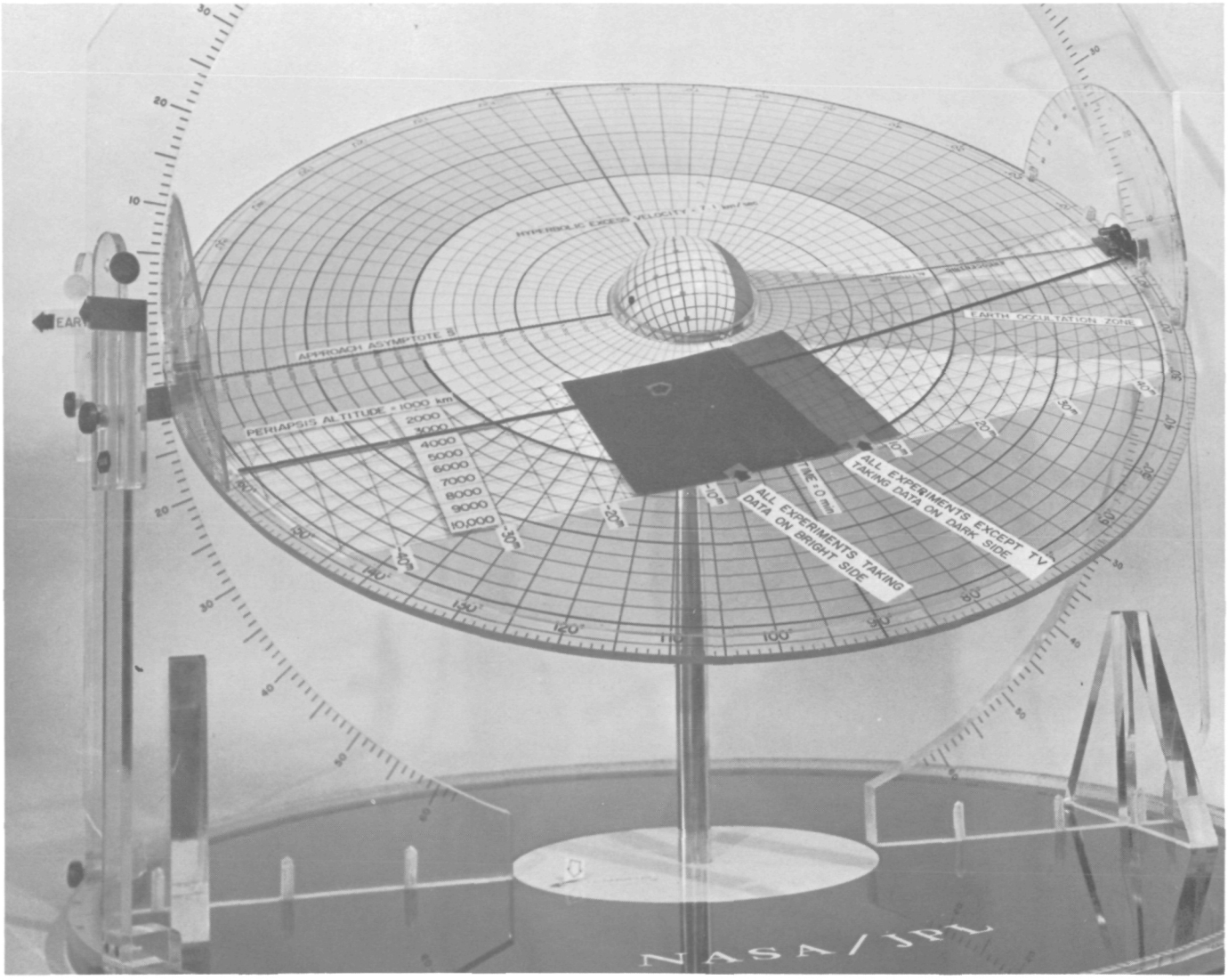

Fig. 1. Scale model view of *Mariner* Mars 1969 nominal trajectory for August 1, 1969 arrival date and $\theta = 35$ deg

closest approach altitude is still 3,000 km, but the Fig. 2 trajectory plane is inclined about 25 deg to the Mars equator. Figure 2 shows that the various event times of interest (bright limb crossing, terminator crossing, occultation entrance, etc.) occur a few minutes later than was the case for the more southerly pass.

Figure 3 depicts those areas on Mars covered by the various scientific instruments for the southerly pass trajectory and is based upon an assumed arrival date of August 1, 1969. Time of closest approach occurs at 05^h20^m GMT, which corresponds to arriving two hours past zenith of the Goldstone tracking station. A total of approximately 13 wide-angle and 13 narrow-angle TV pictures will be taken during the near-Mars phase of the mission. Resolution for the narrow-angle camera is expected to be roughly 100 m per TV line near closest approach.

Figure 4 shows the coverage for the alternate aiming point and is based upon an assumed arrival date of August 10, 1969, with closest approach occurring at about 04^h50^m GMT, which corresponds to arriving at two hours past Goldstone zenith.

Although the above arrival dates and times are the currently-specified nominal values, the scientific investigators are performing studies to determine the optimum arrival times for the two spacecraft. The investigators

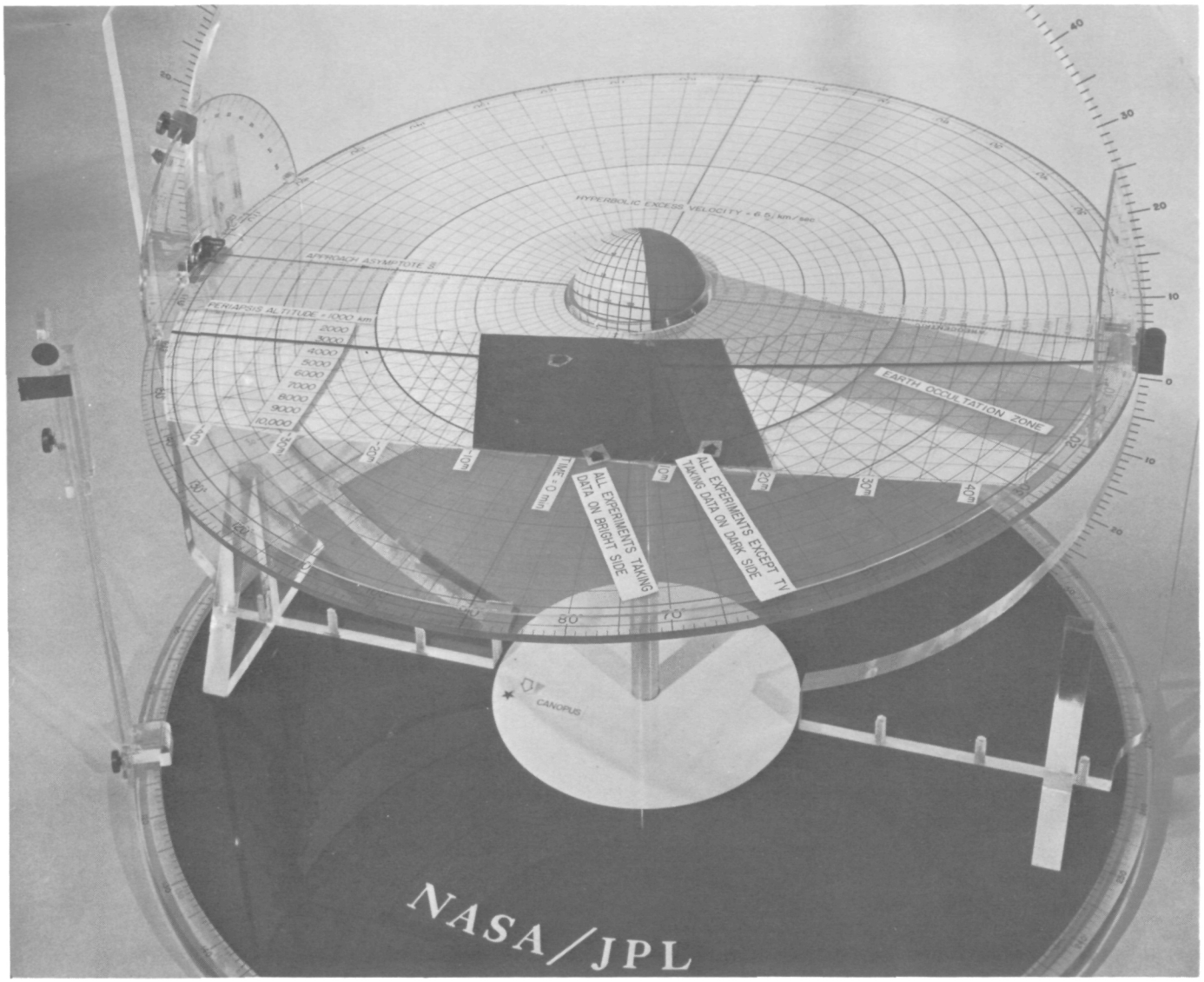

Fig. 2. Scale model view of *Mariner* Mars 1969 nominal trajectory for August 10, 1969 arrival date and $\theta = 0$ deg

have expressed a strong desire to delay the final choice of arrival times for as long as possible in order to make the best possible selection. The *Mariner* Mars 1969 Project Office has agreed to accept this desire but cannot delay the final arrival date selection much past about June 1, 1968, at which time the targeting specification must be prepared for the launch vehicle.

b. PEGASIS computer program. PEGASIS (Planetary Encounter Geometry and Science Instrument Scan) is a 7094 Fortran IV program for processing a near-planet conic trajectory and calculating trajectory and science instrument geometric parameters. Such parameters are needed in preflight trajectory and spacecraft scan platform design, for inflight pre-encounter selection of scan platform attitude, and for postflight analysis of the 1969 Mars encounter. PEGASIS will assist in the preflight task of selecting the final aiming points for the two spacecraft. The assistance will consist of furnishing the principal investigators with detailed pictorial representations of the instrument scans across Mars as functions of aiming point, arrival time, and platform pointing angles. As soon as an accurate inflight estimate of the near-encounter trajectory is made, PEGASIS will be run to select the nominal attitude of the scan platform at near-limb crossing, based on the satisfaction of two main criteria: (1) total TV viewing

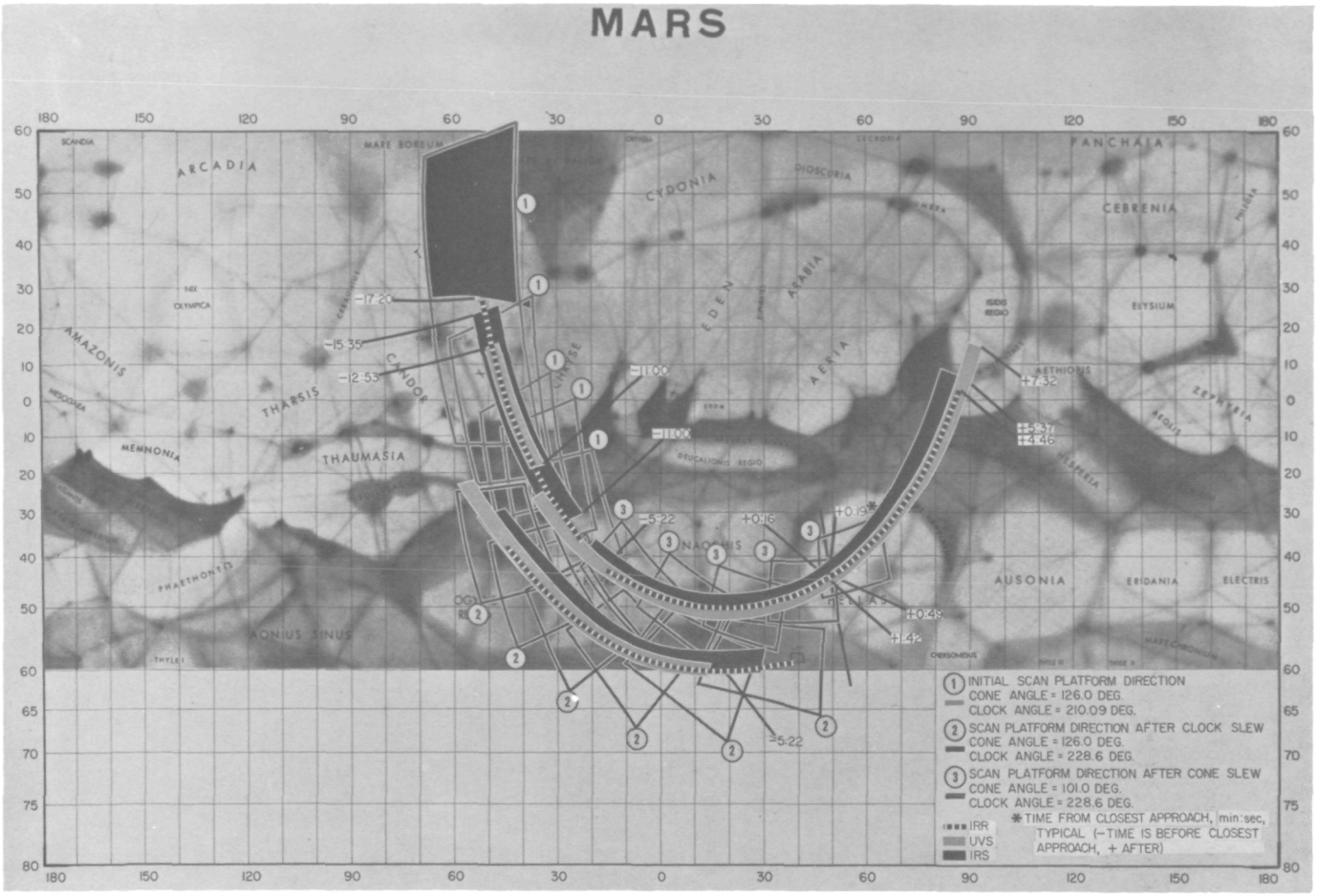

Fig. 3. Science instrument viewing swaths across Mars for Fig. 1 trajectory

time as defined by tape recorder limits, and (2) pointing the ultraviolet spectrometer instrument slit tangent to the local atmosphere at limb crossing. PEGASIS will also be used to determine the time and extent of any subsequent platform slews during the near-Mars pass. Postflight analysis will require the use of PEGASIS to geometrically describe, in the detail necessary, certain characteristics of the scientific data received.

To isolate and process a trajectory, several inputs are needed: (1) the Gregorian calendar date and GMT of closest approach, (2) an inertial identification of the approach asymptote in 1950.0 coordinates (equatorial or ecliptic), (3) the inertial directions of sun, earth, and Canopus at the arrival date, referenced to the standard **S**, **T**, **R** coordinates, (4) the aiming point in **S**, **T**, **R** coordinates, (5) the hyperbolic excess velocity, and (6) the radius and the gravitational constant of the target planet. Three distinct blocks of information are computed. A block of trajectory constants (occultation parameters, parameters at closest approach) is always computed. Time-varying trajectory quantities (distance and direction of target planet and Martian satellites, velocity of spacecraft, etc.) may be optionally printed in another block. Science instrument parameters (limb crossing time, latitude and longitude of image coordinates, etc.) are optionally computed in the third major block, which may consist of sub-blocks. All computations are performed in the 1950.0 ecliptic coordinate system.

The processing of the trajectory (time-referenced to closest approach is the processor) includes search and trigger routines. A maximum of six dependent variables may be searched on, by varying six independent variables. For example, it is possible to determine the aiming point and arrival time to place the sub-solar point at a certain latitude and longitude at closest approach and have the inclination of the trajectory a specified value. The trigger routine will recognize certain events (e.g., limb crossing, given clock angle of planet, time from closest approach)

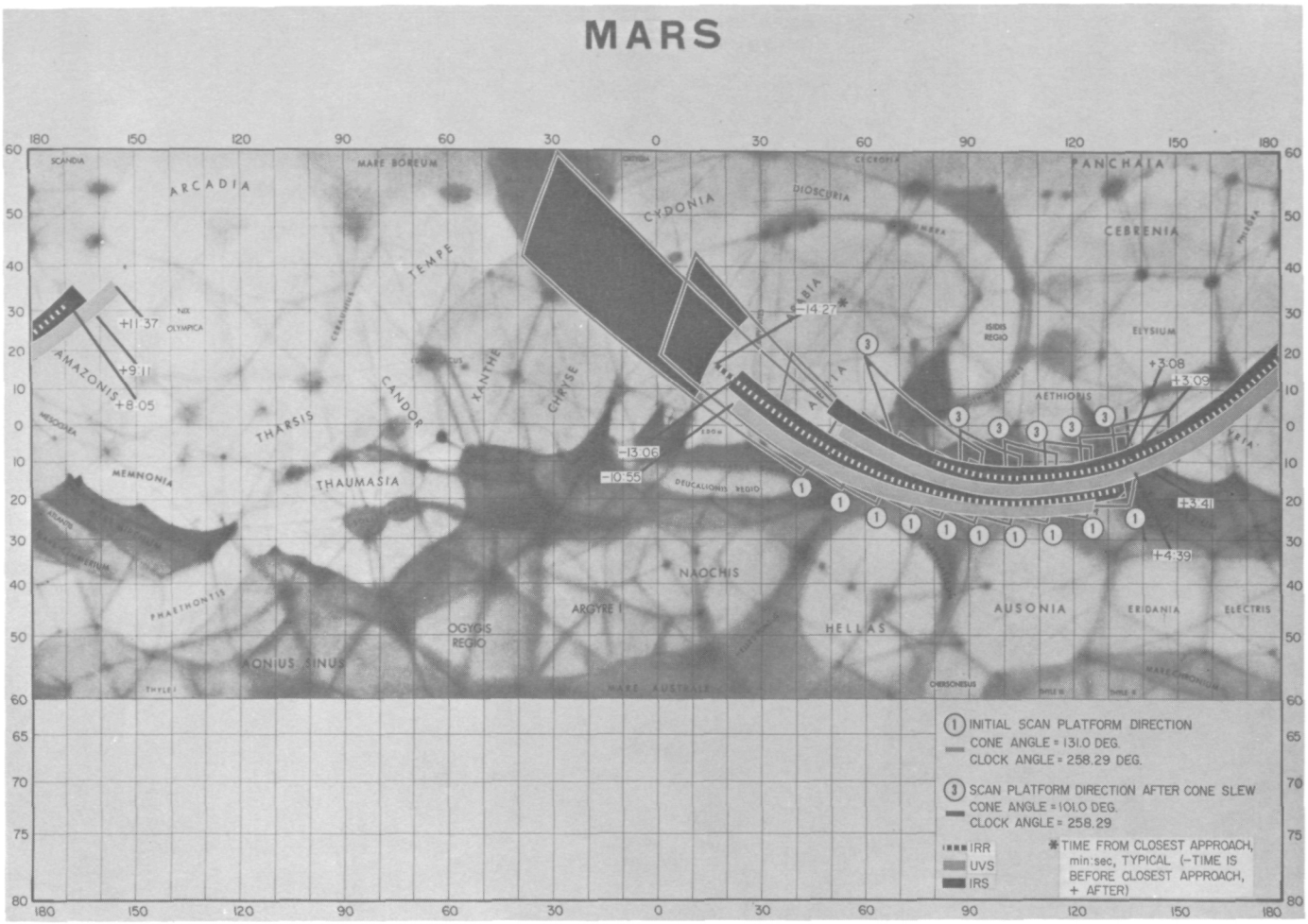

Fig. 4. Science instrument viewing swaths across Mars for Fig. 2 trajectory

and perform the desired operation (print trajectory and scan parameters, exit, continue, change direction of scan platform, etc.).

Output from PEGASIS can be in several forms: (1) standard print of the blocks mentioned above, (2) rectangular coordinate plots of dependent variables as functions of the independent variable time, (3) orthographic projection of spacecraft and instrument traces across Mars, and (4) conformal projection plots of the traces onto a conformally-mapped planet (Mercator's projection).

The package described above constitutes the preflight design program. The inflight version of PEGASIS will run in the Space Flight Operations Facility and, as a result, will be a smaller version of the preflight program. Only those options needed for the inflight activities will be retained, in order not to exceed computer core storage capability. The postflight version of PEGASIS will have an option which will incorporate a complete time-history of the spacecraft attitude during the encounter period, plus any other options necessary to describe the actual spacecraft behavior and event times, in order to geometrically reconstruct the Mars encounter.

3. Orbit Determination

An investigation was undertaken to determine the effects of low elevation angle doppler tracking upon the accuracy of the *Mariner* Mars 1969 orbit. The quantities that were selected to define the accuracy of the orbit are the 1σ uncertainty in the magnitude of $\mathbf{B}$ ($\sigma \mid \mathbf{B} \mid$) and the 1σ uncertainty in time of encounter (σT_f).

Considering two-way doppler data only, elevation angle γ enters explicitly into the computation by the SPODP[1] of

[1]Single Precision Orbit Determination Program.

the data weight $(w_i)^{1/2}$ from the following expression

$$(w_i)^{1/2} = (\tilde{w}_i)^{1/2}\left[1 + \frac{18}{(\gamma_i + 1)^2}\right]\left(\frac{60}{\tau_s}\right)^{1/2} \quad (1)$$

where $(\tilde{w}_i)^{1/2}$ is the *a priori* 1σ uncertainty value (weight) on two-way doppler, γ_i is the elevation angle of the spacecraft (Fig 5), and τ_s is the data sample rate

A data weight $(w_i)^{1/2}$ is computed for each data point at time t_i and arranged to form a weighting matrix that is used to compute the error covariance matrix associated with the least-square estimate of the state vector The equation for the covariance matrix, assuming no *a priori*, is

$$\Lambda = J^{-1} = \left[\frac{\partial F_i}{\partial Q} w_i^{-1} \frac{\partial F_i T}{\partial Q}\right]^{-1} \quad (2)$$

where $\partial F_i/\partial Q$ is the partial of the observables at time i with respect to the state vector Q, and J is the familiar J matrix

If Eq (1) is plotted as a function of elevation angle, an estimate of how the uncertainty on the doppler data changes with elevation angle can be determined Figure 6 is such a plot, and from Fig 6 the 1σ value for the uncertainty in the doppler data is 4% greater at an elevation angle of 20 deg than at a 90-deg elevation angle, 50% greater at a 5-deg elevation angle, and infinite at a 0-deg elevation angle Since the uncertainty in the data enters directly into the computation of the covariance matrix of the state vector, Eq (2), a change in the covariance matrix of the state vector can be expected to occur *when low elevation angle data is used versus when high elevation angle data is used* The following paragraphs will present some numerical results of changes in the state covariance matrix when doppler data taken at low elevation (below 20 deg) angles is substituted for doppler data taken at high elevation angles (above 20 deg) for a *Mariner* Mars 1969 trajectory

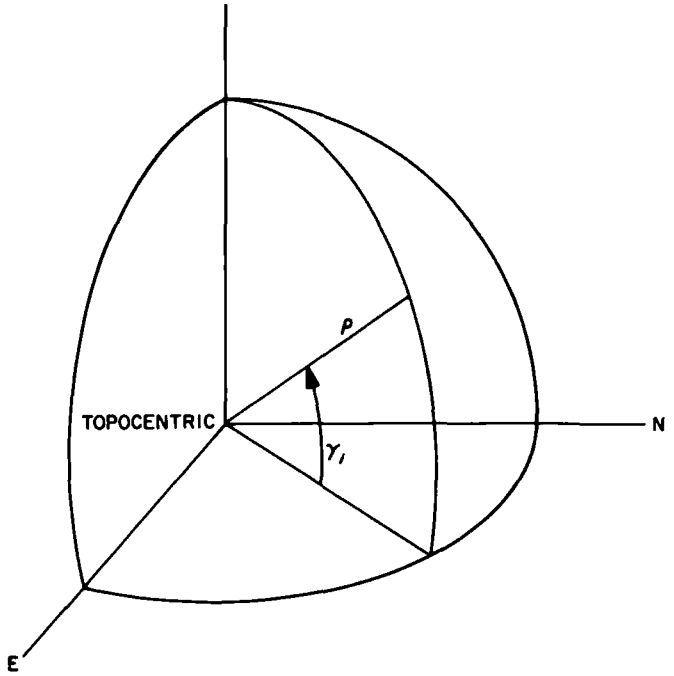

Fig. 5 Definition of elevation angle γ_i

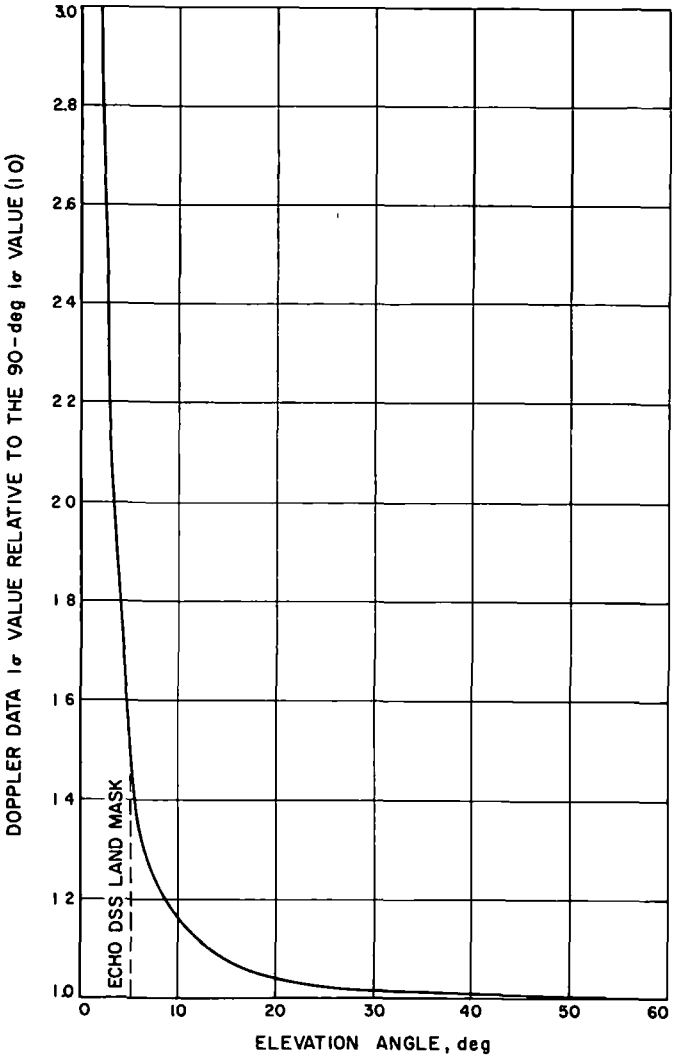

Fig. 6. Degradation of doppler data vs elevation angle

Early *Mariner* Mars 1969 trajectories have the geometric property that produces tracking data, from the northern hemisphere tracking stations, which never exceed an elevation angle of 9 deg for at least the first five days from launch, while the tracking data from the southern tracking

stations exhibit a range of 22 to 90 deg in elevation angle Therefore, the orbit accuracy of a *Mariner* trajectory will be affected when the northern hemisphere tracking stations data are used to determine the orbit The problem becomes one of determining the covariance matrix of the state vector from doppler data taken at low elevation angles and determining another covariance matrix from doppler data taken at high elevation angles and mapping these matrices to encounter in the **B** plane

In order to find the specific change in the uncertainties of $|\mathbf{B}|$ and T_f due to doppler data at low elevation angles, computations of $\sigma |\mathbf{B}|$ and σT_f were performed by the SPODP for two different state covariance matrices The trajectory selected for the study had a 115-deg launch azimuth, a 30-deg dog-leg maneuver, with a launch date of February 16, 1969 This trajectory represents the worst possible viewing geometry for the northern tracking stations [Echo and Cebreros deep space stations (DSS)]. The earth track of this particular trajectory is shown in Fig 7 For all other trajectories the earth tracks tend to lie further north, thus improving the tracking geometry Figure 8 illustrates a stereographic projection of the February 16 trajectory relative to the Echo DSS at Goldstone Figure 9 illustrates the elevation angle history, from 3 to 5 days, for the three southern hemisphere DSSs at Woomera, Ascension Island, and Johannesburg

The computation of $\sigma |\mathbf{B}|$ and σT_f was carried out by the SPODP using the above information plus the additional 1σ uncertainties on range rate (0 003 m/s), station radius and longitude (20 m and 5×10^{-4} deg), AU (100 km), and solar pressure (5%), consistent with JPL Section Report 312-756 [2] In addition, an *a priori* 1σ uncertainty of 100 km in position and 10 km/s in velocity was assumed No effects of small non-gravitational forces and Mars ephemeris errors were considered Finally, since the Cebreros DSS maximum elevation angle did not exceed 5 deg from launch to launch + 5 days, the Cebreros DSS tracking data was not simulated in the study

Four separate computations were made by the SPODP, the first computation was based on tracking data from the Ascension Island, Woomera, and Echo DSSs running continuously from launch to launch + 5 days and using only doppler data above 6-deg elevation The second computation was based on tracking data from the Woomera and Echo DSSs running from launch to launch + 5 days for elevation angle data above 6 deg The third computation was based on tracking data from the Ascension Island, Woomera, and Johannesburg DSSs The fourth computation was based on tracking data from the Woomera and Johannesburg DSSs The quantity of tracking data from the Johannesburg DSS was set equal to the amount of tracking from the Echo DSS in case 2 so that the major difference between the second and the fourth computation was due to the effects of the low elevation angle doppler data Table 2 summarizes these results

An examination of the Echo DSS tracking patterns indicated that the maximum elevation angle from launch to launch + 5 days is only 9 deg and, for the first pass, the spacecraft never rose above 6-deg elevation angle, which was the minimum elevation angle used in this study. Therefore, only 1½–2 h of tracking data is available during an Echo DSS pass

The results summarized in Table 2 represent the values from the model (Eq 1) in the SPODP that express the quality of two-way doppler data as a function of elevation angle Equation (1) was derived from a theoretically computed curve based on a theoretical model

Preliminary information from the Deep Space Instrumentation Facility operations group indicates that the quality of the doppler data is degraded, by an increase in the system noise temperature, when the elevation angle of the spacecraft as seen by the tracking antenna comes within 10 deg of the land mask Since Eq (1) does not

[2] Grimes, D C, *Near-Earth Orbit Accuracies for Mariner '69*, Section Report 312-756, Jet Propulsion Laboratory, November 9, 1966

Table 2. Orbit uncertainties

Case	$3\sigma \lvert B \rvert$, km	$3\sigma T_f$ min	Semimajor axis, km	Semiminor axis, km
1 3-station tracking data (DSSs 72, 41, 12)[a]	915	2 1	309	22
2 2-station tracking data (DSSs 41, 12)	999	2 3	331	32
3 3-station tracking data (DSSs 72, 41, 51)[b]	900	2 0	304	14
4 2-station tracking data (DSSs 41, 51)	1090	2 5	363	26

[a] DSS 72 (Ascension Island), DSS 41 (Woomera), DSS 12 (Echo)
[b] DSS 51 (Johannesburg)

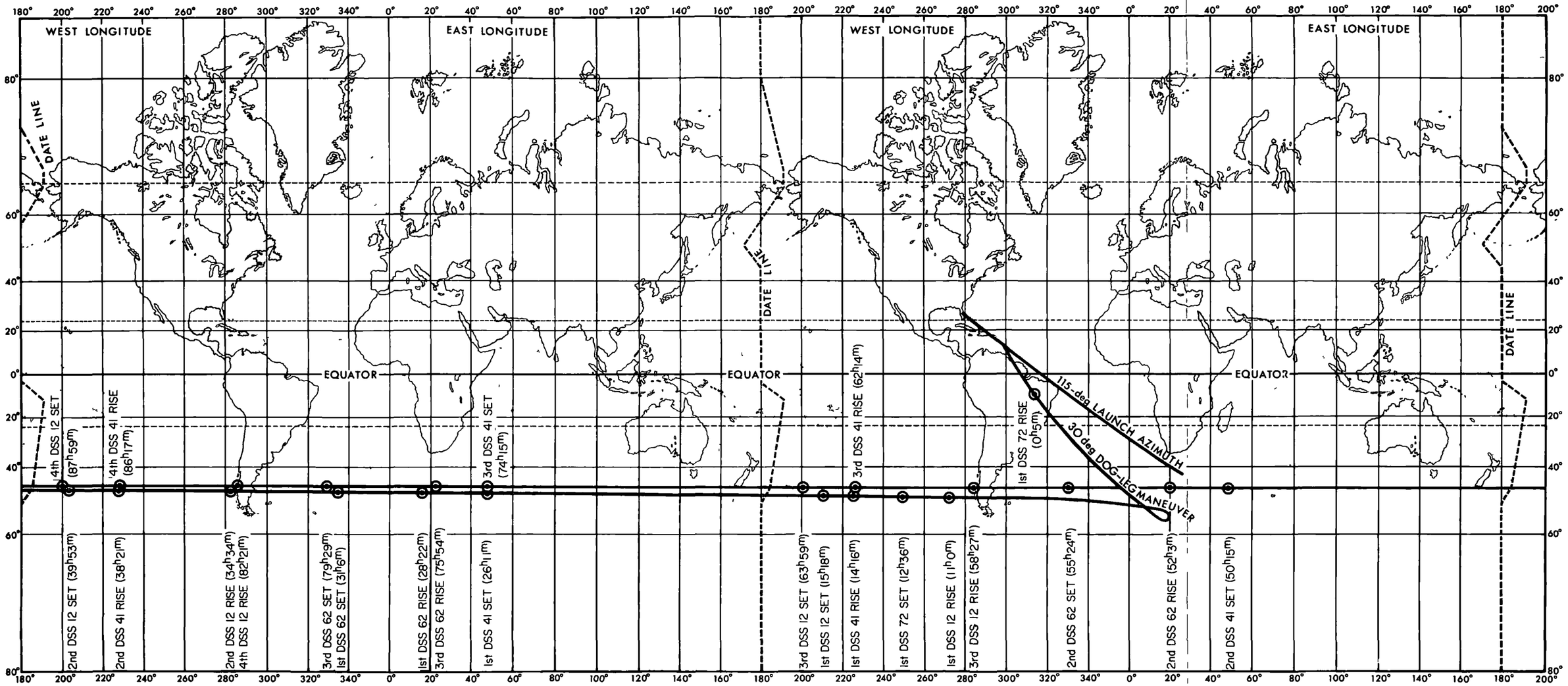

DURING 1st DSS 12 PASS, DEC VALUES ARE

RISE = −50 8 deg
EXTREME ELEVATION = −50 2 deg
SET = −49 5 deg

} BEYOND THE STATION LIMIT OF −47 5 deg (312 5 deg)

DURING 1st DSS 62 PASS, DEC VALUES ARE

RISE = −47 9 deg
EXTREME ELEVATION = −47 9 deg
SET = −47 7 deg

} BEYOND THE STATION LIMIT OF −47 0 deg (313 0 deg)

AT $4^d 20^h 11^m$, THE LATITUDE OF THE SPACECRAFT EARTH-TRACK IS −45 87 deg

DSS 72 (ASCENSION ISLAND), DSS 62 (CEBREROS), DSS 41 (WOOMERA), DSS 12 (ECHO)

Fig. 7. Earth track of February 16, 1969 trajectory

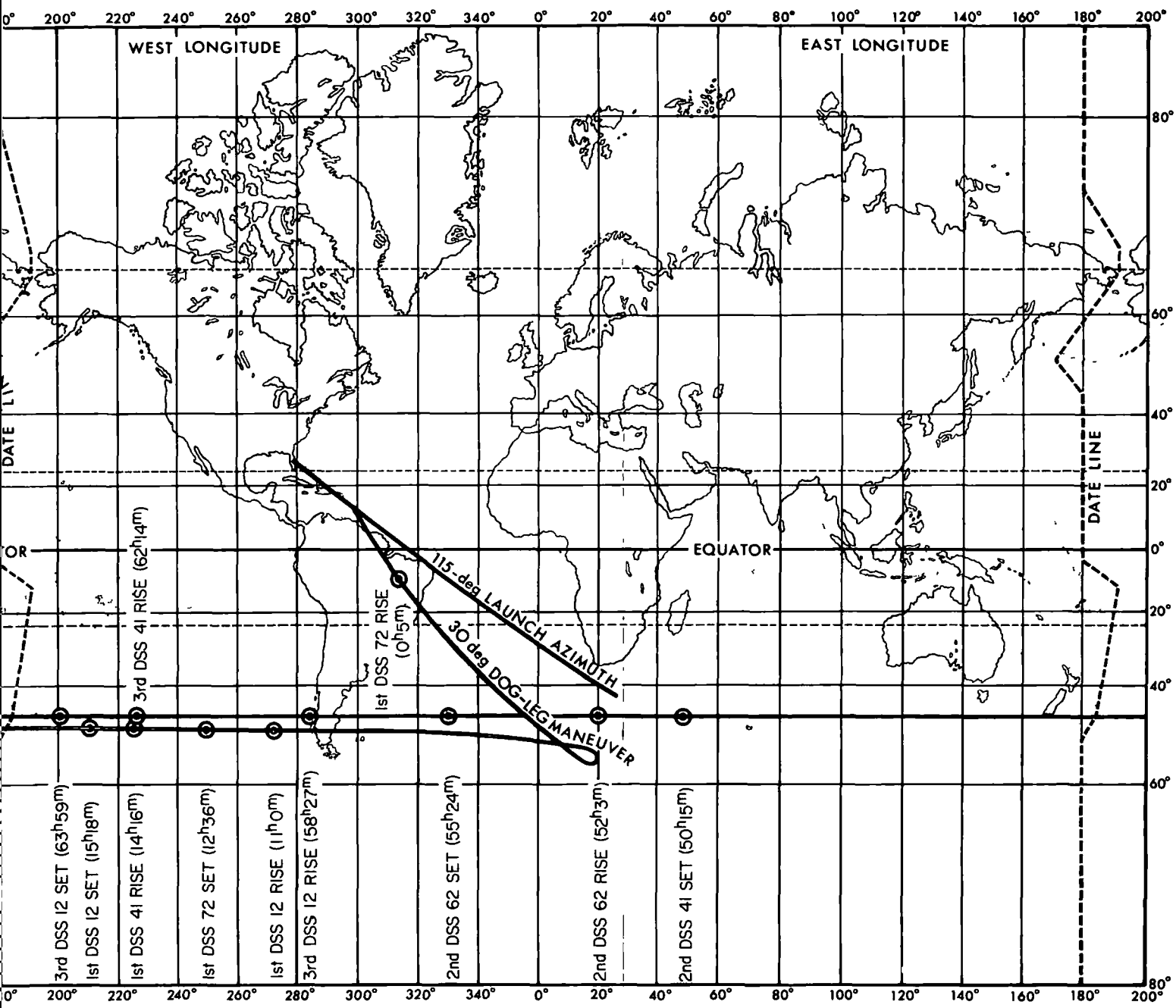

S 62 PASS,
ARE

AT $4^d 20^h 11^m$, THE LATITUDE OF THE SPACECRAFT EARTH-TRACK IS −45 87 deg

= −47 9 deg
= −47 9 deg
= −47 7 deg

} BEYOND THE STATION LIMIT OF −47 0 deg (313 0 deg)

EBRERROS), DSS 41 (WOOMERA), DSS 12 (ECHO)

Fig. 7. Earth track of February 16, 1969 trajectory

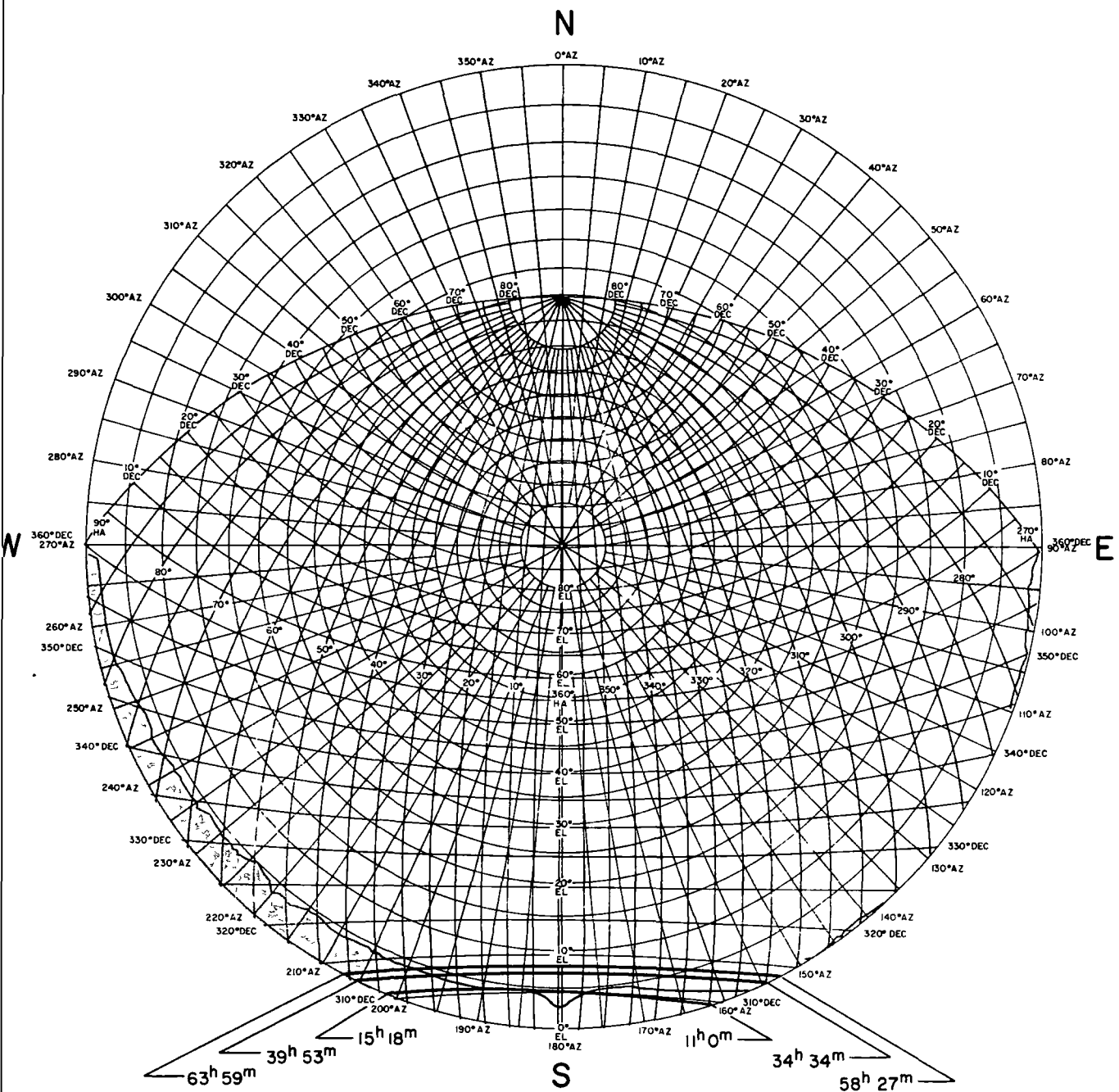

Fig 8. Echo DSS stereographic projection of February 16, 1969 trajectory

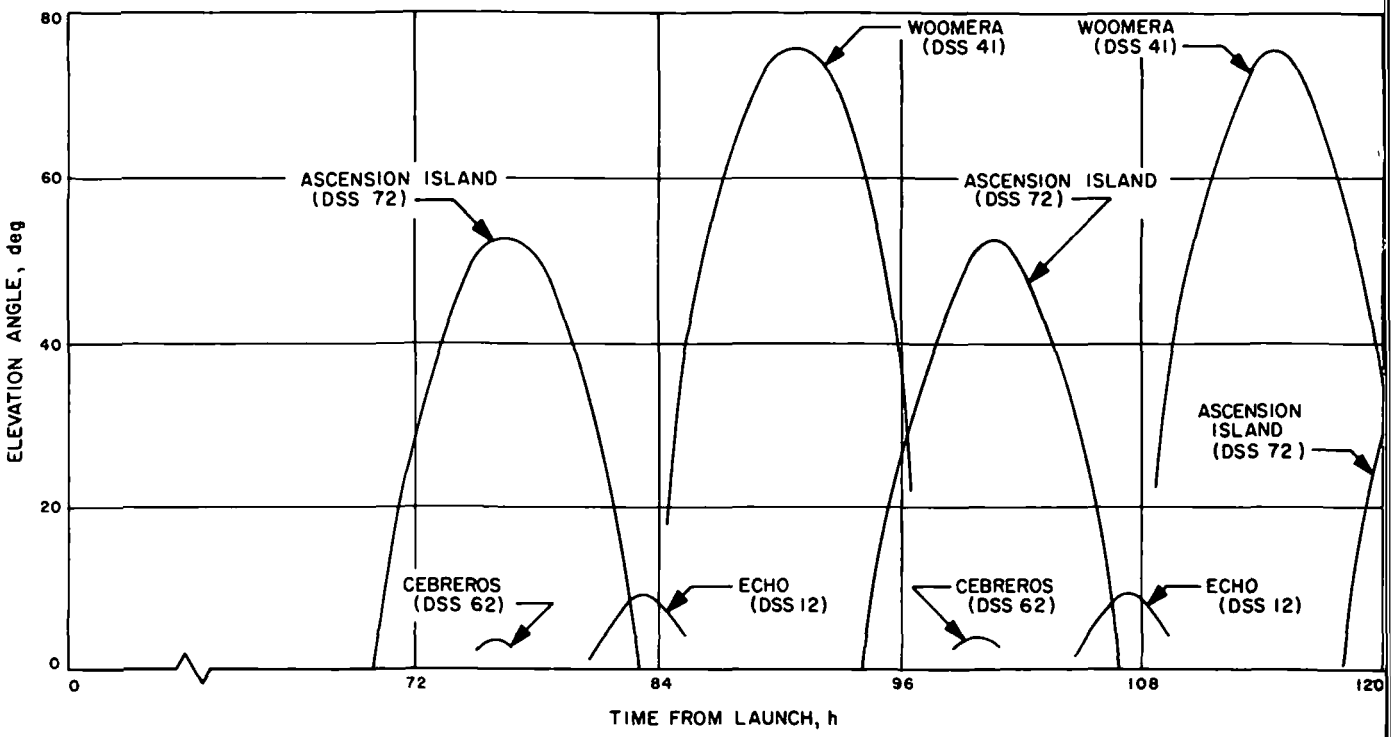

Fig. 9. Elevation angle vs time from launch

consider this effect when weighting the doppler data, another term must be added to Eq (1) to statistically represent this effect on the doppler data Therefore, the results presented in Table 2 are probably optimistic and should not be taken as the final word, but should be interpreted as a first approximation to the question of the effect of low elevation angle doppler data on the orbit accuracy Further information and evaluation on the degradation of the doppler data when it comes within 10 deg of the land mask remains to be determined, and, when this information becomes available, it will be incorporated into Eq (1) to make the model as realistic as possible

4. Planetary Quarantine

a. Introduction. The attitude control jets are located on the *Mariner* Mars 1969 spacecraft in such a manner that, should one of the jet valves stick open during the flight, the spacecraft would receive a net translational velocity increment which would alter its trajectory (in the absence of any corrective action) The purpose of this article is to explore the implications of chance jet valve failures in regard to satisfying the planetary quarantine constraint [3] Information will be presented to indicate the type of aiming-point alterations which could occur as a result of a stuck-open jet valve failure

b. Discussion. Figure 10 illustrates those events which must occur in order that a stuck-open valve failure results in a violation of the planetary quarantine constraint (PQC). We are speaking of the PQC in the sense of establishing a maximum allowable probability of Mars impact by the spacecraft (*not* in the sense of contaminated nitrogen gas reaching Mars, etc , which has been assumed to be negligible) The lower branch of Fig 10 is generally the dominant or controlling branch, since this branch considers a stuck-open valve failure occurrence *after* a second midcourse correction[4] has been used Table 3 summarizes the range of probability estimates assumed for the various branch events Two different launch-date/arrival-date trajectory combinations were chosen in order to observe the effect of different mapping geometries, different probabilities of having performed the second midcourse maneuver, different PQ allocations, different nominal aiming points, etc Let us next investigate how some of the event probabilities were estimated We shall concern ourselves only with events E through I, since events A through D are relatively straightforward and are not as important

[3] The planetary quarantine constraint was defined in SPS 37-43, Vol II, pp 28–33

[4] The *Mariner* Mars 1969 spacecraft currently has a maximum capability of two trajectory corrections

Table 3 Estimated probability ranges for events shown in Fig. 10

Event	February 16, 1969 launch date August 1, 1969 arrival date		March 16, 1969 launch date August 10, 1969 arrival date	
	Estimated range of probabilities	Value assumed for PQ study	Estimated range of probabilities	Value assumed for PQ study
A	0 85–0 90	0 90	0 85–0 90	0 90
B	0 90–0 99	0 98	0 90–0 99	0 98
C	0 90–0 99	0 98	0 90–0 99	0 98
D	0 90–0 99	0 97	0 90–0 99	0 97
E	—	1 2 f	—	1 4 f
F	0 01–0 70[a]	q	0 01–0 70[a]	q
G[b]	0 46–0 99	$1 - \int_0^t P_2(t)\,dt$	0 84–0 99	$1 - \int_0^t P_2(t)\,dt$
H	0 001–0 10	$q_2 = 0\,01$	0 001–0 10	$q_2 = 0\,01$
Probability of Mars impact P_I	—	$0\,355\,qf$ ($\lambda = 1$)	—	$0\,106\,qf$ ($\lambda = 1$)

[a] Author's opinion only for the probability range shown

[b] Refer to Fig 16 for event I probabilities Also note that P (event G) = 1 − P (event I)

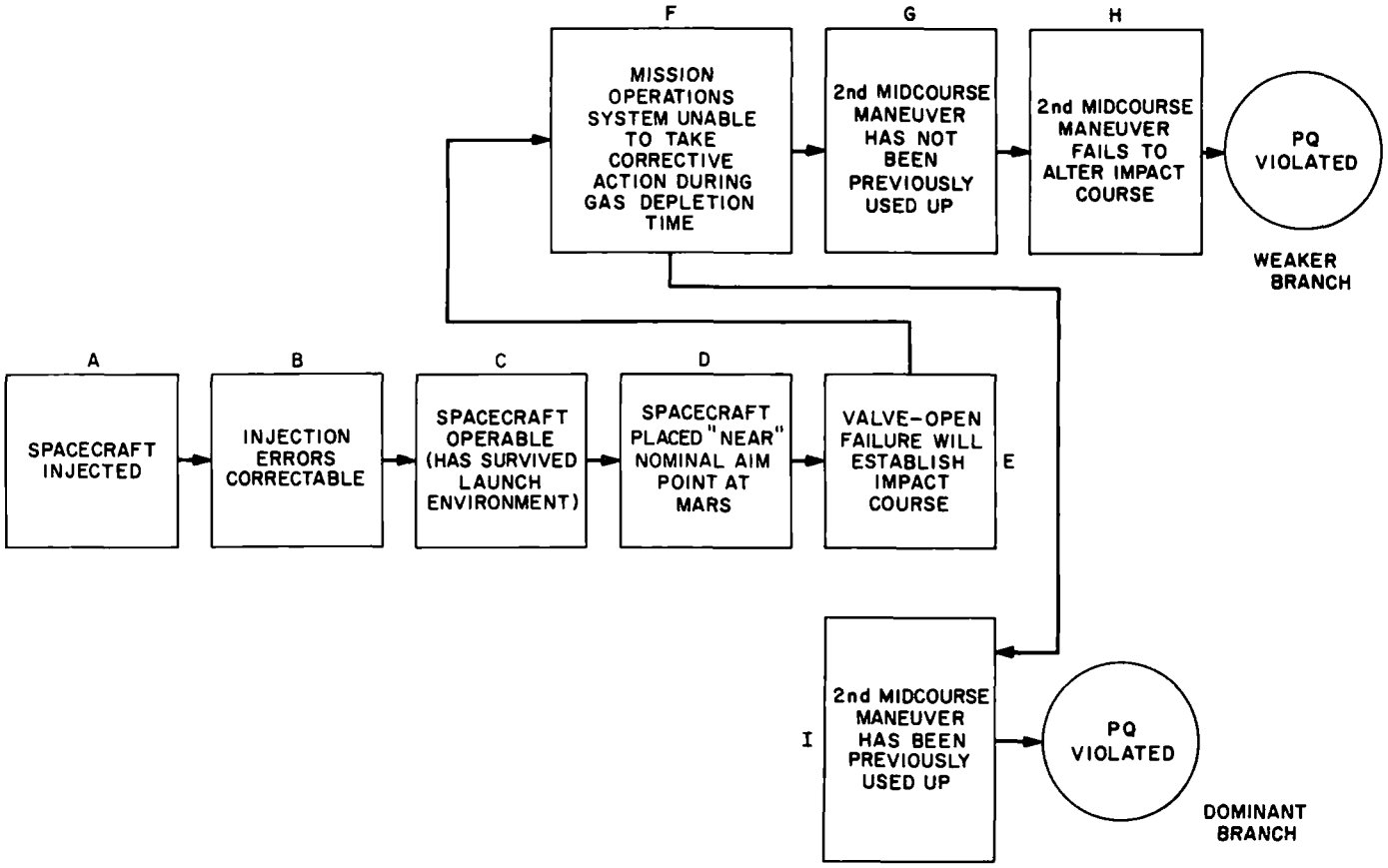

Fig 10. Simplified planetary quarantine violation branches for an attitude control jet valve stuck-open failure

Figures 11 and 12 illustrate the type of aiming point translation which can occur on the February 16, 1969 and the March 16, 1969 trajectory as a result of the velocity increment (ΔV) imparted to the spacecraft from a single stuck-open jet in its cruise orientation Using Fig 11 as an example, if the spacecraft were on the nominal trajectory, and if roll jet R_3 should stick open at 15 days after injection, the aiming point would be moved from the nominal aiming point to the point labeled 15 on the R_3 curve As can be seen from Fig 11, over a large portion of the flight a stuck-open failure in any one of several valves could establish an impact course Figure 13 illustrates the assumed ΔV as a function of the time of the stuck-open failure After the study results (discussed later in this article) were completed, it was learned that the "nominal" gas system life is probably closer to 1300 days than to the 900-day value assumed for the study This is not serious, however, since the effect upon the results is not expected to exceed 5% Figure 14 gives the depletion time of the half-gas system for a valve which is stuck fully open The depletion time could be much longer should a valve stick in a partially open position The depletion time is obviously very important in assessing the ability of the Mission Operations System to react and take corrective action during the valve blow-down period

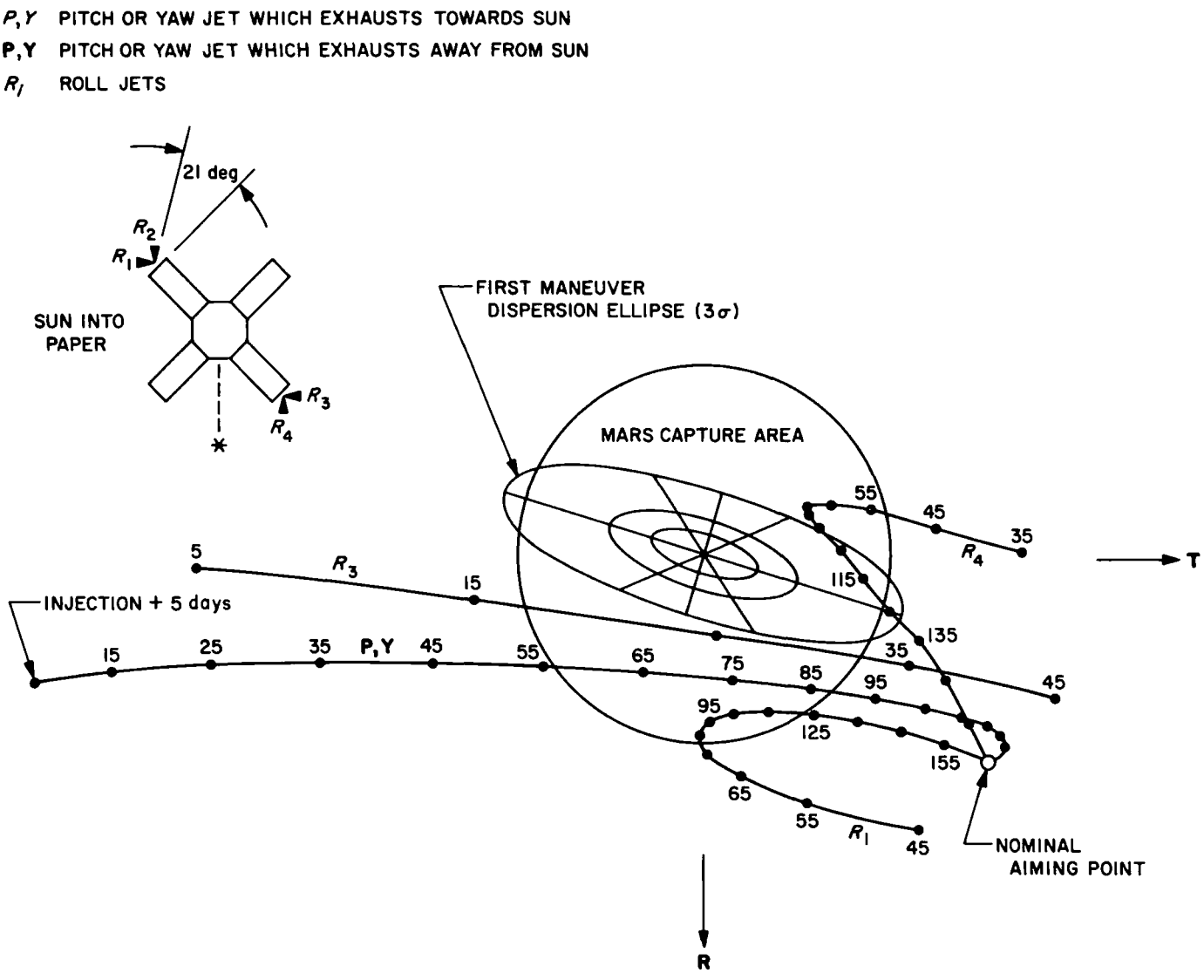

Fig 11. Aiming point translation resulting from a stuck-open attitude control jet valve (February 16, 1969 launch date; August 1, 1969 arrival date)

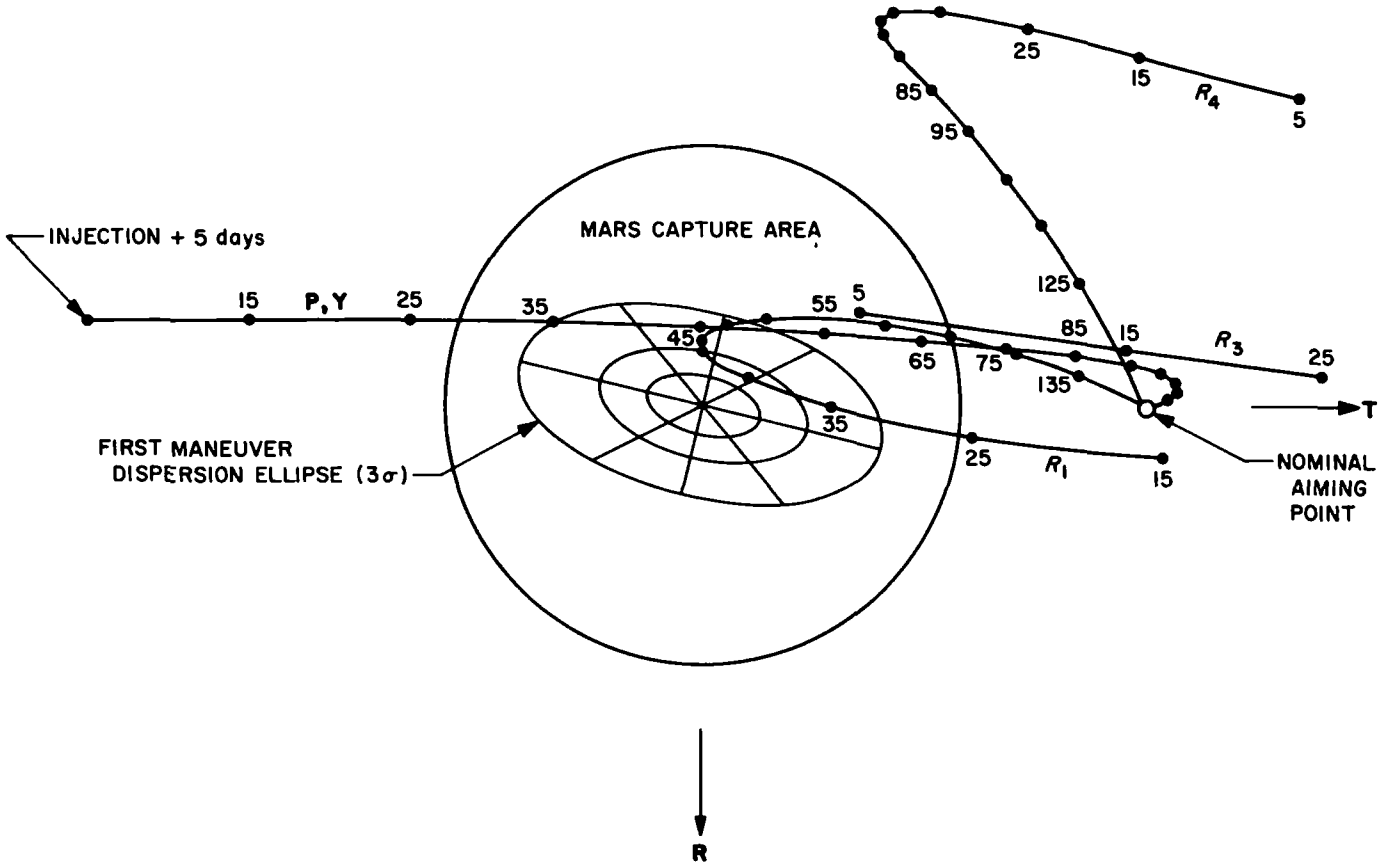

Fig. 12. Aiming point translation resulting from a stuck-open attitude control jet valve (March 16, 1969 launch date; August 10, 1969 arrival date)

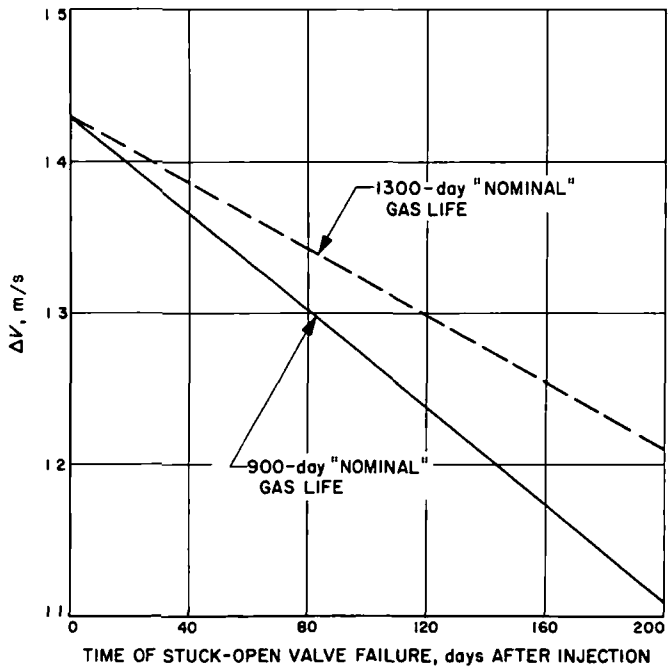

Fig. 13. Translational ΔV imparted to spacecraft from a single stuck-open jet valve

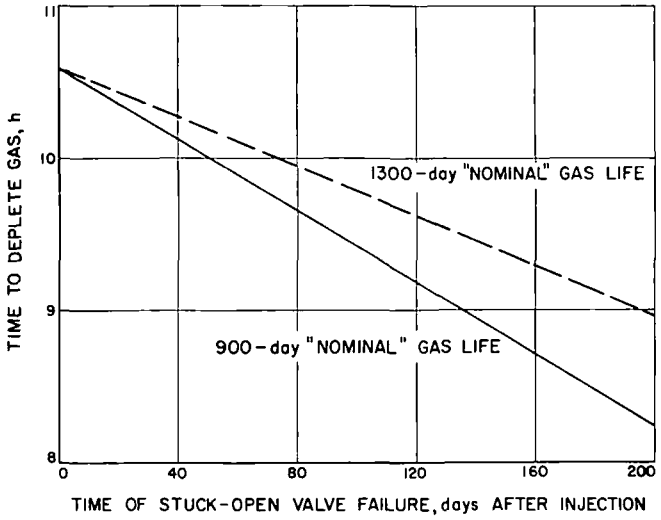

Fig 14 Time to deplete half-gas system for a single valve that is stuck fully open

c. Probability-of-impact calculations. From Figs 11 and 12, it can be observed that the first maneuver dispersion ellipse has been centered at Mars rather than at the nominal aiming point This was done to facilitate the calculation of times when valve failures could establish an impact course, for different trajectory dispersions about the nominal aiming point That is, a trajectory dispersion in a particular direction is "equivalent" to an oppositely directed dispersion in the center of Mars, etc The dispersion ellipse has been partitioned into 36 equi-probability areas where the probability p of being within the jth small bounded area after the first maneuver is $p = 0.0275$ Using a pair of dividers set at the capture radius, it was, therefore, possible to determine quickly the range of critical valve failure times associated with dispersed trajectories for each of the 36 small equi-probability areas The probability of Mars impact was calculated from the following equation (see Table 4 for definitions of symbols used)

$$P_I \approx kpq \sum_{i=1}^{12} \sum_{j=1}^{36} v_{ij} \left[p_{2_{ij}} + q_2 \left(1 - p_{2_{ij}}\right)\right] \qquad (1)$$

where

$$v_{ij} = \left[\frac{T_{ij} - t_{ij}}{(100)(\lambda + 1)}\right]\left[1 + \frac{(\lambda - 1)(t_{ij} + T_{ij})}{400}\right] f \qquad (2)$$

The summation over i is for each of the 12 jet valves, and the summation over j is for each of the 36 equi-probability areas within the dispersion ellipse The constant k is equal to 0.839, which is the product of the event probabilities A through D A linear probability density function (PDF) was assumed for the probability of a valve failure versus time from injection, and the PDF at injection plus 200 days was set at λ times the PDF at injection

Table 4 Nomenclature

f	probability that a *specific* single valve will fail in the stuck-open position in the period from injection to injection plus 200 days, if valve failures are uncorrelated, the probability of *at least* one valve failure is given by $1 - (1 - f)^{12}$
k	product of probabilities of events A through D (Fig 10), $k = (0.90)(0.98)(0.98)(0.97) = 0.839$
P_I	probability of Mars impact as a result of a stuck-open attitude control gas jet failure
p	probability of falling within one of the 36 equi-probability areas into which the dispersion ellipse has been partitioned, $p = 0.0275$
$P_{2_{ij}}$	probability of having previously used up the second midcourse maneuver, if valve i should fail during its critical time between t_{ij} and T_{ij}
q	probability that the Mission Operations System will be unable to take corrective action during a stuck-open jet blow down period, q must, therefore, include learning of the valve failure, initiating *the correct action, and having the spacecraft respond as instructed*
q_2	probability that the second midcourse maneuver will fail when attempted, given that the first midcourse maneuver was previously successful
T_{ij}	for dispersion j, the latest possible time that a stuck open failure in valve i could establish an impact course
t	time, measured from injection in days
t_{ij}	for dispersion j, the earliest possible time that a stuck-open failure in valve i could establish an impact course
v_{ij}	for dispersion j, the probability that valve i will stick open and establish an impact course during the time from t_{ij} to T_{ij}
λ	measure of the slope of the linear PDF for a specific single valve failure, the ratio of the PDF at $t + 200$ days to the PDF at t
Subscript	
i	ith jet valve among 12 jet valves
j	jth area of the 36 partitioned areas

Figure 15 illustrates the PDF model assumed for the probability of performing a second midcourse correction, and is based upon passing through the desired science flyby zone (the smaller of two wedge-shaped regions shown in Fig 5 of SPS 37-43, Vol II, pp 28–33) The second maneuver PDF is higher early in the flight to reflect the project desire that the maneuver not be performed at so great a distance that communications cannot be maintained during the maneuver over the low-gain antenna Figure 16 illustrates the cumulative

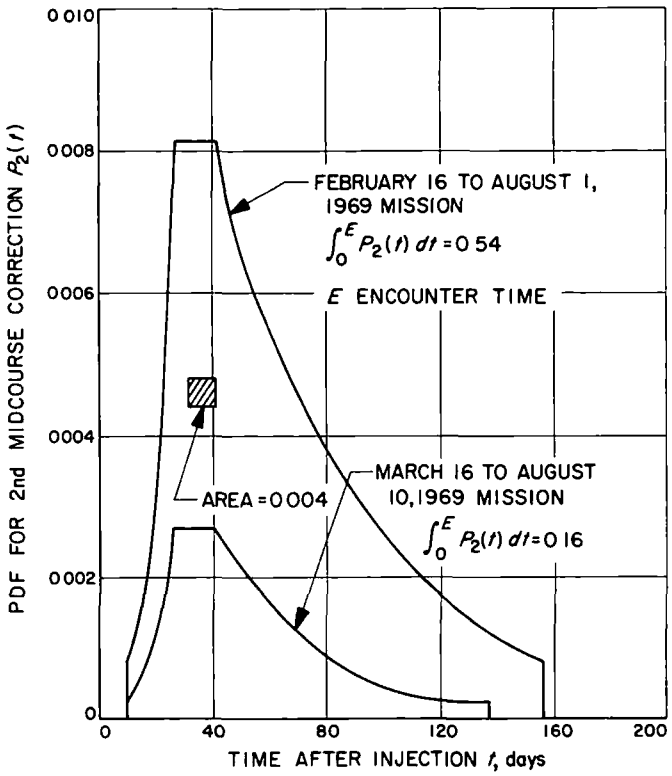

Fig. 15. Assumed probability density function for 2nd midcourse correction

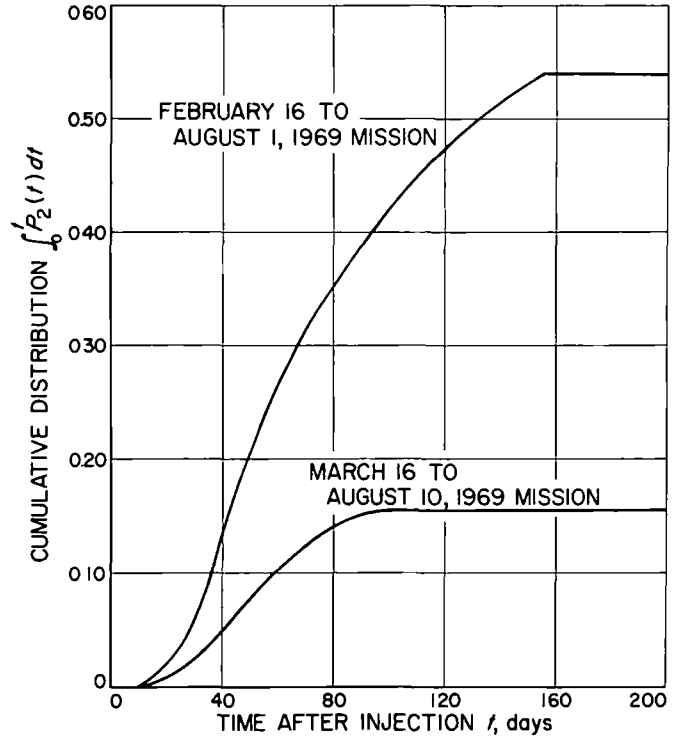

Fig. 16 Cumulative distribution function for 2nd midcourse correction

distribution function associated with Fig 15 The quantity $P_{2_{t_j}}$ shown in Eq (1) may be approximated by reading that ordinate in Fig 16 which corresponds to the abscissa

$$t = \frac{t_{i_j} + T_{i_j}}{2} \tag{3}$$

Figures 16 and 17 are consistent with work done by V N Dvornychenko and G Z Schissell (SPS 37-43, Vol II, pp 28–33), where it is shown that it is desirable to distribute a larger portion of the total 6×10^{-5} PQ mission allocation to the first launch (when trajectory dispersions are larger) and a smaller portion to the second launch

The results of calculating P_I from Eq (1) indicate that a uniform (zero slope, $\lambda = 1$) PDF for a valve failure gives the highest value for P_I over the range of values ($\lambda \geq 1$) considered For the February 16, 1969 case, the largest P_I is 0 355 qf, and for the March 16, 1969 case, the largest value is 0 106 qf For the February 16 case, since the total PQ impact allocation is about $4\,9 \times 10^{-5}$

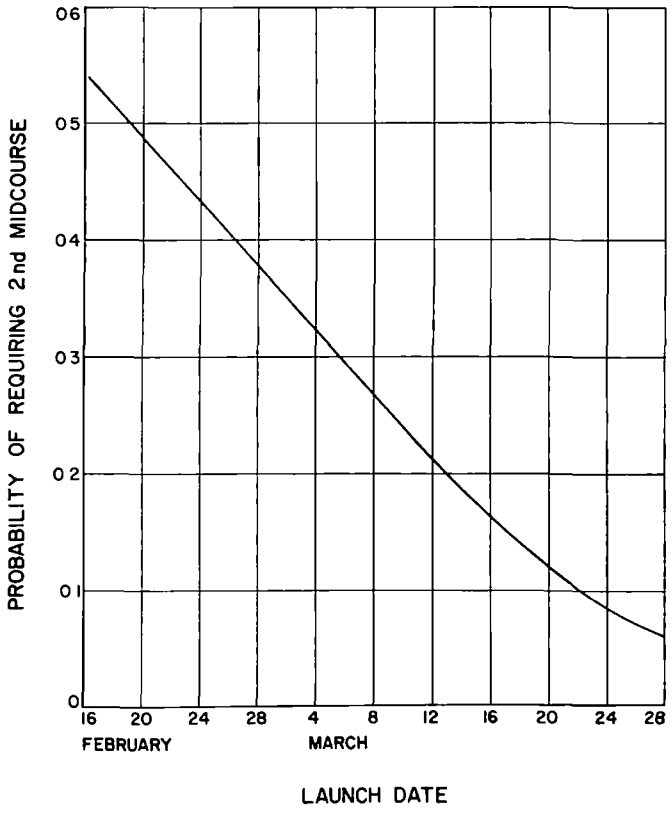

Fig 17. Probability of requiring a second midcourse *correction to pass within the desired science* flyby zone as a function of launch date

(5.0×10^{-5} minus 10^{-6} for ejecta), this results in requiring that $qf \leq 1.38 \times 10^{-4}$. For the March 16 case, since the total PQ impact allocation is 0.9×10^{-5} (1.0×10^{-5} minus 10^{-6} for ejecta), this requires that $qf \leq 0.845 \times 10^{-4}$. However, if the qf product were equal to the numbers noted above, *all* of the PQ impact allocation would be used up by the possibility of jet valve failure, and little or no allocation would remain for the mission aiming-point selection. Previous studies have shown that the mission will not be noticeably penalized (in having to bias the maneuver aiming point and lower the probability of hitting the target zone) if about one-third[5] of the PQ impact allocation is used up by some other source of PQ concern. Figure 18, therefore, presents two constraint curves for the qf product. It is mandatory that the upper curve be met, and we should strive to meet the lower curve in order not to penalize the selection of mission aiming points. In order to generate the curves through the February 16 and March 16 data points, it was necessary to employ a number of assumptions which are too lengthy for discussion in this article. The dip in Fig. 18 is produced because the PQ allocation with launch date decreases initially at a faster rate than the decrease in the probability of requiring a second midcourse maneuver. Although one might now question the criteria which have been used to allocate impact probability with launch date, Fig. 18 does not necessarily indicate poor allocation criteria since there is a reasonable chance that the two launch dates which actually occur may straddle the dip.

[5]This is the portion of PQ impact allocation used up for the early launch dates. A greater portion may be used up for the later launch dates without significant penalty.

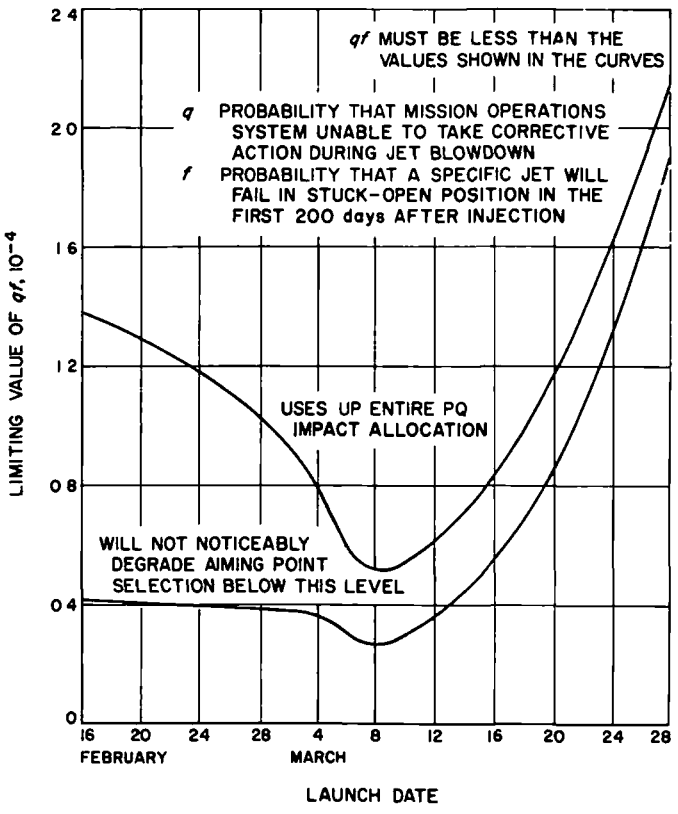

Fig. 18. Constraint curves for the qf product

A variety of information displays can be made from Fig. 18. One fairly significant display is shown in Fig. 19 and indicates, for different assumed values of valve failure probability f, the required level of reliability $(1 - q)$ of the Mission Operations System (see definition of q in Table 4). In order to determine if it is reasonable to expect to meet some of the higher values of $(1 - q)$ shown in Fig. 19, the following questions must be answered:

(1) What is the probability that we will learn of a valve failure in time to try to react?

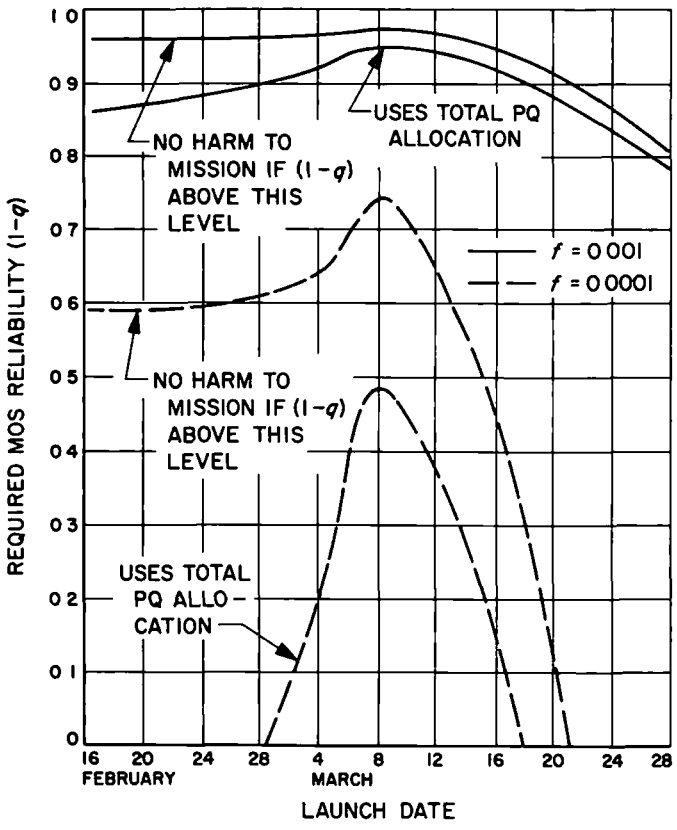

Fig. 19. Required Mission Operations System reliability for two values of f

(2) What is the probability that the Mission Operations System will select the correct action?

(3) What is the probability that the spacecraft will successfully carry out the corrective measures chosen?

Regarding item (1), we can only learn of a valve failure through tracking or telemetry data Since the SIRD[6] requires only 2 passes of tracking data every 5 days, we cannot count on detecting a stuck-open valve failure with the tracking data to the reliability levels shown in Fig 19 Regarding the telemetry data, the current SIRD permits gaps of 5 6 h in the telemetry during cruise Furthermore, even when we are receiving telemetry data, measurements of both limit cycle performance and gas bottle pressures are required before the stuck-open jet can be uniquely identified The limit cycle data is transmitted every 16 8 s on the 100 deck, but the gas bottle pressures are only transmitted once every 56 min on the 400 deck Therefore, considering all of the above time delays, much of the effect of a stuck-open jet may have already occurred by the time the faulty jet has been identified

Regarding item (2), it should be assumed that the Mission Operations System could be trained to select a valid corrective action with a very high reliability

Regarding item (3), we must ask for how long the spacecraft can be maintained in a non-cruise attitude without harm from either power or temperature control considerations If the spacecraft does not need to turn very far off the sun line, it may be possible to remain in such an orientation for many hours On the other hand, if it should be necessary to turn the spacecraft completely away from the sun, the spacecraft may only tolerate such an attitude for a few hours without harm A detailed discussion of the capabilities and limitations of the spacecraft is beyond the scope of this article

d. Conclusions. Over a large portion of the flight the uncompensated occurrence of an attitude control jet stuck-open valve failure can place the spacecraft on an impact course with Mars Although the possibility of such a valve failure is remote, in the small-numbers language of planetary quarantine it cannot be neglected

e. Solution alternatives. Any of the following alternatives will reduce the PQ concern caused by chance jet valve stuck-open failures

(1) "Show" that the product qf is sufficiently small to meet the PQ constraint

(2) Adopt such measures as reducing telemetry coverage gaps, increasing first midcourse accuracy, delaying a second midcourse maneuver until late in cruise, etc

(3) Add a third start capability to the midcourse propulsion subsystem

(4) Relocate the attitude control jets in such a fashion as to cancel out the orbit perturbation effect from a stuck-open valve

As a result of the cost and schedule problems associated with (3) and (4), the *Mariner* Mars 1969 project has adopted alternatives (1) and (2)

5. Effect of IRS Jetting on Celestial Mechanics Experiment

New information on the nature and direction of the gas jetting from the *Mariner* Mars 1969 infrared spectrometer (IRS) experiment led to a reinvestigation of the effects of the IRS cooldown jetting on the celestial mechanics experiment By considering various levels and directions of IRS jetting force during the encounter period, an estimation was made of the uncertainties thereby introduced in the astronomical constants determined from the *Mariner* Mars 1969 tracking data The conclusion of the study is that the careful design, construction, and preflight calibration of the IRS jetting system are critical from the viewpoint of establishing confidence in the results of the celestial mechanics experiment

It has been determined that unknown forces as large as $\pm$ 100 dynes can be tolerated in certain directions, for example, in the ecliptic plane normal to the sun–spacecraft direction, but unknown forces of $\pm$100 dynes in a direction normal to the ecliptic completely invalidate results obtained with data taken during the IRS jetting period If unknown forces greater than 10 dynes are present in a direction normal to the ecliptic, the celestial mechanics experimenters will almost surely disregard all data taken during the jetting Since the exclusion of this data, along with the loss of data during occultation, amounts to a total loss of tracking over a period of a little more than one hour about the closest approach to Mars, it is clear that the IRS experiment could interfere with the celestial mechanics experiment to a considerable degree The implications of this interference with respect to the determination of astronomical constants are that the only serious degradation in accuracy occurs in the mass of Mars which

[6]SIRD = Support Instrumentation Requirements Document

could be three times as uncertain after the reduction of the data as it would be for the case of no IRS jetting In absolute terms, the relative uncertainty in the mass of Mars after the reduction of *Mariner* Mars 1969 range and doppler tracking data could be increased from a value of about 2 to about 6 ppm by the IRS jetting

6 Effect of IRS Gas Venting on Occultation Experiment

The effects of gas ejection from the infrared spectrometer (IRS) cooling bottles were examined regarding their effects on the occultation experiment, especially with respect to the doppler data predictions required by the experimenters The predictions are proposed to be obtained by using the best available orbit (no specification placed by occultation experiment on the celestial mechanics experiment) plus empirical fits to residuals (observed-minus-predictions computed with best available thrust model) just prior to the atmospherically perturbed data The 50-dyne limit[7] on the maximum unpredictable component of force is found sufficient

Dr A J Kliore[7] gives an acceptable amount (53 dynes) of unknown thrust delivered along the line of sight It is acceptable in the sense that, if an error in the phase or time-of-flight of the radio signal occurred from some unknown or unpredictable source of this magnitude, it would be attributed to the Martian atmosphere—but this contribution would be small Specifically, the 2 cm of error[8] would compare to the two-way Mars tropospheric contribution of 400 cm (Footnote 9) and the Mars ionosphere's 130 cm (Footnote 9) This slowly varying error would only degrade the quality of the estimates of the Mars ionospheric scale height The largest error source other than IRS gas jetting would be the unpredictable part of the earth's ionosphere, which might amount to about 4 cm (out of say 1½-m total effect), but should vary more slowly with time

In 1965, the best free-fall trajectory fit to the doppler observations, excluding effects by the atmosphere, was used as the basis for prediction of data during the time when Mars atmospheric effects were noticed The difference between these predictions and the observations during the occultation phenomena was the "data" (Fig 20) The error analysis based on a free-fall model (considering errors in spacecraft position, velocity, Mars mass, and the tracking data) showed that insignificant errors should be expected in the predictions In reality, however, some unmodeled errors did occur due to the earth's atmosphere and trajectory computation imprecision In 1965 the unperturbed tracking data, for hours before encounter, was estimated to have only random errors of the order of 0 06 cm/s, but in 1969, with an unknown gas jet force of 50 dynes acting during 40 min (exclusive of the occultation period), there would be 0 3 cm/s of *systematic* error Therefore, it is concluded that the existence of gas jetting makes it impossible to obtain reasonable predictions from the celestial mechanics experimenter

Another procedure was chosen For immersion, the best available orbit was selected using all non-jet pre-encounter data only Predictions from this orbit[10] were compared with jet (but no Mars atmosphere) affected data It was concluded that no gross or unexpected jet unbalance occurred A parabolic curve was fitted to the data immediately before the occultation These empirical predictions were subtracted from the data and the remainder was ascribed to atmospheric refraction and diffractive (occultation) phenomena

The above error analysis is dependent upon the statistics of the unpredictable portion of the jet force, estimates which are difficult to obtain Therefore, the following case should be used only as an indicator The empirical predictions fit the data, but the +50-dyne force, which acted

[7]Khore, A J, *Impact of IRS Gas Venting on the S-Band Occultation Experiment*, Interoffice Memorandum 311 1-2 Jet Propulsion Laboratory, Pasadena, Calif, July 20, 1967

[8]This is the 1-cm spacecraft motion (obtained from the specification given in Footnote 7) doubled to give total round-trip time delay multiplied by speed of light

[9]These figures are based on 1965 data The 1969 data will probably be affected by a thicker and higher Mars ionosphere due to a smaller solar zenith angle

[10]The best IRS gas jet mean-expected-force model available from JPL Section 292 was used

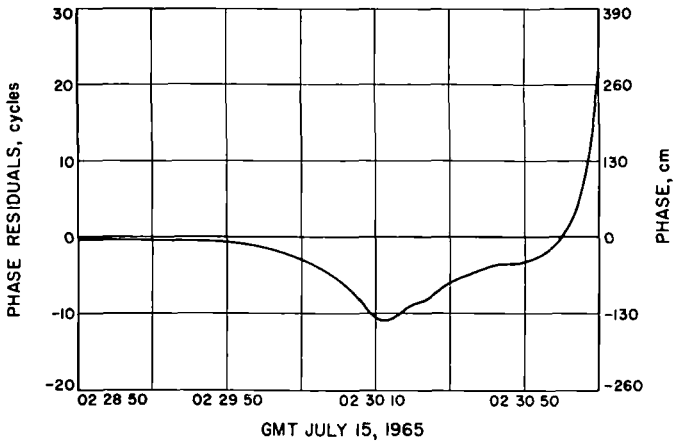

Fig. 20 *Mariner IV* enter-occultation phase residuals

steadily throughout the time of fit, immediately reversed at the time predictions began (the beginning of immersion Mars ionosphere occultation data) Then after 2 min,[11] a result was obtained that is twice that obtained by Kliore, or 2 cm of spacecraft motion, which is 4 cm of error due to atmospheric phase effects This equals about 0 3 cycles (Fig 20) Of course, if the perturbation in position takes place at an angle θ to the earth–Mars line, then the resulting estimates should approximately be multiplied by cos θ.

7 System Test Complex Data System

a. Introduction. A data acquisition, processing, and display tool is described whose principal function is the real-time support of the *Mariner* Mars 1969 spacecraft system tests This computer-based mechanism is called the system test complex data system (STCDS) It is a complex consisting of a modular data input subsystem (DIS), display devices associated with each test area, and centrally located processing and computer equipment Collateral functions of the system are support of subsystem level tests and investigation of automatic test techniques

The basic system is currently being used by the *Mariner* Venus '67 project However, the basic system will be augmented for the *Mariner* Mars 1969 mission because of increased processing requirements and multiple spacecraft test areas

b. Data acquisition. Data streams will be acquired as shown in Table 5, using the devices indicated

c. Description of equipment. A dual computer configuration is planned, consisting of two CDC-3300 computers One machine will be available in July 1967, the second machine will be added in March 1968, and the dual arrangement will be continued until launch of the last spacecraft at the Eastern Test Range In practice, computer A will support system testing, computer B will provide post-test processing capability, hardware and software development and integration time, science subsystems test support, or complete redundant capability to support system testing Two data input subsystems will be employed These will consist of those elements presently employed for *Mariner* Venus '67 with minor modifications, and new modules required for new data streams, viz, parallel digital data, high-rate telemetry, and analog video The block diagram of the system test complex data system is shown in Fig 21 Note that only two of three

[11]This is 2 5 min for 1965, in 1969 the 1 7-times faster probe normal velocity is somewhat offset by the longer prediction time needed because the Mars ionosphere is expected to be thicker

Table 5 Data acquisition

Data stream	Maximum rate, bits/s	Average rate, bits/s	Input device
Telemetry, science channel	270	270 or 66⅔	TIM[a]
Telemetry, engineering channel	33⅓	33⅓ or 8⅓	TIM
Telemetry, high-rate channel	86 4K	86 4K	TIM
Operational support equipment and spacecraft events/status	1 0K	10	ESM[b]
Data automation system TV	16 2K	16 2K	TIM
Science operational support equipment	4 5K	4 5K	DDM[c]
Analog TV	120K	120K	DDM
Analog hardline, low-speed	120	120	AIM[d]
Analog hardline, high-speed	5 3K	80	AIM
Operational support equipment, digital	1 0K	10	DDM
Central computer and sequencer	120	120	TIM

[a]TIM = telemetry input module
[b]ESM = events and status module
[c]DDM = digital data module
[d]AIM = analog input module

system test complexes (STC) will be implemented with displays/controls at any time

Computer and peripherals The computers are identical CDC-3300s, each with the floating point option and 65K word core memory Memory bus is arranged to allow each computer to access both 65K core banks, this to be used primarily for backup or for special requirements

Data input subsystem The basic configuration used to acquire all data from one spacecraft in any operating mode and engineering telemetry from one additional spacecraft is shown in Fig 22 Important design characteristics of the integrated configuration are as follows.

(1) The number of input modules of any type connected to either controller is not critical and is limited only by the number of source (device) codes available.

(2) The scanning of devices by the controller is on a semi-priority basis The higher rate input modules are connected to higher priority scan lines and are scanned first after each word transfer to the computer

(3) Each transmission from any of the devices connected to controller 1 is time-tagged and interrupts the program for processing

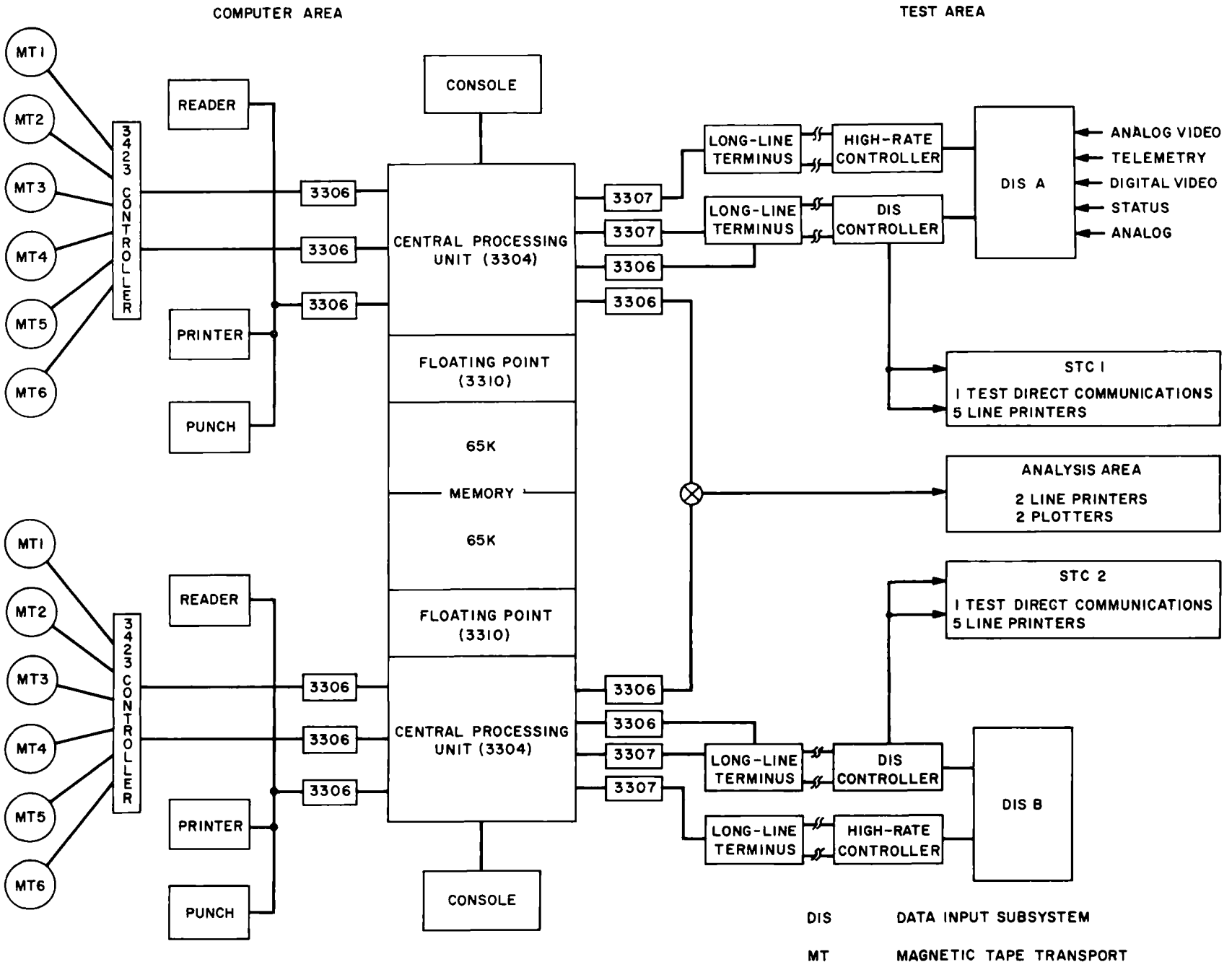

Fig. 21. *Mariner* Mars 1969 system test complex data system

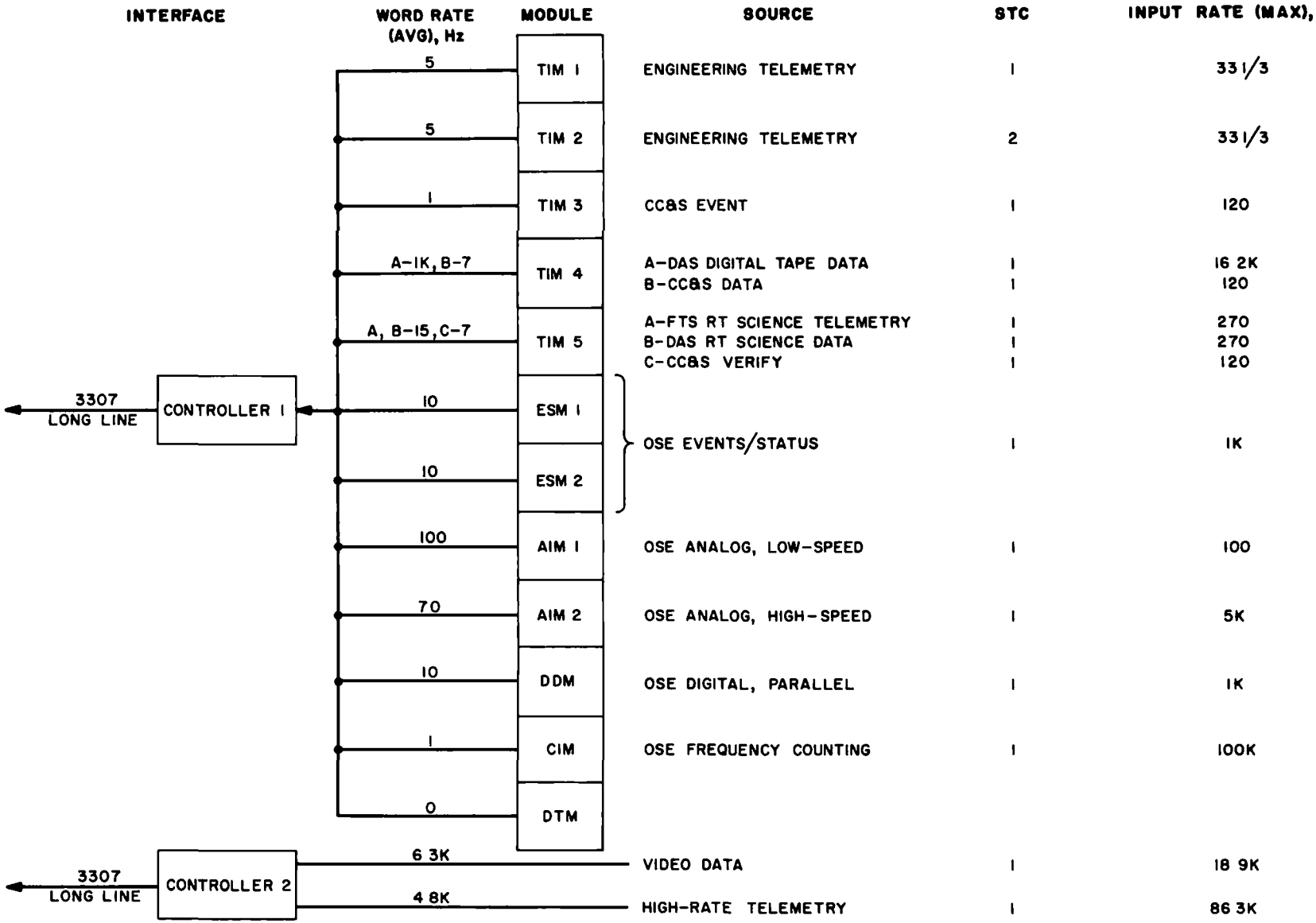

Fig. 22. Data input subsystem

(4) Transmissions of analog video data via controller 2 are accumulated in the computer as a block and time-tagged only once per block Program interrupt for processing occurs only at the conclusion of a complete block of data

(5) The command link from the computer and command distribution to all devices is also serviced by the controller module Commands may be issued under computer program control for any of the following

(a) Control and/or data for self-testing

(b) Control for device on–off switching

(c) Initialize/readout of device

(d) Control and/or data for diagnostic test module (DTM) special tests and routines

(e) Control and/or data for operational support equipment control functions

(6) The remote (STC) line printer and other display devices are operated from an independent input/output channel which is electrically terminated in the controller

(7) TIM 2 (Fig 22) is only required when supporting a second telemetry stream concurrently with STC 1 data acquisition

d Data processing.

Standard capabilities The standard capabilities accessible by any information "byte" are as follows (normally, more than one process from this list is applied to each data piece)

(1) Decommutation/identification These programs accomplish the decommutation of serial pulse-code-modulated data streams, a multiple number of streams, with different decommutation tables, is standard Identification of telemetry channels, analog channels, digitally coded data, event and status channels, and other acquired data channels for directing to the appropriate titling and processing is accomplished

(2) Message suppression Data is tested and displayed only if the value differs from the last displayed value of this channel by an increment X, where the value of X is optionally entered prior or during testing

(3) Alarm message A specially identified message is displayed and audible alarm sounded whenever a data channel value exceeds or is less than optionally entered threshold limit values

(4) Averaging Any numeric value channel may be averaged, and the averaged value processed

(5) Request message A number of sets of specially edited blocks of data can be called up by switch command from the test complex

(6) Units conversion A conversion routine which can convert raw data values to another set of units per an optionally supplied curve or table

(7) Raw data recording All acquired data plus time and other data are recorded for post-test use This process is *not* optional and will be performed without imposing such as a requirement

Special capabilities Within the constraints of time and dollars, almost any algorithm may be applied to the spacecraft and ground equipment data acquired by the STCDS Programs are developed to process specific data in a unique fashion Among those special purpose routines contemplated or coded are the following

(1) Spacecraft (central computer and sequencer) time monitoring and correlation

(2) Facility conditions, logging, and data correlation

(3) Temperature measurements and correlation

(4) Command detector lock

(5) System power calculations

(6) Real-time science data processing

(7) Time differences and durations

(8) Autopilot calculations

(9) Transmit–receive command comparator

(10) Central computer and sequencer program load/playback comparator

(11) Radio–operational-support-equipment calculations

(12) Special tape formatting/recording

(13) Video data formatting/recording

(14) Time-based data plotting

System support software In addition to the programs that perform the processes noted above, additional software is required to perform the functions of system control and programmer support The basic requirements are as follows

(1) Assembly program

(2) Tape update program

(3) Utility conversion routines

(4) Executive control routine

(5) Dynamic control—modification of optional parameters, device mode or state, and display assignments

(6) Message backup overflow reporting

(7) Real-time STCDS diagnostics and failure recovery

(8) STCDS performance monitor

(9) Non-real-time DIS checkout/calibration

8. Data Automation Subsystem Checkout

A computer-based checkout system is being provided for testing the science data automation subsystem (DAS) The checkout system comprises a PDP-7 computer, interface hardware to provide communication of signals between the computer and the DAS, and a computer program to drive the checkout system The checkout system acquires output signals from the DAS and simulates input signals to the DAS The program verifies that the DAS events occurred at the expected times and that the DAS output data is consistent with the simulated input signals Messages are printed if discrepancies are observed

9 Mission Operations

The mission operations are defined as those activities required before launch to plan the launch and post-launch operations, and after launch to execute these plans, and to obtain and process spacecraft information, commands, and related data until the end of the mission Figure 23 shows the mission operations operational organization

a. Design approach. The mission operations design will be optimized to meet the mission requirements set forth in Part I of the Mission Plan and Requirements Document, PD-91, and at the minimum practicable cost

The mission operations will be designed to operate both spacecraft on different flyby missions in the event both are successfully injected in good operating condition However, successful accomplishment of the mission objectives requires completion of either, but only one, flyby mission All project systems should strive to accomplish both missions in the event that all spacecraft systems are operating successfully

The design of the mission operations will not require continuous tracking and/or telemetry coverage of the spacecraft during the entire mission by the facilities of the tracking and data system but will be able to exploit continuous coverage if available

The ability to receive spacecraft telemetry data and to command the spacecraft by earth-based radio command, using assigned tracking and data system facilities, will be a prime mode of operation during standard mission operations

The design of the standard mission operations will not exceed the committed resources of the tracking and data system as stated in the NASA Support Plan

Sufficient flexibility will be incorporated into the design of the mission operations to permit modification of the aiming point of either or both spacecraft after launch

The mission operations design will incorporate sufficient time for adequate operational testing and training before launch and during cruise prior to encounter to insure successful accomplishment of the mission

b. Reliability criteria. The mission operations will be designed to be as simple as practical consistent with external constraints and required capabilities

The standard mission operations will be designed to use existing technology to the maximum degree possible The mission operations design will accommodate a realistic rate of failures and outages and incorporate appropriate recovery procedures

Provision will be made in the design of the mission operations to insure the ability to command the spacecraft at any time between launch and the end of the mission within two hours of identification of the need to command the spacecraft

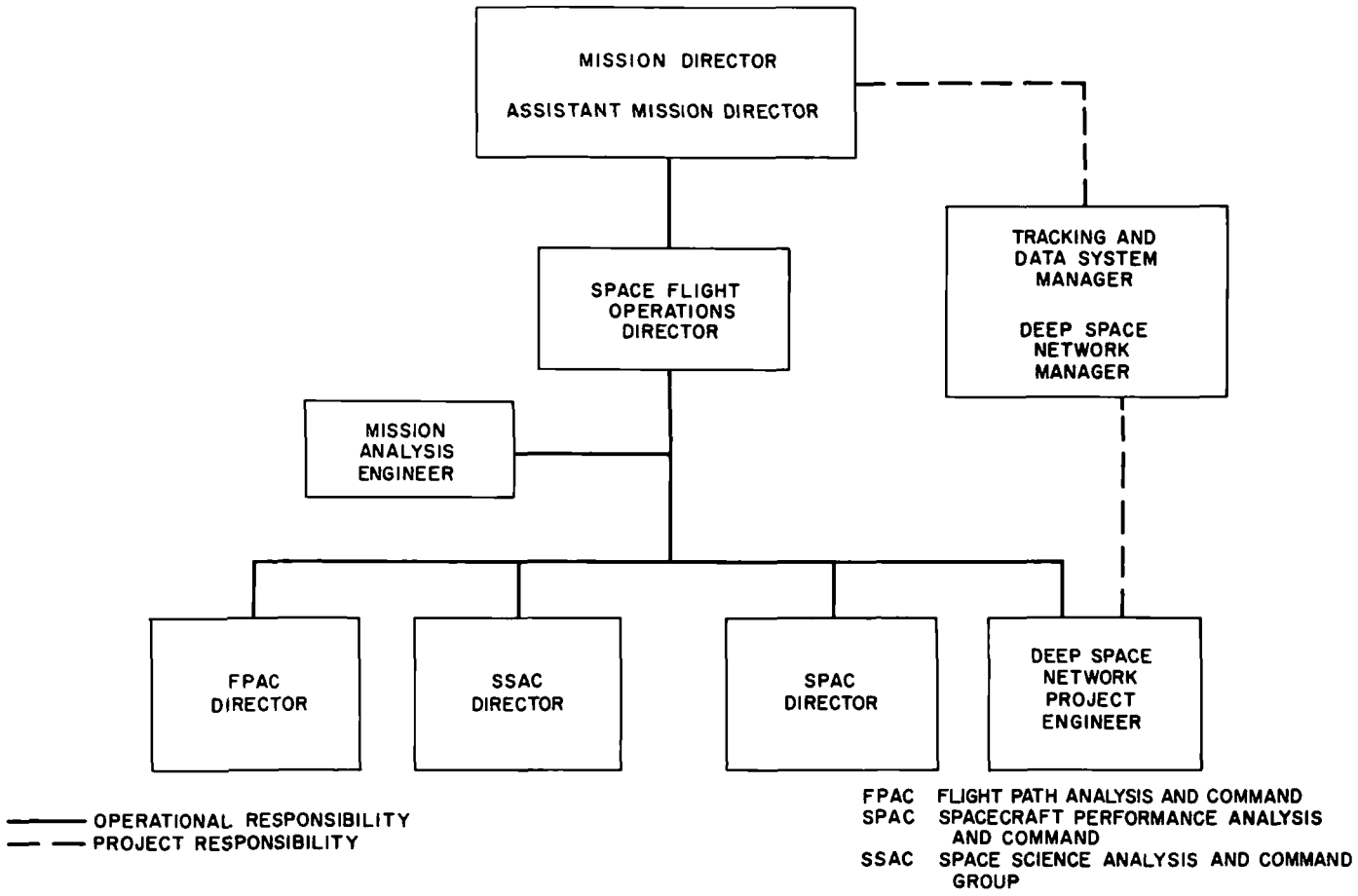

Fig. 23. Mission operations operational organization

C. Project Engineering

1. Spacecraft System Design

a. Weight control. A portion of the spacecraft system design task is concerned with weight control Under this effort, and to determine whether the design weight was becoming stabilized, a histogram was prepared of allocated weight and design weight This diagram is presented in Fig 24

The allocated weight for the spacecraft is the aggregate of the subsystem allocations The changes visible on the step-curve of allocated weight are associated with specific Engineering Change Requirement (ECR) controlled design changes at the subsystem level, except for the last one, which was associated with a comprehensive re-evaluation of weights, resulting in the increase of the spacecraft total allocation to 900 lb on August 11, 1967 The design weight curve is based on independent assessments and estimates by the cognizant engineers on their various subsystems and is the actual prediction of spacecraft weight

The last change in design weight reflects the removal of the approach guidance subsystem from the design Pending ECR action, this is not yet reflected in the allocation With this change, the design weight stands at 863 73 lb

b. TV coverage. A study was conducted during the reporting period on the possibility of increasing the television photographic coverage in the far encounter sequence The present plan calls for each spacecraft to obtain approximately eight narrow-angle pictures (one tape track on the analog recorder) during this phase The study will be described in the next reporting period

c. Attitude control. A study was begun concerning effects on the mission of the failure of an attitude control cold-gas jet The attitude control subsystem is designed

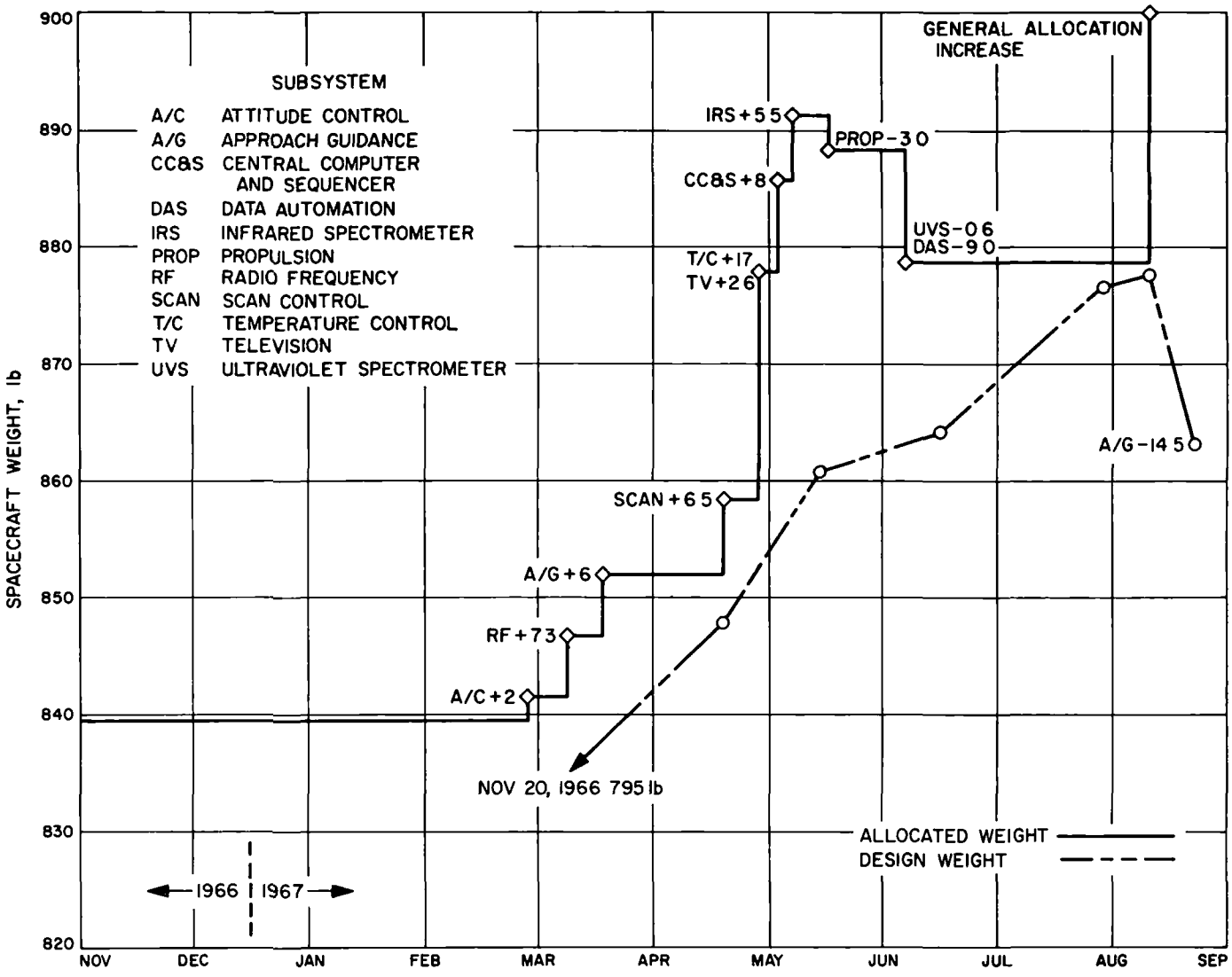

Fig. 24. *Mariner* Mars 1969 spacecraft weight history

with dual gas systems to survive such an inflight anomaly, but deleterious flight path effects are possible

D. Guidance and Control

1. Power Subsystem

a. Solar array panels. The present design for the solar array panels incorporates 2 × 2 cm N-on-P solar cells that have nominally 1 Ω-cm resistivity, solder on silver–titanium deposited coatings, and are nominally 18 mil thick

Kovar tabs of a new design in *Mariner* Mars 1969 are used to assemble solar cells into submodules, and new techniques are employed to limit solder filleting along the edges of the tabs, and to limit the quantity of solder used. Tests have indicated these modifications will increase solar panel reliability in space environment Solar cell cover glass has been changed from 0211 Corning 6-mil microsheet to 20-mil fused silica to reduce solar array radiation degradation There is a 3.5% decrease in solar array output power due to the loss of solar flux transmissibility through the thicker glass However, should there occur a major solar proton flare, it is estimated that array power degradation would be 22% with the 6-mil cover glass and only 12% with 20-mil fused silica Solar array weight increase due to the new cover glass is 12 lb, an increase of about 12% for the power subsystem

The nominal maximum solar array power output at Mars encounter during the mission is 518 W with the solar intensity at 69 mW/cm^2, and at a temperature of 2°C

b. Energy storage system The *Mariner* Mars 1969 18-cell sealed silver–zinc alkaline battery will have a nominal capacity of 43 A-h, or 1200 W-h, at temperature ambients between 14 and 32°C The minimum capacity at Mars encounter will be 900 W-h Maximum charge current to the battery will be under 1 A and will taper down to zero charge rate as a function of the relative potentials of the unregulated dc power bus and the terminal voltage of the battery

Vibration levels associated with the *Mariner* Mars 1969 *Centaur* booster are about twice those of *Mariner* Venus 67 between 600 to 2000 Hz Modifications have been made in the *Mariner* Mars 1969 battery cells, battery packaging design, and battery chassis design to increase mechanical integrity at these higher vibration levels Adhesive and potting compounds have been selected for better adhesive characteristics to the Cycolac container, and for better damping properties New assembly techniques have been employed for wire lead stress relief and battery plate immobilization The webbing design of the magnesium battery chassis has been modified Recent tests have demonstrated increased mechanical reliability The modifications increase the battery weight by 2 5 lb to 31 2 lb, exclusive of the chassis

c. Power conditioning equipment. Mariner power conditioning equipment units have been redesigned for *Mariner* Mars 1969 The maneuver booster regulator and the maneuver 2 4-kHz inverter of past missions were used only during attitude maneuvers, or as standby in the event of a main regulator failure The present design incorporates a main power chain consisting of the main booster regulator and the main 2 4-kHz inverters, and a similar standby power chain Automatic switching to the standby power chain occurs in the event of a failure in the main power chain Figure 25 shows the power subsystem configuration

In former designs, a pulse from the central computer and sequencer clock synchronized the main and maneuver 2 4-kHz inverters, and the flight telemetry subsystem utilized its own monitor oscillator for synchronization In *Mariner* Mars 1969 the 2 4-kHz power source provides the master clock pulse for the spacecraft and both the main and standby 2 4-kHz inverter assemblies incorporate a crystal-controlled clock Other changes in the *Mariner* Mars 1969 power conditioning equipment include

(1) Separate circuitry for the battery charger and boost converter

(2) An attitude control subsystem sun gate signal to be routed to the boost converter to confirm solar array sun orientation

(3) Packaging of the single- and three-phase 400-Hz inverters in one module

(4) A new module containing fuses for all spacecraft heaters

E. Telecommunications

1. Spacecraft Telecommunications System

Figure 26 shows the major functional elements of the telecommunications equipment being built for the *Mariner* Mars 1969 spacecraft The four subsystems are discussed separately below

a. Radio frequency subsystem. The radio frequency subsystem (RFS) receives uplink command and ranging signals transmitted by the Deep Space Instrumentation Facility (DSIF) and transmits telemetry and ranging signals to the DSIF Figure 27 shows the RFS block diagram Received and transmitted frequencies are in the S-band When no uplink signal is being received, the transmitted frequency of 2195 MHz (nominal) is governed by an onboard crystal oscillator When the receiver detects and achieves phase lock to an uplink signal, the transmitted frequency is 240/221 times the received frequency (2115 MHz nominal) When the spacecraft-transmitted frequency is under control of the onboard oscillator, the DSIF can accomplish one-way doppler tracking When the spacecraft-transmitted frequency is under control of the uplink received frequency, the DSIF accomplishes two-way doppler tracking The receiver and exciter portions of the RFS are functionally similar to those utilized for *Mariner IV*

The spacecraft receiver recovers command and ranging information from the uplink signal Command data is sent to the flight command subsystem Ranging data, when present in the uplink signal, is sent through the RFS ranging channel to modulate the spacecraft transmitter in order to provide the turn-around ranging function This ranging function can be turned on or off by means of ground command A composite telemetry signal from the flight telemetry subsystem also modulates the spacecraft transmitter

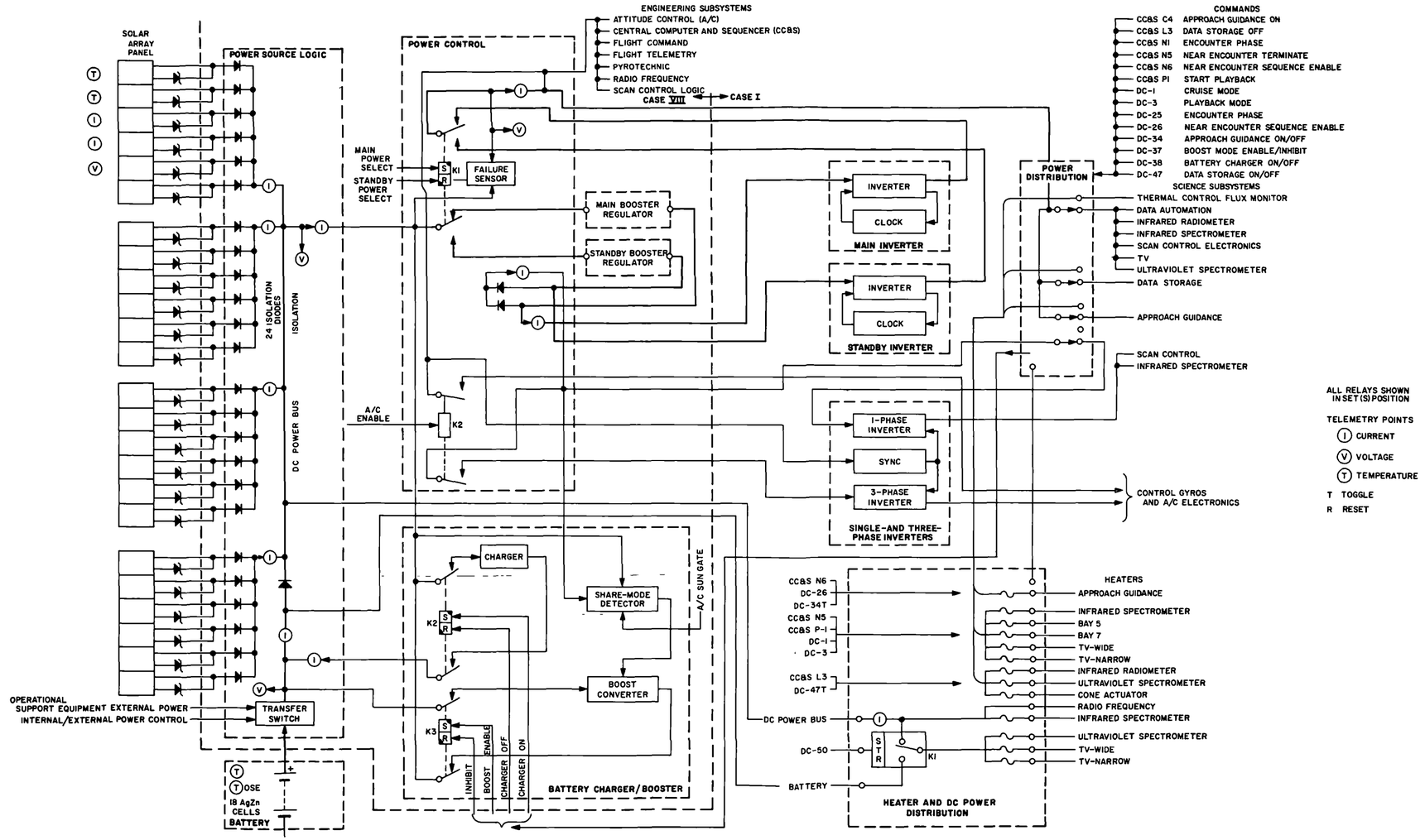

Fig. 25. *Mariner* Mars 1969 power subsystem

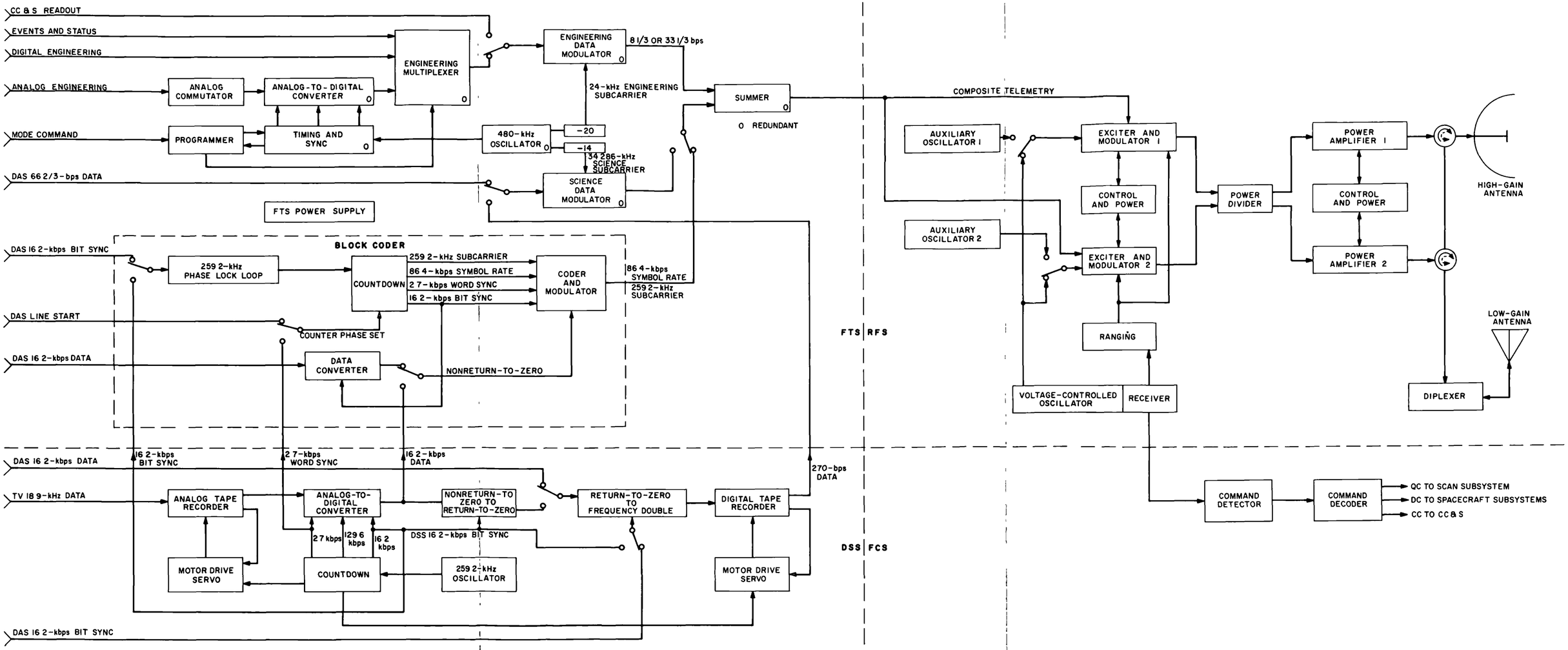

Fig. 26. *Mariner* Mars 1969 spacecraft telecommunications system

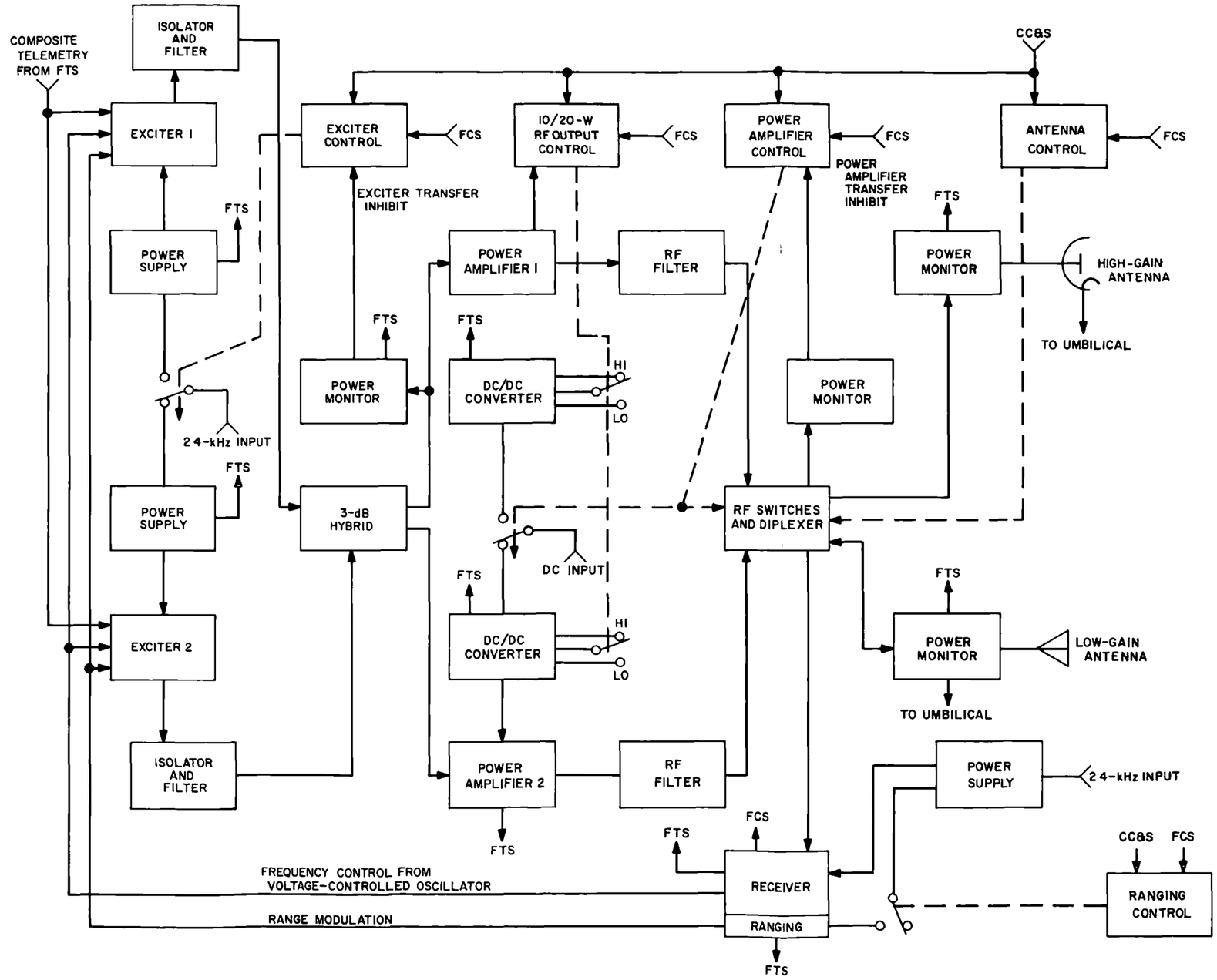

Fig. 27. Radio frequency subsystem

Page intentionally left blank

The receiver operates continuously and is a narrow band, automatic phase tracking, double conversion superheterodyne The receiver input stage is a balanced mixer, using hot carrier diodes giving a noise figure improvement of about 2 dB compared to that experienced with *Mariner IV* The spacecraft transmitter consists of two exciters and two traveling wave tube (TWT) amplifiers This differs from *Mariner IV*, where one TWT and one cavity triode amplifier were used Either exciter may be used with either amplifier, providing a fully redundant transmitter capability Switching between exciters and amplifiers is accomplished automatically by circuits which periodically test exciter and amplifier output If the outputs are below a specified threshold, automatic transfer to the redundant equipment is accomplished Switching may also be performed by ground command Each of the amplifiers can be operated at 10- or 20-W nominal output Power output change is by ground command and is accomplished by adjustment of operating voltages Input drive is constant

The RFS uses two antennas The high-gain antenna, used for transmitting during and after encounter, employs a 40-in -diameter parabolic reflector and a right-hand circularly polarized feed It is fixed to the spacecraft in such an orientation that the earth enters its beam (approximately 8 deg from the antenna boresite axis) about 150 days after launch and remains within the effective beam more than a month following encounter The low-gain antenna, also circularly polarized, is mounted on the sunward side of the spacecraft and has a hemispherical pattern approximately symmetrical about the roll axis It is used to receive at all times and to transmit during cruise

b. Flight command subsystem. The flight command subsystem (FCS) provides the following general functions

(1) Receives from the spacecraft radio subsystem the composite command signal containing the command word information and synchronization information

(2) Acquires phase coherence (lockup) with the synchronization information, which is a pseudo-random signal, and establishes a phase reference signal and bit synchronization signal

(3) Demodulates the command word information which is a biphase-modulated sinusoidal subcarrier, using the phase reference established by the synchronization process, and detects and reconstructs the command word data bits

(4) Provides a detector lock signal indicating whether or not detector synchronization with the received signal has been established

(5) Decodes the command word data bits and provides discrete momentary switch closures to the proper spacecraft user subsystem

(6) Decodes the command word data bits and directs a serial binary bit word, representing coded command data and bit synchronization information, to the spacecraft central computer and sequencer subsystem

(7) Decodes the command word data bits and directs a serial, variable length pulse train to the scan subsystem

FCS element relationships are shown in Fig 28 Three types of commands are transmitted to the spacecraft (1) direct command (DC) words provide a momentary switch closure to spacecraft subsystems, (2) coded command (CC) words provide serial bits to the spacecraft central computer and sequencer (CC&S) subsystem representing trajectory correction maneuver and update program information, and (3) quantitative command (QC) words provide a variable number of momentary switch closures to the scan subsystem

The command detector performs the first four FCS functions listed above The detector data channel selects the command word information from the composite command signal by means of a bandpass filter at the data subcarrier frequency The subcarrier is phase-coherently demodulated and filtered The output is then reconstructed into binary bits by a decision circuit and storage circuit and the resulting command word bits are directed to the decoder Pseudonoise (PN) command sync information is recovered from the sync subcarrier by the detector sync channel and used to maintain detector lock

The command decoder processes detected command words, reads the addresses, and outputs either a switch closure to the addressed subsystems in the case of a direct command, a serial bit word representing a coded command (with accompanying sync information) to the CC&S, or a serial pulse train of variable length to the scan subsystem in the case of a quantitative command Each type of command is recognized by its start code and processed by the appropriate command channel

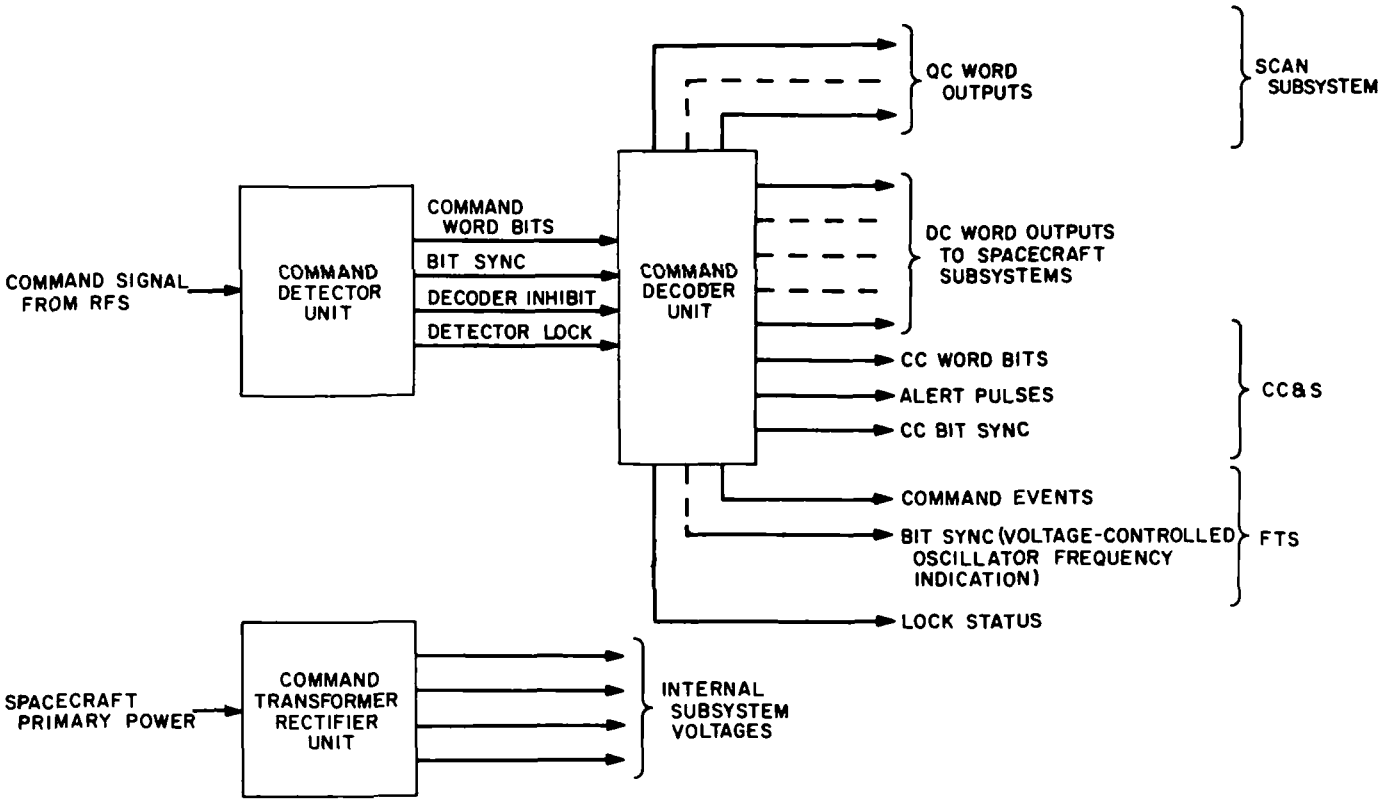

Fig. 28. Flight command subsystem

The FCS is designed to operate with 53 DCs, four QCs, and five CCs The command detector differs from that used in previous *Mariner* spacecraft The uplink command modulation is a composite of the command words described above and a PN synchronizing code Sync acquisition in the earlier design was accomplished by adjusting the clock in the ground command generator to run at a slightly different frequency from that of the spacecraft command detector This caused the received PN code to drift in phase relative to the local (spacecraft) code When the two codes came into phase, acquisition could take place

In the new detector, frequency offset is not used Instead, the local PN code is stepped 1 bit at a time until acquisition occurs After each step, a correlation is made for one PN cycle as a test of synchronism The new detector provides more sensitive performance, a much higher probability of acquisition under weak signal conditions, and the advantage of a fixed ground clock frequency

c. Flight telemetry subsystem. The conditioning, encoding, multiplexing, and subcarrier modulation of engineering data and the subcarrier modulation and block coding of scientific data are performed by the flight telemetry subsystem (FTS) Approximately 90 measurements obtained by transducers and electrical pick-offs distributed throughout the spacecraft constitute the engineering telemetry data Science data from the data automation subsystem (DAS) or the data storage subsystem (DSS) include digitized TV picture data and outputs of the infrared and ultraviolet spectrometers and the infrared radiometer The FTS provides an engineering channel during cruise, encounter and playback, and either a medium-rate science channel or a high-rate block-coded channel during encounter and playback The FTS differs from that used in earlier *Mariner* spacecraft in the following ways

(1) The subcarrier frequencies are much higher—24 and 34 286 kHz versus 150 Hz (at 8⅓ bps) or 600 Hz (at 33⅓ bps) This relieves carrier acquisition problems caused by telemetry sidebands being very close to the carrier frequency

(2) There are three data channels rather than one Engineering telemetry is separate from science data and is continuously available without mode switching

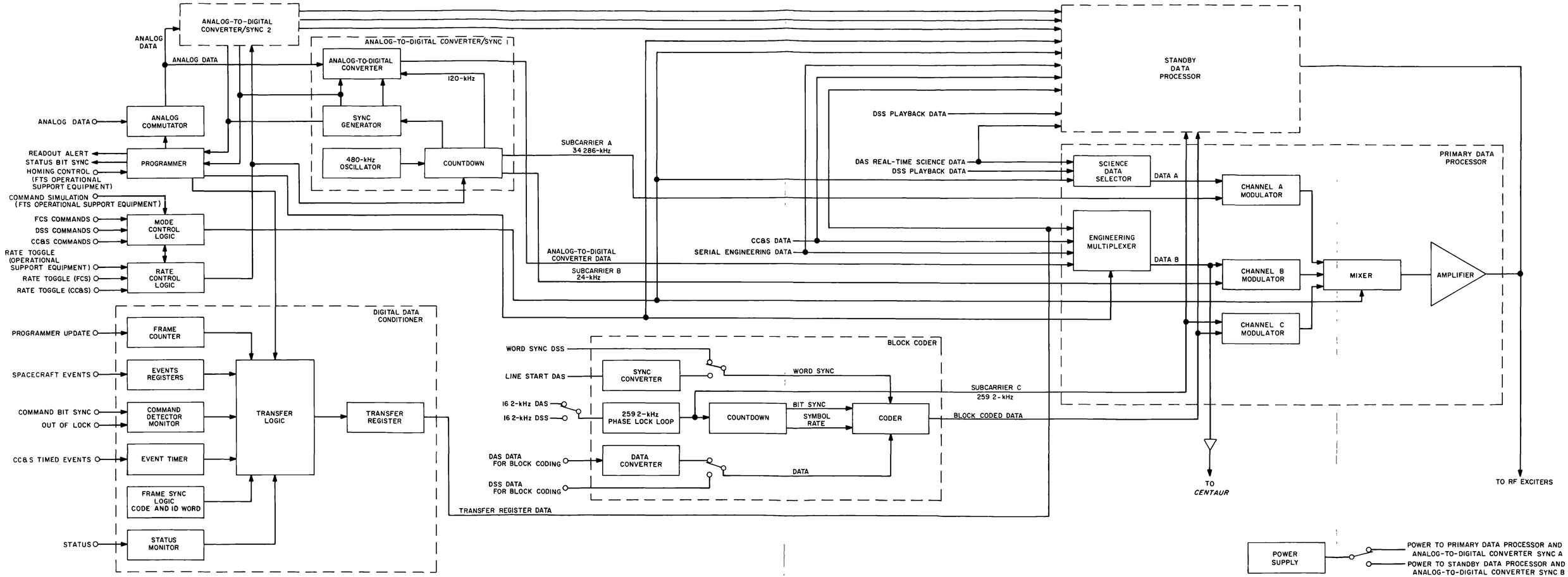

Fig. 29. Flight telemetry subsystem

Page intentionally left blank

The third channel, containing 16 2-kbps block-coded data, is available as a part of the high data rate experiment

(3) There is no separate spacecraft-generated bit synchronization code and subcarrier Synchronization is accomplished in new ground equipment which recognizes transitions within the data stream

(4) Four data rates are employed 8⅓ and 33⅓ bps for engineering, 66⅔ and 270 bps for science

A block diagram of the FTS is given in Fig 29 Data modes and rates are given in Table 6 The engineering measurements are commutated in ten decks sampled at four rates A whole data frame (at least one sample of every measurement) requires 14 min at 33⅓ bps, 56 min at 8⅓ bps Frame synchronization and subcommutation indexing are provided by words in the highest speed deck The engineering data biphase-modulates a 24-kHz subcarrier During encounter, the science channel accepts 66⅔-bps serial digital data from the DAS The format includes infrared and ultraviolet spectrometer and infrared radiometer data with instrument calibration status and engineering data During playback, the FTS accepts data from the DSS Combined TV, ultraviolet spectrometer, infrared spectrometer, and indexing and utility data stored on the digital tape recorder are played back first at 270 bps Then a portion of the TV data stored on the analog tape recorder is transferred to the digital tape recorder by means of an analog-to-digital converter Once again, the digital tape recorder is played back to FTS at a rate of 270 bps The process is continued until the analog data is completely transmitted Science data biphase-modulates a 34 286-kHz subcarrier

As an engineering experiment, the 16 2-kbps high-rate channel utilizes block coding in FTS and the 210-ft diameter antenna at the Mars deep space station to telemeter science data During encounter, the high-rate channel may be used to transmit in real time the 16 2-kbps data being placed on the digital tape recorder During playback, TV data on the analog tape recorder may be fed directly to FTS (rather than to the digital recorder) through the analog-to-digital converter at a 16 2-kbps rate Within FTS, the serial digital stream accepted from either DAS or DSS is passed through a block coder, which translates the 6-bit data words into words of 32 symbols The symbol rate is then 86 4 kbps The symbols biphase-modulate a 259 2-kHz subcarrier

Table 6. Data modes

Channel	Cruise rate, bps	Encounter rate, bps		Playback rate, bps	
		1	2	1	2
Science	Not used	66⅔	Not used	270	Not used
Engineering	33⅓ or 8⅓	33⅓ (8⅓)[a]	8⅓ (33⅓)[a]	8⅓ (33⅓)[a]	8⅓ (33⅓)[a]
High-rate	Not used	Not used	16 2 k	Not used	16 2 k

[a] Not normally used

The modulated engineering subcarrier is combined with either the modulated medium-rate science subcarrier, or the modulated high-rate subcarrier to form a composite telemetry signal which is then fed to the RFS The relative amplitude of the two components of the composite signal is adjusted so as to properly allocate the transmitter power between the two data channels

d. Data storage subsystem. The data storage subsystem (DSS) provides buffering between the high rate at which data is acquired by the TV and other scientific instruments and the lower rate at which these data can be returned to earth A total of $1\,8 \times 10^8$ bits of data can be stored The subsystem consists of a digital tape recorder and its electronics, an analog tape recorder and its electronics, an analog-to-digital converter, and control and power electronics (Fig 30) The *Mariner* Mars 1969 DSS differs from previous *Mariner* practice in that it uses two tape transports, one digital and one analog, rather than one digital machine Each transport is similar to the earlier design except that 4 tracks are available instead of 2, the packing density is higher, and the record and playback speeds are different

During the far encounter phase, the DSS stores data representing approximately eight high-resolution TV pictures during the period of from 45 to 12 h prior to closest planet approach The analog recorder will be started before each picture is to be recorded and stopped at the completion of each picture All data from this phase shall be stored on one track on the analog recorder only

In the near encounter phase, the DSS stores data representing approximately 12 narrow-angle and 12 wide-angle TV pictures during the period of closest approach All the TV data is stored on the analog recorder In addition, every seventh picture element is digitized and placed on the digital recorder along with ultraviolet and infrared spectrometer and infrared radiometer data At the completion of this recording sequence the analog recorder will be full, the digital

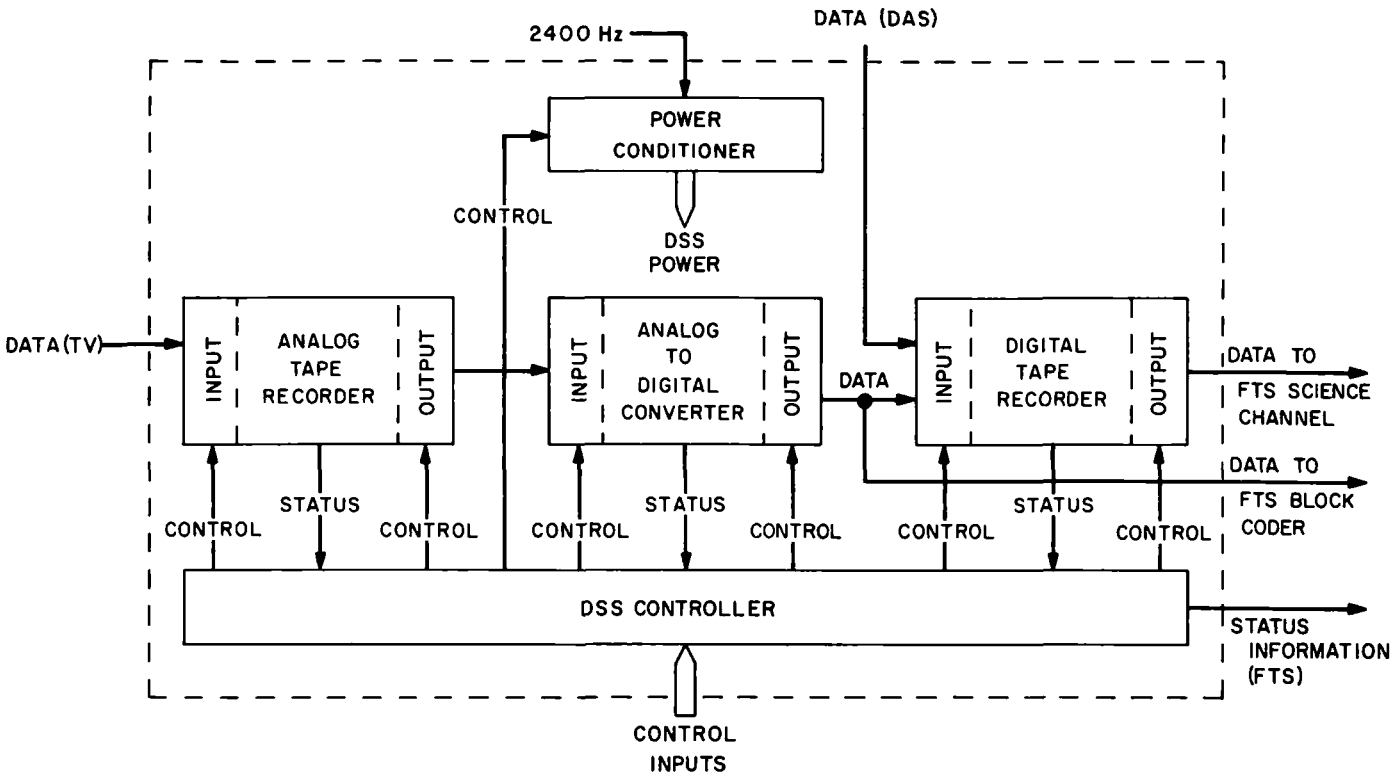

Fig. 30. Data storage subsystem

recorder will have recorded three tracks After the instrument traces cross the terminator on Mars, the DSS stores data from the ultraviolet and infrared spectrometers and the infrared radiometer for approximately 6 min past terminator crossing This, the final encounter data, is stored on the fourth track on the digital recorder

The playback sequence begins after closest approach This sequence consists of the following

(1) Reproducing all stored data from the digital recorder and sending it to the FTS Playback of the data is at 270 bps The digital recorder data stored during encounter are nominally played back two times

(2) Reloading the digital recorder by transferring analog data through the analog-to-digital converter to the digital recorder

(3) Repeat of Step (1) (The digital tape recorder is not played back twice following an analog-to-digital transfer) The process of reloading the digital recorder from the analog recorder and playing it back is repeated (total of seven cycles)

When the high-rate option is employed, analog recorder data is passed through the analog-to-digital converter and sent to the FTS block coder at 16 2 kbps (Digital recorder data is played back at 270 bps) The playback continues until commanded to stop

F. Space Sciences

1. Television Subsystem

a. Introduction. The primary scientific objectives of the photographic experiment for the *Mariner* Mars 1969 flyby, assisted by the boresighted infrared radiometer experiment, are (1) to determine the general physiography over much of the planet at a resolution significantly better than that obtainable from the ground and to topographically categorize the basic light and dark areas in terms of their seasonal variations, (2) to further explore, both geographically and in resolution, the unknown planetary surface for additional clues as to its origin, and (3) to obtain sufficient coverage at a suitable resolution to distinguish on the basis of crater morphology and other criteria, between an episodic and continuous history

b. Instrument description. In order to meet the scientific objectives, particularly in terms of both high spatial resolution and large area coverage, a two-camera, ultra-slow scan vidicon television system with optics having a

10 1 focal length ratio has been designed Both cameras are identical except for lenses and shutters The cameras are electromagnetically deflected and focused to obtain the spot size required for high-resolution operation Pictures are acquired by sequentially exposing the wide-angle and narrow-angle cameras at 42 24-s intervals as the spacecraft flies by Mars Due to trajectory characteristics and spacecraft velocity, this shuttering interval will allow the acquisition of approximately 26 pictures during near encounter Additionally, 8 pictures will be taken at 4-h intervals by the narrow-angle camera beginning 48 h prior to encounter To permit the camera view angles required, both cameras are mounted on a positionable scan platform having two degrees of freedom Since each picture comprises 704 lines, each containing 945 pixels (picture elements), $2\,2 \times 10^7$ pixels of information about Mars will be obtained from each spacecraft This amount of data when converted to binary form to the accuracy desired (8 bit or 256 levels) would result in a requirement for onboard storage of $1\,8 \times 10^8$ data bits To overcome this problem, a form of data compression is used wherein one-seventh of the pixels are converted to 8-bit binary form in real time and stored on a digital tape recorder with the two most significant bits (128 and 64) suppressed At the same time, all pixels, in analog form, are high-pass-filtered (with automatic gain control), cubed (low-contrast, high-frequency information amplified to increase modulation index), then stored on the analog tape recorder by direct bias recording Direct recording permits increased bit packing density, allowing all elements to be stored in real time Subsequent to the playback of the data on the digital tape recorder, the analog tape machine plays back the data into a 6-bit analog-to-digital converter, the output of which is recorded on the digital recorder for playback to earth Since seven times as many bits are stored in equivalent analog form as can be accommodated by the digital tape recorder, seven "analog-to-digital" transfers and seven digital tape playbacks will be required to return all of the picture data

Implementation of the television subsystem can be conveniently considered in seven major functional blocks (Fig 31)

(1) Camera A head

(2) Camera B head

(3) Camera A drivers

(4) Camera B drivers

(5) Logic and data control

(6) Data converter

(7) Power supply

Camera A head This subassembly contains the vidicon tube, the low-noise preamplifier, the cathode drive amplifier, the target voltage switching network, deflection, focus, and alignment coils, and associated voltage and signal distribution circuitry The preamplifier, with an FET[12] source-follower input, provides impedance matching with the vidicon, and a transfer function of 20 mV/nA signal current The output feeds a postamplifier with a voltage gain of about 300 (adjustable) A high-light input ($\approx 0\,2$ ft-cd-s) results in a 4-V peak-to-peak signal output

The cathode driver amplifies an 18 9-kHz square wave and applies it to the vidicon cathode at a sample rate of one cycle per pixel Varying between 0 and +8 V, this signal turns the electron beam on and off to generate the 9 45-kHz bandwidth video Thus, the signal seen out of the preamplifier is an 18 9-kHz carrier with both sidebands modulated by video

The gain switches select the desired tap on a voltage divider between the preamplifier and the postamplifier. The gain steps-down in factors of 1 7 from maximum to provide optimum signal levels to the data converter when commanded by the automatic aperture control Two temperature transducers are provided for engineering monitoring of the thermal environment The associated optics comprise a 50-mm T4 lens and a single-solenoid actuated rotating disk shutter of the *Mariner IV* type The shutter action occurs when one of four holes in the disk is rotated in front of the vidicon target, 1/10 s later, a further 45-deg rotation of the disk places a solid portion of the disk in position, ending the exposure The four holes carry color filters mounted such that one complete rotation of the shutter disk results in exposures being made through filters in the sequence — orange, green, orange, green Microswitches actuated by a cam follower riding on the disk edge provide signals to indicate which filter was used for a particular frame, and to re-index the disk in the event of an open shutter condition

Camera B head This subassembly differs from camera A head only in the optics and shutter A 508-mm catadioptric telescope provides images through a twin-solenoid, two-blade shutter The solenoids are sequentially pulsed, resulting in one blade uncovering the central aperture and the second blade covering the aperture

[12]FET = field-effect transistor

1/100 s later The lateral movement of the blades is reversed for each subsequent exposure, eliminating the need to reset the shutter and decreasing the total number of operations required Open shutter protection is inherent in this mechanization

Both camera A and B heads are mounted on the two-axis scan platform, and both sets of optics are provided with transparent, command-deployable, protective covers The camera heads are mechanically and electrically identical except for shutter and optics and, without these components, are functionally interchangeable

Camera A drivers This major block contains the line and frame sweep circuits, the control grid (G_1) voltage switch, the shutter driver, and the automatic aperture control The line and frame circuits generate 50-ms and 42 24-s (respectively) ramp voltages and drive the vidicon yoke to provide deflection and establish the scanned raster As each camera is erased and primed for 42 24 s following the 42 24-s readout time, the sweep voltages are increased so as to deflect the beam over an area larger than that readout At the same time, the frame sweep is changed to a 20-kHz sine wave superimposed on a 32-s retrace This "firehosing" of the target is concurrent with a switch in G_1 level to provide a high current–density defocused beam The resulting action is a bombarding of the target with electrons, establishing an equipotential condition and thereby "erasing" the previously imaged picture

The G_1 switch provides the scan and erase potential switching of the vidicon control grid

The shutter drive provides the pulses to drive the shutter solenoid The pulse spacing is normally $\approx$120 ms, however, a 60-ms speed is obtainable when commanded by the automatic aperture control

The automatic aperture control varies the "exposure aperture" of the entire system towards maintaining operation in the proper sensitivity range for the illumination conditions encountered This is accomplished by varying the preamplifier/postamplifier gain and the exposure time Since exposure time has two levels and gain has four levels, eight possible ranges can be selected Acting on information from the video level indicator circuit which monitors digital video levels, the automatic aperture control can switch up or down, one or two ranges at a time The particular parameter to be switched is determined by the automatic aperture control, which considers its own output circuit state and compares this with the magnitude of change desired based on the video level indication The total aperture (input light to output data number ratio) variation possible, including encoder range, will accommodate a change of illumination of 200 1

Camera B drivers These circuits are identical with the camera A drivers except for the shutter circuit which provides pulses to the twin-solenoid shutter Exposure times available are 12 and 6 ms The G_1 voltages and the sweep levels are optimized for the vidicon and yoke in the camera B head

Logic and data control All camera sequencing control originates in this major block A rectangular line pulse is generated from the data automation subsystem supplied line start and video start pulses The rectangle pulses are counted down to frame rate (42 24 s) by binary logic The frame rate and intermediate logic rates from the count-down circuits are logically combined to obtain timing functions for scan, erasure, blanking, and shuttering of both cameras A and B

All telemetry circuitry is contained in the logic and data control Four slowly changing levels from each camera are converted to pulse widths and sampled by the data automation subsystem for inclusion in the real-time telemetry format

The functions monitored are control grid voltage, camera head temperature, focus coil current, and vidicon anode potential Sampling occurs approximately 10 times per TV frame, sequentially, in a synchronous manner so that all functions appear twice per TV frame and two of them 4 times

Camera status is indicated by the following six binary bits per camera

Digital 128 video level	1 = yes
Digital 64 video level	1 = yes
Target voltage, high-low	1 = high
G_1 voltage, high-low	1 = high
Exposure time, fast-slow	1 = slow
Filter position, red-green sequence	1 = red

These status bits, commutated between cameras, are stored in a shift register which is read out by the data automation subsystem 30 times per TV frame and inserted into the real-time telemetry format

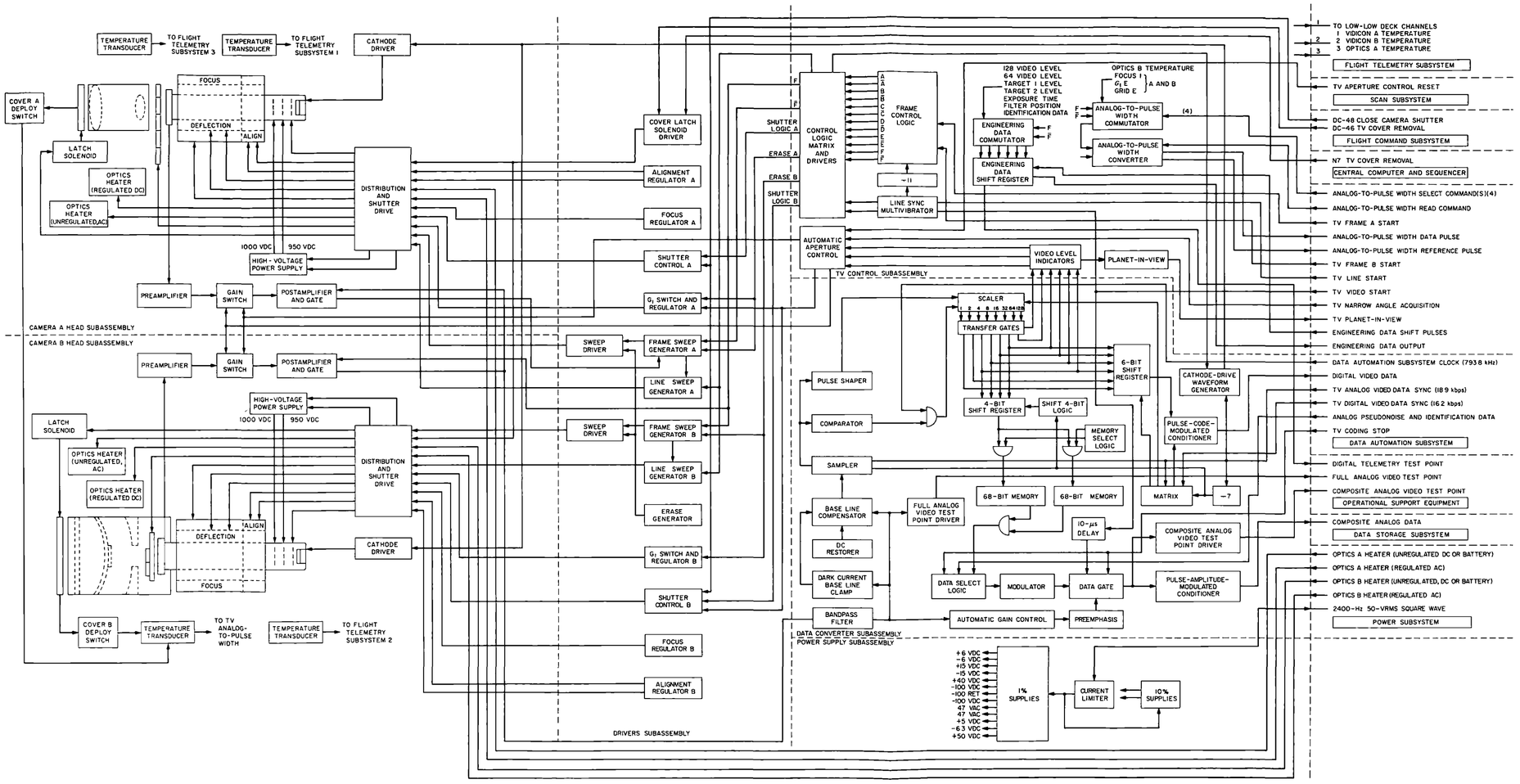

Fig. 31. *Mariner* Mars 1969 TV subsystem

Page intentionally left blank

PAGE MISSING FROM AVAILABLE VERSION

Data converter This unit receives video from both mera preamplifiers and conditions it for storage on the gital and analog tape recorders The video gate toggles frame rate such that a continuous stream of video is t out This combined video is sent through two chanls The analog channel automatic gain controls and e-emphasizes the video to optimize the levels seen by e analog tape recorder for linear recording The autoatic gain control circuit has a time constant of one-third a line To monitor the automatic gain control function ground picture reconstruction, selected digitized picre elements (every 28th of the original) are inserted o the sync pulse times between each line of video ta Additional coding data (PN sequence, frame and e ID, etc)[13] from the data automation subsystem are serted at this time

The video routed to the digital channel is sampled to tain every seventh element which is then converted an 8-bit binary value representative of the element nplitude These digital bits are sent to the digital tape corder via the DAS At the same time, the 28th element mpler and the video level indicator look at the elents The sampler stores its bits until the following nc pulse time, then dumps them into the analog video eam The video level indicator considers the peak lues seen during part of each line, and informs the mera A and B automatic aperture control circuits for namic range changing purposes

Power supply This major block receives 2400-Hz, -V rms square-wave power from the spacecraft power bsystem Approximately 32 W will be required to supy driving voltages for the TV subsystem The input wer is transformed to desired levels, rectified, filtered, d regulated Focus coil current is regulated for coil sistance changes with temperature Overcurrent limitg is provided in the primary circuit Limiting occurs at 0% of operating current in the event of short circuiting

c. ***Performance and physical characteristics.*** Physical aracteristics and constraints of the TV subsystem are ven in Table 7 Table 8 gives camera A and B perrmance characteristics

d. Design and testing. The breadboard electronic sysm has been fully evaluated and has demonstrated, nder laboratory conditions, that the instrument design capable of achieving the stated scientific objectives

PN = pseudonoise, ID = identification data

Table 7. TV subsystem components physical characteristics and constraints

Component	Size, in	Weight, lb
Camera A	9 × 5 × 4	7 (on scan platform)
Camera B	32 × 10 × 10	28 5 (on scan platform)
Logic and data control	6 × 14 × 1½	3
Camera drivers	6 × 14 × 1½	4
Data converter	6 × 14 × 1½	3
Power supply	6 × 7 × 2	4

Table 8 Camera A and B performance characteristics

Characteristic	Camera A	Camera B
Effective focal length, mm	50	508
Focal ratio	f/3	f/2 5
Normal shutter speed, ms	120	12
Angular field of view, deg	11 × 14	1 1 × 1 4
Active target raster, mm	9 6 × 12 5	9 6 × 12 5
Aspect ratio	1 3068 1	1 3068 1
Active scan lines per frame	704	704
Frame time, s	42 24	42 24
Total line time, ms	60	60
Active line time, ms	50	50
Line sync time, ms	10	10
Black mask time (approx), ms	1 5	1 5
Active picture elements per line	945	945
Maximum surface scale (@ 3000 km), m/TV line	1020	94 8
Video base band, kHz	9 45	9 45
Video sampling frequency, kHz	18 9	18 9
Video pass band, kHz	9 45–28 35	9 45–28 35

Evaluations have included verification of interfaces with both the data automation subsystem and the data storage subsystem, with more extensive parametric evaluations being conducted with the data storage subsystem Prototypes of both the narrow-angle and wide-angle optical systems, also in the environment of the laboratory, have demonstrated performance in excess of the design requirements

A prototype instrument, including both optical systems and shutters, is complete and scheduled for extensive evaluation, which will include subjecting the subsystem to the thermal environment as well as verification of calibration methods and techniques Proof test model fabrication has commenced and is scheduled for completion at the end of the next reporting period

2. Infrared Spectrometer Subsystem

a. Introduction. The infrared spectrometer will acquire data relevant to the possible presence of life (current and past) on Mars. To assist in supplying the answers, the infrared spectrometer will attempt to detect:

(1) The presence of an oxidizing or reducing atmosphere.

(2) The presence of polyatomic molecules that suggest biochemical processes, affect the ambient surface temperature, and limit ultraviolet light flux at the surface.

(3) The compositional variations of atmospheric constituents relative to geographical locale.

Other valuable data concerning surface composition, gas temperature, albedo, surface temperature, and atmospheric photochemistry will be obtained.

b. Description. Radiation is collected by an f/2.3, 10-in. Dall-Kirkham telescope and divided by a beam splitter into two separate paths. In one path, the radiation is analyzed in the 1.9- to 6.0-μ band, while in the other path, the radiation is analyzed in the 4.0- to 14.3-μ band. The radiation in each path is modulated by a tuning fork chopper and then passes through a circular variable interference filter which rejects all radiation except for that within a very narrow band. The nominal wavelength of each band passed is dependent upon the angular position of the filter. Wavelength scanning is accomplished by rotating the filters.

The long wavelength channel uses a HgGe detector cooled to 22°K by a two-stage gaseous nitrogen-hydrogen cryostat. The short wavelength channel uses a PbSe detector cooled to 135°K by conduction to a radiation plate. The output of each detector is amplified, filtered, and synchronously demodulated. After demodulation, the signals are conditioned through a logarithmic compressor and fed to a multiplexer for digital conversion by the analog-to-pulse width converter and the data automation subsystem. The data automation subsystem controls the sequencing of the multiplexer and sampling of the analog-to-pulse width converter. The data is then ready for recording and/or transmission to the earth.

c. Physical and electrical characteristics. The infrared spectrometer telescope–monochromator is located on the scan platform and weighs approximately 19 lb. The gas system, consisting of two pressure vessels, weighs approximately 12 lb and is also mounted on the scan platform. Figure 32 shows the telescope–monochromator minus the electronics and gear train.

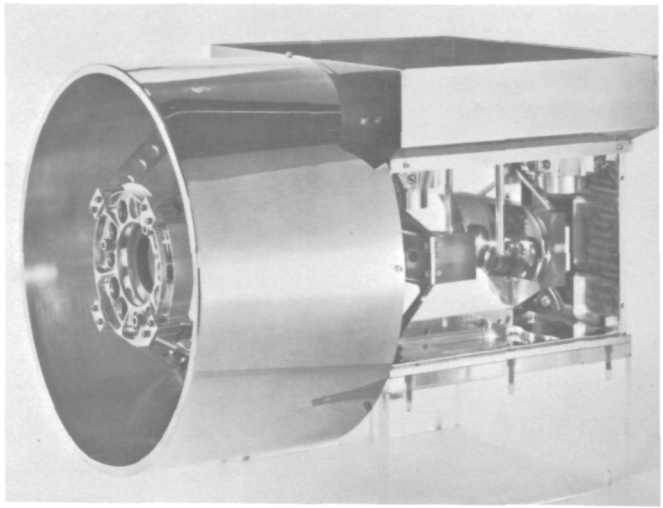

Fig. 32. Infrared spectrometer telescope–monochromator (less electronics and gear train)

The power required by the infrared spectrometer is:

(1) 4 W of 2.4-kHz square wave for the electronics during encounter.

(2) 2 W of 400-Hz square wave for the motor during encounter.

(3) 4 W of 2.4-kHz square wave for heaters during cruise.

(4) 4.5 W of dc for thermostatically controlled heaters during cruise and encounter.

d. Design and testing. The electronics breadboard and another unit, the flight configuration breadboard, have been built and the flight configuration breadboard is undergoing testing. The temperature control model and the structural test model were recently delivered to the Jet Propulsion Laboratory.

3. Ultraviolet Spectrometer Subsystem

a. Introduction. The scientific objectives of the ultraviolet spectrometer (UVS) experiment are:

(1) To detect the presence of certain atoms, ions, and molecules in the upper atmosphere of Mars. The atmospheric species of primary importance to the experiment

re

Species	Wavelength, Å
Atoms	
Hydrogen	1216
Oxygen	1304
Nitrogen	1200
Carbon	1657
Ions	
Molecular nitrogen	3914
Carbon monoxide	4264
Carbon dioxide	2880
Molecules	
Nitrogen	1354, 3371
Nitric oxide	2150
Carbon monoxide	2160
Cyanogen	3876

he wavelengths listed are the nominal wavelengths where the species will be sought While there may not e sufficient solar energy to excite other atmospheric pecies, it will be a secondary objective to seek species uch as krypton (1235 Å), xenon (1470 Å), metallic ions, nd other molecules in the spectral range being examined

(2) To measure the scale height and altitude range of ach of these constituents The altitudes considered most kely are listed below with a nominal value for the scale eight of each species, based on present knowledge of he Martian atmosphere

Species	Altitude, km	Scale height, km
Atoms		
Hydrogen	250–30,000	1000
Oxygen	250–1000	70
Nitrogen	100–200	70
Ions		
Molecular carbon monoxide	250–400	70
Molecules		
Nitrogen	100–200	24
Nitric oxide	100–200	24
Carbon monoxide	100–200	24
Cyanogen	100–200	24

(3) To measure the Rayleigh scattering from the lower atmosphere and the ultraviolet reflectivity of the planetary surface Molecules that absorb in the ultraviolet, such as ozone, will be measured if present in sufficient quantities

b. Optics. The optical portion of the ultraviolet spectrometer consists of an occulting slit telescope, focal length 25 cm, and a scanning Ebert spectrometer, focal length 25 cm The instrument's field of view is restricted by a baffle box placed in front of the primary mirror The telescope primary mirror focuses the image on an occulting slit, and the secondary mirror images the light from the occulting slit on the entrance slit of the Ebert monochromator Light from the entrance slit fills half of the Ebert mirror The mirror collimates the light and directs it toward the grating The dispersed light from the grating is focused on the two exit slits by the remaining half of the Ebert mirror The two separate exit slits provide signals to two separate photomultiplier channels which operate in different wavelength bands Light passing through the exit slits enters the sensors and is converted to electrical signals that are proportional to intensity Figure 33 illustrates the optical layout of the instrument

c. Electronics. Each photomultiplier tube has a separate set of electronics The signals from the photomultiplier tubes are integrated and processed by two sets of sample and hold circuits such that the analog outputs are a true representation of the anode currents in the photomultiplier tubes after integration These analog signals are then digitized by the data automation subsystem Figure 34 is a block diagram of the ultraviolet spectrometer

d. Physical characteristics. The ultraviolet spectrometer is mounted on the spacecraft scan platform and will operate within the temperature range of -10 to $+10$°C The total weight of the instrument is 30 lb and requires 12 W of 2 4-kHz spacecraft power The engineering model, minus the electronics module, is shown in Fig 35

e. Testing. The updated engineering model, which includes as many of the prototype features as feasible, is presently being tested These tests include dynamic mechanical testing with the optics included, and electronic interface testing with the data automation subsystem Thermal analysis studies are also being conducted on the engineering model

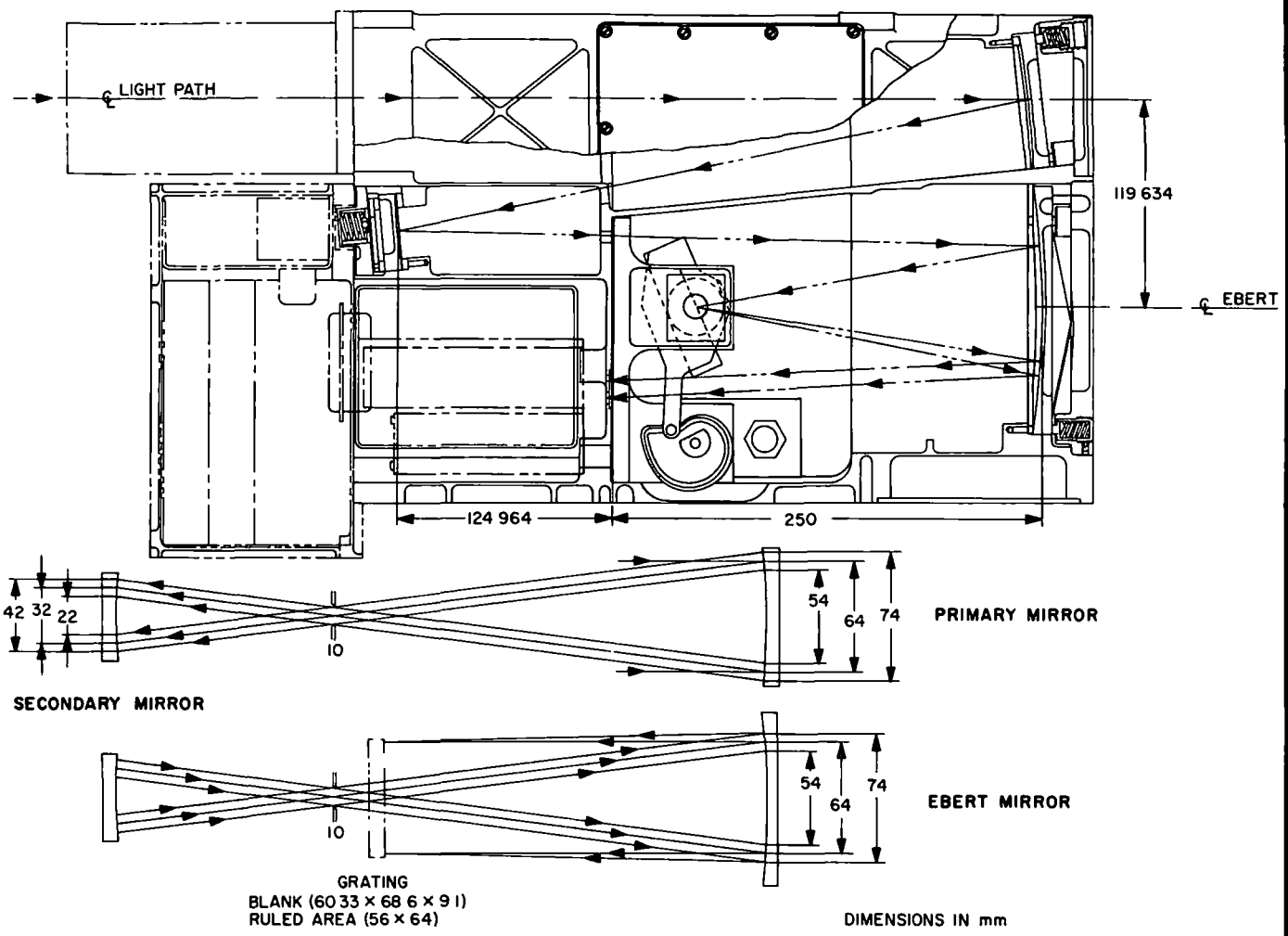

Fig. 33. *Mariner* Mars 1969 ultraviolet spectrometer physical configuration

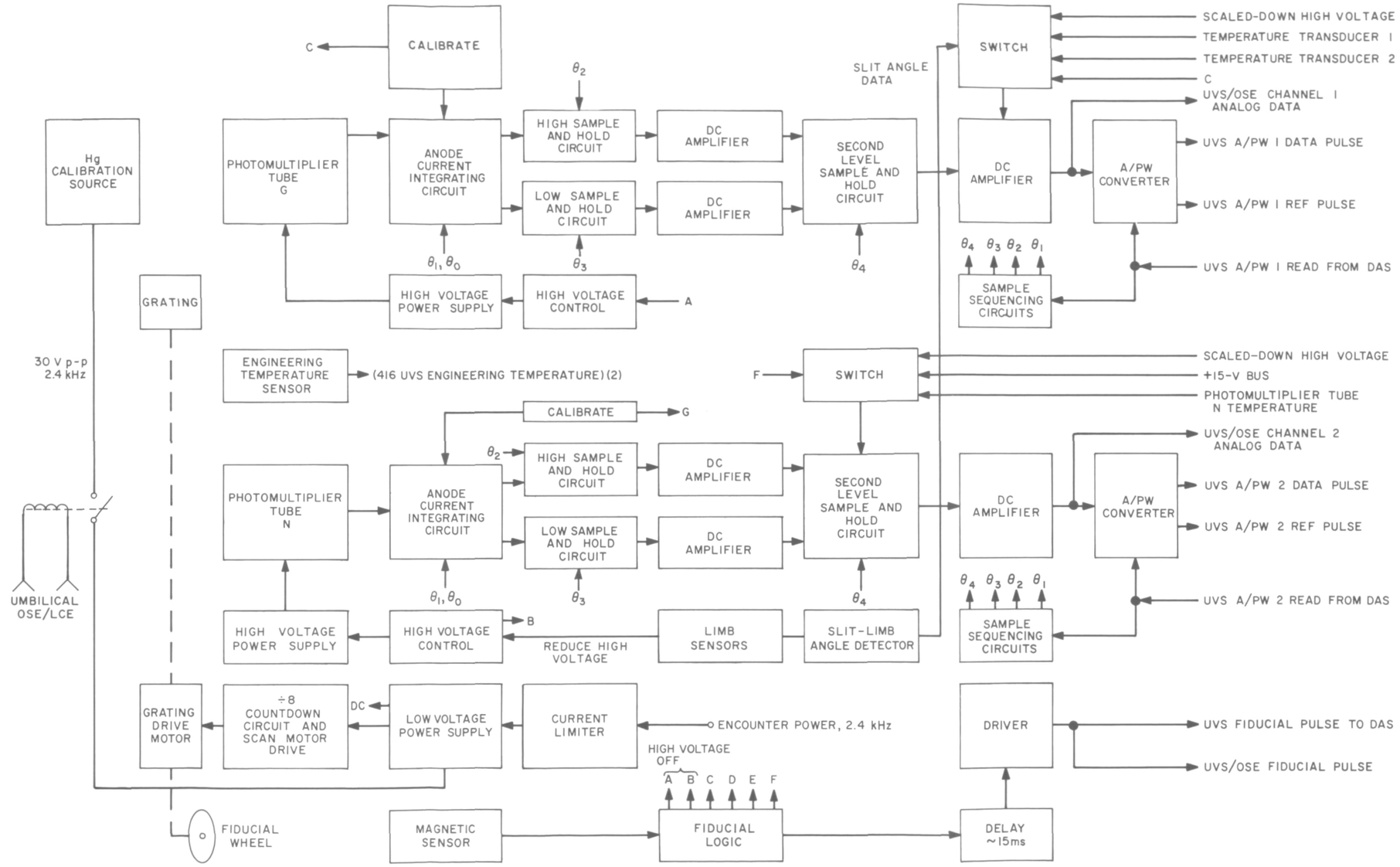

A/PW ANALOG-TO-PULSE WIDTH
LCE LAUNCH CRAFT EQUIPMENT
OSE OPERATIONAL SUPPORT EQUIPMENT
UVS ULTRAVIOLET SPECTROMETER

Fig. 34. *Mariner* Mars 1969 ultraviolet spectrometer functional block diagram

Page intentionally left blank

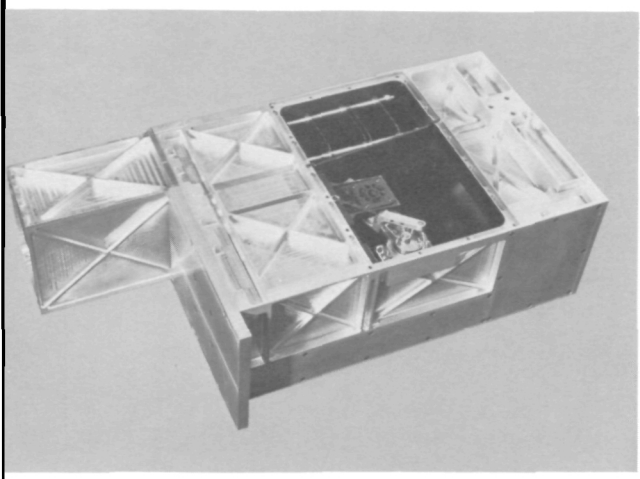

Fig. 35. *Mariner* Mars 1969 ultraviolet spectrometer engineering model without electronic modules

Infrared Radiometer Subsystem

a. Introduction. The scientific objectives of the infrared liometer experiment to be flown on the *Mariner* Mars 69 spacecraft are to determine the temperature of the id surface of Mars and to aid in identifying cloud tures by temperature measurements.

b. Subsystem description. The infrared radiometer con- ns two channels; one covers the spectral range of 8–12 μ, d the other covers the range of 18–25 μ. Each channel ilizes identical detectors consisting of a five-junction ries-connected bismuth-antimony thermopile.

A three-position scan mirror is driven by a digital step- ng motor to select the radiation input to be measured pace, planet, or thermal reference). The scan mirror rects the optical signal to separate f/0.86 1-in.- ameter refracting telescopes. Each telescope is sealed a package containing both the detector and a spectral er.

During the portion of the duty cycle in which the rared radiometer views empty space, memory and re- ring circuits are activated to remove the effects of ernal thermal offsets. Nonzero output voltages are ased by precision differential amplifiers and stored on w-leakage capacitors. The output signal from the detec- s, when the mirror is in the space position, is chopped d summed with the error voltages from the memory d restore circuits to produce zero output voltages. The storing circuits are then disconnected and the memory pacitors maintain the space reference for the duration the scan cycle, which includes viewing the planet veral times and a calibration thermal plate once.

The output of the summing amplifier is then further amplified, synchronously demodulated, and filtered. The resulting output is digitized to 10-bit accuracy by an analog-to-pulse width converter controlled by the data automation subsystem for transmission to earth. Figure 36 is a block diagram of the infrared radiometer.

c. Electrical and physical characteristics. The infrared radiometer operates from 2.4-kHz square-wave power and consumes 3 W. The weight of the instrument is 5 lb, and it is mounted on the spacecraft scan platform where it will operate within the temperature range of -30 to $+30°$C.

d. Design and testing. A thermal control model of the infrared radiometer has been completed and will undergo thermal evaluation. A breadboard instrument has been built and completely tested. The prototype instrument is under construction and is 50% complete.

5. Data Automation Subsystem

The data automation subsystem (DAS) controls and sequences the science instruments, accepts and converts the resulting measurement data, codes and formats the data into frames, provides temporary (buffer) storage, and routes the data to either the flight telemetry subsystem (FTS) or the data storage subsystem (DSS) for direct or delayed transmission to earth.

The data automation subsystem includes the logic portion and the power converter. The subsystem will occupy a volume of 541 in.^{3}, use 649 integrated circuits, 486 discrete components, will weigh approximately 13 lb, and consume 19 W of 2.4-Hz power. A block diagram of the subsystem is shown in Fig. 37. The science instrument interfaces are only grossly described on the left because of their complexity. The interfaces with the other spacecraft subsystems are shown in detail on the right.

There are two paths of data sent from the data automation subsystem to the other subsystems. The real-time data is sent to the flight telemetry subsystem at 66⅔ bps. The data to be recorded on the digital tape recorder is sent to the data storage subsystem at 16.2 kbps.

The real-time data format is shown in Fig. 38. The format is comprised of 280 bits. The start of the format is defined by a 15-bit pseudonoise (PN) sequence which repeats itself every 4.2 s. The words in the format are divided into 10-bit segments for convenience in the decoding logic. The frame count indicates the number

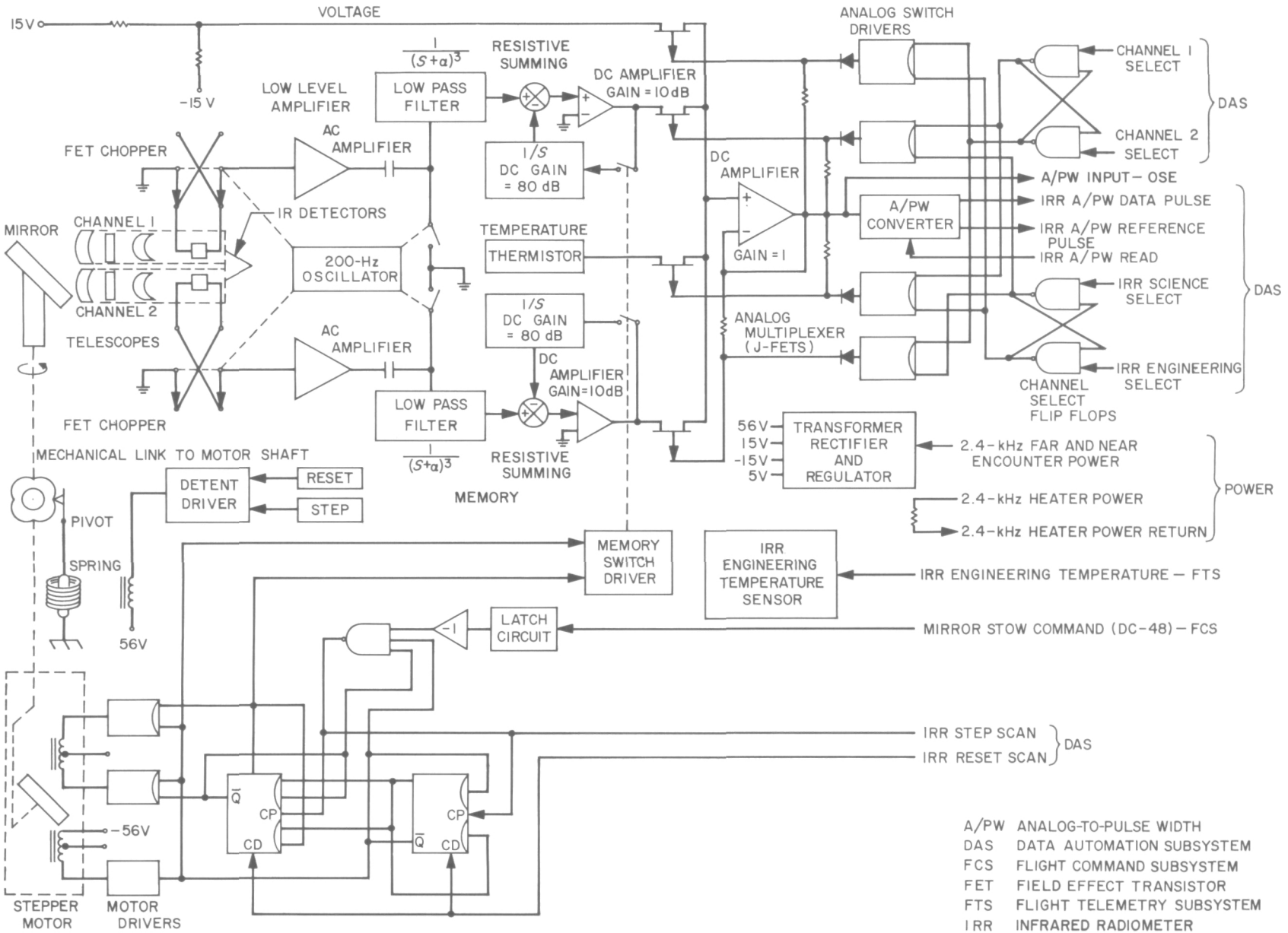

Fig. 36. *Mariner* Mars 1969 infrared radiometer

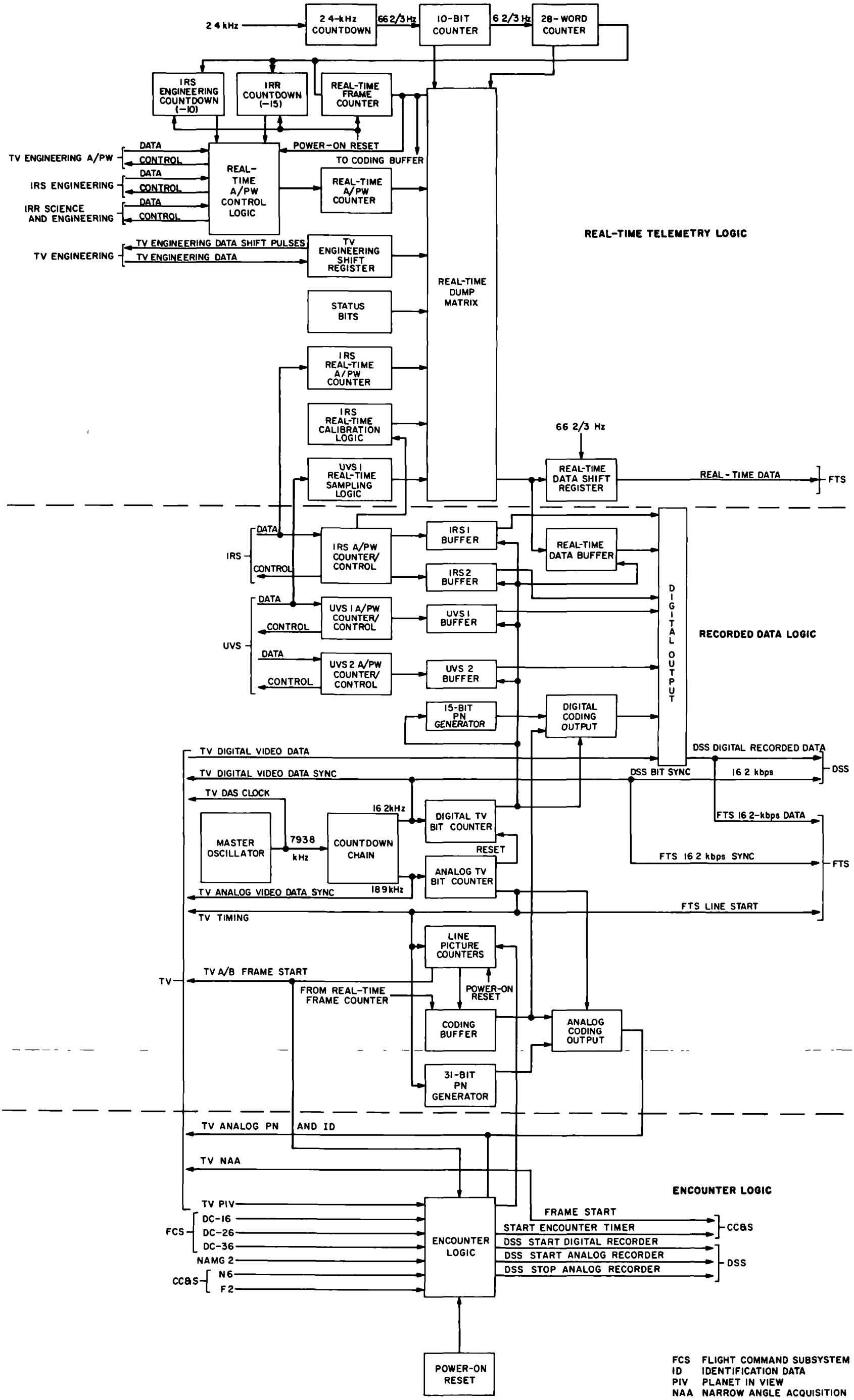

Fig. 37. *Mariner* Mars 1969 data automation subsystem

Page intentionally left blank

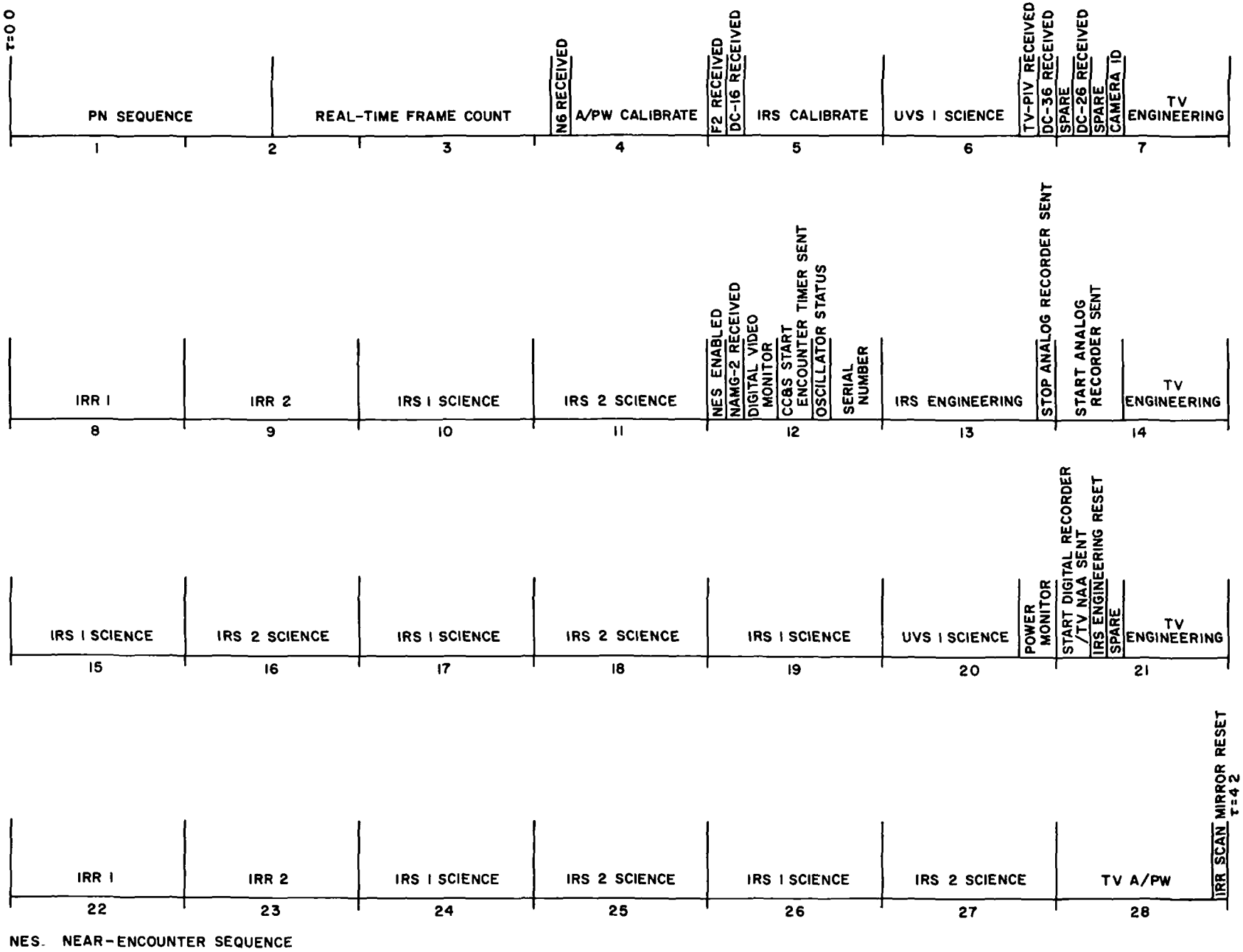

Fig. 38. Data automation subsystem real-time data format

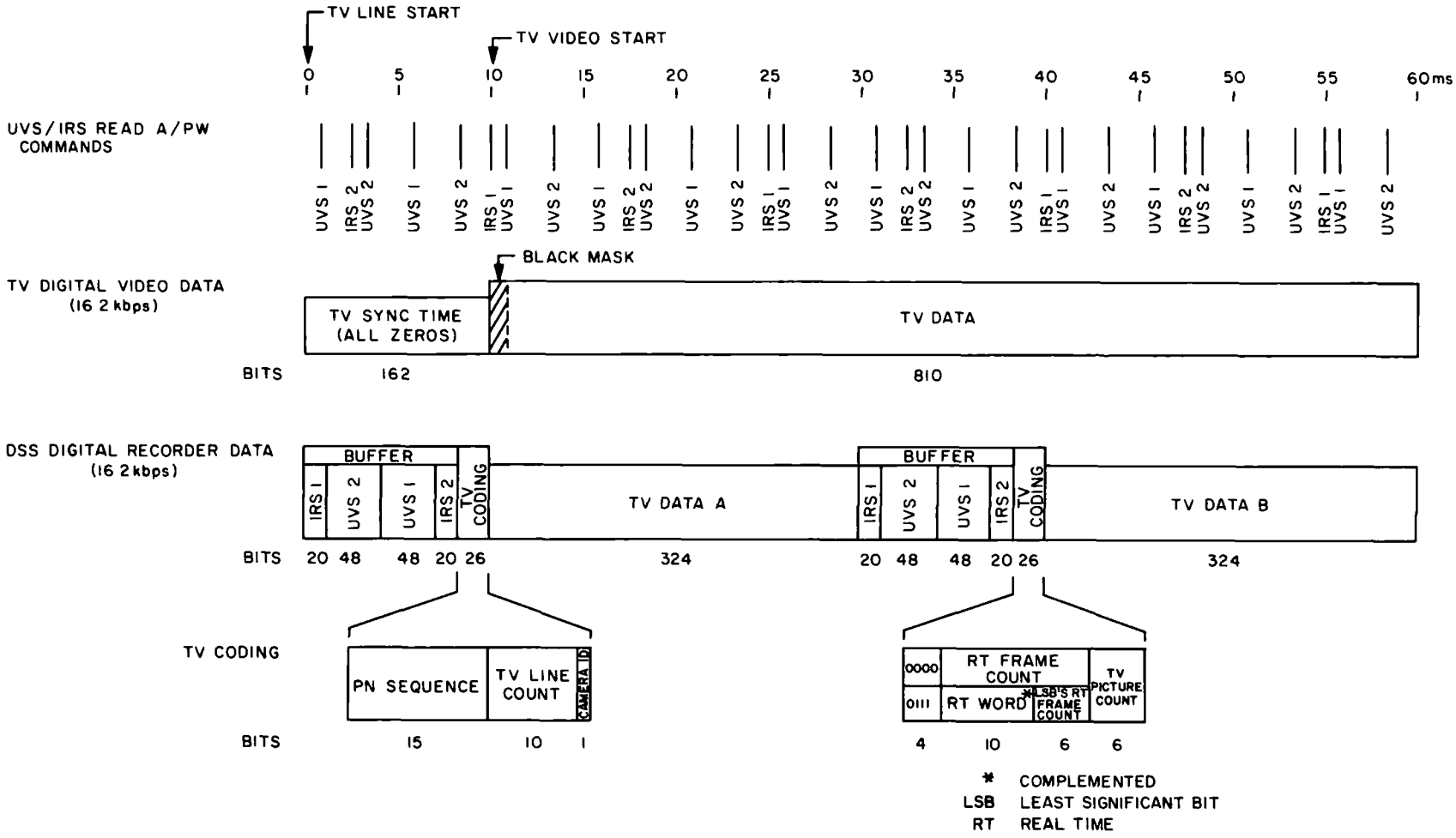

Fig. 39. Data automation subsystem digital recorded data format

of real-time frames (4 2 s) that have been cycled through at any time There are several words which contain bits of general spacecraft and data automation subsystem status These bits contain such information as the receipt of commands sent from earth and the sensing of the planet by the narrow-angle Mars gate (NAMG)

The infrared spectrometer (IRS) science data in the real-time format is a small fraction of that instrument's data, inserted into the recorded data stream This will allow redundancy in the two data streams The ultraviolet spectrometer (UVS) data in the real-time format is a selected wavelength of the ultraviolet spectrum (Lyman Alpha) This again represents redundant information The infrared radiometer's (IRR) data is exclusively inserted into the real-time data All real-time data is recorded on the digital recorder The other significant information in the format consists of science/engineering measurements, such as TV automatic gain control and temperatures needed for calibration purposes The format will remain the same without a mode change from the time power is applied until power is turned off

The digital recorded data format is shown in Fig 39 The television data is outputted in two discrete 20-ms periods out of every 60-ms TV line The ultraviolet spectrometer data, infrared spectrometer data, and TV coding are inserted into the remaining two 10-ms slots along with the real-time data The recorded data must be time-shared between the TV, the ultraviolet spectrometer, and the infrared spectrometer because of the tape recorder utilization The instrument data sampling rates determine the ratio of time-sharing The TV data is sampled at 16 2 kbps (one out of every seven TV elements), the ultraviolet spectrometer data is sampled at 3 2 kbps, and the infrared spectrometer data is sampled at 1 3 kbps The ultraviolet spectrometer and infrared spectrometer data are sampled and stored in a 136-bit solid-state buffer memory This buffer is read out every 30 ms to the digital tape recorder When this occurs, the TV video data which was being recorded is inhibited in the data automation subsystem The top portion of the figure shows the timing when the data automation subsystem commands the instruments to perform analog-to-digital conversions

The data automation subsystem also sends several commands to the instruments for reasons such as moving the mirror in the infrared radiometer and starting the TV subsystem vidicon scanning Another very important function performed by the data automation subsystem involves its timing control and coding of the TV information directly recorded on the analog tape recorder The data automation subsystem also sends important control commands to the central computer and sequencer (CC&S) and the data storage subsystem, such as start analog tape recorder, start digital tape recorder, and start near-encounter timer

The complete breadboard logic for the data automation subsystem has been assembled and tested over temperature and power voltage margins The subsystem has better than 10% voltage margins from -25 to $+90°C$ The breadboard data automation subsystem has been tested with the TV breadboard subsystem with very encouraging results The breadboard power converter has been assembled and tested by itself and with the breadboard logic No problems exist During testing of the analog-to-pulse width (A/PW) converters, one failure was noted, this is believed to be a bad weld

A first article (one tray with representative mechanical and electrical elements) has been fabricated, assembled, and has undergone several environmental tests One integrated circuit failure occurred in the thermal-vacuum testing This failure will be analyzed

The prototype data automation subsystem is presently being assembled and will be system tested early in the next reporting period The proof test model is expected to be delivered to the Spacecraft Assembly Facility on approximately February 15, 1968

Page intentionally left blank

IV. *Voyager* Project

PLANETARY-INTERPLANETARY PROGRAM

A. Introduction

1. Objectives

The primary objective of the *Voyager* Program is to carry out scientific investigations of the solar system by instrumented, unmanned spacecraft which will fly by, orbit, or land on the planets Emphasis will be placed on acquisition of scientific information relevant to the origin and evolution of the solar system, the origin, evolution, and nature of life, and the application of this information to an understanding of terrestrial life The primary objective of the *Voyager* missions to Mars is to obtain information relative to the existence and nature of extraterrestrial life, the atmospheric, surface, and body characteristics of Mars and the planetary environment by performing automated experiments on the surface of, and in orbit about, the planet A secondary objective is to further our knowledge of the interplanetary medium between the planets Earth and Mars by obtaining scientific and engineering measurements while the spacecraft is in transit

2. Project Plan

All *Voyager* missions will be conducted as events of an integrated program in which each individual flight forms a part of a logical sequence in an over-all technical plan of both lander and orbital operations The *Voyager* design will provide for the carrying of large scientific payloads to the planet, the telemetering of a high volume of data back to Earth, and long useful lifetimes in orbit about the planet and/or on the planetary surface Hardware will be designed to accommodate a variety of spacecraft, capsule bus, and lander science payloads, mission profiles, and trajectories Particular emphasis will be given to simple and conservative designs, redundancy wherever appropriate, and a comprehensive program of component, subsystem, and system testing

Overall direction and evaluation of the *Voyager* Program is the responsibility of the Office of Space Science and Applications (OSSA) of the National Aeronautics and Space Administration (NASA)

An interim project management office consisting of OSSA personnel has been established at Pasadena, California, for *Voyager* Project management, supported by the Jet Propulsion Laboratory (JPL) of the California Institute of Technology in the mission analysis and engineering area The following system responsibilities have been assigned To JPL, surface laboratory system, tracking and data acquisition, and mission operations system, to Marshall Space Flight Center (MSFC), the *Saturn V* launch vehicle system and spacecraft system, to Langley Research Center (LaRC), the capsule bus system

3 Technical Description

Two identical planetary vehicles will be launched by a single *Saturn V* launch vehicle Each complete planetary vehicle is to consist of a flight spacecraft, flight capsule bus, and surface laboratory Science experiments will be conducted from the orbiter during descent and on the planet surface The sterilized flight capsule bus will be designed for separation from the flight spacecraft in orbit, for a Mars impact trajectory, for entry into the Mars atmosphere, for descent to the surface, and for soft-landing the surface laboratory, which will have surface lifetimes of months The surface laboratory will contain all power, sequencing, and communications for the conduct of surface operations

4 Sequence of Events

The Surface Laboratory System plan has been implemented as follows

The procurement for the total capsule system was assigned to two Phase B JPL contractors who performed preliminary design activities from June 1, 1967 through August 31, 1967 The schedule for Phase B extensions and for Phase C contractor selection has been indefinitely postponed

B. Project Engineering

1. Environmental Requirements· Effect of the Molecular Sink of Space on the Survival of Bacterial Spores

a. Introduction. A planetary quarantine policy concerning space exploration was established by NASA in 1963 [1] To fulfill the goals set forth within this policy, constraints have been established on all space flight to the planet Mars, whether they orbit, land, or fly by, to prevent the release of viable organisms on the planetary surface

Investigation has been made of the possibility of microbial release from the spacecraft due to meteoroid collision, vibration, and accidental planetary impact In order to evaluate space environment as a potential barrier to the transportation of terrestrial life forms from one planet to another, studies have been made in the field of high and ultra-high vacuum (ultra-high vacuum being defined as pressures lower than 10^{-8} torr)

b. Previous studies. Data comparisons of previous studies conducted by other investigators within this area are at best difficult, because of the multiple test variables In some instances, conventional vacuum chambers were utilized, while in other cases all glass systems were used Microbial support menstruums have varied from ashless filter paper to glass fibers Both mercury and oil diffusion pumps have been employed

Figure 1 schematically illustrates some of the contamination problems that can be encountered with mechanical vacuum systems Contamination can result from the seals or from the diffusion pump In addition, particles originating from the test hardware may be reemitted back to the test items from the wall or adjacent gas molecules

References 1 to 4 give varying results of viability of *B subtilis* var *niger* and *B mycoides* in vacuum of from 10^{-5} to 10^{-9} torr for different durations of time

This divergency in results may be attributed to several factors It is possible that the use of oil diffusion pumps in some investigations resulted in a protective effect for the test specimens, due to contamination of the test environment with oil Conversely, in other studies, a lethal effect upon the test microorganisms may have resulted from the use of mercury diffusion pumps Thus, the data obtained from these investigations, while indicative, does not yield the quantitative information necessary for a probability estimation of microbial survival under environments encountered during space flight

c. Present study. Our objective was to delineate the individual and/or combined effects of ultra-high vacuum and temperature on the viability of *B subtilis* var *niger* spores using the thermal–vacuum relationships obtained from the *Mariner IV* solar panels during interplanetary cruise to Mars Outer space conditions were simulated through the use of a unique facility, the "Space Molecular Sink Laboratory (Molsink)" (SPS 37-30, Vol IV, pp 79–84)

As noted by Chuan and Wallace (Ref 5), the simulation of outer space vacuum conditions in a ground-based laboratory is not based upon the active properties of space, but essentially on a "permissive" quality (so named by Chuan and Wallace) This permissive quality is based upon outer space vacuum conditions, which allow particles emitted from space vehicles to escape freely The probability that these molecular particles will return to their source is practically nil, because of an extremely large molecular mean path Therefore, the

[1] NASA Administration Management Manual 4-4-1, September 9, 1963

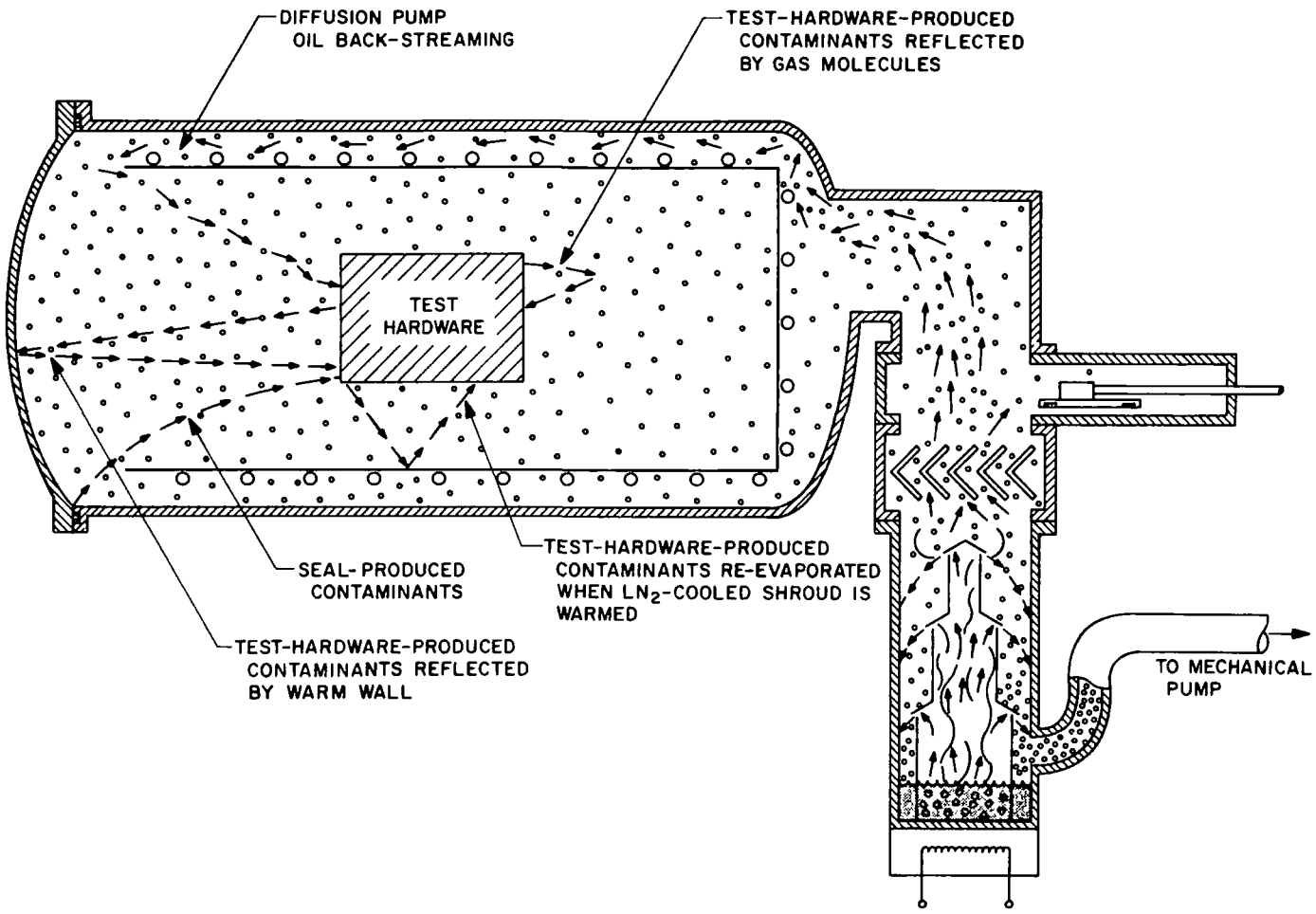

Fig. 1. Contamination sources in conventional high-vacuum systems

description of the molecular conditions in a space chamber should be concerned with permissiveness, whenever the quality of simulation is discussed The mean free path of a molecule within a space simulator can only be as great as the largest dimension of the chamber, thus the permissive quality of any chamber is physically limited, even if the gas density level inside of the chamber is disregarded Molecules leaving the test article will hit the chamber wall and if the wall is not a perfect sink, many of them will return to the test article

The crux of the problem encountered in space simulation studies is that, while torr measurements indicate the condition of the chamber as related to vacuum, they do not indicate the dynamic situation that is encountered by the test item In smooth walled or radial fin chambers, the majority of molecules leaving the test item return to it after wall deflection, only a small portion being captured by the cold wall or removed by pumping However, in the Molsink, a different condition prevails Of every 10,000 condensable molecules emitted by the test item, only one returns, the rest being removed by the molecular trap This is a significant point when considering biological materials If molecules leaving the test item do not return to it because of molecular entrapment, the exposed air and water surrounding the individual spore should be drawn off It is possible that other constituents of the spore may be similarly affected, and studies to investigate this possibility should be performed

Figure 2 is a schematic drawing of the Molsink facility, which consists of an ultra-high vacuum chamber, 2 ft in diameter, and the necessary support equipment The Molsink employs solid-state mechanical, cryo, chemical, and ionization pumps to remove gases emitted by the test item The heart of the chamber consists of a longitudinal wedge-finned molecular trap which is cooled to

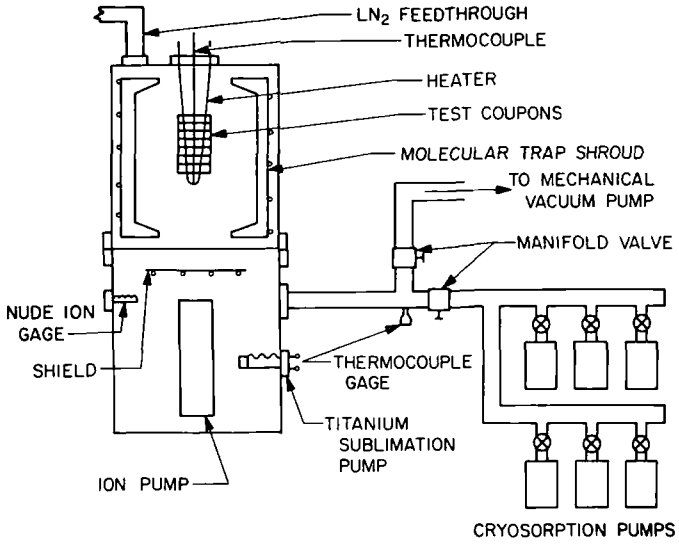

Fig. 2. Molsink facility

−300°F with liquid nitrogen (LN_2) during the test The tangential angles of the fins provide a capture coefficient of 99 97% of all condensable molecules, such as H_2O As such, the probability that a molecule emitted by the test item will be captured on first encounter with the wall is extremely high Noncondensable molecules are removed by both the ion and titanium sublimation getter pumps, whereas the liquid nitrogen-cooled cryosorption pumps remove both condensable and noncondensable molecules Conventional extreme high-vacuum and cryogenic instrumentation and controls are used to monitor test conditions

For purposes of preliminary testing, a four-tier test ladder was constructed and simulated hardware (stainless steel strips) was attached to the ladder by means of small spot welds The Molsink test strips and controls were inoculated with *B subtilis* var. *niger* spores and air dried for 1 h, after which the ladder was lowered into the test chamber (Fig 3) The chamber was mechanically rough-pumped in the viscous flow regime to eliminate back-stream contamination This was followed by fine roughing with the five cryosorption pumps, and at this point, the ion pump, titanium sublimator, and molecular trap were employed Individual heaters for each tier of the test ladder were activated, and the test strips were stabilized at test temperatures Central thermocouples indicated and controlled the temperatures by means of strip recorders After exposure to the test conditions, the strips were removed from the ladder and assayed for viable survivors Seven-day thermal and thermal vacuum tests were conducted, and the effects of pumpdown and repressurization isolated by experimentation

Initial studies have verified the feasibility of using the Molsink to determine the effects of simulated outer space on the survival of bacterial spores, and analysis of preliminary data indicates a lethal synergistic effect of vacuum and temperature upon the test spores

These studies will be completed within the next few months and the effects of temperature and vacuum on the viability of *B subtilis* var *niger* spores exposed on simulated space hardware will be reported

C. Propulsion

1 Sterilizable Initiators for Electroexplosive Devices

The development of the technology required to meet specific *Voyager* Surface Laboratory requirements has been a prime objective of the pyrotechnic subsystem advanced technology effort One phase in this effort makes an evaluation of the high-temperature characteristics of electroexplosive initiators The temperatures of concern are those specifically associated with the *Voyager* thermal sterilization requirements Also of importance is the resistance to initiation from electrostatic discharge and radio-frequency interference

For the purpose of evaluating the effects of sterilization temperatures, the single bridgewire *Apollo* standard initiator (SBASI) configuration was selected, and a pyrotechnic mixture different from that used in the existing SBASI was selected This pyrotechnic mixture was chosen for its electrically nonconducting properties which would

Table 1. Sterilizable SBASI test plan summary

Test sequence and parameter	Conditions
(1) Electrostatic discharge	25 kV from a 500-pF capacitor (a) Pins to case (b) Through bridgewire
(2) Dielectric strength	500 Vdc, 60 s, 2 MΩ (min) 500 Vac, 60 cycles, 500-mA leakage (max)
(3) No fire	1 1 ±0 05 A, 1 W, 5 min at 160°F
(4) Bridgewire resistance	Between 0 95 and 1 15 Ω
(5) Heat sterilization	9 cycles, 36 h/cycle, to +300°F and again at ambient
(6) Bridgewire resistance	Between 0 95 and 1 15 Ω
(7) Radio-frequency interference	9000 MHz, 1 W

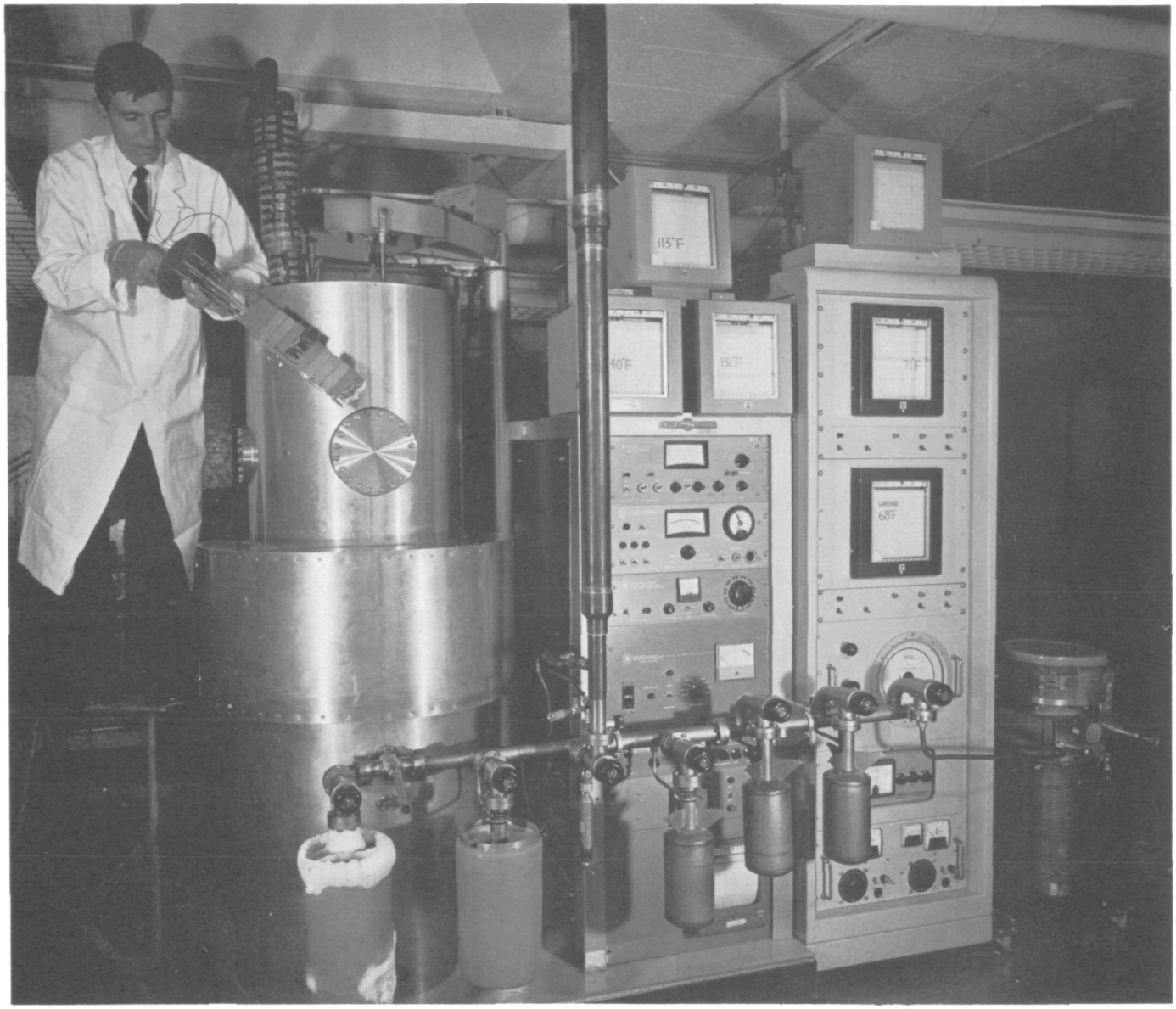

Fig. 3. Prototype test ladder being lowered into the Molsink test chamber

reduce or eliminate the sensitivity to initiation from electrostatic discharge and radio-frequency emissions. The fabrication and testing of the SBASI are being performed by Space Ordnance Systems, Inc., under contract to the Jet Propulsion Laboratory.

Table 1 contains a summary of the significant test parameters. In addition, other standard tests of the initiators will be performed (vacuum, temperature, shock, etc.).

An initial lot of the SBASI was loaded and subjected to 300°F and the application of 1 A–1 W of energy. When the initiators were conditioned to −200°F (a temperature which certain pyrotechnic devices may be exposed to when required to function) and functioned at this temperature, one failed to fire, and the time from current application to peak pressure of the other three initiators was excessive. A detailed analysis of this abnormal behavior was performed, and it was determined that when the electrical energy of the 1 W–no-fire test was dissipated as thermal energy during the 300°F sterilization period, the pyrotechnic mixture in contact with the bridgewire reached a temperature of 625°F and subsequently degraded.

The requirement to perform the no-fire test at the sterilization temperature was reviewed. It was concluded that in order to expedite the test program so that the other aspects of the evaluation could be explored, the no-fire test would be performed at a lower temperature—160°F. A lot of SBASI are presently being fabricated for completion of the test program.

2. Voyager Site Alteration Study

The possibility of detrimentally altering the surface and atmosphere of Mars by the *Voyager* capsule bus retrorockets presents a problem which has received considerable attention. The *Voyager* site alteration study was initiated to provide a thorough evaluation of all known aspects of Mars surface alteration which might be anticipated from the terminal-descent rocket mechanization for a soft lander.

The overall goal of the *Voyager* site alteration study is the development of an analytical method of predicting the degree and type of site alteration resulting from the exhaust products of the capsule descent rocket engines. This tool will significantly aid in the definition of the surface laboratory system (SLS), particularly in the area of establishing requirements for science sample acquisition deployment and in defining any required limitations on the capsule bus terminal-descent mechanization. The plan as shown in Fig. 4 involves the development of necessary analytical techniques supported by a concurrent experimental test program. This latter program provides input data to the analytical studies and a data check for correlation purposes.

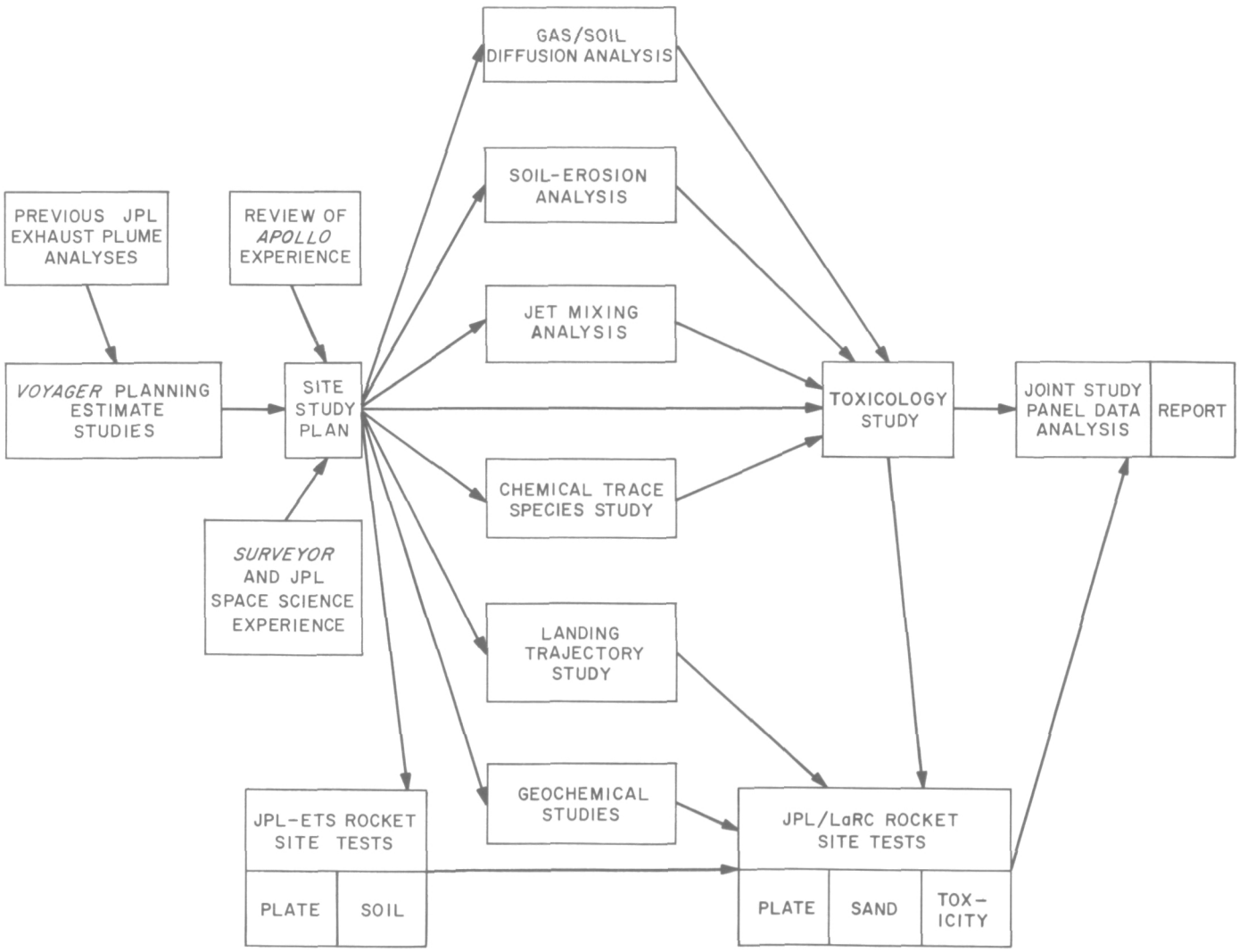

Fig. 4. Site alteration study plan

a. Analytical studies. Three analytical study contracts have been placed. These are a nine-month Gas/Soil Diffusion Analysis Contract and a two-month Soil Erosion Study Contract with TRW, Inc., and an eleven-month Jet Mixing Analysis Contract with the University of California at Santa Barbara. Additional study efforts which have been undertaken within the Laboratory include a chemical trace species study, a landing trajectory study, a soil chemistry interaction study, and a water vapor condensation analysis.

Among these in-house analytical efforts, the water vapor condensation analysis has been completed. The results of this study show that it is thermodynamically possible for the exhaust from a typical storable bipropellant rocket engine to produce condensed phase water on the Mars surface or in the atmosphere adjacent to the surface. The superposition of real effects, however, such as: (a) diffusion rate into the atmosphere at large, (b) finite heat-transfer rates from the cold surface to a warmer vapor-laden gas, and (c) the extent of supersaturation and suitable nucleation sites make the reality of such results uncertain. The possibility has pointed out the need for further evaluation and a water vapor experiment has been programmed into the forthcoming comprehensive test program to be conducted at LaRC, jointly sponsored with JPL.

b. Experimental studies. Analysis and evaluation of test results from some exploratory tests conducted at the JPL Edwards Test Station were performed. The primary objective of this exploratory program was to obtain order-of-magnitude heating, erosion, and chemical data to substantiate analytical models in the near-field of the landing site. Secondary objectives were to evaluate experimental and measurement techniques and to elucidate potential problem areas to be considered in planning the more comprehensive test program to be conducted at LaRC.

The data which were evaluated were acquired from thirteen rocket-firing tests. All tests were conducted under conditions of simulated Mars atmospheric pressure (5 to 20 mbar) and employed a modified *Surveyor* vernier sea-level rocket engine. This engine was selected out of deference to the scaling simile of a typical *Voyager* terminal-descent propulsion system derived in the *Voyager* soft-lander study in Ref. 6. Modification of the sea-level model engine by the addition of a 20:1 expansion ratio nozzle produced a quarter-scale model of the *Voyager* study propulsion system, providing a 1:1 correlation in gasdynamic scaling parameters such as plume shape, flow field, temperature field, gas properties, etc.

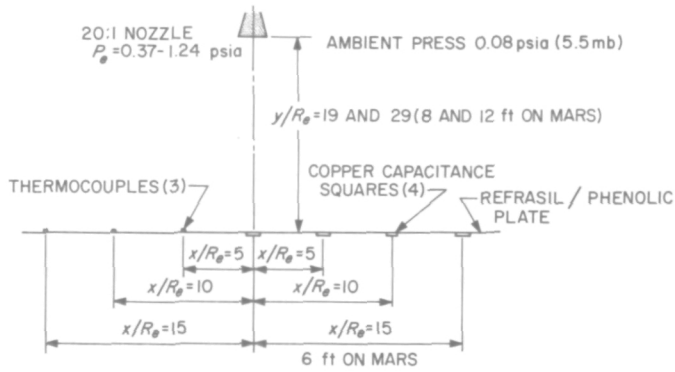

Fig. 5. Test conditions, flat-plate heat-transfer tests

The test conditions for the normal-impingement flat plate heat-transfer tests are depicted schematically in Fig. 5. Separation distances (nozzle to plate) of 19 and 29 nozzle radii were evaluated over a thrust throttle range of approximately 4:1. Using the quarter-linear-scale factor, these separation distances correspond to 8 and 12 ft on Mars, respectively. Incident heat-transfer rates typically varied inversely proportional to the square of the distance from the stagnation point as shown in Fig. 6. These preliminary results also suggest that incident heat-transfer drops to near zero at a lateral distance of ten nozzle radii. For purposes of comparison, the solar heat flux on the Mars surface is estimated to be in the range of 0.00037 Btu/in.^{2}-s (55.6 W/ft^2).

All tests were in the duration range of 3 to 10 s, to assure that stability had been achieved in the flow field. The mass of the copper calorimeter squares imbedded in the target plate was selected to function well below the melting point for that duration. An unexpected transient heat-transfer phenomenon was encountered which later justified the choice of the nominal test duration (10 s). A representative stagnation-point temperature versus time curve, as shown in Fig. 7, reveals two distinct linear (hence, constant heat flux) regimes as a function of time. A transient heat flux of roughly 20 times the steady-state value was noted to last roughly 1 s. This transient phenomenon is thought to be indicative of the time required to establish the system of shock waves and flow field associated with stagnation point flow.

The test conditions for the mineralogical (and cratering) tests are depicted schematically in Fig. 8. Again separation distances of 19 and 29 nozzle radii (limited by facility dimensions) were evaluated, but under throttled

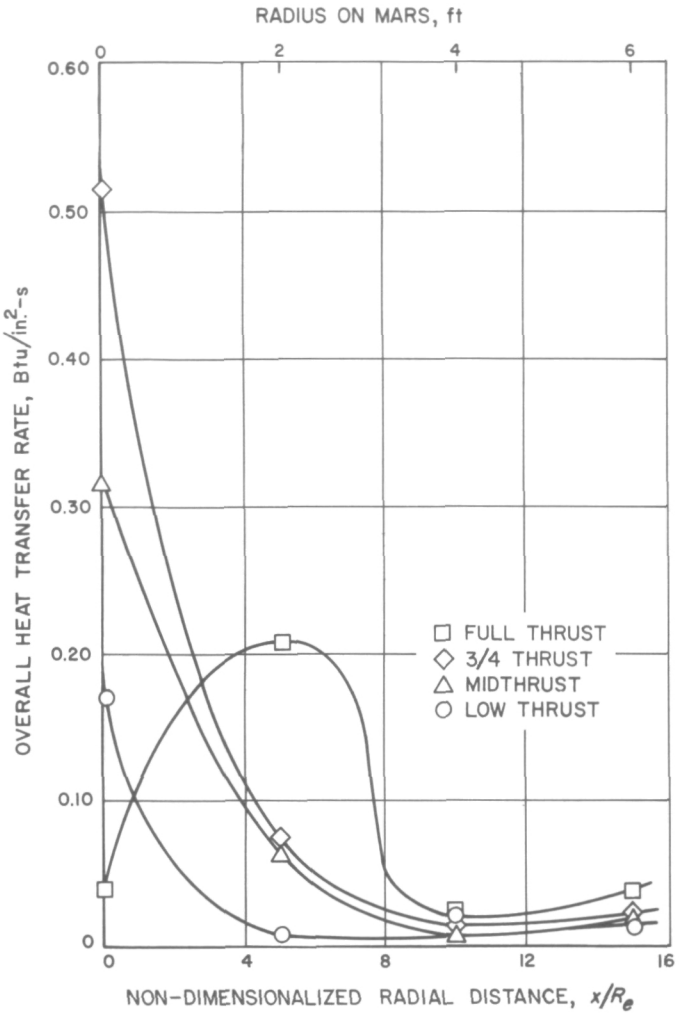

Fig. 6. Overall surface heat-transfer rate versus radial distance from stagnation point

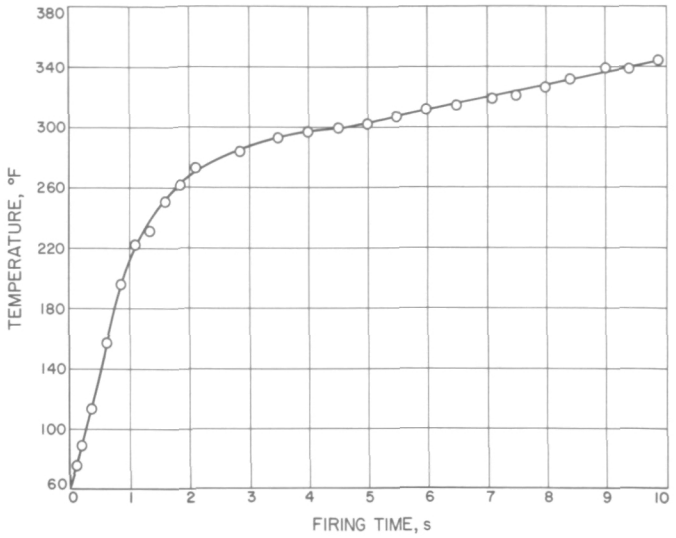

Fig. 7. Temperature versus firing time

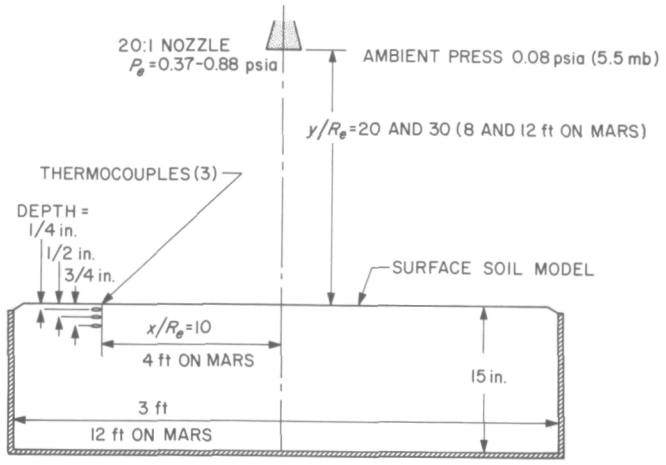

P_e = NOZZLE-EXIT STATIC PRESSURE
R_e = NOZZLE-EXIT RADIUS
y = SEPARATION DISTANCE, NOZZLE TO PLATE
x = RADIAL DISTANCE FROM STAGNATION POINT

Fig. 8. Test conditions for mineral soil test

engine conditions of minimum (25%) and midthrust (50%). The reference soil was a mixture of minerals in the following volumetric proportions:

Quartz sand (SiO_2), 80%

Calcite ($CaCO_3$), 5%

Gypsum ($CaSO_4 + 2H_2O$), 5%

Kaolinite ($H_4Al_2Si_2O_9$), 5%

Limonite ($2Fe_2O_3 + 3H_2O$), 5%

No attempt was made to create a Mars "soil model," with the exception of particle-size range, which was made representative based upon current estimates for purposes of studying erosion and/or cratering. The average particle size was in the range of 80 μ, the sand being predominantly 100 μ and the minerals in the range of 5 to 30 μ. Minerals were chosen which would have the greatest probability of changing phase or composition due to the thermal environment. They were selected to be a representative sampling of a larger listing of minerals which are of concern from a Mars geological standpoint. This listing is characterized by: (1) those containing water; (2) halides; (3) carbonates; (4) sulfates; and (5) reducible or oxidizable substances such as iron, iron oxides, hydrocarbons, and graphite. Data collection was limited to pre- and post-test sampling of the soil for

chemical analysis and subsurface soil-temperature sensing. High-speed color cinematography was employed to study crater formation and growth during each test. All tests were again in the range of 3 to 10 s duration, 10 s being the duration of the constant velocity terminal-descent phase as outlined in the *Voyager* study.

The most significant results in this exploratory test program came as a result of the "sandbox" testing. First, X-ray diffraction analysis of mineral samples, both crater ejecta and crater surface material, showed no detectable chemical change in any of the samples. Analysis is continuing, but it is hypothesized that the exposure time of each particle was insufficient for reactions to proceed actively, even in the high-temperature environment. Second, no temperature rise was noted at the test point located at 10 nozzle radii and 0.25-in. depth beneath the original surface.

Analysis of the high-speed color motion pictures revealed significant characteristics of crater formation and growth and time dependence of gas diffusion into the soil. For test durations in excess of 3 s, a very rapid soil eruption occurred after shutoff, displacing a large part of the crater soil. This would imply a significant effect of diffusion-trapped gases reemerging after engine shutoff. Post-test inspection revealed soil fracture lines and a secondary slump near the crater rim as might be expected if the crater soil lifted and resettled. These characteristics can be seen in Fig. 9.

These tests are considered to be conservative, because the 3 to 10 s at a fixed minimum elevation over the simulated landing site is much more severe than a constant velocity descent to the minimum elevation.

Negotiations have recently been completed for a comprehensive joint JPL/LaRC rocket/surface interaction test program utilizing the greater altitude facility size capability and *Apollo* support experience of LaRC. The test program will be directed toward far-field effects, including gasdynamics and soil mechanics, soil chemistry,

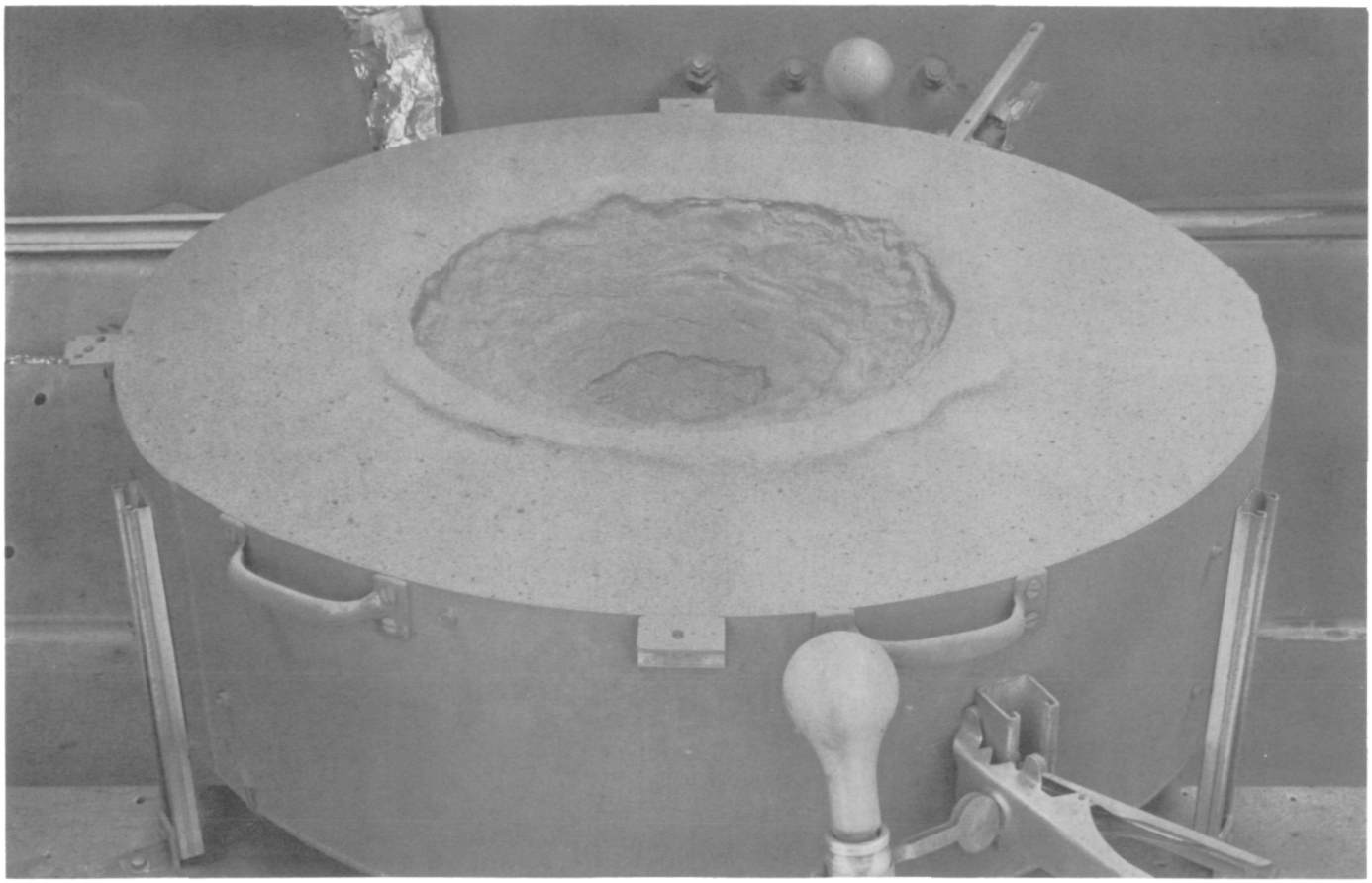

Fig. 9. Typical soil eruption after 10 s of firing

distribution of engine exhaust, and biology. Operating conditions will include both static (fixed engine) and dynamic (falling engine) simulations. Monopropellant and bipropellant engines are currently being prepared at JPL in support of this program.

D. Telecommunications

1. Spacecraft Traveling Wave Tube Amplifier (50 W) Development

a. Introduction. The objective of this project is to provide a tested and proven flight-quality 50-W traveling wave tube amplifier (TWTA) package for spacecraft use, utilizing techniques within the current state of the art of traveling wave tube (TWT) development. The 50-W TWTA (Fig. 10) being developed consists of a 50-W TWT, a power converter, and an RF output filter. The TWT power converter and RF filter will be packaged in a pressurized container to prevent high-voltage breakdown during the launch or entry pressure profile. The specifications for the completed amplifier are summarized in Table 2. The RF output filter is a five-section iris-coupled bandpass filter, the purpose of which is to prevent interference to spacecraft receiver and provide suppression of the TWT-generated harmonics. RF amplification occurs in the TWT, which is a periodic-permanent-magnet focused metal-ceramic device (Fig. 11). The power converter has a nondissipative switching regulator input, which allows operation from 25 to 50 Vdc, following by the inverters, transformers, rectifiers, and filters necessary to provide the correct voltages for TWT operation. The TWTA package will be a stainless steel hermetically sealed container. This container will be filled with sulfur hexafloride gas (SF_6). This gas was chosen because of its excellent dielectric characteristics, especially its resistance to voltage breakdown at critical pressures. This gas is chemically inert and nonpoisonous.

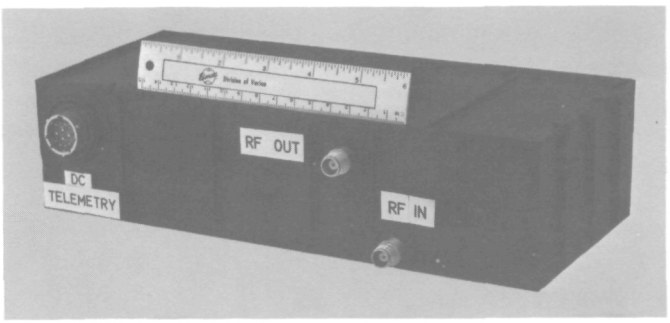

Fig. 10. Spacecraft traveling wave tube (50 W) amplifier engineering model

Table 2. Spacecraft traveling wave tube amplifier (50 W) specifications

Parameter	Requirement
RF power output	50 W minimum
DC power input	185 W maximum
DC input voltage	+25 to +50 V
Frequency range	2.29 to 2.30 GHz
Gain	30 dB minimum
Weight	10 lb maximum

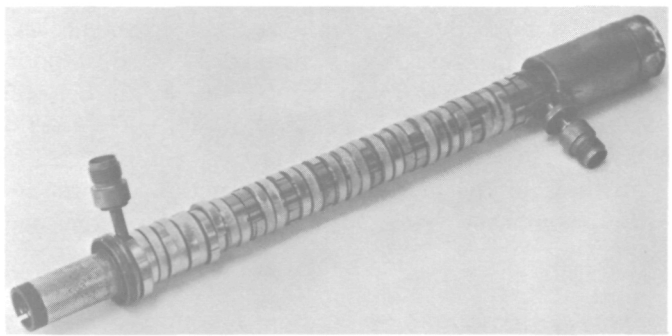

Fig. 11. Periodic permanent magnet (50 W) focused traveling wave tube

b. TWT development. Power TWTs flown in previous spacecraft have been limited to a maximum RF power output of 20 W. The requirement for 50 W of RF output power made it necessary to redesign the TWT structurally as well as electrically to provide the required thermal dissipation capability. In the first few TWTs built, difficulties were experienced with vacuum leaks, cathode activation problems, and thermal distruction of the electron beam collector. These basic problems have been corrected.

An unusual variation of VSWR with frequency was noted on several of the early TWTs. These variations were traced to discontinuities on the TWT helix structure which could be seen in X-rays (Fig. 12). When the TWTs were disassembled, the helix discontinuities were found to be caused by broken support rods. The TWT helix is supported by three beryllium-oxide ceramic rods spaced at 120-deg intervals around the outside of helix. These rods extend the length of the TWT. These rods were broken because of the difference in the thermal expansion coefficients of the beryllium-oxide ceramic and the stainless steel tube body. The breakage occurred when the TWTs were heated to 400°C during bake-out. This problem was finally solved by a molybdenum liner which

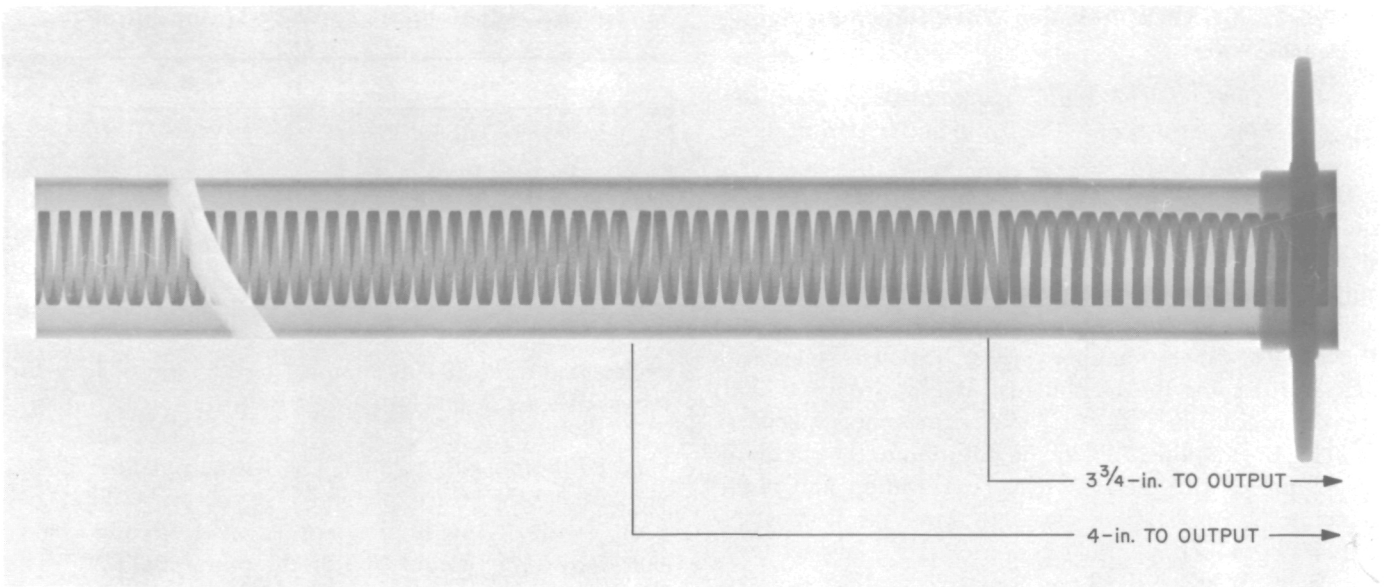

Fig. 12. X-ray of a TWT with broken helix support rods

allows some relative movement between the rods and the tube body, and by careful control of the interference fit between the rods and the tube body.

The most recent tube development problem is a 1.13-GHz oscillation, which occurs when the TWT is in operation when connected to the output bandpass filter. The bandpass filter acts as a short circuit at some frequencies. All of the RF power generated at these frequencies is reflected back into the TWT. Oscillation occurs when this energy is again reflected from the TWT internal attenuator and amplified in the TWT output section. This problem should be solved by using an internal attenuator which is a better RF match at the oscillation frequency. To provide the improved match, the attenuator must be physically longer than the attenuator now being used. In order to avoid reducing TWT gain below the specification limits, the total tube length is being increased by one magnetic period (0.400 in.). Since the other electrical requirements have been met by earlier experimental TWTs, the TWT design should be complete once this problem has been solved.

c. Power converter development. Redesign of the power converter was necessary because of the discontinuance of the formerly used type of transistor. This redesign has now been completed, and an engineering model operating with a dummy load indicated an efficiency of 88% at 30 V input and 86% at 50 V input. These data were taken at room temperature.

The first attempt to operate the engineering model power converter at −10°C revealed that insufficient drive was supplied to the transistor bases at this low temperature. The resulting excessive dissipation led to destruction of the inverter power transistors. Increasing the transistor base drive to provide a sufficient safety margin might slightly reduce the efficiencies reported above.

d. RF output filter. The RF output filter is a modification of a commercially available filter design. This filter has met all of its design specifications, including that of less than 0.3 dB insertion loss. The filter development is felt to be complete.

e. TWTA package. A TWTA package with an experimental TWT, the prototype filter, and a dummy power converter installed has been subjected to shock and vibration testing. These tests have resulted in the addition of internal stiffening ridges on the amplifier lid. These new ridges are at right angles to the existing external ridges. This addition was made necessary by an oil-canning effect noted during vibration testing. During the first shock tests the tie-down screws were found to be insufficient. The amplifier package is now restrained by a total of six 8-32 screws. Later tests confirmed that the arrangement is satisfactory. The engineering model power supply has been operated with one of the experimental tubes yielding an overall conversion efficiency of 30% from dc to S-band. The efficiency did not include RF output filter losses, since the experimental TWT used was unstable when operated with the output filter.

2. High-Impact 20-W Traveling Wave Tube Amplifier Development

a. Introduction. The high-impact 20-W TWTA described herein consists of a TWT and an RF output filter.

The RF output filter is a combined band-rejection and low-pass filter. This combination is required to prevent interference to the spacecraft receiver, and to provide suppression of the TWT-generated harmonics. The TWT is a metal ceramic device, basically similar to the *Mariner IV* power amplifier (Fig. 13). The electrical specifications for the combined TWT and output filter are summarized in Table 3. The environmental specifications for the amplifier include, in addition to the standard type-approval qualification tests, sterilization and high-impact tests. Sterilization consists of three 36-h heat cycles at 145°C in a nonoperating condition. High-impact tests consist of 10,000 *g* shocks of 1-ms duration in each of three mutually perpendicular directions with the TWT operating immediately prior to the shock.

The goals of this development are:

(1) Development of high-impact technology.

(2) Demonstration of a flight prototype 20-W TWTA with the ability to survive a 10,000-*g* 1-ms shock in any orientation.

In order to accomplish the above goals it is currently planned to subject the final deliverable prototype amplifier to the full type-approval cycle, three sterilization cycles, and three 10,000-*g* impact tests followed by a life test of at least 20,000 h.

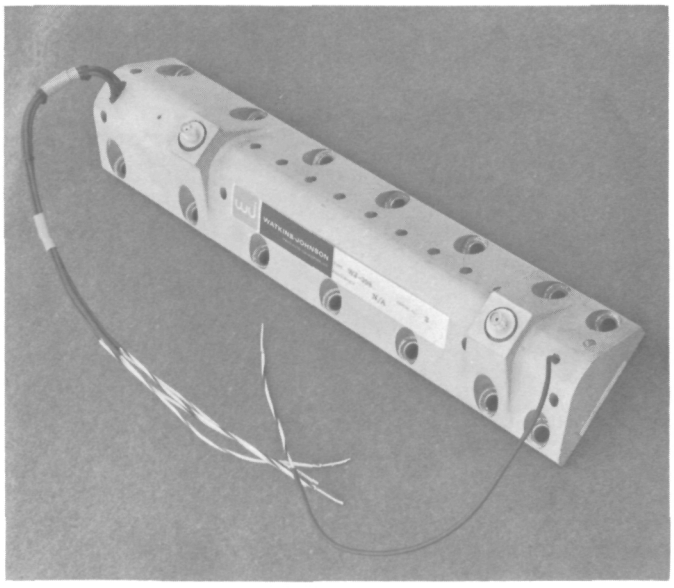

Fig. 13. High-impact TWT

Table 3. High-impact 20-W TWTA specifications

Parameter	Requirement
RF power output	20 W min
DC power input	60 W max
Frequency range	2.29 to 2.30 GHz
Gain	25 dB min
Weight	4.5 lb max

b. RF output filter status. The RF output filter development has been completed. The prototype filter has been fabricated and shock-tested and is now being stored, awaiting completion of the prototype TWT. The RF output filter specifications met before and after shock testing are summarized in Table 4.

c. TWT electrical performance. The first TWT fabricated, upon completion of component shock testing, operated at a frequency of 2.3 GHz with a saturation gain of 41 dB, a power output of 24.5 W, and an overall efficiency greater than 30%. Since these characteristics compare favorably with the state of the art in medium-power TWTs, the electrical design of the high-impact TWT is considered adequate, and no further effort will be expended to improve efficiency on this project. This decision was made after considering the relative values

Table 4. Band rejection and harmonic filter specifications

Electrical requirements	
Capacity	25 W cw
Load VSWR	5:1 max
Connectors	OSM-type
Pass-band characteristics	
Frequency	2.290 to 2.300 GHz
Attenuation	0.5 dB max
VSWR	1.2 max
Stop-band characteristics	
Frequency attenuation	2.108 to 2.128 GHz 86 dB min
	4.580 to 4.600 GHz 20 dB min
	6.870 to 6.900 GHz 12 dB min
	9.160 GHz and higher 5 dB min

of the project goals, even though the specification requirements stated in Table 3 are not met.

Cathode depletion is the factor that normally limits the life of a TWT. To ensure that the operating conditions of the cathode in the final tube are conducive to lifetimes greater than 20,000 h, a cathode temperature study was conducted. A cathode was operated in a test setup with geometry closely simulating that of the final TWT assembly. This test resulted in a calibration factor which allows setting the cathode temperature in the final TWT very close to the optimum temperature for maximum cathode life.

d. Environmental tests results. TWT WJ-398 SN 3 was shock-tested at JPL at gradually increasing shock levels. Figure 14 gives the transfer characteristic and Fig. 15 the performance comparison after the high-impact shock series. As a result of this series of shock tests, two design deficiencies were revealed. The TWT capsule has been fabricated from high-strength cast aluminum. This material was too brittle, and a crack developed across the center of the tube casing. This deficiency will be corrected by the use of a wrought aluminum material for the final capsule design, and by relocating shear pinholes to avoid stress concentrations. The crack had no effect on the TWT electrical performance.

A more serious deficiency was revealed in the cathode support cone. The TWT cathode is supported by a seamless stamped cone of Hastalloy B material. This material was selected for its good strength at the elevated temperatures required for cathode operation. Analysis of the data taken during the shock tests, the post-test X-rays, and dissection of the tube indicates that the electrical changes seen after shock numbers 4, 11, 12, and 13 are the results of cathode support cone failure. Earlier components tested had indicated that cathode support during shock was the most significant problem area to be solved. The cathode support in the TWT tested consisted of a 0.002-in.-thick Hastalloy B stamped cone, reinforced

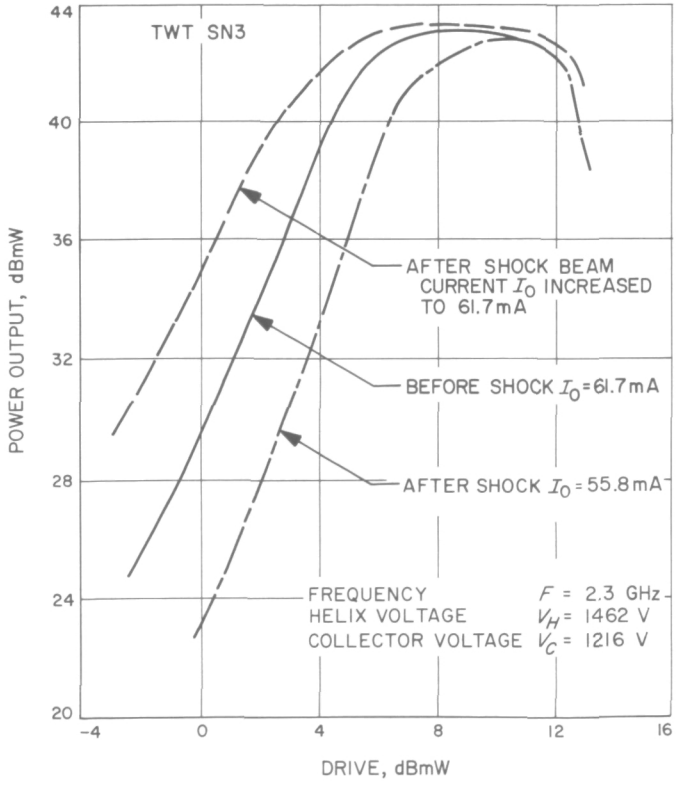

Fig. 14. WJ-398 SN 3 transfer characteristic comparison after high-impact shock series

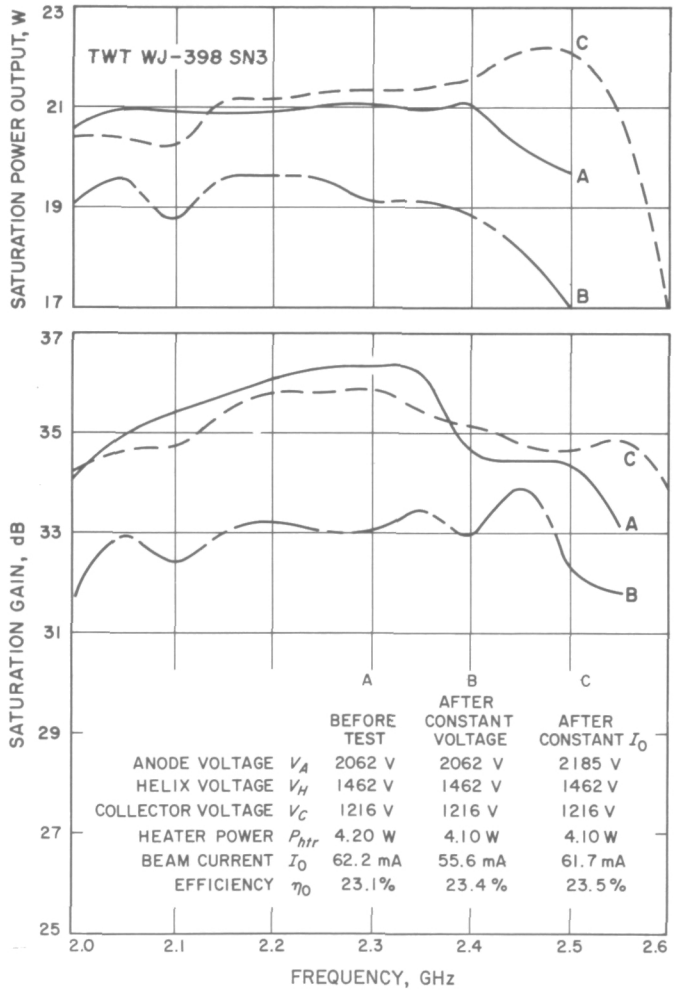

Fig. 15. WJ-398 SN 3 performance comparison after high-impact shock series

by an additional 0.002-in.-thick cone spot-welded over the upper end of the basic support cone. Static tests had indicated that the support would be adequate; however, the combination of dynamic loading and thermal stress experienced in the actual tube were apparently not correctly simulated. In order to correct this deficiency a series of test units is being fabricated from Hastalloy B and Inconel 625, in 0.002-in., 0.003-in., and 0.004-in. thicknesses with varying heat treatments. These cones will be evaluated by both dynamic and static testing to determine the optimum final design. The minimum thickness possible is desired, since thermal conduction power losses are directly proportional to cone thickness. However, the cone must be sufficiently thick to withstand the 10,000-g shock loading.

The primary effect of the shock test damage on TWT operation was a shift in the electron gun perveance, resulting in a 0.4-dB decrease in saturated power output with constant electrode voltages (Fig. 14), and a reduction in saturation gain, resulting in a 2.3-dB overall output degradation (Table 5). When the anode voltage was raised to restore the original beam conditions, power output and efficiency returned to pretest values. This indicates that the shock-test damage was confined to the electron gun, and in particular the cathode support cone.

After the shock test the TWT was tested satisfactorily in the temperature range of from -20 to $+85$°C. In addition, the tube was cycled in a nonoperating condition for 39 h at 150°C without any further shifts in the tube's electrical operating characteristics.

e. Deliverable prototype status. Fabrication of TWT SN 4 has been completed with the exception of the electron gun assembly. Fabrication of the electron gun assembly will be delayed until dynamic and static tests of the various cathode support cone designs being evaluated are complete.

Table 5. TWT SN 3 performance comparison before and after shock-test series

Telemetry data comparison (spacecraft conditions invariant)		
Parameter	**Before shock series**	**After 15 impacts**
Frequency	2.3 GHz	2.3 GHz
Power output	43.23 dBmW = 21.05 W	40.92 dBmW = 12.4 W (unsat)
Gain (constant drive = 6.9 dBmW)	36.3 dB	34 dB
Overall efficiency	25.6%	—
DC power	82.4 W	73.3 W
TWT input VSWR	1.39	1.32
TWT output VSWR	1.11	1.13
Laboratory performance comparison (beam current invariant)		
Parameter	**Before shock series**	**After 15 impacts**
Frequency	2.3 GHz	2.3 GHz
Saturation power output	43.23 dBmW = 21.05 W	43.35 dBmW = 21.6 W
Saturation gain	36.3 dB	36.25 dB
Beam efficiency	23.1%	23.8%
Overall efficiency	25.6%	25.4%
Input VSWR	1.39	1.32
Output VSWR	1.11	1.13

References

1. Prince, A. E., and Bakanauskas, S., Technical Memorandum WCLT-TM 58-146. Wright Air Development Center, Air Research and Development Command, USAF, Wright-Patterson AFB, Ohio, 1958.

2. Morelli, F. A., Fehlner, F. P., and Stembridge, C. H., *Nature*, Vol. 196, p. 106, 1962.

References (contd)

3. Brueschke, E. E., Suess, R. H., and Willar, M., *Planet. Space Sci.*, Vol. 8, p. 30, 1961.

4. Davis, H. S., Silverman, G. J., and Keller, W. H., *Appl. Microbiol.*, Vol. 11, p. 202, 1963.

5. Chuan, R. L., and Wallace, D. A., *Self-Contamination of Test Articles in Space Chambers*, Celestial Research Corporation, South Pasadena, Calif., 1965.

6. Thompson, R. P., and Casani, E. K., "*Voyager* Standardized Soft Lander Study Report, VPE-14," Engineering Planning Document 459, Jet Propulsion Laboratory, Pasadena, California, January 5, 1967.

Page intentionally left blank

Page intentionally left blank

V. *Surveyor* Project

LUNAR PROGRAM

A. Introduction

The *Surveyor* A-21 model flight spacecraft (Table 1) will demonstrate the technique of making soft landings on the moon, extend our knowledge of lunar characteristics and determine the suitability of sites for *Apollo* spacecraft landings.

Surveyor I, the first flight spacecraft, was launched from Cape Kennedy, Florida, on May 30, 1966, and soft-landed on the moon on June 2, 1966. By June 14, when lunar sunset occurred, approximately 100,000 commands had been received by the spacecraft; 10,338 pictures of the spacecraft and its immediate vicinity had been transmitted. During the second lunar day 899 additional pictures were received.

Mission B, which initially gave every appearance of the success of mission A, was terminated in the early morning of September 22, 1966. The spacecraft and all other increments of the mission performed nominally up to execution of the midcourse thrust maneuver. At that point, vernier engine 3 failed to ignite; the resulting imbalance of thrust from vernier engines 1 and 2 imposed a tumbling motion on the spacecraft, from which it failed to recover. Subsequent attempts to fire the vernier engines eventually increased the tumbling rate to 146 rev/min. The main retrorocket then was ignited, and at that time contact was lost with the spacecraft. At 2:53 a.m. PDT, following continuous receiver search for the spacecraft with no results, mission B was terminated.

Table 1. Model and vehicle designations

Designation	Description
SC-1–7	Flight spacecraft with engineering and limited science payload
A-21	Model designation for spacecraft SC-1–7
A-24	Former model designation for spacecraft with proposed scientific payload
T-21	Model A-21 prototype system test spacecraft
T-2	Simplified spacecraft for evaluation of terminal descent propulsion and flight control subsystems
S-2	Test spaceframe for vibration, shock, and static structural tests
S-6, -7	Test spaceframe for vernier propulsion system tests
S-9	Structural test model
S-10	Temperature control model

Because of the high degree of success of the mission up to the point of the midcourse thrust maneuver, data of considerable value were derived. It has contributed valuable guidance for future *Surveyor* missions.

Surveyor III was successfully launched from pad 36-B at Cape Kennedy, Florida, April 17, 1967, PST. After being placed in a parking orbit, the spacecraft was injected into a lunar trajectory. Subsequent flight events took place in a normal manner, and a landing was accomplished at a point about 3 mi from the projected landing point in a crater of the Ocean of Storms, April 19.

Despite some early ambiguous telemetry, the spacecraft was in a generally good condition. Following initial TV camera operations, surface sampler experiments were conducted. Four trenches were dug; the largest was 2 in. wide, 10 in. long, and 7½ in. deep. *Surveyor III* also provided the first photographs of an eclipse of the sun by earth.

By the end of its first lunar day, the spacecraft had responded to more than 30,000 commands and returned 6315 pictures. A brief and inconclusive thermal experiment was conducted after sunset, and then all operations were discontinued until dawn of the second lunar day.

Hughes Aircraft Company (HAC), Space Systems Division, is under contract to fabricate the *Surveyor* A-21 spacecraft. The launch vehicle, a combination *Atlas/Centaur,* is provided by General Dynamics/Convair (GD/C). Control, command, and tracking functions for the *Surveyor* missions are performed by the *Surveyor* Mission Operations System and the Jet Propulsion Laboratory (JPL) Deep Space Network.

B. Power Systems

1. Engineering

With the accomplishment of the *Surveyor IV* launch, all requirements for HAC solar panels, auxiliary batteries, and auxiliary battery controls as power subsystems units are completed. The Eagle-Pitcher auxiliary battery contract was terminated June 12, 1967.

Surveyor IV battery selection and performance were satisfactory. Flight batteries for SC-5 are being processed, and support batteries for SC-6 and -7 are on schedule.

As a part of *Surveyor IV* failure review, the power subsystem was reviewed in detail, and tests were made of several possible failure modes. Results were inconclusive, insofar as pinpointing a cause assignable to the power subsystem.

Solar panels have been processed on an adequate schedule. Two "B" liens existed. One was against unit consent-to-ship because of type approval testing (TAT), which has now been completed. The other, based on damage caused by low-temperature exposure of the panel, has been removed from SC-5 by JPL waiver of predawn lunar landing requirements. However, it remains open for SC-6 pending JPL tests on special TAT of panel serial number (SN) 6.

Laboratory tests were performed to determine possible spacecraft damage due to an improper test configuration wherein under "transmitter power on" or "radar altimeter and doppler velocity sensor (RADVS) on" the main battery is connected, the battery charge regulator switched to unregulated bus, and the main power switch opened. The test demonstrated no damage.

a. Solar panel. On June 12, 1967 HAC installed solar panel SN 5 on *Surveyor IV*.

JPL solar panel SN 6, partially celled, was delivered to HAC on June 16 for the type approval qualification drop test. The panel was installed on the S-9 vehicle for vibration and drop tests, which were completed July 12. The panel was removed from the S-9 vehicle to the solar panel clean room for inspection and shipment to JPL/Electro-Optical Systems (EOS). The inspection disclosed a minor gouge on the back surface of the panel and one cover-glass void. Six container corner blocks were severely damaged, requiring replacement. The panel was returned to EOS for testing on Table Mountain. This test will conclude TAT of the type 251167 JPL solar panel.

On June 23 JPL solar panel SN 3 was processed through vibration and vernier engine vibration (VIB/VEV) and shipped to JPL/EOS. A Table Mountain performance test was conducted July 6, and the panel was subsequently shipped to Air Force Eastern Test Range (AFETR). Acceptance testing at AFETR was completed July 21 and installation on SC-5 was scheduled for August 5, 1967.

On July 21, 1967 JPL solar panel SN 5 was tested at Table Mountain, shipped to AFETR, and acceptance

tested. The panel is currently in bonded stores at AFETR as SP-2.

Shimming requirements for installation of JPL solar panel SN 2 were checked. Installation on SC-6 was scheduled for on or about August 5, 1967, and will undergo VIB/VEV.

Having cleared the materials review board, JPL solar panel SN 4 is in bonded stores pending installation on SC-7.

Serial number 7 and 8 structural test model-type panels were delivered for SC-5 combined system test and joint flight acceptance test (J-FACT), respectively.

b. Batteries. Surveyor III reliability tests. Main battery SN 106 was selected as a typical flight quality battery for *Surveyor III* reliability tests. The battery was tested to simulate transit, touchdown, and nine days of lunar operation.

Figure 1(a) presents the battery terminal voltage, pressure, and temperature during the simulated lunar operation. The sharp rise in the temperature profile at 165 h was due to difficulty in regulating the temperature of the vacuum chamber. Figure 1(b) shows the voltage spread of the cells on charge (a measure of balance and uniformity among the cells) and charge current. As noted in Fig. 1(b), the voltage spread was a maximum of 40 mV, well within the specification of 100 mV. Figure 1(b) also shows that the battery was completely charged at the end of 60 h of operation where the current drops to zero. It is also noted that it accepts a small amount of charge after TV and antenna solar panel positioner (ASPP) operation.

Battery SN 106 was also used in an experiment to determine at what temperature the *Surveyor III* battery would cease to operate as it entered lunar night and at approximately what temperature the battery would begin to accept charge at the start of the second lunar day. Figure 2(a) shows the temperature, pressure, and terminal voltage of the battery during the test.

Cell reversal occurred at 22°F, after about 5 h of discharge at 7 A. Cell number 1 reversed to −1.778 V, and the discharge rate was lowered to 200 mA. Figure 2(b) shows the voltage spread of the cells during the test. The cell unbalance diminished to a nominal value when the discharge rate was decreased and increased as the temperature decreased. This portion of the test showed that the battery will sustain at least a 200 mA load down to −450°F.

Figure 2(c) is a scale expansion of the simulated pulse discharge and continuous charge due to the operation of the TV, ASPP and high-power transmitter during lunar sunrise. The test indicated that the battery should be capable of operation at lunar sunrise, after it has warmed up to about −40°F and that high on-charge voltages should be expected, i.e., 34.8 V at 2 A.

Ten days after the cold temperature test the battery was discharged at 5 A to 17.5 V at 75°F, and it yielded 132 A-h. The battery accepted a recharge of 185 A-h with every indication that the battery was still in good condition.

Surveyor IV flight battery selection. Main batteries SN 120 through 127 were potential candidates for *Surveyor IV* flight. From these batteries, SN 122, 123, and 125 were selected as the most uniform batteries and best flight candidates. Table 2 summarizes the characteristics of the three flight batteries. After completion of flight acceptance test (FAT) procedures at AFETR, SN 123 was selected as the prime flight battery, with SN 122 and 125 as backup units.

Surveyor IV flight data. Main battery SN 123 was installed on *Surveyor IV* as planned and performed as expected. Figure 3, *Surveyor IV* flight data, was compared to *Surveyor III* flight data and *Surveyor IV* solar thermal vacuum (STV) information. Information up to the point of data loss indicated nominal performance.

STV testing. During the report period, SC-6 completed STV phases A and B. Phase A was conducted on battery power using SN 117. Figure 4 is a plot of battery voltage, temperature, and pressure during the phase A test. No anomalies were noted in battery performance, and a subsequent discharge and recharge indicated the battery was capable of additional normal operation. A repeat STV phase-A test was run on battery power using SN 128.

Lunar night survival. A test program is under way to obtain additional data on main battery performance under expected lunar night conditions. The data will be used to establish relationships between voltage, pressure, discharge rate, state of charge, and temperature. Recommendations for optimizing survival will be made.

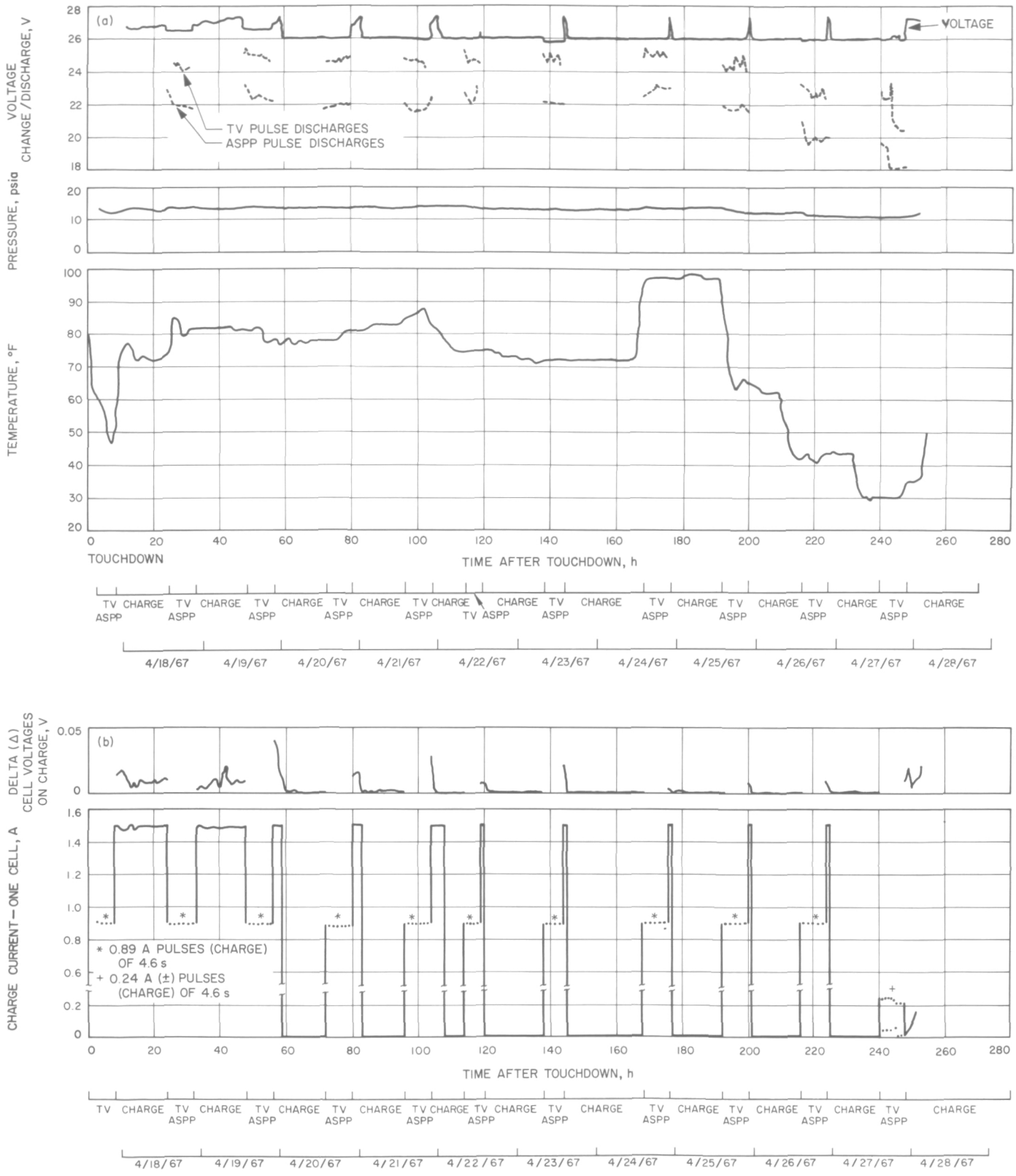

Fig. 1. Main battery SN 106 reliability tests during simulated lunar operation: (a) terminal voltage, pressure, and temperature; (b) voltage difference between individual cells during charging and current change

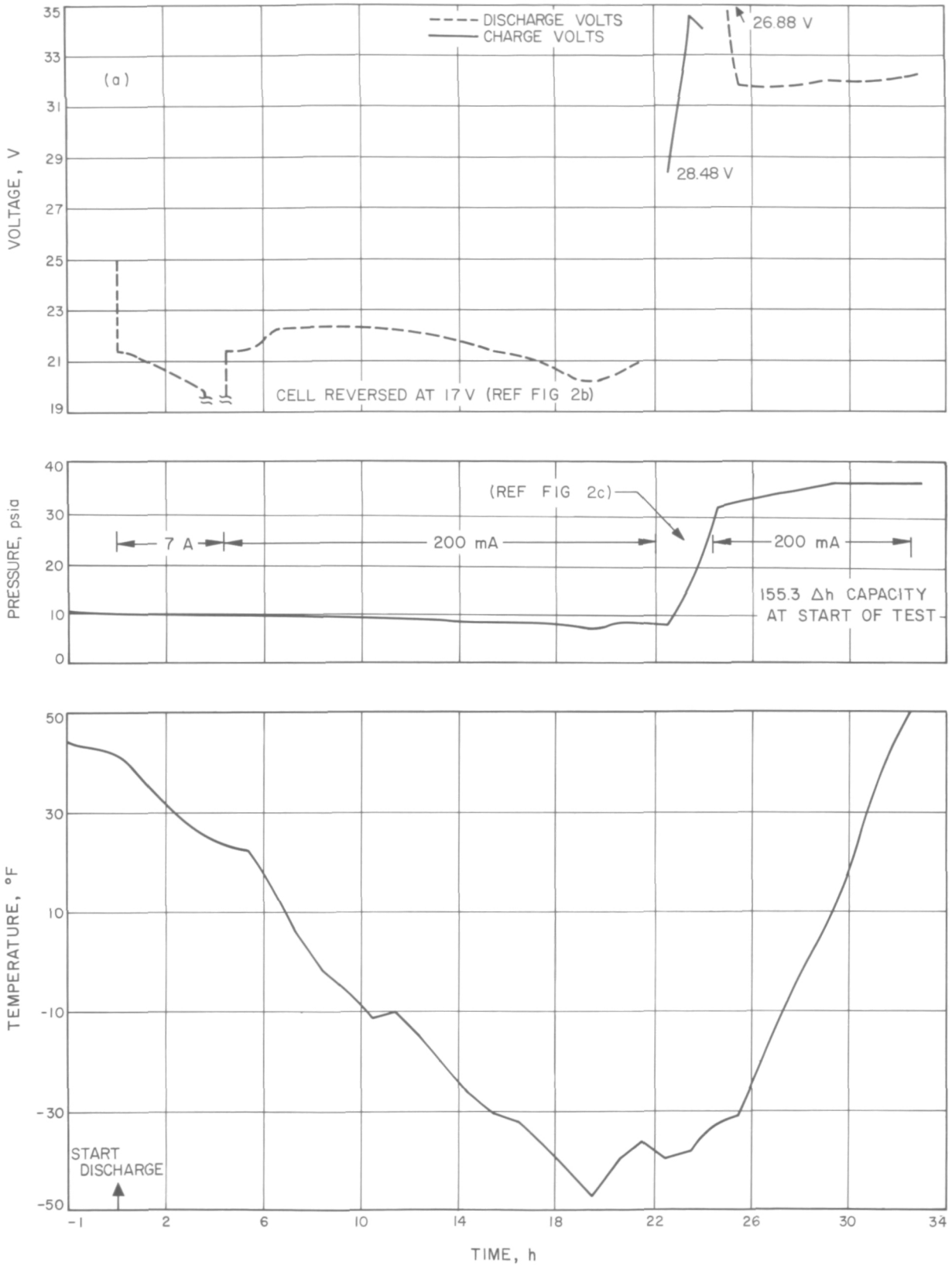

Fig. 2a. Main battery SN 106 test during lunar sunrise simulation: temperature, pressure, and terminal voltage during low-temperature phase

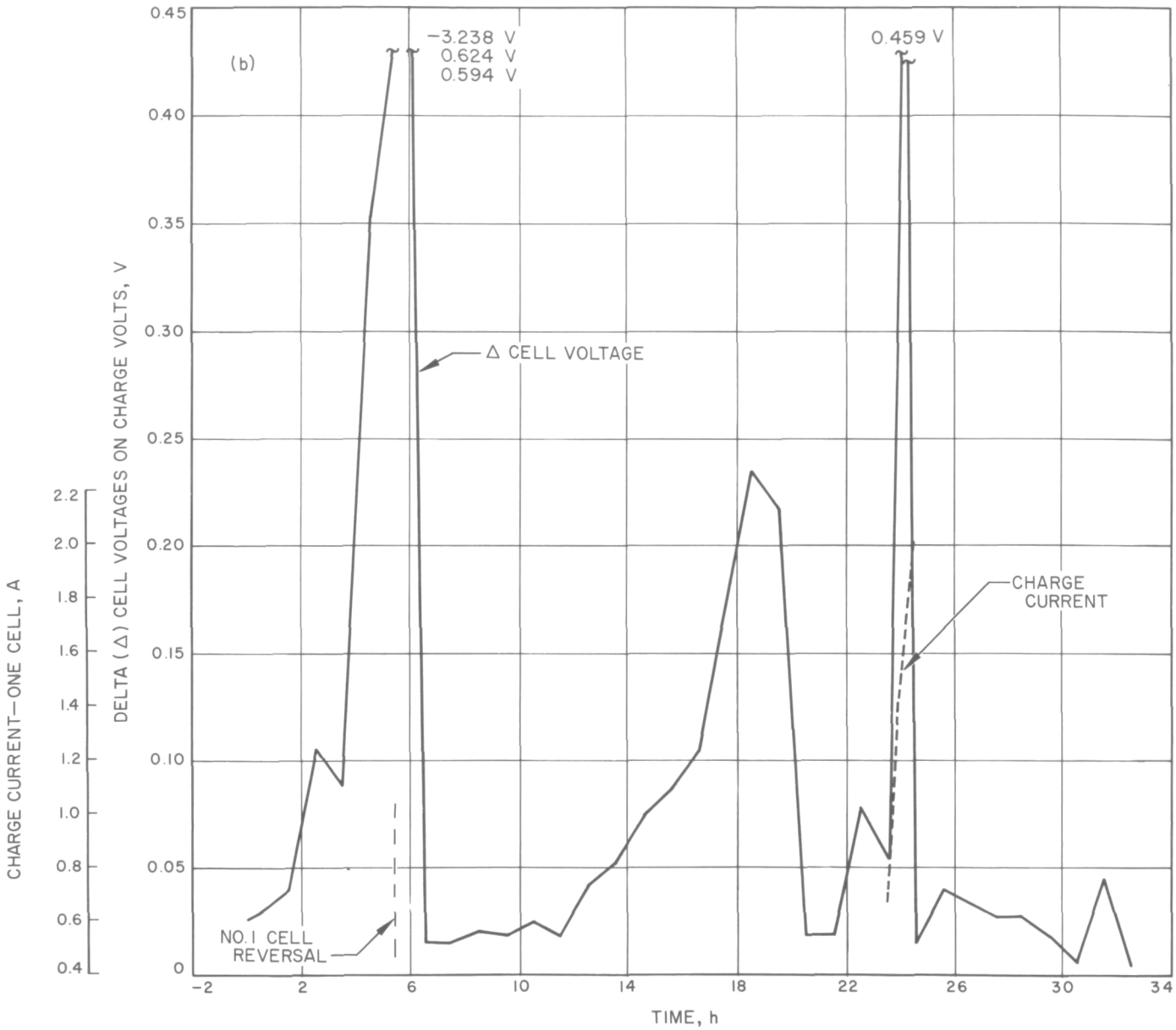

Fig. 2b. Main battery SN 106 test during lunar sunrise simulation: difference between individual cells on charge and discharge

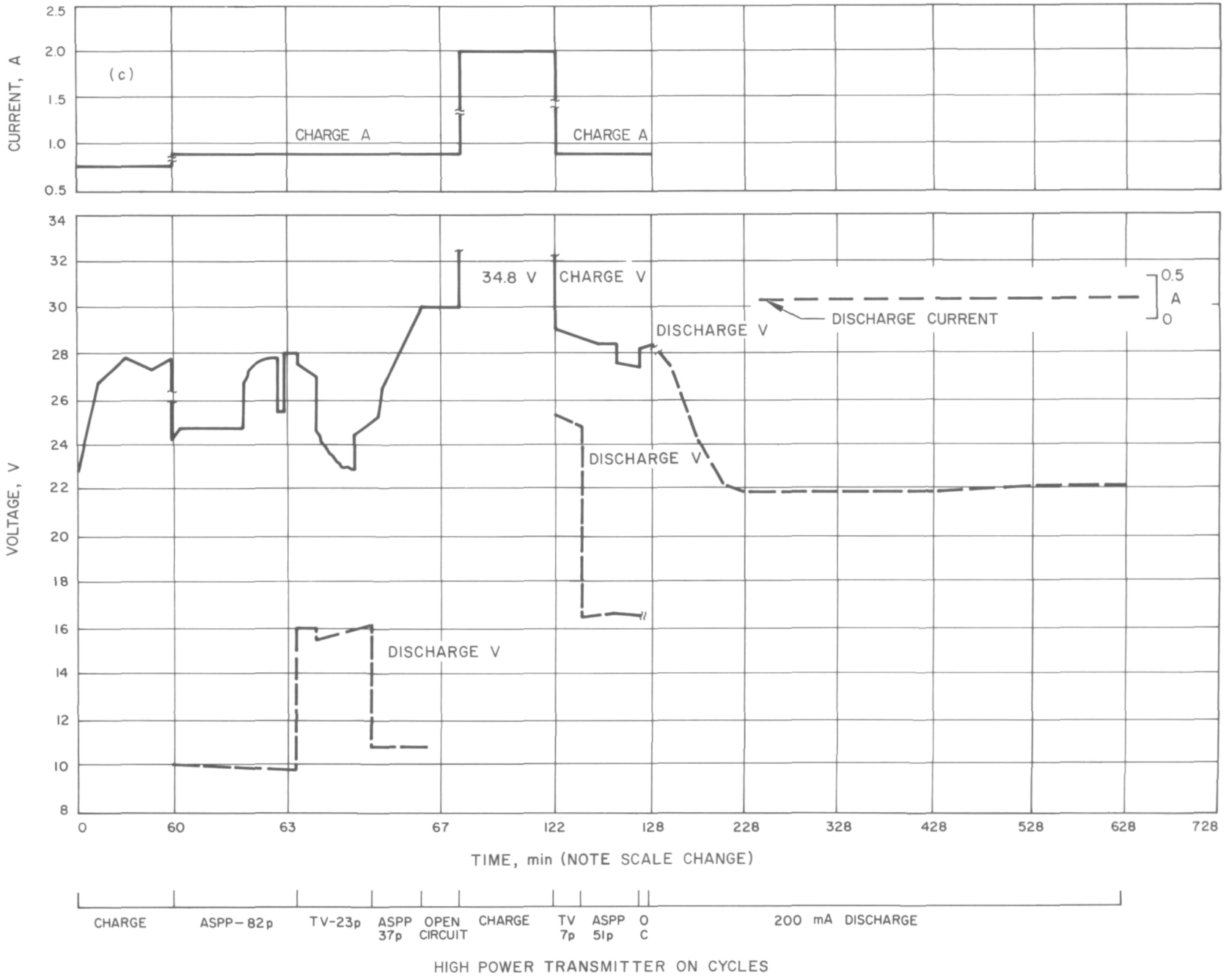

Fig. 2c. Main battery SN 106 test during lunar sunrise simulation: scale expansion of pulse discharge and charge data

Table 2. Flight battery summary

SN	Capacity data		Voltage data					
	Electric Storage Battery Co., (ESB) A-h input	HAC A-h approximate input after float	ESB final 85-A pulse, V	HAC 50-A initial FAT pulse, V	HAC fourth pulse, FAT, A		HAC sweep discharge, A	
					50	70	50	70
122	183.8	186.3	19.36	20.15	19.27	18.50	19.25	18.87
123	183.8	186.1	19.65	20.14	19.25	18.40	19.25	18.87
125	177.8	183.6	19.64	20.10	19.29	18.49	19.50	19.0

SN	Miscellaneous data						
	Age, 7/14/67, days	HAC helium leak rate, cm^3/s	AFETR helium leak rate, cm^3/s	End of charge cell spread at AFETR, V	Materials review board actions	ESB monoblock A-h spread	Pressure buildup on charge
122	58	3.9×10^{-6}	9.1×10^{-6}	0.056	Wire touching magnesium canister	3.8	None
123	58	3.8×10^{-6}	1.4×10^{-5}	0.041	OK	3.0	None
125	58	3.9×10^{-6}	2.5×10^{-5}	0.079	OK	6.2	None

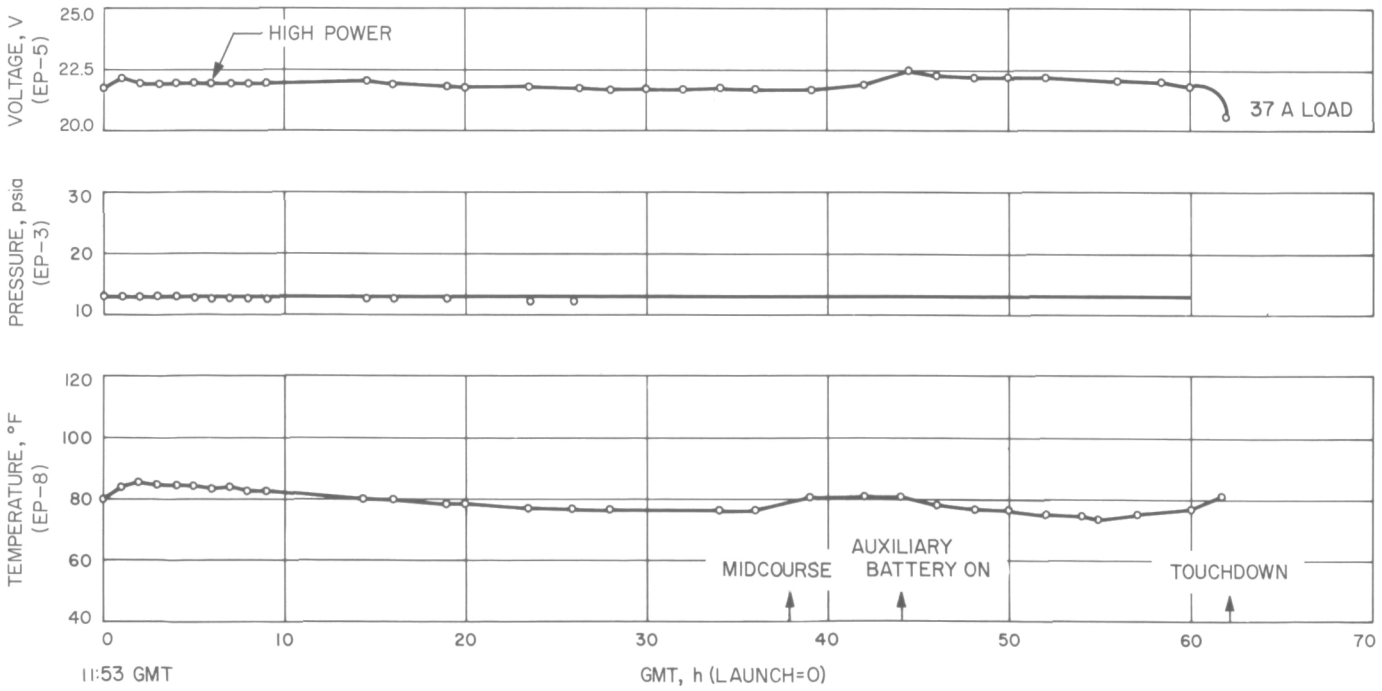

Fig. 3. Main battery SN 123 operation during *Surveyor IV* flight

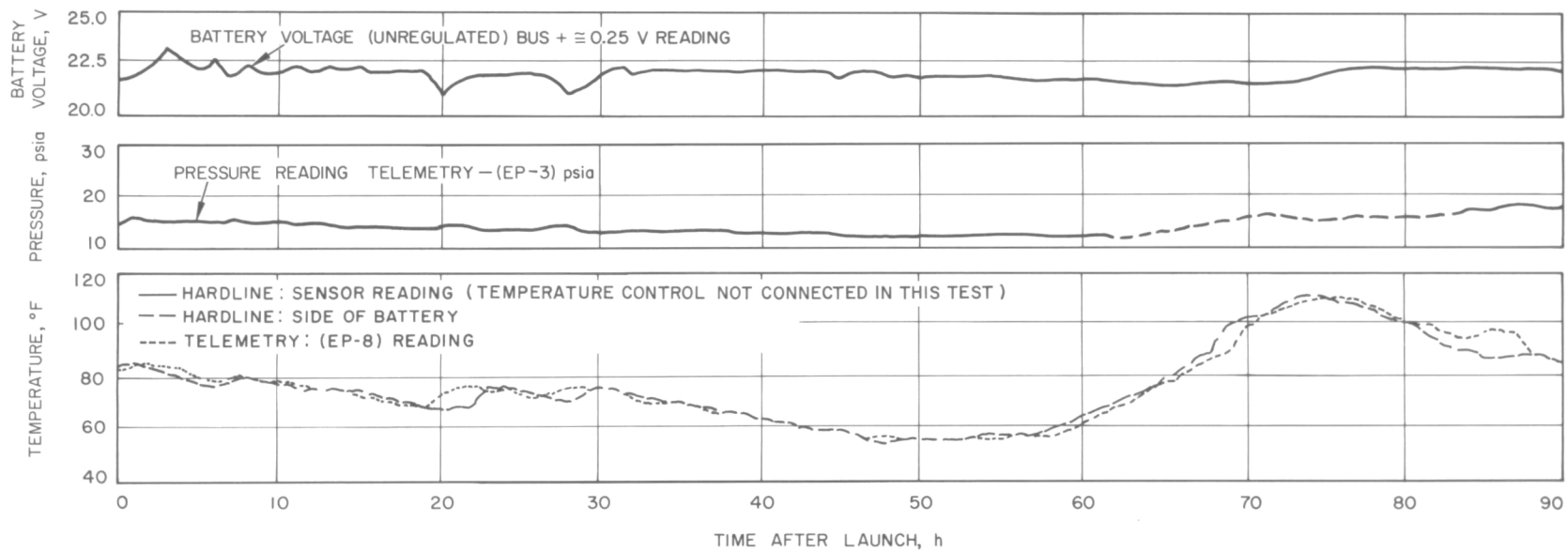

Fig. 4. Main battery SN 117 operation during SC-6 STV phase A

Six main batteries will be utilized to study the effects of low temperatures encountered during lunar night on battery performance. Three batteries will be operated simultaneously over a time-temperature profile simulating a spacecraft lunar night energy profile. Battery temperature will be maintained at 20°F for approximately 132 h into lunar night while dissipating 2100 Wh of energy. Following this, the battery load will be decreased to 230 mA, and temperature will decay in accordance with the predicted profile to a lower limit of −165°F. At the conclusion of lunar night simulation (354 h) the batteries will be heated to −40°F (the lowest practical temperature at which charging is recommended), and an attempt will be made to charge each battery.

Three batteries will be completely discharged at 20°F to determine the amount of energy available at this temperature. They will be raised to room temperature to establish predicted existence of residual energy, and then will be subjected to the lunar night temperature to evaluate the effects of freezing a fully discharged battery. At the conclusion of the low-temperature operation, attempts will be made to charge the batteries. A report covering the above tests will follow their conclusion, which is scheduled for late August 1967.

c. Lunar night survival. A lunar night survival study is reported in Ref. 1. Section A of this report covers material with a direct bearing on the power subsystem. The battery portion of this effort is described in Section IV of the document.

The addition of radioisotope heaters, while of major interest, is probably limited to SC-7 for schedule reasons. The plan is to introduce heaters totaling approximately 5 W each into compartments A and B. JPL has concurred in this effort and authorized a go-ahead under change order No. 164.

Negotiations have been undertaken with Atomics International to build eight (four 2.5 W and four 2.7 W) units and dummy test models for weld control testing. The best present delivery schedule for these heaters is September 5, 1967.

d. Main power switch. A special test on main power switch SN 13 was performed to obtain additional confidence in switch operation after being in storage for many months without activation. The test was designed to verify proper switch operation and to measure contact resistance. Three readings and switch transfers were performed as follows:

(1) 2-A test on terminals 12, 13

37 mV	Specification value 100-mV
25 mV	maximum
17 mV	

(2) 2-A test on terminals 11, 12

5 mV	Specification value 100-mV
5 mV	maximum
5 mV	

(3) 50-A test on terminals A1, A2

14 mV	Specification value 50-mV
17 mV	maximum
24 mV	

Since the main power switch is hermetically sealed and since the unit life is rated for 10,000 cycles, no further testing is considered necessary on the switch to verify flight acceptance. This test will be repeated on SN 7, which was assigned to SP-1.

2. Manufacturing

a. Boost regulator. Boost regulator SN 12 was removed from SC-7 and returned to the unit area for repair to the EP-14 shunt, which required the replacement of one broken resistor. While in rework, the four mounting screws were also replaced.

A TAT review meeting was held June 6, 1967 to review and approve the TAT data on boost regulator SN 14 and battery charge regulator 12.

Boost regulator SN 9, class 3, together with its filter choke, was returned from AFETR for special tests in connection with the *Surveyor IV* failure review.

b. Battery charge regulator. While demating battery charge regulator SN 11 on SC-5, the jackscrews were stripped. The unit was returned to Hughes Aircraft Co., Culver City, California for disassembly and recovery of the loose nuts and washers. The unit was reassembled and returned for installation on the spacecraft.

The suspended action on MEPCO resistors, used in battery charge regulator SN 13, was lifted by ITR 2557.

C. Flight Control Subsystem

1. Engineering

Surveyor lunar hopper kit thermal tests.

Flight control electronics unit thermal vacuum tests conducted for lunar hopper. The flight control electronics unit (FCEU) thermal vacuum tests, designed to evaluate FCEU performance under the lunar environment expected at vernier engine static firing and spacecraft liftoff, consisted of comparative measurements of the FCEU thrust control circuit gains over a temperature range of 40 to 175°F in a vacuum. Another test was performed to evaluate the effect of heat soaking the FCEU at 250°F in a vacuum.

All functional tests of the FCEU were performed on the flight control sensor group (FCSG) flight acceptance test (FAT) console. The environmental tests were performed in the C-3 thermal vacuum chamber. Thermal control of the FCEU was accomplished by piping lexol through plumbing attached to the FCEU support fixture, augmented by hotplates above and below the support fixtures. Thermocouples were distributed throughout the FCEU, as shown in Fig. 5.

The advanced flight control programmer (AFCP) oscillator circuit, which provides FCEU timing and power sync pulses, failed during the high-temperature soak. After the programmer was replaced, a final thermal vacuum test was performed with the FCEU at 48°F. No significant parameter changes were observed throughout the temperature range. Comparison of the FCEU functional test data taken before and after environmental tests indicates no degradation of FCEU functions.

IRU thermal tests for lunar hopper. Thermal tests were conducted to measure IRU performance under the lunar thermal environment expected to exist at vernier engine static firing and spacecraft liftoff. Although a warmup procedure was provided in the *Surveyor III* and *IV* hopper kits so that the IRU could be operated at its design temperature, the test was conducted to obtain measurements of IRU functions over an expanded temperature range of 130 to 200°F. The test consisted of comparative measurements of the gyro precession rate in response to a fixed torquer input, gyro response to the earth's rate, and comparative measurements of the accelerometer output signal at the various temperatures. A test was also performed to evaluate the effect of cold-soaking the IRU in a vacuum.

All IRU functional tests were performed on the IRU FAT console. With the exception of the functional tests and the vacuum cold-soak, the tests were performed with the IRU in the Conrad temperature chamber. The IRU was positioned to provide approximately 0.2 g input to the accelerometer, and oriented to provide as equal a distribution of earth's rate input into each gyro as possible. Five thermocouples (TC) were distributed to monitor IRU temperatures (Fig. 5).

The relative changes of the gyro signal generator scale factor (or gyro transfer function) with temperature, computed from gyro precession rates, are shown in Fig. 6.

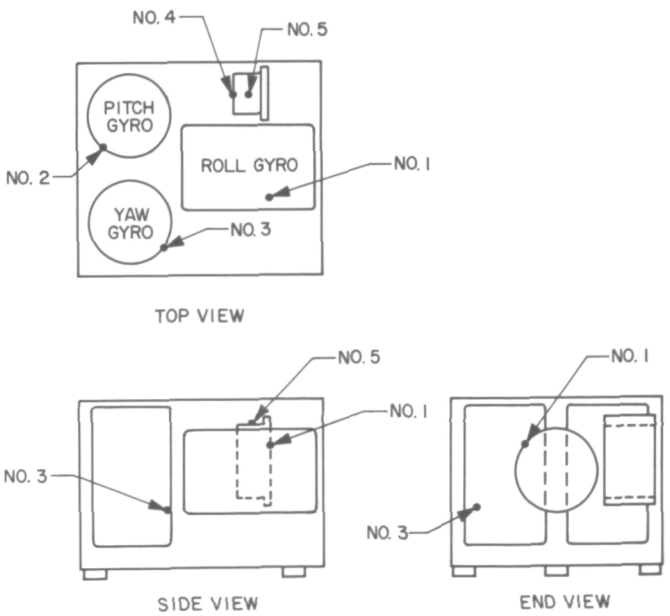

Fig. 5. Thermocouple location in the IRU

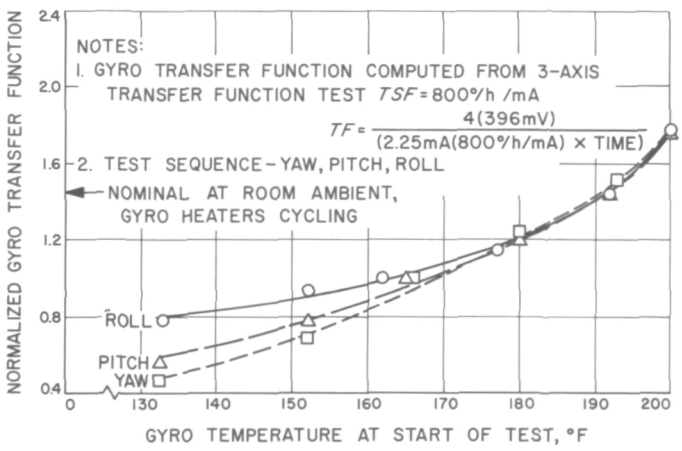

Fig. 6. Normalized gyro transfer function vs IRU temperature

Because the IRU begins to heat up when power is applied, the test results are affected by the sequence in which the gyros are tested. Relative changes of the accelerometer scale factor with temperature, computed from the magnitude of the accelerometer output signal at approximately 0.2 *g*, are illustrated in Fig. 7.

Although no attempt was made to simulate the heat transfer characteristic of the IRU in the lunar environment, the rate of temperature rise in the unit, from an initial temperature at application of IRU power, has been plotted in Fig. 8.

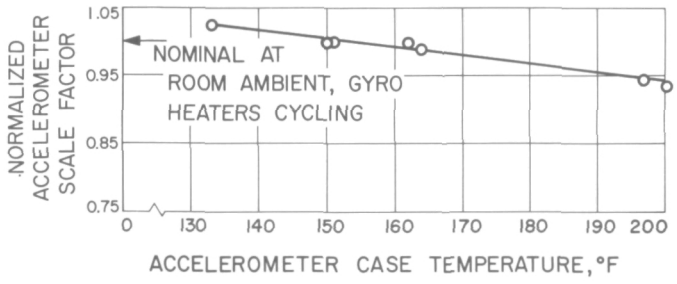

Fig. 7. Normalized accelerometer-scale factor vs IRU temperature

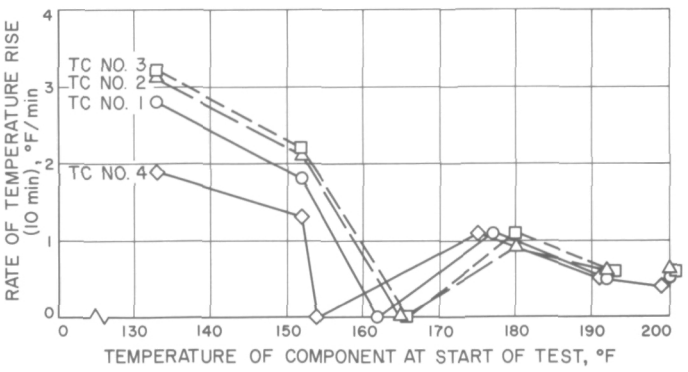

Fig. 8. Rate of temperature rise vs initial IRU temperature

2. Manufacturing

a. Flight control sensor group hardware. All flight control sensor group (FCSG) hardware had been delivered prior to this report period; however, it was necessary to rework the SC-5 and -6 FCEUs.

As stated in the previous report, the SC-5 FCSG was to be visually inspected before shipment to the Air Force Eastern Test Range (AFETR) to determine the status of the connector sockets in the electronics harness. This inspection was performed, and, because of discrepant spring detents found in the connector sockets, the electronic harness had to be changed.

During SC-6 mission sequence testing, the flight control magnitude register failed to load. Preliminary investigation indicated that the problem was in the flight control programmer. The sensor group was removed and returned to the test laboratory for verification of the problem. Testing of the unit in the laboratory did not exhibit the same type of problem, but difficulty was experienced in loading the register. The electronics unit was disassembled and the AFCP was returned to the unit testing area for further testing and replacement of a suspected flip-flop module.

Because of the time required to evaluate the programmer problem discussed above, the SC-7 FCSG was installed on the SC-6 spacecraft. The unit previously removed from SC-6 has been repaired and is now on SC-7.

b. Accelerometer hardware. The retromotor accelerometer removed from SC-3 has completed vendor rework and complete retest at HAC. The unit will now be assembled to the SP-2 flight control sensor harness.

c. Attitude gas jet nitrogen system. Increased gas jet leakage of clockwise jet 2 on SC-5 was noted during system testing. The leakage was not considered significant in terms of mission effect and was dispositioned as suspended action to be watched and further evaluated during AFETR checkout. A spare gas jet (SN 10) was cycled an additional 5000 times on each side prior to AFETR shipment in preparation for possible replacement of the leaky jet.

The SP-1 attitude gas jet supply has been returned from AFETR and is now being upgraded to the configuration of SC-5 and subsequent spacecraft.

d. IRU hardware. The IRU, SN 13, previously installed on the SC-7 FCSG and then removed for use on SC-6, was returned for rework because the pitch gyro fixed drift parameter was out of specification tolerance. The unit was removed from the sensor group and returned to the unit area for rework; however, testing in the unit area failed to disclose any functional discrepancy. The measured pitch gyro fixed drift was well within specification limits. Subsequently, the IRU was tested with two other sensor groups and, again, the pitch gyro exhibited excessive fixed drift. Attempts to isolate the problem were unsuccessful.

The pitch gyro was then removed and returned to the vendor, along with the roll gyro which was also removed

because of gradual mass unbalance deterioration noted around the input axis during the above tests. The unit is now awaiting the return of repaired gyros from the vendor before further rework can be accomplished.

e. Radar altimeter doppler velocity sensor ECP-10—double sideband signal data converter. Signal data converter serial number (SN) Y-1 is presently in FAT but is being temporarily delayed pending correction of out-of-specification range test results. At present, SN Y-2 is not in work. The Engineering Change Proposal (ECP) 10 design review package has been completed, and the design review will soon be scheduled.

Other work in progress includes some hardware redesign studies on the radar altimeter spread RF spectrum problems under different range conditions, ECP-2 repair and checkout, and rework of several signal data converter SN 5 subassemblies.

D. Telecommunications

All RF flight hardware has been delivered to the spacecraft bonded stores area; however, transmitter problems continue to plague the spacecraft systems operations. Most of the problems, involving all but two of the remaining transmitters, appear to be due to design margins and the traditional variable capacitor instabilities. It is quite possible that the problems currently being encountered have always been present and are being uncovered at this time because of a recent requirement to continuously record the receiver static phase error signals. Corrective action has been of a "band-aid" nature; and, because of schedule constraints, it appears this pattern will remain throughout the program.

Efforts to determine if an RF system failure was involved in the SC-4 mission termination have been fruitless. During this report period there was a minimum of activity in the area of signal processing and command manufacturing or engineering. The last of the flight units had been initially delivered during the previous reporting period. Several units that were returned from spacecraft test and operations for repair and rework due to test induced problems have been redelivered to bonded stores.

The investigation as to the feasibility of fusing critical telemetry power lines has been terminated, due to the failure of available fuses to qualify for flight use.

An investigation of spacecraft command system testing was undertaken at JPL. A report (IOM 273-B-932, dated August 21, 1967) has been generated. As a result, several additional tests that could be incorporated to give increased confidence in the integrity of the command subsystem are being studied. Schedule considerations appear to preclude a comprehensive retest program. The actual history of failure of the command subsystem is quite low, considering the high frequency of commands utilized during each spacecraft test.

E. Radar Altimeter and Doppler Velocity Sensor

To establish the magnitude of the tracker errors that occur during normal crosscoupled sidelobe determination, the nonlinearity effect upon crosscoupled sidelobe rejection levels for "main line" doppler velocity sensor trackers was studied.

The voltage gain characteristic functions for each tracker were obtained by measuring the tracker outputs for several values of input voltage, using a signal bandwidth of 1.1 kHz.

The method of computation of the nonlinear error is based on a mathematical model of the system in which the logic circuit compares the output of two trackers, after prescribing suitable attenuation of the outputs, to determine if one of the trackers is locked to a sidelobe. One tracker, with gain function $A(V)$ of input signal V, is assumed to be tracking a main beam. The other tracker has a gain function B and is assumed to be tracking a signal of unknown origin. The rejection level is considered to be a voltage level at the input to the tracker B preamplifier. It is established by the value of attenuators in either the A or B channels to the comparator, which the logic specifies on the basis of the A and B channel preamplifier gain states. An equivalent attenuator of value W is used in the model.

F. Thermal Engineering

Solar thermal vacuum testing of the SC-6 spacecraft was performed. The TV camera-3 warmup prior to terminal descent was at a slower rate than on previous spacecraft. It is believed that the larger TV hood and mirror assemblies contribute a large heat loss and cause this phenomenon; however, the thermal performance is satisfactory for flight. Temperature data from vernier engine No. 1 indicated anomalous behavior. The data are being reviewed and the engine subjected to additional testing in order to resolve the anomaly. All other components performed nominally during the test phases.

A special study was performed to recommend ways to increase the lunar night survival probability of future

spacecraft. The use of isotope heaters in compartments A and B was recommended to ensure lunar night survivability.

A study was performed to evaluate *Surveyor IV* thermal performance prior to loss of telemetry data. The thermal behavior of all spacecraft subsystems was normal during the transit mission phase. Sixty-three of the 75 thermal sensors on board the spacecraft were within 5°F of their nominal predicted values, and 70 thermal sensors were within 10°F of their nominal predicted values. The absence of thermal anomalies suggests that the sudden loss of signal was not thermally induced.

G. Structures, Mechanisms, and Spacecraft Integration

1. Structural

a. Shock absorbers. In addition to SN 13, which indicated a preload failure during the previous report period, both SN 20 and 21 failed preload tests at the Air Force Eastern Test Range (AFETR). Retest of SN 13 at HAC, El Segundo, and SN 20 at AFETR, however, showed acceptable and normal preload force levels. The erroneous failure reports of SN 13 and 20 were caused by inexperienced test crews and inadequate torque wrenches at AFETR; steps have been taken to eliminate both problem areas.

Analysis of SN 21, which failed at both AFETR and El Segundo, indicated the preload failure was caused by increased internal friction due to drying out of the piston seal. Several short compression strokes were made to allow the seal to be lubricated by the unit's hydraulic fluid. Retest of the unit demonstrated acceptable preload force. Although the dry seal condition would have no effect on landing performance, a revision to the preload test procedure will eliminate a dry seal situation during preload tests.[1] SC-5 shock absorbers (SN 8, 10, 11 and

[1]SN 21 is being held up by engineering for a period to exceed 30 days. The old preload test is to be repeated to determine if exercising and, thus, wetting the seal is effective for at least the 30-day period.

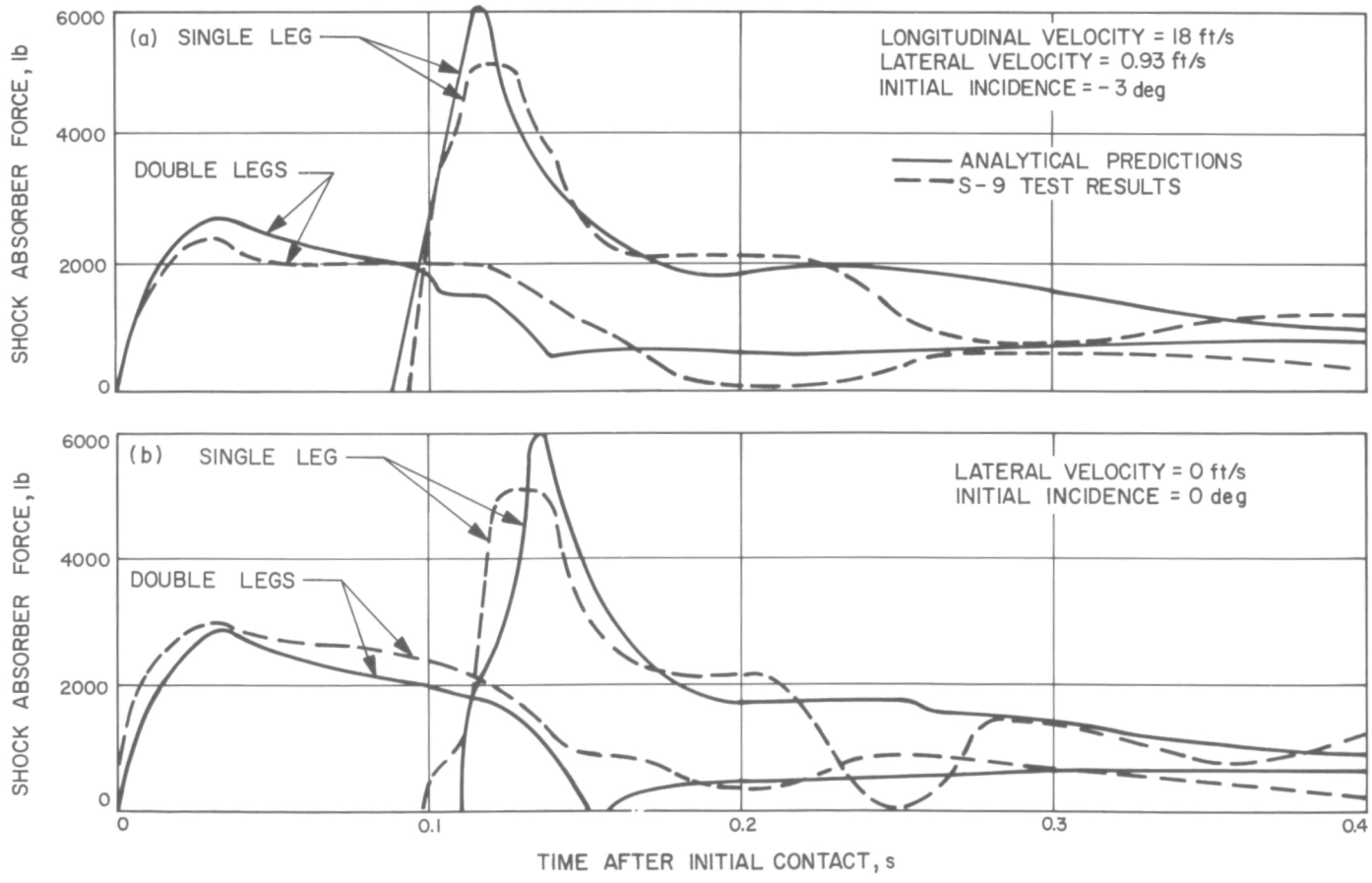

Fig. 9. Comparison of S-9 drop test shock absorber loads with analytical simulation: (a) drop 1; (b) drops 2 and 3

spares SN 13, 19, 20) are at AFETR ready for preflight checkout and installation.

b. Dynamics analysis.

S-9 *drop test.* Effort is under way to correlate the structural loads obtained from S-9 drop tests with those predicted by analysis. Only the correlation of the shock absorber loads has been completed to date; the correlation for drops 1, 2, and 3 is shown in Fig. 9.

Delayed vernier engine cutoff. The effect of the *Surveyor* spaceframe impacting rocks during landing has been examined to assess how much improvement in performance would result from lower landing velocities achieved by delayed vernier engine cutoff.

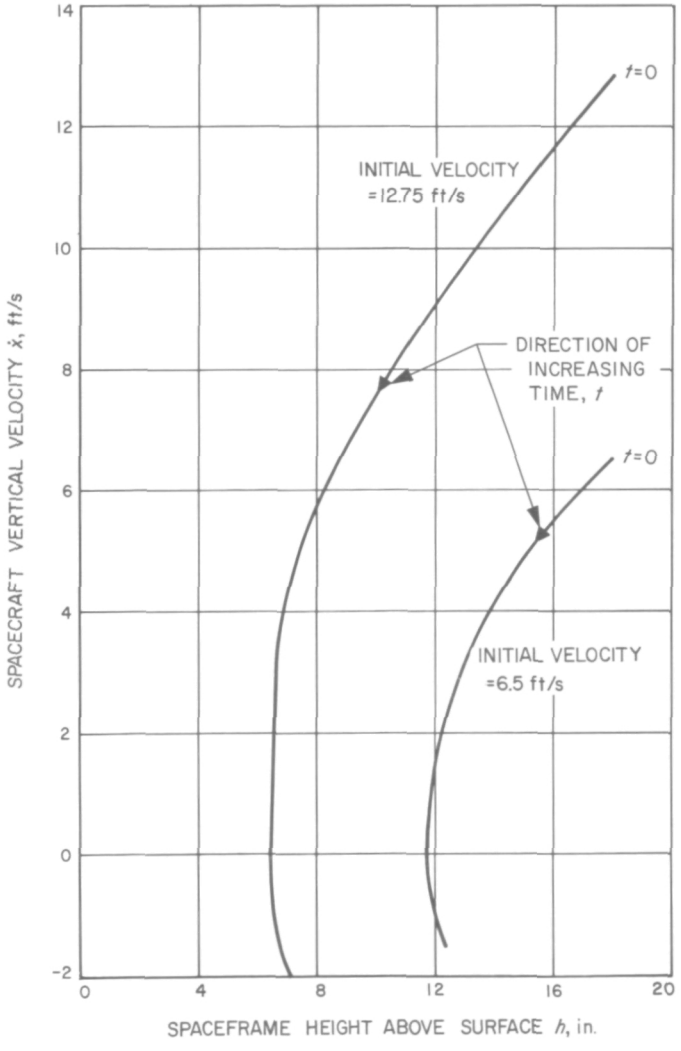

Fig. 10. Spacecraft vertical velocity spaceframe height above surface (normal loading)

Spacecraft spaceframe velocity versus surface clearance was plotted for two specific touchdown conditions. Structural loads occurring during a standard (no protuberance impact) landing under these conditions were then combined with additional loads resulting from spaceframe protuberance impact to determine allowable impact velocities. Using the results in conjunction with the curves of Fig. 10, allowable rock heights were established for various spacecraft components (Fig. 11). Some allowable rock heights barely exceed the minimum spaceframe surface clearance value; so no performance gain is evident using this analytical approach.

c. Surveyor III postmission analysis.

Launch phase structural response loads. During liftoff, and for the initial 5 min of powered flight, spacecraft accelerometer data were recorded in real time; a review of the data verified that all spacecraft accelerometers operated normally. The vibration levels at launch and the magnitude and duration of inflight shock transients were similar to values experienced during the *Surveyor I* flight.

The vibration environment experienced by accelerometer CY 520 (the only continuous signal) is summarized in Table 3.

Table 3. Vibration data for CY 520 during *Surveyor III* launch

Flight event	Recorded value
Liftoff:	
$T_0 - 0.2$ s	3.3 *g* zero to peak (single spike)
T_0	0.8 *g* rms (estimated)
$T_0 + 4$ s	0.4 *g* rms (estimated)
$T_0 + 8$ s	0.1 *g* rms (estimated)
Atlas booster engine cutoff	1.75 *g* zero to peak (one cycle pulse of 0.8 s duration)
Insulation panel jettison	Transient, 10 *g* zero to peak decayed to 0 *g* in 0.08 s
Boost engine jettison	15 or more extremely sharp peaks[a] $>$ 6 *g* with 3 peaks $>$ 10 *g* (no oscillatory decay)
Nose fairing jettison	Six cycle oscillation; maximum level 1.0 *g* zero to peak; approximate frequency 18 Hz
Atlas sustainer engine cutoff	Single pulse less than 0.5 *g* zero to peak
Atlas vernier engine cutoff	
Atlas/*Centaur* separation	High frequency transient $>$ 10 *g* zero to peak decayed to 0 *g* in 0.15 s

[a]These transients are probably the result of telemetry "dropout." Similar spikes occurred on channel 14 during switching when signals were not being monitored.

Landing dynamics. Simulation of *Surveyor III* landing dynamics has been achieved using a three-dimensional mathematical model which incorporates a flight control system. The simulations have considered recorded time histories of shock absorber strain gages, flight control gyro errors, and vernier engine thrust commands, together with pertinent information obtained from postlanding TV coverage. One objective of the analysis was to produce a set of strain gage time histories for each landing event which uses impact velocities that are consistent with the simulated trajectories flown by the mathematical model between each landing event. This would result in a consistent simulation of the entire landing phase.

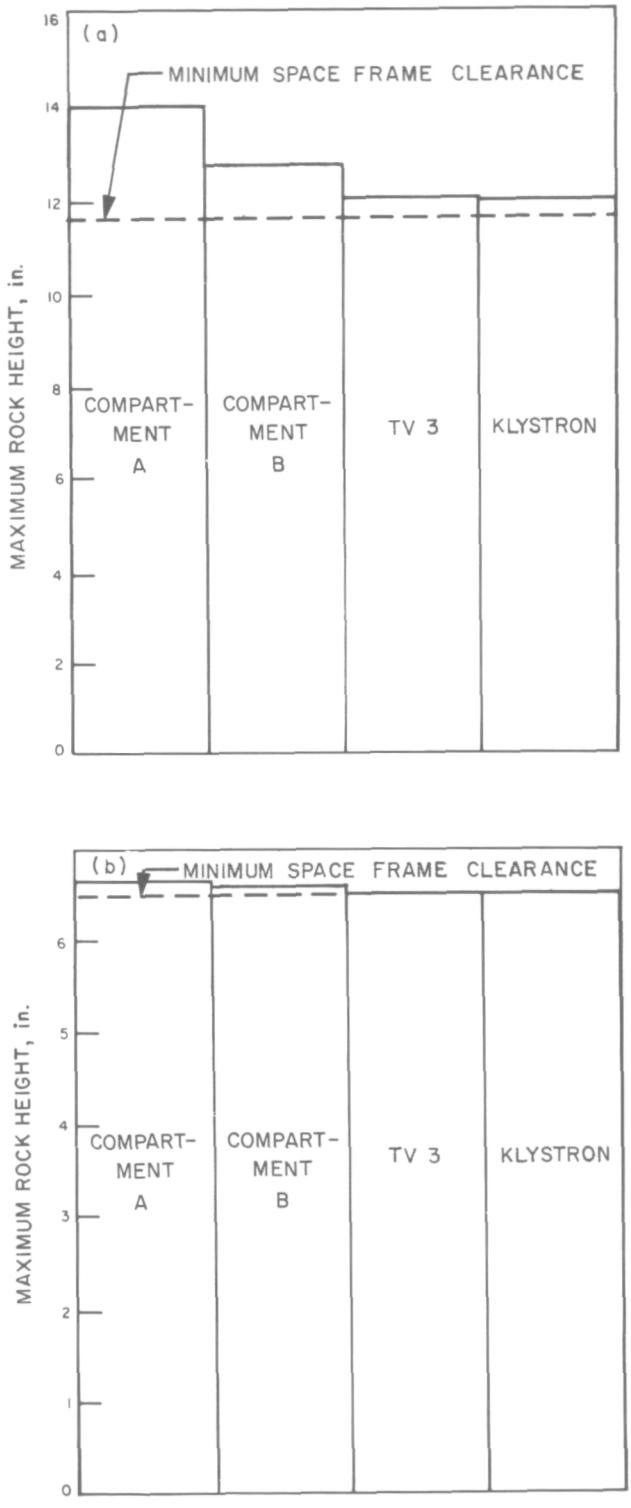

Fig. 11. Maximum rock heights for several spacecraft components: (a) normal landing, V_0 = 6.5 ft/s; (b) normal landing, V_0 = 12.75 ft/s

Very good correlation between simulated and flight strain gage data was obtained by considering horizontal touchdown velocities of 0.5, 2.5, and 3.0 ft/s, respectively, for landing events 1, 2, and 3. The value of 0.5 ft/s for event 1 is well within the flight control 3σ lateral velocity range of 1.5 ft/s; 3 ft/s for event 3 is consistent with TV observations of the distance to the footpad 2 imprints and the time between landing events 2 and 3, as indicated in the strain gage records. However, assuming the vehicle horizontal at the time of touchdown, it is not possible to produce a consistent set of impact velocities; therefore, the increases in horizontal velocity during events 1 and 2 must be due to horizontal components of vernier thrusts. It can be seen that the touchdown reactions alone cannot fully account for the increase in lateral velocity between events 1 and 3. Because of this, it is considered probable that the roll axis of *Surveyor III* was not aligned perfectly with the lunar vertical during its inertial hold. By holding the vehicle with a tilt in the downhill direction, the vehicle would pick up additional lateral velocity during its flight between landings. Using a tilt of 0.5 deg in the computer program gave lateral velocities that were very close to those that produced the best matchings with flight strain gage histories.

d. Dynamics tests.

S-9 test vehicle. The S-9 vehicle was used as a test fixture to support spacecraft hardware during a series of type approval vibration and drop tests. Although antenna solar panel positioner (A/SPP) part number (PN) 3035092 was the principal assembly tested on the S-9 vehicle, other SC-5 structures that were qualified included the following: thermal covers for compartments A and B; thermal compartment C; a JPL-furnished solar panel; alpha scattering sensor head deployment mechanism; TV auxiliary viewing mirrors; vernier engine bracket 1; and flight type A/SPP pin puller assemblies.

The vibration phase of the S-9 type approval test (TAT) program consisted of two B- and three C-level tests. The conditions for each test are presented in Table 4.

Test conditions for the three simulated lunar landing drop tests are given in Table 5. Following completion of each test, a limited functional test was performed on the A/SPP, and a visual inspection was made of all components being qualified. Drop tests 1 and 2 were completed without apparent structural damage or operational impairment of the A/SPP. After test 3, it was observed that both relock pins on the A/SPP solar arms had disengaged, causing the solar panel to shift downward. A complete functional check of the A/SPP revealed no additional damage to the performance of the unit. Optical measurements of the A/SPP also demonstrated that all posttest alignment values were within acceptable tolerances.

Lifting capability of soil mechanics/surface sampler. The soil mechanics/surface sampler (SM/SS) was incorporated on *Surveyors III* and *IV* to perform picking, digging, and trenching operations. The extension/retraction scissor mechanism (lazy tongs) is extended on the lunar surface by springs provided at the linkage joints (opening

Table 4. Vibration test conditions

Test level	Test	Axis of vibration	Sweep frequency range, Hz[a]	Sine level, g peak[b]	Random level, g rms
B	1	Lateral, normal to leg 2	5–15 15–50	0.88 1.05	None
B	2	Lateral, normal to leg 3	5–15	0.88	None
C	3A	Lateral, normal to leg 3	5–15 15–50 50–100	1.0 1.2 2.0	None
C	3B	Lateral, normal to leg 3	100–1500 1500–100	2.0 2.0	6.75 6.75
C	4A	Lateral, parallel to leg 3	5–15 15–50 50–100	1.0 1.2 2.0	None
C	4B	Lateral, parallel to leg 3	100–1500 1500–100	2.0 2.0	6.75 6.75
C	5A	Longitudinal, along roll axis	5–50 50–100	2.5 2.0	None
C	5B	Longitudinal, along roll axis	100–1500 1500–100	2.0 2.0	6.75 6.75

[a] All sweep rates are 1 octave/min.
[b] Double amplitude displacement is limited to 0.9 in.

Table 5. Simulated lunar landing test conditions

Test	Spacecraft orientation	A/SPP polar angle position, deg	Slope of surface, deg	Initial angle of spacecraft, deg	Drop height,[a] ft	Equivalent lunar longitudinal touchdown, ft/s
1	Leg 1, downhill	0	15	–3	5.04	15
2	Leg 1, downhill	36-1/2	15	0	5.04	20
3	Leg 3, downhill	36-1/2	15	0	5.04	20

[a] Drop height is the minimum vertical distance between the test article and surface prior to release.

up of torsional springs) and it is retracted by a motor-driven tape attached to the last link just above the shovel base. The operating envelope for the SM/SS is shown in Fig. 12.

The friction forces obtained from calibration tests of the *Surveyor III* prototype SM/SS mechanism were used as the starting point for the analysis of the operating limits.

The maximum operating limit of the SM/SS mechanism in a vertical plane corresponds to the condition when the weight of the alpha scattering sensor head is balanced by the spring force at the particular mechanism extension, and the friction forces acting in a direction opposing the extension. This shows that the SM/SS can operate adequately in its specified envelope.

A generalized diagram showing operating limits corresponding to a range of friction forces (from zero to the available extension force) is prepared to illustrate these limits for other levels of friction forces (Fig. 13). These data are summarized in Fig. 14 to define the upper limit for friction forces as a function of extension distance.

2. Mechanical

a. Antenna/solar panel positioner. The A/SPP provides mounting, positioning, position indicators, and launch and landing locks for the planar array antenna and solar panel. The antenna support structure includes controllable axes for roll, elevation, solar, and polar rotations. The drive for each axis uses a solenoid stepper motor for power and a wire-wound potentiometer for position indication.

Antenna solar panel positioner PN 3035092. All units of the PN 3035092 basic and PN 3035092-1 series have been delivered and apply to SC-5, -6, -7 and their spares requirements. The -1 configuration incorporates the improved potentiometer wiper-to-shaft attachment.

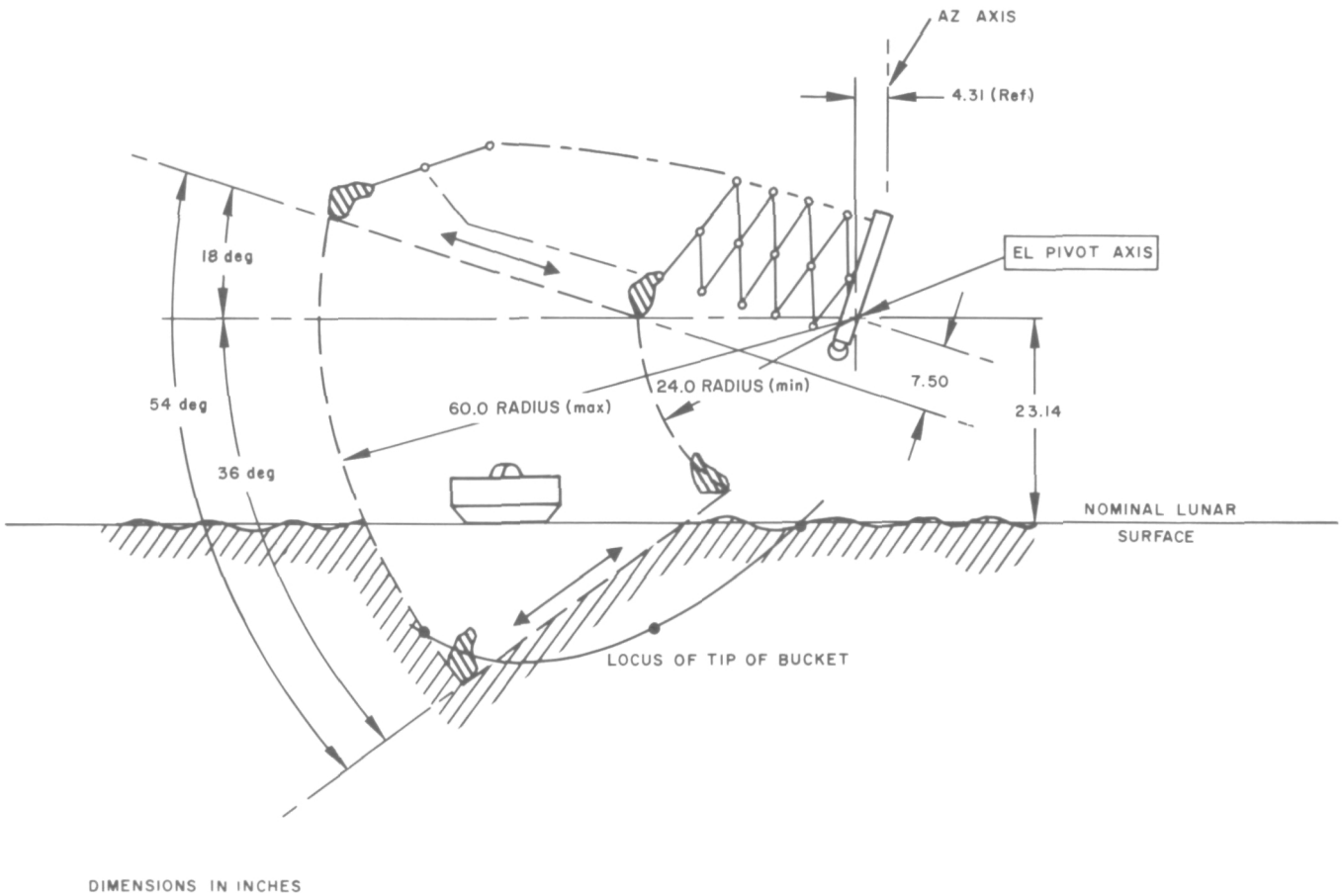

Fig. 12. Operating envelope of SM/SS bucket

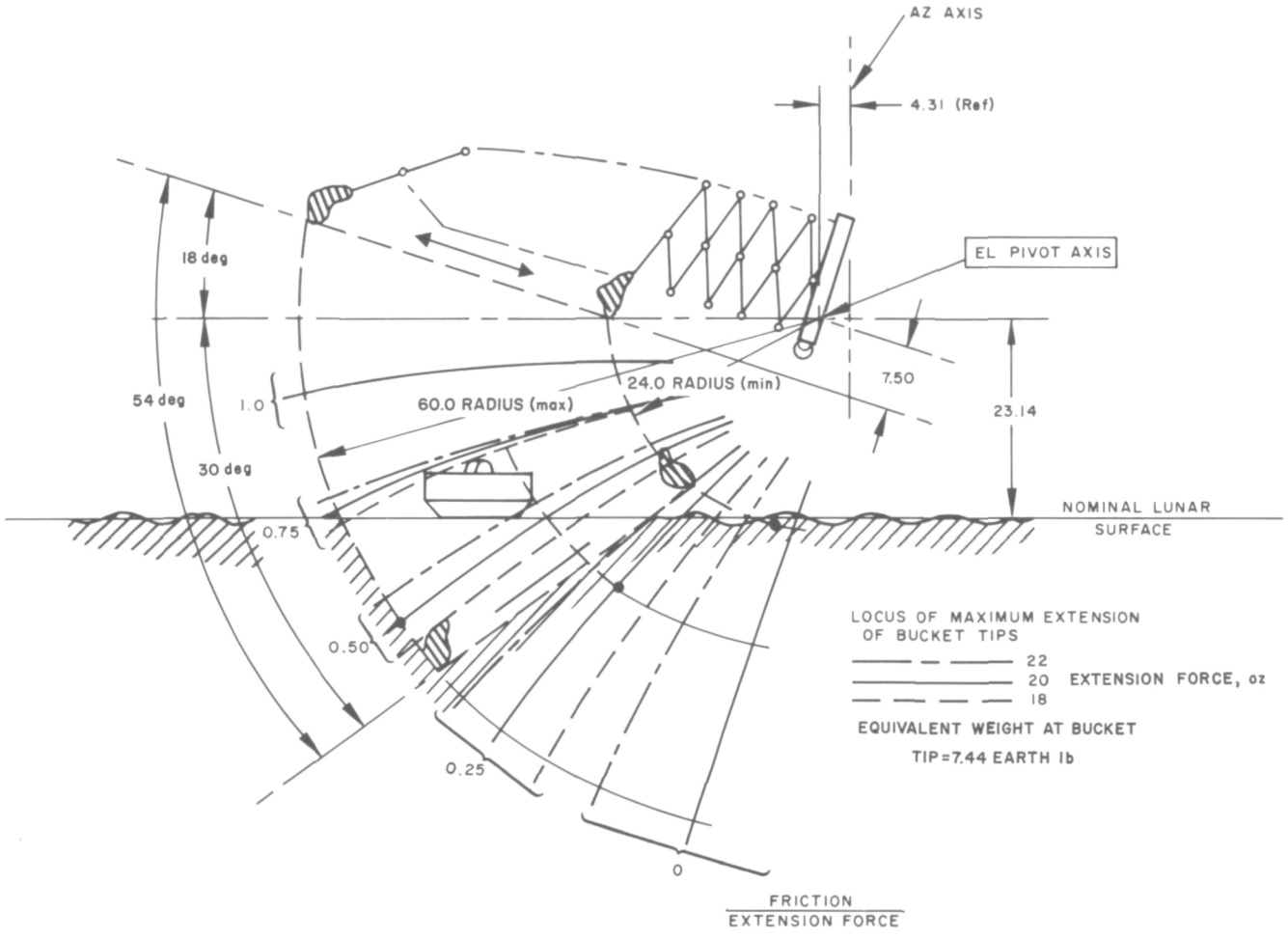

DIMENSIONS IN INCHES

Fig. 13. Effects of extension force F_0 and friction force on shape of maximum extension

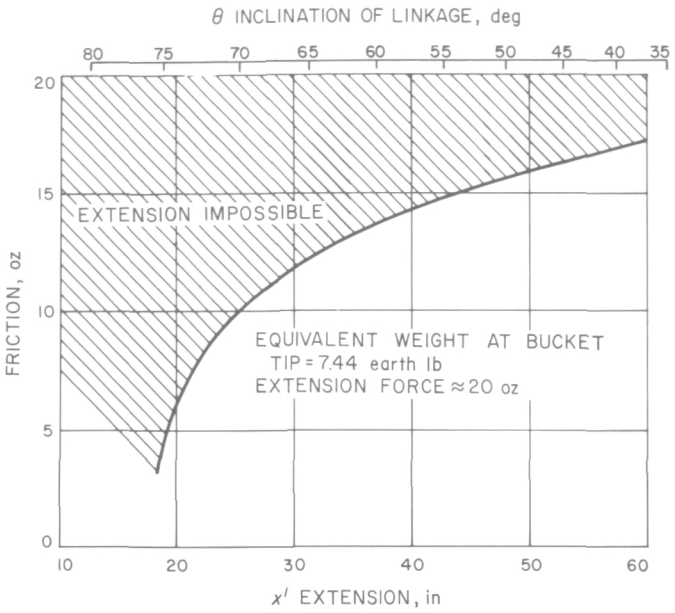

Fig. 14. Upper limit for friction vs extension distance

The PN 3035092, SN 2, unit is on SC-5 at AFETR; PN 3035092-1, SN 1 and 2, are on SC-6 and -7, respectively, and in systems test in El Segundo. The PN 3035092-1, SN 3 unit, a spare for SC-5 and subsequent spacecraft, is ready for shipment to AFETR.

The PN 3035092, SN 1, unit completed the type approval test program (Table 6). Except for the following problems, the unit passed all requirements:

(1) Solar landing lock module switch from connector 81P14, pins 1 and 2, indicated posttransit condition. The switch should have changed from closed to open while engaging the landing relock pin puller; however, the switch was open before and after, with cause unknown. The switch is being examined in the components laboratory.

(2) A shear wire was broken in an attempt to retract the elevation axis pin puller. This was contrary to the test procedure, which calls for removal of the complete pin puller assembly to prevent breakage. A new shear wire was installed and testing resumed.

(3) After the third drop, both solar axis landing locks were retracted enough to allow the solar panel to change position from transit at 270 deg to approximately 280 deg. With the pins retracted, the full load was transferred to the solar drive output shaft and mounting screws. The load was great enough to introduce a 1-deg, 55-min twist in the output shaft. During postenvironmental optical alignment, the pins retracted again when operating the solar drive in the positive direction against the transit locks. Investigation revealed that, in the course of TAT and associated repeated handling, sufficient lubricant had been transferred to and burnished into the taper holes to cause the overall coefficient of friction value to fall below the tangent of the half-taper angle.

(4) At the end of the second high-temperature operation under vacuum, the polar drive would not operate. Disassembly of the drive revealed that one of the pins holding the planetary gears in the transmission first stage had slipped out because of poor staking of the carrier.

(5) When disassembling the A/SPP for inspection after completed test, three of the solar drive mounting screws were missing. Continued disassembly of the A/SPP revealed that all six mounting screws for the roll drive were missing. However, the tight fit between the mast and the drive prevented dislocation of the drive in relation to the mast. Engineering will replace all drive mounting screws and

Table 6. Output torque capability of drives before and after TAT

Drive	Output torque drive production acceptance test			Output torque after TAT		
	Current, A[a]	Clockwise, in.-lb	Counterclockwise, in.-lb	Current, A[a]	Clockwise, in.-lb	Counterclockwise, in.-lb
Roll	9.8	456	451	10.3	340	290
Solar	9.8	450	465	10.3	360	425
Elevation	9.8	465	463	10.3	380	400
Polar	10.5	38	35	11.6	20.5	22.0

[a] These drives were tested before the TAT to the current limits in the left-hand column and tested after TAT to the current limits in the right-hand column. The before and after torques are not directly comparable.

secure them with lock wire; SC-5 has been reworked at AFETR, and SC-6 and -7, as well as the spare A/SPP, are being upgraded accordingly.

Two lock pin redesign approaches were instigated. In each case, the objective was to ensure that the prevailing friction coefficient was larger than the tangent of the pin half-taper angle. One approach involved an increase of friction (omitting drylube) without changing taper angle. The other retained present lubrication but involved a new taper angle (one-half of present) with associated rework of taper holes and fabrication of new pins.

Engineering was released to: (1) remove the lubrication from the taper pins and (2) for the taper change to implement the second approach. The thermal gradient test structure was upgraded for use in a load test to verify the unlubricated taper pin change. The required hardware and tooling changes were made to support both plans, and cold welding and friction coefficients were investigated. Data on cold welding parameters such as pressure, temperature, vacuum, time and materials were researched. The investigation into cold welding eliminated that possibility. Tests to determine the pin puller retraction capability and its margin under the most adverse conditions indicated a positive margin.

Coefficients of friction were determined for various configurations of base material, surface finishes and degrees of molybdenum disulfide contamination. Consideration of all this information gave equal confidence to each plan. The decision was made, however, to incorporate plan one, which required only removing the dry lubricant from the taper pin and cleaning and anodizing of the tapered hole.

Preparation of A/SPP TAT unit for the penalty drops. The twisted solar drive shaft was replaced with a new shaft. Roll and elevation drives were reworked to make it possible to install strain gages on the output shafts. In order to verify the capability of the new solar axis landing lock pin pullers a fourth drop was planned, using the exact flight configuration and the identical conditions attending the original failure. A fifth drop was also planned with a specific amount of MO_2 contaminant being introduced into the tapered holes. This test also was done with the same drop environment as the fourth drop. Both drop tests were performed with no indication of pin retraction.

b. High-torque stepper motor and transmission. Completion of the spare motors and drives has been delayed during this report period because of unacceptable finishes on parts, such as carburizing and dry lube; in some cases, parts have been refinished twice. This last drive (polar) is now being assembled.

H. Systems Analysis

1. Thrust Profiles for Vernier Engine Qualification Tests

A vernier engine test has been planned under 3σ type conditions (engine and propellant temperature, shutoff valve clearance, thrust command profile) to qualify the existing flight engines for subsequent spacecraft flights with regard to the shutoff problem. Test profiles designed to satisfy this objective are given in Fig. 15 and Table 7. Because the terminal descent conditions are variable, development of a limit (3σ) type thrust command profile for a vernier engine test is a compromise. Since it is not certain whether high or low thrust levels are more severe with respect to the shutdown problem, profiles A and B were developed for these conditions. The rationale for the thrust levels and duration of each phase of the profiles is described sequentially in the following paragraphs.

The preretrovernier phase is fixed in duration under control of the flight control programmer. The thrust level command is midthrust plus that required for moment control. Since the moment control requirements are expected to be small and the duration is short, midthrust was selected for both profiles.

The maximum duration of the retroengine phase is expected to be near 43 s, and this value was selected for the thrust profiles. Retroengine disturbance moments could require engine thrust levels near 100 or 30 lb; these levels were selected for the A and B profiles, respectively. For profile A, operation at 100 lb thrust for the total retroengine phase would result in a propellant usage for the total profile in excess of the capacity of the spacecraft tank pair associated with each engine. The loss in ability to operate near the maximum thrust level for the retroengine phase (to cancel out a large disturbance moment) was recognized as one of the tradeoffs when the selection was made to switch to the unmanifolded propellant feed system. Because of the natural shift in propellant center of gravity to reduce the disturbance moment during the period, the penalty is not as serious as would otherwise be indicated. Thus, a profile of declining thrust to the midthrust level was selected for this phase. Since propellant limitations were

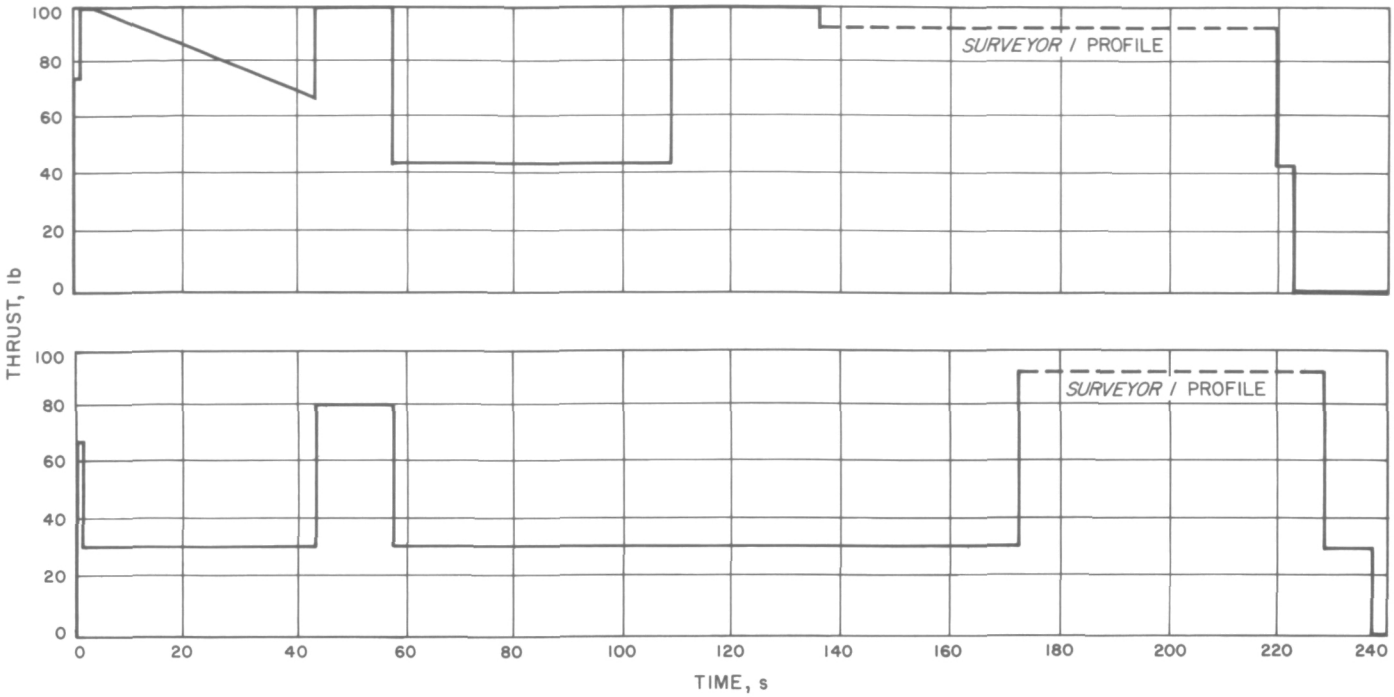

Fig. 15. Vernier engine test profiles

Table 7. Thrust profiles

Period	High burnout/high thrust 550 ft/s, zero midcourse			Low burnout/low thrust 280 ft/s, maximum midcourse			*Surveyor I*	
	Thrust level, lb	Duration, s	Impulse Δ/*Surveyor I*, lb-s	Thrust level, lb	Duration, s	Impulse Δ/*Surveyor I*, lb-s	Average thrust, lb	Duration, s
Preretro engine	67	1	1	67	1	1	66	1
Retro engine	100/67	43	885	50	43	−1416	66	41
Retro engine separation	100	14	112	80	14	−168	92	14
Minimum acceleration	44	51	1347	30	115	2553	39	23
Range velocity descent	100/SC-1	111	2700	SC-1	56	−2576	92	84
Constant velocity	44	3	−102	30	9	36	39	6
Total		223	4943		238	−1570		
Propellant required, lb		60			36			42

not applicable to the low thrust profile, a constant 30-lb level was used.

The retroengine separation interval is controlled by the flight control timer to 14 s. During this interval, the engines are commanded to a high thrust level by an open-loop thrust command. The combination of this command level uncertainty and moment disturbance requirements results in an engine thrust level between 80 and 100 lb. The extreme values were selected for the profiles for this period.

The duration of the intervals associated with the vernier descent period was based upon Monte Carlo computer simulation results for a 45-deg unbraked impact angle approach (Table 8). The length of each phase was established by a tradeoff between the phases in

Table 8. Terminal descent duration intervals

Condition	Minimum acceleration, s	Range/velocity descent, s	Constant velocity, s	Total vernier, s	Total terminal, s
High burnout velocity					
Nominal	39	85	6	130	188
99%	68	113	9	(190)[a]	(248)
99%				155	213
Low burnout velocity					
Nominal	58	52	6	116	174
99%	115	71	9	(195)	(253)
99%				176	234
July 4, 1967 profile	44	100	12	156	212
Surveyor I profile	23	84	6	113	169

[a] Values in parentheses are not 99% values.

which total time and propellant requirements were constraints, and emphasis was placed on high thrust time or low thrust time for profiles A and B, respectively. The limits on thrust level for the minimum acceleration and constant velocity phases are 30 and 44 lb. Thus, these limits were used for these phases. The thrust command for the range/velocity descent phase was derived from *Surveyor I* telemetry data. Since this phase for *Surveyor I* was shorter than that desired for profile A, the thrust command for the remainder of the period was selected as 100 lb to simulate a saturated acceleration command, which is normal when the descent contour is acquired in the upper region of a descent segment.

The impulse required in excess of the *Surveyor I* descent was determined to provide recommended test profiles, realistic in terms of propellant requirements. Assuming a specific impulse of 280 s for this excess, the propellant required for each profile is given in Table 7.

2. TV Viewability of Footpad Depressions and Soil Mechanics Surface Sampler Area After Liftoff and Translation

The purpose of this study is to evaluate TV viewability of footpad depressions and the surface sampler scoop area for selected short hop translations and also to support real-time evaluation. The TV viewability evaluation is concerned only with actual physical obstruction of view and does not include sun angle or other factors.

The direction of liftoff and translation which offers TV visibility of both footpad-2 and -3 depressions and placement of footpad-2 depressions within reach of the soil mechanics surface sampler (SM/SS) for analysis is approximately 305 deg clockwise from the $+Y$-axis. This hop direction also ensures that the spacecraft will not land in or pass over a previous SM/SS analysis area that may be unsatisfactory for a footpad landing site. The optimum translation directions for each distance analyzed are:

Hop distance, in.	Translation direction (clockwise from $+Y$-axis), deg
6	330
12	315
18	300 to 315
24	300 to 310
30	300 to 310
36	300 to 310
42	300 to 315
48	300 to 315

These selected hop directions provide maximum visibility of footpad-2 and -3 depressions, maximum access to footpad-2 depression with the surface sampler, and assurance that the spacecraft will not pass over or land on a previously disturbed SM/SS area. In general, the depression of footpad-2 provides better viewability than the depression of footpad-3. The 18-in. and greater translation distances offered a wider choice of hop directions in terms of footpad depression visibility. A 6-in. hop will never expose a full footpad depression and provides a minimum choice of translation directions.

Tables 9 and 10 represent a review of the compiled information regarding TV viewability and SM/SS considerations. Table 9 lists the optimum translation direction for each distance analyzed based on a combined

Table 9. Best individual translation direction for each distance

Translation		Footpad 2			Footpad 3
		Depression		Percent footpad in previous SM/SS area	Percent visibility of depression
Distance, in.	Direction, deg azimuth	Percent visible	Percent access by SM/SS		
6	330	57	90	0	48
12	315	100	100	0	90
18	300–315	100	100	0	100
24	300–310	100	100	0	100
30	300–310	100	100	0	100
36	300–310	100	100	0	100
42	300–315	100	100	0	100
48	300–315	100	100	0	100

Table 10. Visibility and SM/SS evaluation

Hop distance, in.	Maximum depression visibility			SM/SS scoop sector analysis	
	Azimuth,[a] deg	Percent of footpad 2	Percent of footpad 3	Safest direction (not land in old sector), deg	Maximum access to depression by SM/SS, deg
6	330 ± 2	57	48	345 ± 37	345 ± 22
12	315 ± 2	100	90	352 ± 75	352 ± 60
18	307 ± 7	100	100	345 ± 75	322 ± 45
24	7 ± 7	100	100	322 ± 100	322 ± 30
30	30 ± 30	100	100	322 ± 130	315 ± 22
36	30 ± 30	100	100	322 ± 130	315 ± 22
42	30 ± 30	100	100	315 ± 140	315 ± 22
48	30 ± 30	100	100	307 ± 150	308 ± 15

[a] All azimuths are measured clockwise from the +Y-axis.

evaluation of both maximum visibility of footpad depressions and SM/SS considerations. Table 10 presents a separate evaluation of maximum footpad depression visibility and the most valuable SM/SS considerations, with the appropriate translation direction for each. Table 10 should be of benefit if the optimum translation direction of Table 9 is not satisfactory and a tradeoff between TV viewability and the SM/SS is required.

The *Surveyor III* TV viewability layout of Fig. 16 provided the basis for the viewability study. All tables and figures were derived from it. The layout was assembled from available information, *Surveyor I* TV photographs, and graphical projections on scale drawings of the spacecraft. Figure 16 represents that area on the lunar surface which cannot be seen by TV survey camera 3 because of physical spacecraft obstructions. The lunar surface was assumed to be parallel to and approximately 18 in. from the spacecraft's *X-Y* plane. The visibility of Fig. 16 is an approximation and is not intended to be exact. The layout does not show areas of visibility between the spacecraft frame members unless they are of a large unobstructed sector.

3. Effect of Altitude Marking Radar/Spacecraft Alignment on the *Surveyor III* Mission

The midcourse capability required for the *Surveyor III* mission, assuming existing estimates of booster performance, was less than 30 m/s (3σ). Any known altitude

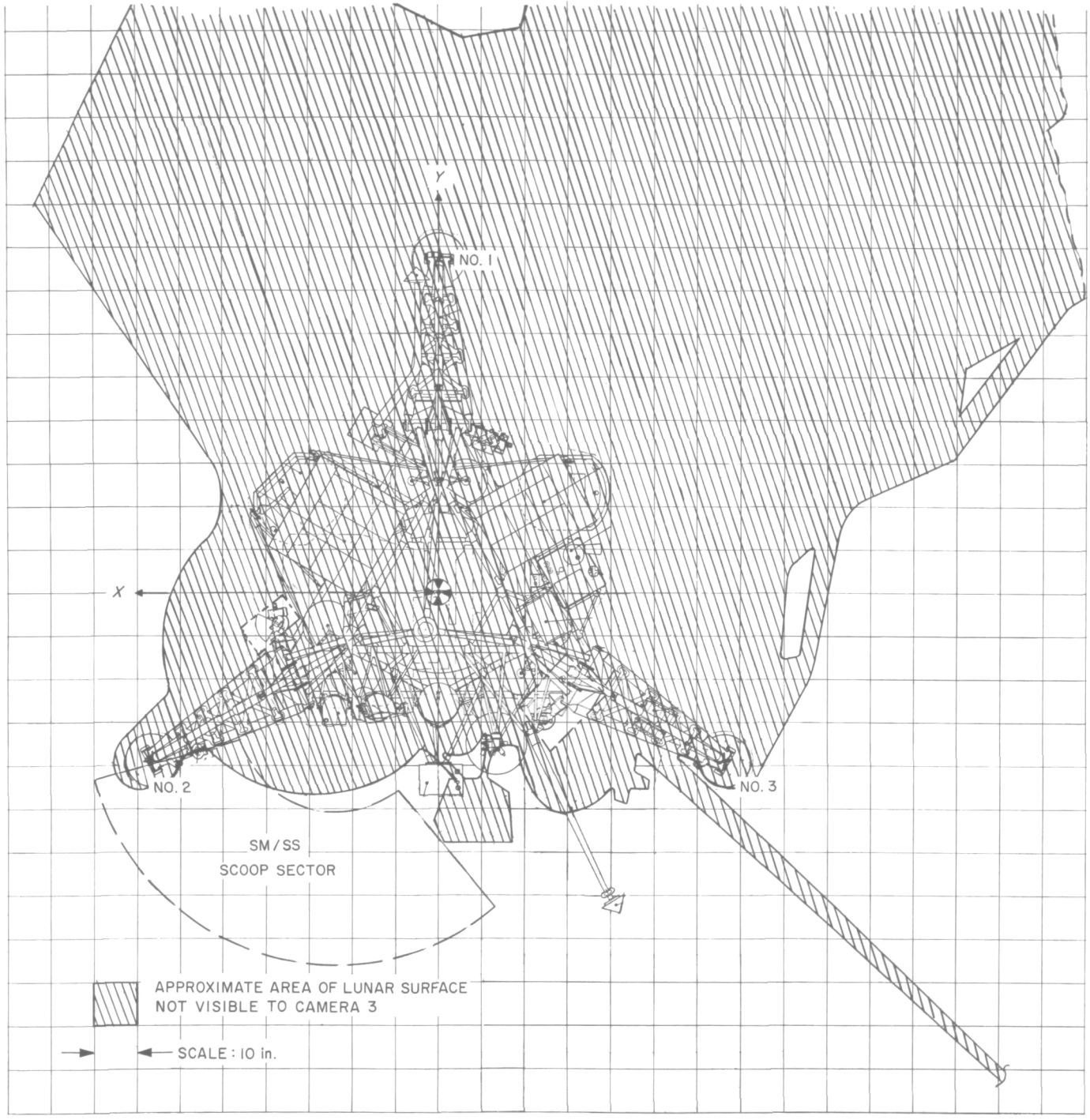

Fig. 16. Lunar surface visibility from TV camera 3

marking radar (AMR) beam-to-spacecraft axis misalignment was compensated during flight by adjustment of the time delay between the AMR mark and retroengine ignition. Misalignment uncertainties less than 1 deg were acceptable for the first 2 days when the flight path angle γ was 40 deg, since the resulting midcourse capability was greater than 30 m/s and larger uncertainties could have been tolerated for smaller flight path angles (γ = 25 deg). The error in burnout altitude resulting from AMR misalignment in the trajectory plane is given in Fig. 17 for different flight path angles γ.

The degradation in *Surveyor III* performance due to AMR beam axis misalignment was studied before the launch under three possible conditions. Case 1 assumed no modification of the present terminal descent design to provide additional margin for AMR misalignment. Considering the AMR misalignment as a bias on the nominal burnout altitude, the effect on the mission depends upon the direction of the misalignment. If the AMR beam angle γ_A is greater than the flight path angle γ (including

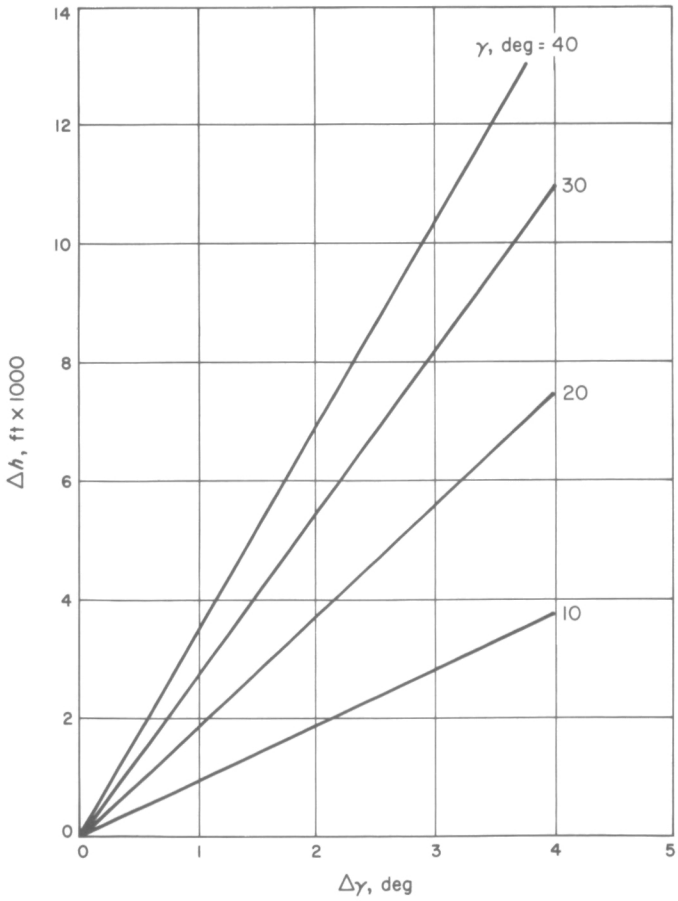

Fig. 17. Altitude error vs misalignment error of the AMR

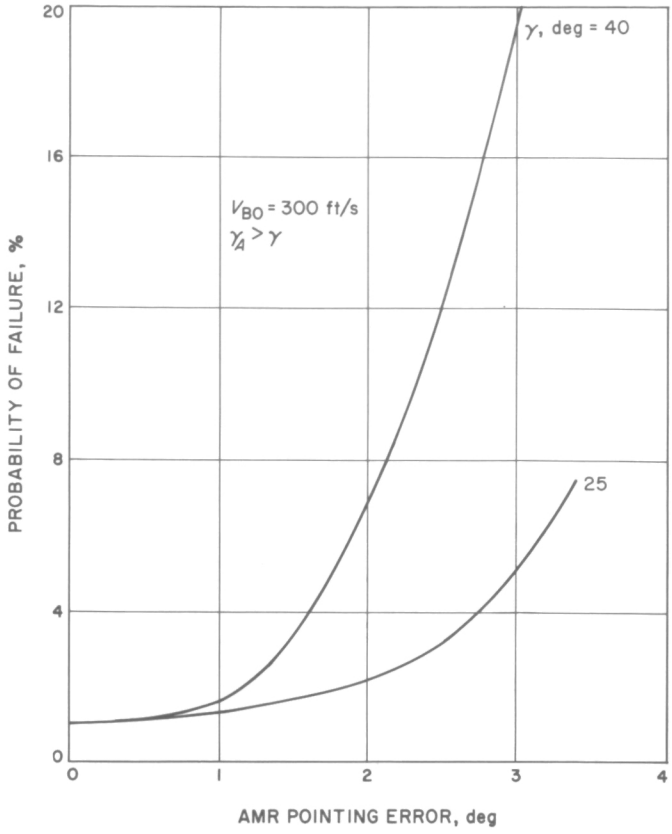

Fig. 18. Vernier acquisition descent

burnout direction bias angle), the nominal burnout altitude is lowered and the probability of failing to acquire the vernier descent contour increases from the design value (Fig. 18). For a 1-deg AMR pointing error, the probability of failure is approximately 2% for γ = 40 deg. If γ_A exists, the probability of not having sufficient vernier propellant to soft land increases, as indicated in Fig. 19. A 1-deg AMR pointing error produces a corresponding probability of failure of approximately 4% for γ = 40 deg. The probability of failure does not exceed 1% for $\alpha < 1.4$ deg under the α = 25 deg condition since a 4-lb propellant excess is predicted to exist for this condition.

In the second case considered, it was assumed that any known significant misalignment of the AMR would be compensated during the mission by adjusting the time delay between the AMR mark signal and the retro engine ignition command to achieve the desired nominal burnout altitude. If the nominal burnout altitude were increased above the design value to provide for large AMR alignment uncertainties, the maximum midcourse capability would be reduced, as indicated in Fig. 20. A 1-deg (3σ) uncertainty in AMR alignment would reduce this capability to 38 m/s for γ = 40 deg. The propellant excess

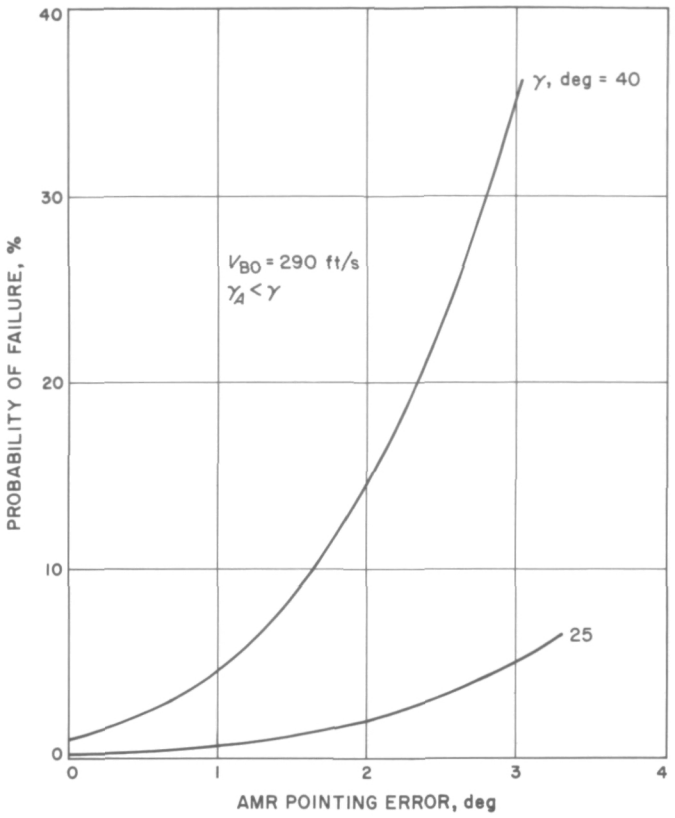

Fig. 19. Sufficient vernier propellant

for the $\gamma = 25$ deg condition prevents any loss in midcourse capability for uncertainties less than 2.4 deg. This case was considered to be the most appropriate for evaluating the effects of AMR misalignment on the *Surveyor III* mission.

The final case analyzed assumed a conservative protection against an unknown AMR misalignment by increasing the nominal burnout altitude by the altitude equivalent of the estimated AMR misalignment and assuming that the estimated misalignment could either increase or decrease the burnout altitude as a bias. The effect on midcourse capability is indicated in Fig. 20. The maximum midcourse capability for a 1-deg bias is 29 m/s for $\gamma = 40$ deg. For $\gamma = 25$ deg, the midcourse capability is not reduced for bias angles less than 0.7 deg.

4. Trajectory Studies: Focusing Factor and Errors in B-Space

Analysis has yielded an accurate method of focusing a dispersion ellipse in B-space to one on the lunar surface. The focusing factor may only be accurately applied to perturbations in the trajectory plane. The focusing presently incorporated in the midcourse and terminal guidance (MTGS) program does not include the effect of perturbations in impact velocity; yet a Monte Carlo technique has shown that, in some cases, they must be taken into account. The method developed includes both the perturbations out of the trajectory plane and the perturbations in the impact velocity. This more accurate method of focusing will be included in the MTGS prior to mission E.

The uncertainties in B-space, as a result of various midcourse corrections applied at various times, and the 99% circular miss dispersion on the lunar surface, as a function of U_3 for various critical plane corrections, have been determined.

5. Sun Trace in Spacecraft Coordinates During Parking Orbit

To assist the study of the temperature variation experienced with each of the vernier engines during the *Surveyor III* parking orbit, *Centaur* roll rates were obtained; and the path of the sun in spacecraft coordinates was determined.

The spacecraft orientation is assumed known at the first *Centaur* main engine cutoff (MECO1) with the −Y-axis pointing towards earth and the −Z-axis pointing in the direction of the inertial velocity vector. Roll rates during the parking orbit were −0.24 deg/s for approximately 100 s and −0.17 deg/s for the remainder of the time until the second *Centaur* main engine ignition (MES 2). Concurrently, the spacecraft Z-axis is maintained perpendicular to earth center to spacecraft vector. The rate of Z-axis movement is coincident with the orbital rate, which is approximately 90 min/360 deg.

The sun's path for future missions has also been determined, to facilitate temperature predictions. However, it is not possible to predict *Centaur* roll rates, and thus Fig. 21 is only intended to bound the spacecraft Z-axis to sun angle for missions E, F, and G. The angle is shown plotted against time in parking orbit. Zero time is parking orbit injection or about 9.8 min after launch. Representative days are shown using launch window openings (solid lines) and launch window closings (dashed lines). The termination of each line represents the approximate time of *Centaur* second ignition. An asterisk on a curve represents earth shadow exit. That is, to the left of this point, the spacecraft is in the earth's shadow.

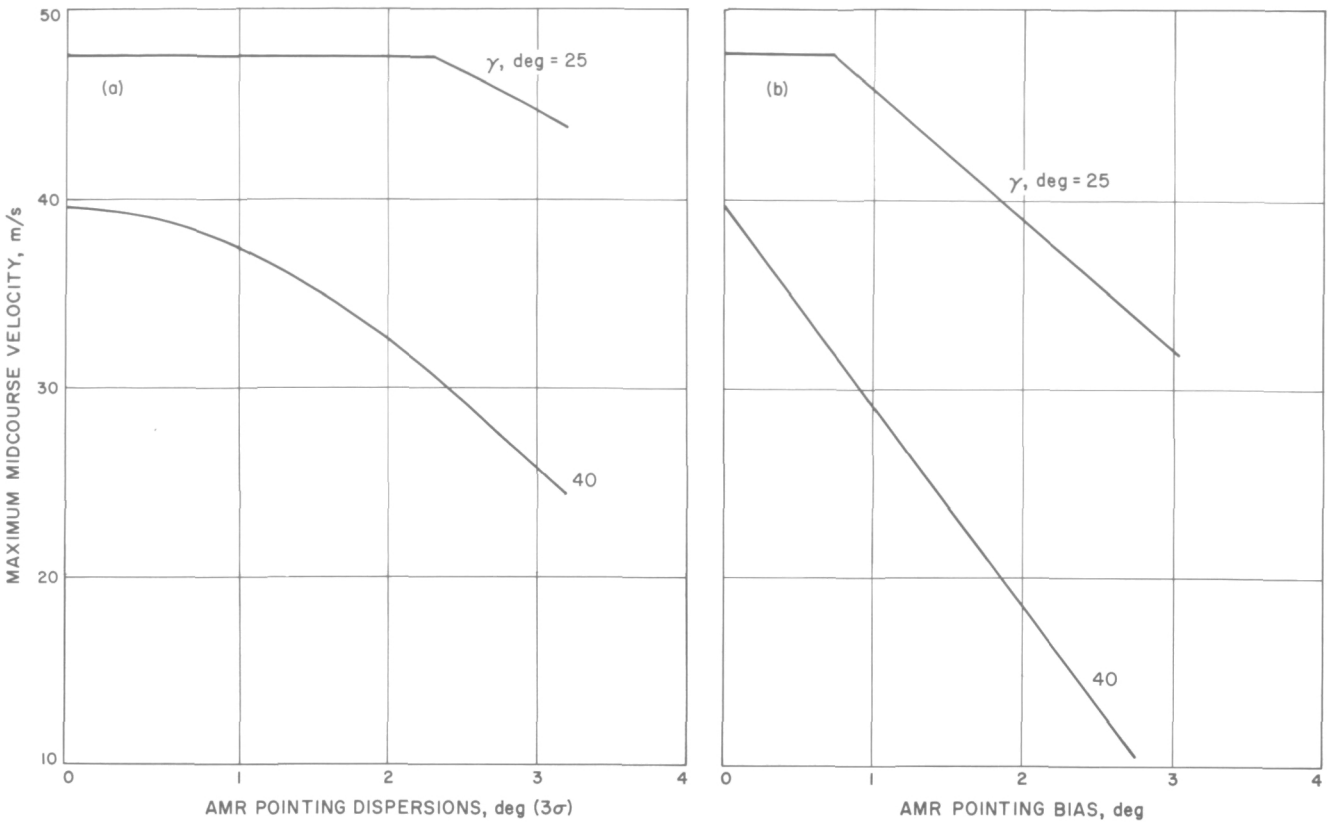

Fig. 20. Effect of AMR misalignment on *Surveyor*: (a) second case: time delay adjusted; (b) third case: burnout altitude compensation

6. Selected Midcourse and Touchdown Parking Orbit Guidance Data for September 1967 Trajectories

The figure-of-merit program (lunar miss) has been executed using six covariance matrices, which describe the injection statistics of six standard parking orbit trajectories, all in September 1967. These matrices include *Centaur* guidance platforms with Honeywell 177 accelerometers.

The 3σ semimajor axes of the miss ellipses range in length from 1157 to 2415 km; 3σ unbraked impact velocity error varies from 5.76 m/s to 7.77 m/s; and 3σ time-of-flight error ranges from 26.19 to 37.92 min — all evaluated for uncorrected miss. The sensitivities of terminal parameters to a velocity change at midcourse are given for six trajectories for midcourse time of 15 h. The 1σ velocities necessary to correct miss only, miss and velocity, and miss plus time of flight are included, along with the associated errors in time of flight and impact velocity.

7. October Eclipse of Moon

Should SC-5 survive the lunar night, or should the launch slip to October, the landed spacecraft would spend 2 h and 20 min in the umbra or complete shadow. Table 11 gives the eclipse particulars.

Table 11. October lunar eclipse data

Condition	Day	GMT, h	Minute
Moon enters penumbra	18	07	09.8
Moon enters umbra	18	08	24.4
Total eclipse begins	18	09	44.8
Middle of eclipse	18	10	15.2
Total eclipse ends	18	10	45.5
Moon leaves umbra	18	12	04.9
Moon leaves penumbra	18	13	20.5

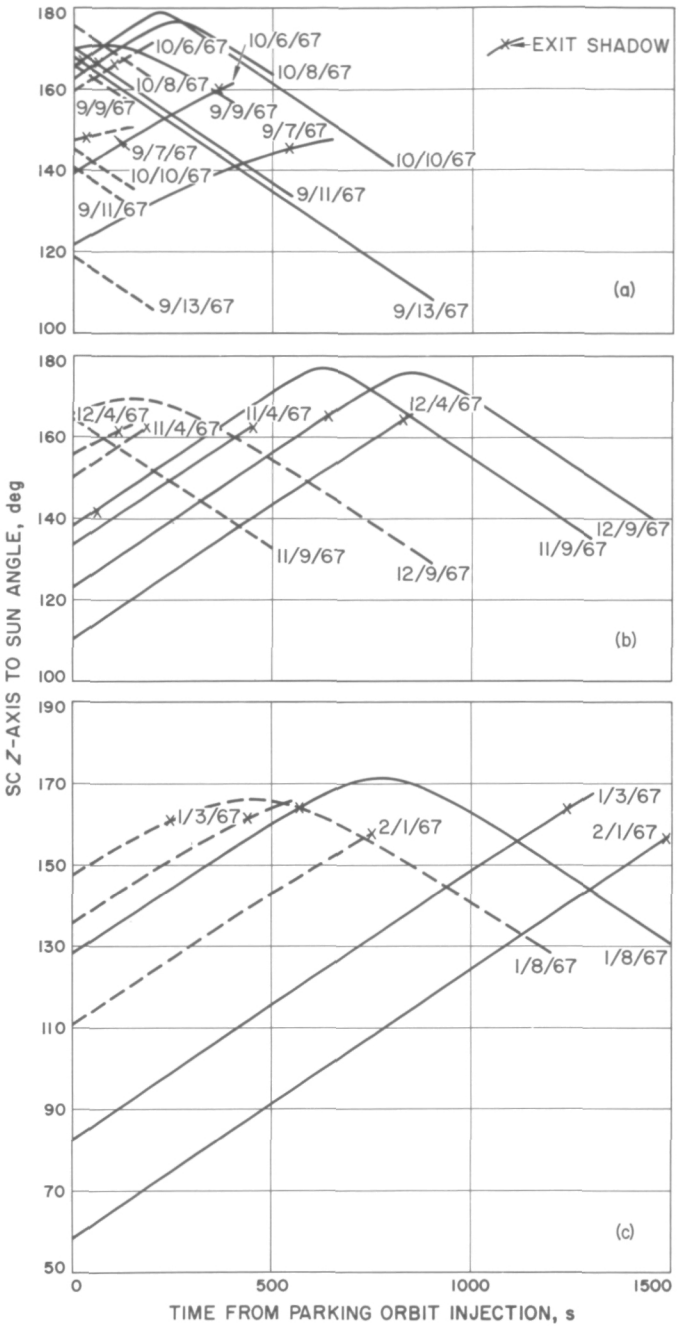

Fig. 21. Sun orientation: (a) mission E; (b) mission F; and (c) mission G

8. *Surveyor* Thrust Vector Pointing Error for Midcourse Maneuver

This subsection presents the general computation method and the significant results of the Monte Carlo computer simulation that calculates the pointing error between the vernier engine thrust vector and the spacecraft velocity vector for the midcourse maneuver.

Compensation for the nominal midcourse thrust axis misalignment error due to prelaunch alignment offsets and support bracket bending reduces the 99% pointing error between 0.1 and 0.2 deg.

Parametric studies of the effect upon the pointing accuracy of different premidcourse attitude maneuvers show that the 99% pointing error for the compensated case under *Surveyor III* weight and alignment conditions varies between 0.60 and 0.80 deg, depending upon the attitude maneuver sequence.

The numerical values are, in general, the specification values. The vernier engine support bracket bending spring constants are taken from static test data.

The mean gyro drift rates are zero in this study with the 1 deg/h allowance taken versus the 3σ dispersion. The program has the capability of employing inflight measured means and dispersions of the gyro drift rates. Therefore, real-time flight analysis of the effect of compensating for the mean gyro drift rates can be made with this computer simulation.

For the *Surveyor III* cases studied, the nominal earth alignment angles of the vernier engines were employed. The *Surveyor I* and *Surveyor II* cases used the actual measured angles. Uncertainty in an alignment angle was taken to be the total specification tolerance. Thus, the results are slightly conservative in that the measurement uncertainties of the actual prelaunch earth alignment angles are smaller than the values assumed.

I. Systems Engineering

1. Lunar Night Survival Study Report

A lunar night survival study was initiated and has been completed during this report period to determine lunar night survivability improvements for *Surveyor* spacecraft.

This report includes the effects on survivability by introducing radio isotope heaters into the compartments, reduction of compartments thermal losses, and power system modifications. Low temperature performance of the power subsystem, telecommunication subsystem, television subsystem, related control items, components materials, and processes were considered. Failure mode effects of equipment not used after touchdown and their interfaces with the command decoding and signal processing subsystems were also considered.

The result of this study indicated that the addition of radio isotope heaters to compartments A and B offers the only significant practical improvement in night survivability. Although system compatibility cannot be assured until system tests are completed, a request for authorization to procure isotope heaters for possible incorporation into SC-7 was initiated. Immediate procurement would allow such heaters to be installed on SC-7 for solar thermal vacuum system test.

The addition of isotope heaters into SC-5 and -6 was not recommended since isotope delivery dates did not allow sufficient system verification tests prior to flight. Operational sequence changes only, in the same general manner as recommended for *Surveyor IV*, were recommended for SC-5 and -6. Other spacecraft modifications considered do not significantly improve survivability.

The probability of survival without the addition of radio isotopes in the compartment could not be determined accurately. It is believed that the spacecraft has a reasonable chance of surviving. However, not enough is known about the very low temperature performance of the spacecraft design and variations of components and production techniques from spacecraft to spacecraft to make a specific statement of probability of survival. Weak points cannot be positively identified and fixes proposed. In order to determine survival capability, 100% cryogenic testing of spacecraft control items is required. This test program would severely impact current schedules and therefore was not recommended.

A detailed discussion of the lunar night survival problem is contained in Ref. 1.

2. Television Subsystem Developments

At NASA/JPL direction, the television survey camera will be modified to provide vidicon tubes capable of surviving the lunar night. The plan, which has been implemented, is basically as follows: Install the SP-1 camera on SC-5; replace the vidicon tubes in the SC-6 and -7 cameras with tubes removed from the approach cameras. At this time, the SP-1 camera has been installed on SC-5, and PVT-4 television calibration has been completed. A vidicon has been installed in the SP-2 camera for installation on SC-7. Some problems have been encountered and are currently being evaluated to determine their effects.

The vidicon changeout provided the feasibility of modifying the gain in the SC-6 and -7 cameras to eliminate the over-deviation problem experienced on *Surveyor IV* and subsequent television cameras. This change will be implemented only in SC-6 and -7. The over-deviation will be adjusted for by offsetting signals in ground equipment filters for SC-5. This has proven to be satisfactory, as found in tests run at the Deep Space Network.

An analysis was accomplished to evaluate the effects, in terms of interference with television and capability of resolution of particles on the magnet at various light angles, of placing a magnet on footpad 2. The analysis concluded there would be no interference, with the footpad stowed, on TV for magnets of the configuration being considered for use at levels less than about 2000 G. The presence of particles greater than 0.02 in. can be discerned. To determine particle configuration, the sizes would have to be greater than 0.1 in. The first tests to determine camera interference were run with a magnet of about 80 G placed at various intervals from 8½ in. to adjacent to the camera. No effect in the video picture was discerned. Additional tests will be run with magnets as high as 750 G, since it is currently planned to use magnets of this level.

3. *Surveyor IV* Terminal Descent Malfunction Evaluation

At 11:52:29.215 GMT (4:52:29.215 PDT) on Friday, July 14, *Surveyor IV* was launched from pad 36B at the Air Force Eastern Test Range. The launch was nearly perfect, with the spacecraft being injected into its translunar trajectory by the single-burn *Centaur* at 12:04:57 GMT. All subsequent spacecraft operations, including separation, sun and star acquisition, midcourse correction, coast, and preterminal descent maneuvers, were performed in a textbook manner with no significant anomalies until the sudden loss of signal from the spacecraft near the end of the retroengine burn period. Contact with the spacecraft was never regained subsequent to this signal loss, even though all conceivable nonstandard procedures were attempted.

Immediately after failure of the *Surveyor IV* mission, a detailed data review and analysis was started to analyze all spacecraft data and to identify the failure mechanism, or potential failure mechanisms, that caused the failure. A preliminary report has been prepared, but no definite cause for the failure has yet been established. A final report is being published during this period.

Failure modes that have been considered include the following:

(1) Possible explosion of the retromotor, fuel tanks, and/or shock absorbers.

(2) Possible structural failure of key structural elements resulting in subsequent disintegration of the spacecraft.

(3) Possible harness failure in a critical area.

(4) Possible unit failures.

J. Propulsion

1. Main Retroengine

a. Surveyor IV. Following loss of transmission from *Surveyor IV* on July 16, 1967 a propulsion subcommittee was formed to review the propulsion system as a possible spacecraft failure mode. The subcommittee was composed of JPL, HAC, and Thiokol Chemical Corporation (TCC) senior propulsion personnel. All pertinent flight data were thoroughly reviewed. The history of engine A22-9, as well as the design and test history of the retroengine program, were examined. All trouble and failure reports and material review board actions were reviewed, and a failure analysis was conducted. The investigation concluded that no data could be found to support the possibility of a retroengine failure and that the probability of a retroengine failure based on the failure analysis and history of the engine is very low.

b. SC-5. The flight engine for SC-5 is A21-28. X-ray and safe and arm (S&A) checkout of A21-28 was completed July 27. The X-rays were satisfactory, but the S&A did not pass the pin retention test. When the replacement S&A also failed this test, the unit from A22-12, the *Surveyor IV* spare, was substituted successfully.

The SC-5 spare engine, A21-29, was shipped from TCC July 5, 1967 with flight preparations completed July 24. A small dent was detected on one of the three skirts. Visual inspection and dye penetrant tests were employed to inspect for damage. Stress analysis personnel at TCC and HAC reported the dent condition to be acceptable.

c. SC-6. The flight engine for SC-6 is A21-29. The S&A check will be repeated prior to flight. An anomaly in the SC-6 spare engine, A22-11, is currently under investigation. AFETR ambient X-ray revealed a small bulge in the insulation boot. The boot was touching the case wall insulation, and the area between the boot bulge and propellant was questionable. Thus, the engine was shipped to Thiokol, where it was determined that the boot and wall insulation were not attached. The engine was then shipped to Allegany Ballistic Laboratory, where additional X-rays of the engine conditioned to 20°F were taken. These X-rays confirmed that the boot was free of the wall insulation, having pulled away at 20°F. However, a questionable area was detected in the liner near the equator. This condition will require more investigation.

Three additional engines, including the reject engine, A22-5, and two of the three remaining A21 qualification engines, will be subjected to ambient and low-temperature X-ray to develop a wider base for X-ray analysis. Assuming that several engines reveal conditions similar to A22-11, one will be dissected to determine what was shown in the X-ray. If this investigation results in the rejection of A22-11, then A22-12 will serve as the SC-6 spare.

d. SC-7. Engine A22-12 is planned for use as the SC-7 flight engine.

2. Vernier Propulsion System

a. System analysis.

Consent documentation. Unit consent-to-ship actions were held on four thrust chamber assemblies. All other vernier propulsion system hardware has been accepted at the unit level for all spacecraft except for thrust chamber assemblies for SC-7 and two spares and five of the SP-3 spare propellant tanks.

Postmission analysis. The propulsion input to the *Surveyor III* postmission analysis report was completed and submitted for publication. *Surveyor IV* failure was investigated, and a postmission analysis report is in preparation.

b. Spacecraft servicing, El Segundo.

SC-5. Following vibration testing, the propulsion system was deserviced and prepared for vernier engine vibration (VEV).

After VEV, the propulsion system was prepared for shipment by installing the vernier propulsion system (VPS) manifold pressurization assembly and pressurizing the helium tank to shipping pressure. The system was leak tested at combined system test prior to shipment to Air Force Eastern Test Range (AFETR).

SC-6. The SC-6 propulsion system was deserviced following vibration testing and prepared for VEV and shipment.

SC-7. The leg-2 fuel tank was installed on the spacecraft. The tank previously on leg-2 was removed and used to replace a tank on SC-5.

c. Spacecraft servicing, **AFETR.** *Surveyor IV* successfully completed all system testing at AFETR, and propellant loading was completed June 23, 1967. Load was within 0.04 lb for fuel and 0.10 lb for oxidizer. Following loading, a postpropellant bladder leak test was performed which demonstrated the integrity of the propellant bladders.

Following propellant loading, the injector area was continuously sampled for leakage and vacuum purged. An alternate plan to provide injector protection by dry nitrogen purging the shroud following nozzle plug removal was developed for use in the event of a launch hold after nozzle plug removal. Such a hold did not materialize.

The VPS was continuously sampled with the toxic gas detector for leakage following propellant loading. No sensible leakage was detected on *Surveyor IV*.

SC-5, during the report period, was received at AFETR, and has progressed satisfactorily into the prelaunch testing. A leaking oxidizer check valve detected during the VPS functional test was replaced when it failed to clear itself after extensive gas purging. The leg-1 fuel tank bladder, found to have helium leakage slightly in excess of the specification value of 72 cm^3/h, was replaced. The propulsion system has otherwise performed satisfactorily.

d. Propellant tanks. During this period, research was directed towards gathering test data on the bladder leak test after propellant loading using ullages of 5% for oxidizer and 2% for fuel. For the oxidizer testing, a set of three good bladders was tested, as well as a set wherein the leg-2 bladder had a 2100-cm^3/h leak. The tanks were loaded to 5% ullage, then vacuum purged on the gas side for 1 h; cold trap samples were taken. The low-leakage bladders gave a total of 0.6 g of NO_2 in the five samples, compared with 2 g of NO_2 in five samples for the high-leak rate bladder. For fuel testing, a set of three good bladders and a set wherein the leg-2 bladder had a leak rate of 2500 cm^3/h were tested. The tanks were loaded to a 2% ullage; then a 10-h soak period was allowed to simulate AFETR off-load time before the samples were taken. Fuel results were not as obvious as were oxidizer results. The set of bladders exhibiting low helium leakage initially indicated about 0.3-mg MMH for each sample, and only traces during a repeat test. The set which included the bladder showing 2500 cm^3/h gave between 0.6 and 1.4 mg per sample for two tests, and increased during a repeat test to 4 mg per sample. Test results indicated that the low-leak rate bladders could be distinguished from the high-leak rate bladders.

These tests were successfully carried out on *Surveyor IV* after propellant loading. Both the fuel and oxidizer systems gave results indicative of good bladders.

Analysis has continued on the bladder which failed on SC-5 during solar thermal vacuum testing. The bladder was returned to the vendor and subjected to materials property tests, fit check, and microtome photo analysis. The bladder was found to be undersize, thus supporting the tensile failure mode theory. A definite cause for the shrinkage cannot be assigned. However, possible causes are high heat gun temperatures at installation, and heating due to inadvertent and prolonged tank heater operation with the tank empty. An added factor may be improper installation of the bladder introducing a fold or a twist which effects a reduction in dimension.

e. Check and relief valves. Four check and relief valves have been through an extended type approval test program to determine their performance at temperatures up to 170°F.

The purpose of these tests was to demonstrate that the valves would perform above the crack-flow and reseat type approval test temperature 125°F after extended exposure to propellant-saturated helium at the higher temperatures of 150 and 170°F. Two valves which had been removed from SC-5 and two new valves which had been subjected to flight acceptance testing were exposed to propellant saturated helium for 14 days, vibrated in one axis at flight acceptance test vibration levels, and then pressurized with 750-psig propellant saturated helium and held at 150°F for 66 h.

After the above exposures, each valve was functionally tested five times with saturated helium at the following temperatures: 140, 150, 155, 160, 165, and 170°F. Initial test data from these tests show that valve performance was as expected at the higher temperatures and that propellant exposure did not degrade valve performance.

f. Lunar hopper confidence test. The lunar hopper confidence test is an attempt to simulate the thermal and propellant vapor exposure experienced by *Surveyor I's* oxidizer relief valve. A 50-h coast phase simulation at 700 psig and 60°F was followed by a posttouchdown thermal profile closely patterned after that of *Surveyor I*.

Fifty hours after touchdown and every 6½ h thereafter, the relief valve was functioned, and helium saturated with propellant vapor was allowed to flow through the valve until it reseated.

Sixty-four relief valve cycles were accomplished with over 454 h of propellant vapor exposure experienced. Temperatures were increased from 60 to 250°F. No valve leakage was noted. Crack and reseat values did not change significantly from their initial values of 830 and 820 psig during the first 20 cycles and were predictable up to 185°F. Crack and reseat values averaged 825 and 790 psig, respectively, for the remaining cycles.

In addition, a regulator in the same setup was allowed to flow at a rate similar to a low-thrust lunar hop requirement and successfully locked up at 770 psig and 150°F.

No more effort is to be expended on lunar-hopper studies or tests.

3. Vernier Engine Surface Interaction Experiments[2]

An article in SPS 37-40, Vol. VI, pp. 11–15, discussed an experiment in which a *Surveyor* vernier engine was fired onto a dusty surface oriented parallel to and 12 in. from the engine exit plane. While the engine was firing, a stable column of soil was observed extending from the surface to within 2 in. of the nozzle exit plane along the centerline of the engine.

This experiment was in the first group of a series of tests conducted to investigate the effect of a vernier engine exhausting onto a surface positioned in the same location and attitude as the lunar surface is beneath a landed *Surveyor* spacecraft. All tests were conducted in the JPL facility at Edwards Air Force Base.

The test facility, in addition to the engine and its propellant feed system, consisted of engine and propellant temperature conditioning equipment, data measuring and recording equipment, and a test cell in which the engine was fired.

The test cell is capable of maintaining a pressure level of 0.01 to 0.02 psia while the engine is firing. Before ignition, the test cell is evacuated by mechanical pumps to a level near the operating pressure level; a hyprox steam ejector is then used to reduce the cell pressure to its operating level and maintain it there during the vernier engine firing.

The test reported in SPS 37-40, Vol. VI, was preceded by a similar experiment, which requires some discussion. Here, after all the equipment had been installed in the test cell, the test cell was evacuated with the mechanical pumps; the hyprox steam ejector was turned on; and the engine was ignited. When the steam ejector came on, however, the soil exploded from its container because the gases and liquids trapped in the soil had not been given sufficient time to diffuse from the soil. The consequent pressure difference across the soil was sufficient to overcome its weight. Observing this, it was decided to make the next test using only the vacuum pumps to evacuate the chamber; it was this test which was reported in SPS 37-40, Vol. VI.

Because only the mechanical pumps were used to reduce the test cell pressure, this pressure was higher than normal during the engine firing at 0.112 to 0.156 psia. A successful method of solving for the characteristics of the vernier engine flow field has not yet been obtained; consequently, an accurate estimate of the vernier engine exit plane pressure is not available. Based on one-dimensional supersonic flow theory, the engine exit plane static pressure is estimated to be between 0.06 and 0.09 psia. Thus, it seems likely that the engine was overexpanded during this test.

Typically, a slightly overexpanded exhaust flow exhibits the familiar "Mach diamond" shock structure by which it adjusts to an ambient pressure greater than its exit pressure. Examination of the flow field within the Mach diamonds shows a divergent flow, while that outside the diamond yields a convergent flow.

At this point it can be postulated that the pressure distribution on a plane surface perpendicular to an engine axis and intersecting an overexpanded exhaust flow field in one of the Mach diamonds would be characterized with a local minimum at the engine centerline. Such a pressure distribution would be sufficient to explain the stable soil column observed in this test.

The test described in SPS 37-40, Vol. VI, was conducted in June 1966. The following September an additional series of tests (SPS 37-43, Vol. I, pp. 7–11) was undertaken to investigate the interaction between a firing vernier engine and simulated lunar soils. Again the engine was positioned such that its axis was perpendicular to the surface of the soil, and its exit plane was 12 in. above the soil surface. The engine throat and exit radii are 0.25

[2]Prepared by JPL Technical Section 384.

and 2.545 in., respectively. In this series of tests three different types of soil were used:

(1) A loose, coarse soil.

(2) A compacted, coarse soil.

(3) A compacted, coarse soil with a 2-in. overlay of loose, fine soil.

Before each test, the soil was placed in the test cell for overnight exposure to vacuum maintained by the mechanical pumps to allow trapped gases and liquids to diffuse from the soil. The mechanical pumps kept the test cell pressure at 0.01 psia. Shortly before engine ignition, the test cell was opened for 1 h to bleed propellants, after which it was again closed and the vacuum reapplied. During the engine firing, the cell pressure was maintained between 0.01 and 0.02 psia by the hyprox steam ejector.

Figures 22 and 23 are photographs showing, in lower foreground, the soil surface as it was acted upon by the vernier engine exhaust. The photographs are enlargements of 16-mm high-speed (250 frames/s) motion picture frames. The soil used in this test was a compacted, coarse soil overlayed with 1.5 in. of loose, fine soil; the soil was intentionally cohesionless. The engine fired with a chamber pressure of 67 psia, equivalent to a thrust level of approximately 30 lb_f. As can be seen in the photographs, the large stable column of soil observed in the earlier tests is no longer present and has been replaced by a small stable mound of soil approximately 2 in. high.

Relative to the exhaust flow field, the only difference between the test described in SPS 37-40, Vol. VI, and the test described above was the change in the pressure

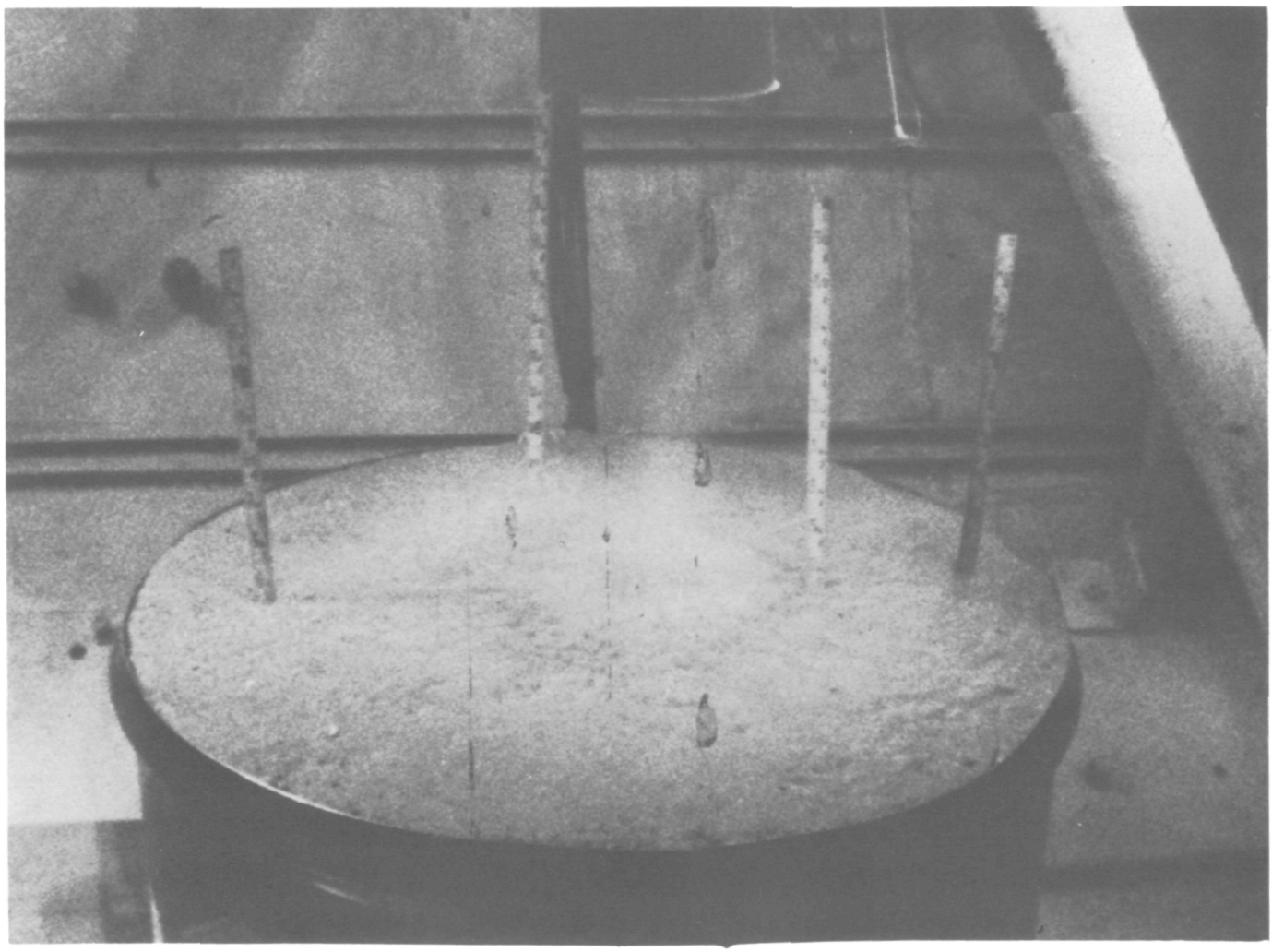

Fig. 22. Photograph of the engine and soil at vernier engine ignition

at which the test cell was maintained during the engine firing. This change, however, resulted in a dramatic difference in the soil behavior. This result now lends credence to the discussion of the effects of Mach diamonds above. Still to be explained, however, is the stable mound of soil observed in the photographs of the more recent experiments.

The divergent contour of the *Surveyor* vernier engine is of the overturned bell variety. That is, the slope of the nozzle wall contour at the engine exit plane is parallel to the engine centerline. Because the test cell pressure is less than the nozzle exit plane static pressure, the exhaust flow does not exit the nozzle as a parallel flow but tends to diverge at the exit plane. The nozzle contour at the exit does not permit this, since it is parallel to the nozzle centerline; consequently, the supersonic exit flow is turned, and this turning is accomplished with an oblique shock wave. This oblique shock wave is reflected once at the nozzle centerline. Downstream of the reflection point the flow is divergent. This in turn would produce a local minimum in the pressure distribution on a surface aligned perpendicular to the flow at the nozzle centerline. However, one would not expect the effect here to be as strong as it is within the Mach diamonds, since the flow in the overexpanded case is much more confined.

Figure 24 is a graph of the radial distribution of pressure in the soil measured during one vernier engine firing. The engine was positioned 12 in. above the initial soil surface; engine chamber pressure was 89 psia 0.12 s after ignition; and engine thrust was 47 lb_f. The soil pressure

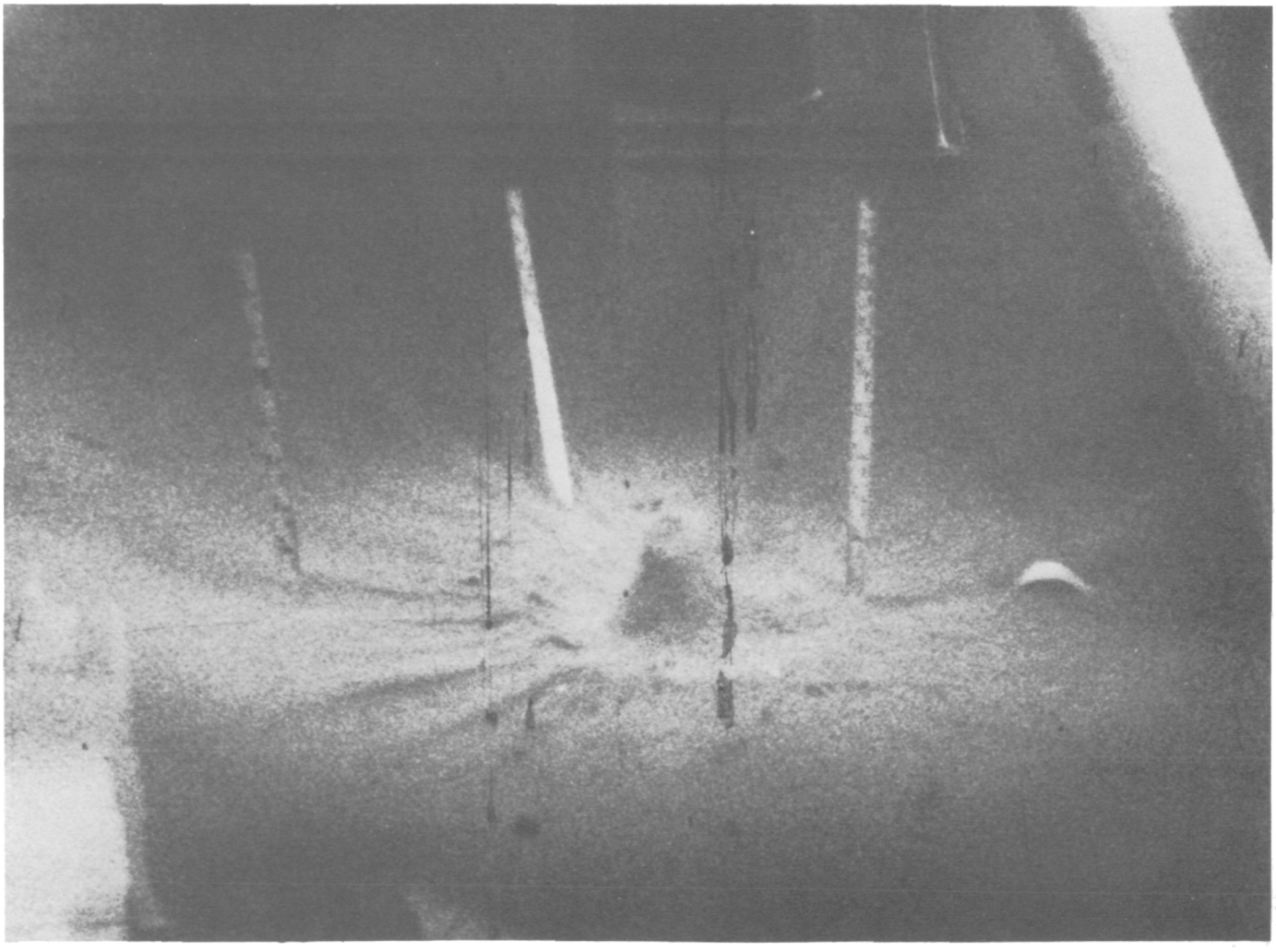

Fig. 23. Photograph of the soil surface as acted upon by the vernier engine exhaust

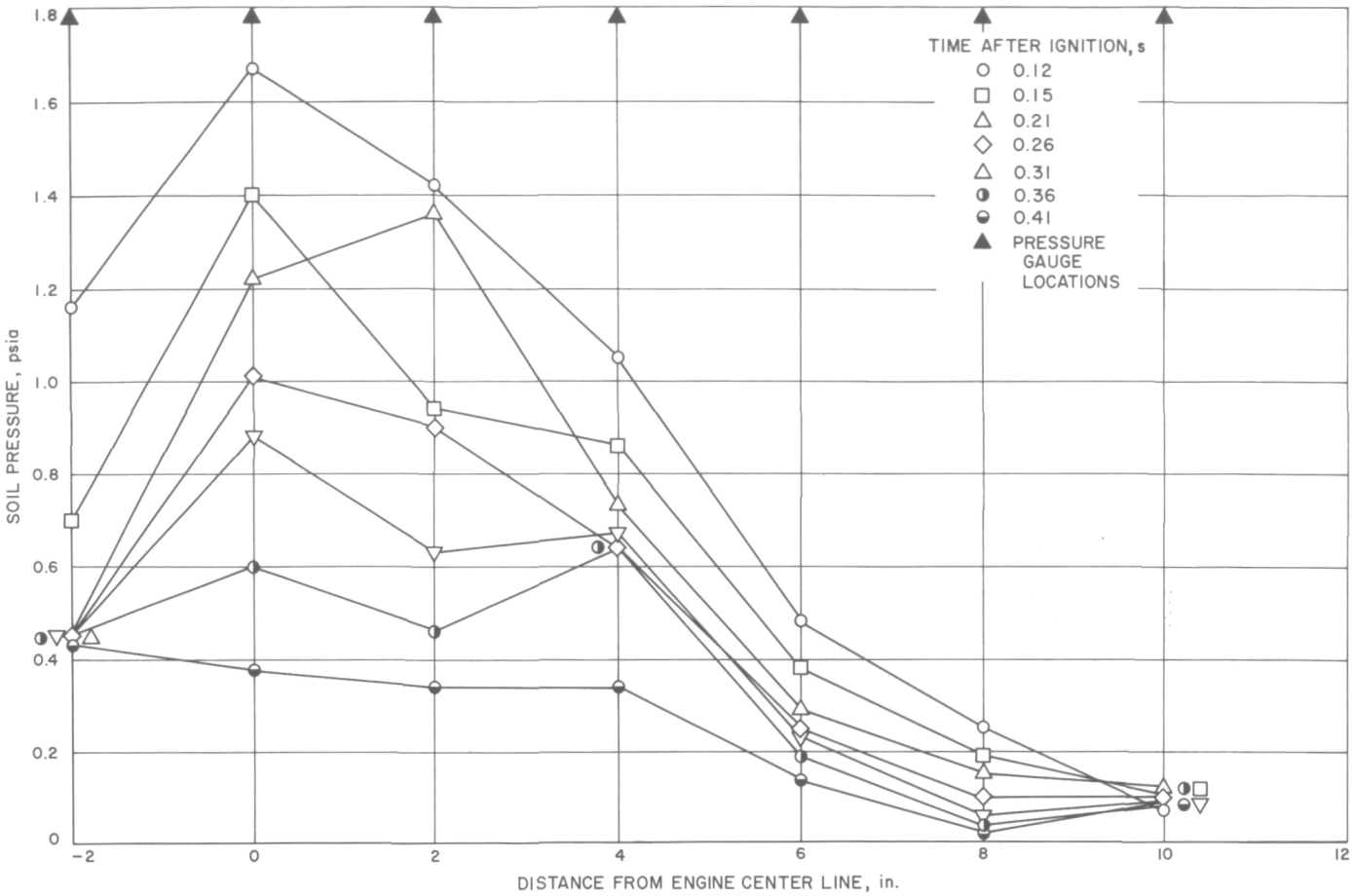

Fig. 24. Soil pressure profile of *Surveyor* vernier engine firing

transducers were located 1 in. beneath the initial soil surface; their radial locations are indicated on the figure. The different curves on the plot are pressure contours for a constant time after vernier engine ignition. The test from which the soil pressure distribution was taken is not the same test from which the enclosed photographs were taken. The only difference between the two tests was in the type of soil involved. The soil used in the test from which the soil pressure distributions were taken was a loose, coarse, cohesionless soil.

In examining the data presented in the curves of pressure distribution, note that the buried transducers respond not only to the local gas pressure, but also to the weight of soil above the transducer. The small mound of soil at the engine centerline, therefore, casts some doubt on the meaning of the pressure recorded by the centerline pressure transducer. Despite this uncertainty, the data do not preclude, and occasionally support, the possibility of a local minimum in the soil pressure distribution at the engine centerline.

In summary, it seems likely that the cause of the large, stable soil column observed in the test reported in SPS 37-40, Vol. I, pp. 11–15, is an overexpanded exhaust flow resulting from a test cell pressure greater than the vernier engine exit plane pressure. This conclusion is supported by the drastic reduction in the extent of the soil column observed in later tests (Figs. 22 and 23). These later tests differed from the earlier experiments, relative to the exhaust flow field, only in the reduction of test cell pressure.

In the later tests, however, a small, stable mound of soil on the engine centerline was observed. It is postulated that this is the result of an overturned exit contour which causes an oblique shock structure to stand in the nozzle exit flow. Such a shock structure could cause a local minimum in the surface pressure distribution to exist at the nozzle centerline. A plot of the measured surface pressure distribution is presented in Fig. 24. Because the pressure transducers were responsive to the weight of soil above them in addition to the local gas pressure, these

data are somewhat uncertain. However, these data do not exclude the possibility of such a local minimum in the surface pressure distribution; they merely fail to positively confirm this supposition.

K. Deep Space Network Test, Operations, and Training

1. Mission D Operations

Pioneer station (DSS 11). During the mission, Goldstone provided support for four passes, including the midcourse maneuver, terminal descent, and spacecraft revival attempts. The maneuver portions of the mission were executed using command tapes previously transmitted from the Space Flight Operations Facility (SFOF). The midcourse maneuver was executed without any anomalies and the spacecraft remained stable and completely controllable. The terminal descent was a standard sequence with all commands transmitted at the predetermined time until loss of contact with the spacecraft, at which time the mission became nonstandard. The remainder of the third pass was utilized in an unsuccessful attempt to reacquire a signal from the spacecraft. Revival attempts were made with no success throughout the fourth pass.

A unique feature of this mission was the provision that had been made to switch the command data console (CDC) input/output from the Pioneer station antenna to the Mars station antenna for either receiving telemetry from the spacecraft, or sending commands to the spacecraft, or both. The CDC input was switched to the Mars station during the second pass, and an increase in signal level of 8.5 dBm was noted when utilizing the 210-ft dish.

Tidbinbilla station (DSS 42). Canberra provided support for four passes, two of which occurred during the transit portion of the mission. During the final two passes, unsuccessful attempts were made to reestablish contact with the spacecraft. No significant problems with either the spacecraft or ground equipment were encountered during these two tracking periods.

Johannesburg station (DSS 51). Johannesburg, originally scheduled as a backup station, provided support for three passes. There were no operational or equipment problems in the CDC area during the mission.

2. Modification Kit Installations

Command data console modifications were completed at DSSs 11, 42, and 51. Modifications included those that satisfy the ground rule of keeping all DSIF CDC units as interchangeable as practicable.

3. Personnel Deployment

Numerous reassignments of station personnel are taking place to assist with the spacecraft system test and data evaluation efforts at HAC El Segundo prior to mission E. Some station personnel returned to attend a 1-wk alpha scattering seminar held at JPL and Goldstone.

4. *Surveyor* Operations Chief Handbook

Revision E of SSD 68089R, "Surveyor Operations Chief Operational Aids Handbook," is being prepared, with publication and distribution expected by August 14, 1967.

5. DSN Training

Training of DSN personnel for their eventual assumption of CDC maintenance and operations responsibility from HAC continued. (This transfer has already been implemented at DSS 42.) Such transfer of responsibility will reduce project costs and effect a more efficient utilization of the permanent mission dependent equipment personnel. Mission control personnel for each mission will continue to be provided by HAC. For mission D, DSN personnel were assigned to all crews. The full DSIF crew complement has been trained at DSS 42 and DSS 51, and operated during the mission.

6. General

The alpha scattering multiplexed telemetry compatibility test procedure (11-14) was prepared and distributed, and operational forms for the on-site alpha scattering identification log were prepared and distributed.

L. Payload

1. Soil Mechanics/Surface Sampler Subsystem

a. Introduction. The soil mechanics/surface sampler (SM/SS) subsystem is part of the payload designed to manipulate a portion of the lunar surface near the spacecraft. Survey TV camera-3 will permit viewing of these operations. The visual data obtained during such operations as picking, digging, scraping, and trenching, combined with an assessment of the forces being developed during these operations through motor current telemetry, may provide significant information related to lunar surface characteristics.

The SM/SS subsystem consists of a mechanism, auxiliary electronics and thermal compartment, and installation substructure and wiring harnesses. The mechanism performing operations on the lunar surface is controlled by

the auxiliary electronics housed in its own thermal compartment. The auxiliary electronics receives and decodes ground commands, and provides power and signal conditioning for the SM/SS subsystem.

In compliance with change order 156, June 2, 1967, work has begun to add the SM/SS to SC-7.

b. Payload systems integration. Delivery of all control items to SC-7 and completion of the SM/SS SC-7 initial systems checkout occurred during the report period. In accordance with special test request 275, initial systems checkout was conducted on SC-7.

The following were tested and verified for conformance to specifications:

(1) Physical arrangement and mounting.

(2) Structural and electrical interface.

(3) Wiring harness.

(4) Regulated and unregulated voltage line currents.

(5) Command response.

(6) Signal outputs.

(7) Pin puller circuits.

(8) Heater operation.

(9) Absence of electromagnetic interference.

(10) Stowage.

In addition, calibration data on the increments of movement and the motor currents were collected. During a portion of the test, an anomaly caused by grounding the thermal plate on the auxiliary was encountered. Since it is desired that the radiator plate remain grounded for purposes of static electrical discharge, the auxiliary was removed and has been modified. After modification, the auxiliary was vibrated and tested at the unit level prior to reinstallation on the spacecraft. After the unit was reinstalled, a short portion of special test 275 was conducted (the step that had previously failed). The retest was successfully completed August 11, 1967.

c. Engineering. It was necessary to fabricate a pickup device that would attach to the alpha scattering sensor head so that the sensor head could be deployed by the SM/SS within physical limits determined by the cable length and spacecraft substructures. Various pickup devices were fabricated and tested during July 6 through 14, 1967. It was found that a definite thickness-to-height ratio exists; and, in general, the device should be as small in diameter as possible and have as much height as practical. The pickup devices were tested by installing the SM/SS, an alpha scattering deployment mechanism, and an alpha scattering sensor head on the M-13 mockup spacecraft in the payload systems laboratory, and a redeployment area plot was made for each of the devices. Six pickup devices were tested; their configurations are as shown in Fig. 25. Figure 26 shows the test pattern obtained for the pickup device selected.

d. Support analyses. Studies were conducted to determine the TV viewability, and the operational area of the SM/SS on SC-7. Included in these analyses were the initial deployment points for the alpha scattering sensor head for 10- and 15-deg spacecraft slopes. The results show that approximately 88% of the SM/SS operational area on the nominal lunar surface can be viewed by means of survey TV camera-3, with most of the remainder of the area viewable by means of the SC-7 mirror. Results of these analyses were incorporated in subsystem detail specification 289177 and were distributed to other affected areas.

2. Alpha Scattering Experiment Subsystem

a. Introduction. The alpha scattering experiment on SC-5, -6, and -7 will be used for qualitative and quantitative composition analysis of lunar surface materials. The lunar surface will be bombarded with 6 MeV alpha particles from sources contained in the instrument. Backward scattered alpha particles, as well as protons generated within the lunar surface materials by the incident alpha particles, will be detected by solid-state detectors. The instrument is capable of detecting the presence of all elements except hydrogen, helium, lithium, and beryllium with a detection threshold of approximately 1% by atom.

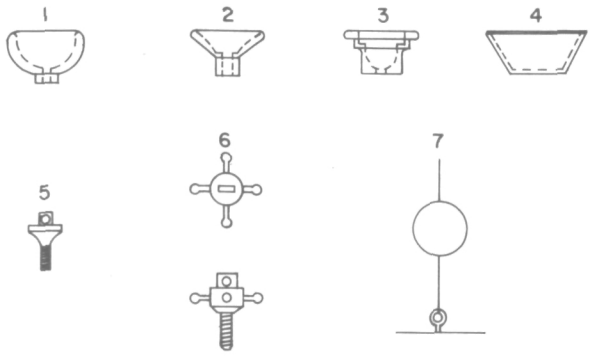

Fig. 25. Pickup device configurations

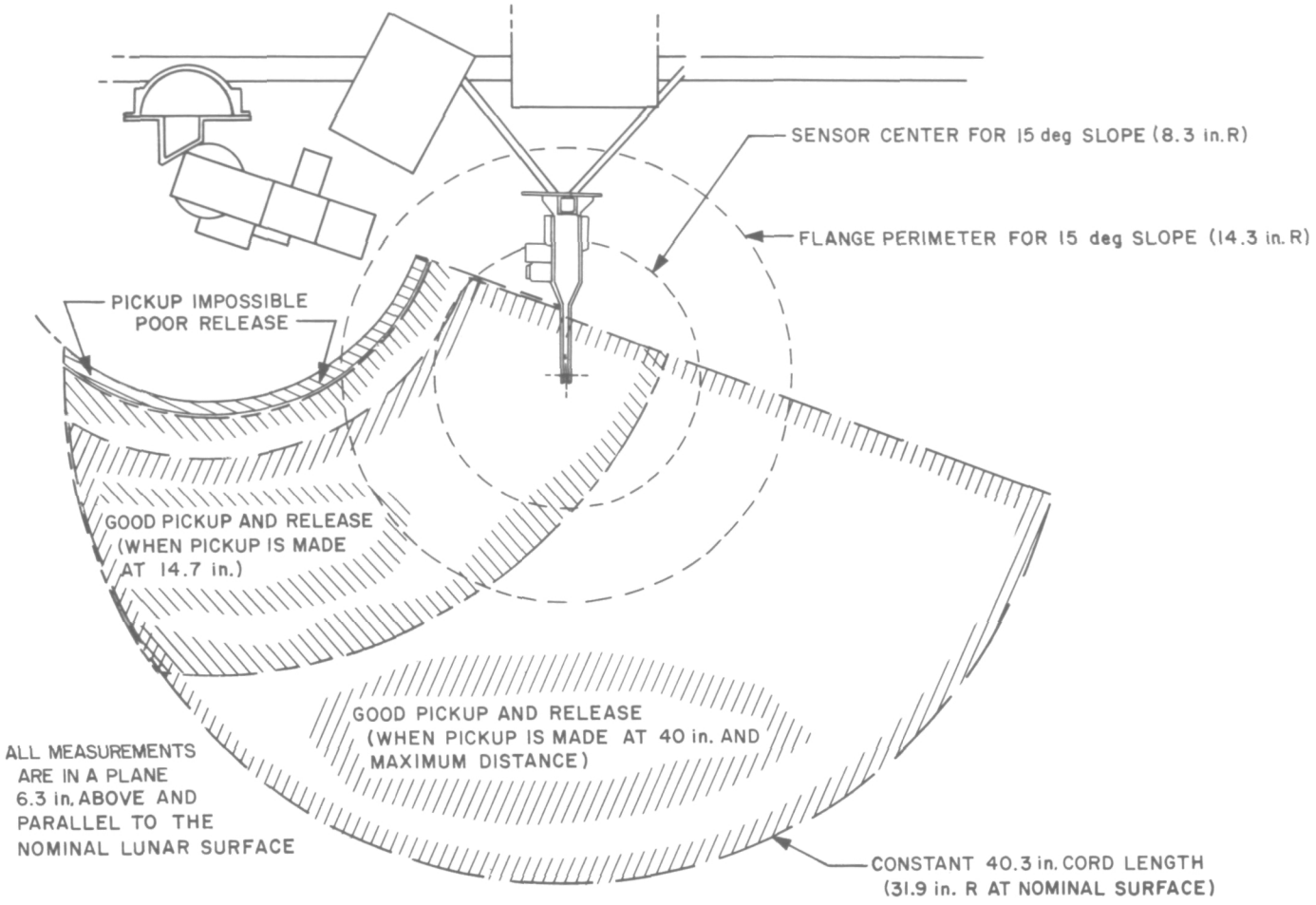

Fig. 26. Redeployment areas for alpha scattering sensor with pickup 5

The alpha scattering instrument consists of three parts: sensor head, electronics, and standard sample assembly — all of which are supplied to HAC as government-furnished equipment (GFE). The required electrical interfaces between the instrument and the spacecraft are provided by an auxiliary unit, which affords command decoding, signal processing, and power management, and by direct connection to the basic bus, which provides instrument clocks, temperature sensor current, and commutation of engineering data. The electronics and auxiliary units are contained in a new thermal compartment-C. A heater maintains the compartment-C plate radiator within the operating temperature range of the auxiliary and electronic units.

A deployment mechanism attached to the spacecraft provides for stowage and deployment of the sensor head. The experiment is operated in three positions:

(1) Stowed position, utilizing a standard sample contained in the deployment mechanism.

(2) Background count position, approximately 15 in. from the lunar surface.

(3) Deployed on the lunar surface.

b. Experiment payload integration. Significant progress has been accomplished during this report period in conducting experiment integration tests, both in the payload systems laboratory and at the spacecraft level.

System integration tests during the report period consisted of the following:

(1) Subsystem integration and compatibility testing of the alpha scattering subsystem to be used for SP-2 spares.

(2) Retest of the SC-6 alpha scattering instrument to investigate noise events in the alpha channel which were out of specification during system mission sequence testing.

(3) Test of the effect of radioactive isotope heaters on the alpha scattering subsystem.

(4) Alpha scattering testing on SC-5, -6, and -7.

(5) Combined SM/SS alpha scattering instrument design and integration for SC-7.

Detailed integration and compatibility tests were performed on the alpha scattering subsystem to be used for SP-2 spares. The subsystem tests utilized system basic bus units or simulated basic bus units to provide realistic interfaces between the subsystems. Details of the specific tests conducted are presented in the following paragraphs.

The alpha scattering subsystem to support the SP-2 spares for SC-5, -6, and -7 were assembled on the M-13 spacecraft, and complete subsystem integration tests were successfully completed with no discrepancies noted.

c. Subsystem engineering. Prior to vibration tests of SC-5, the bushing for the deployment mechanism upper pin puller was found cracked. The cause of failure was due partly to excessive adhesive applied during assembly and partly to misalignment of the pin puller during installation. Although noncritical, the bushing was replaced. All other deployment mechanisms were inspected and, where necessary, the bushings replaced.

After vibration and deployment tests of the alpha scattering instrument, the bumper that protects the deployment mechanism from excessive shock was found to be loose. The cause of failure was a design deficiency of the bumper. New bumpers were designed to incorporate mechanical as well as adhesive attachment of the part that had become loose. New bumpers have been installed on all flight deployment mechanisms.

d. Government-furnished equipment. The F-3 sensor head and digital electronics were delivered to HAC July 7, 1967. Standard samples SN 5 and 6 were delivered July 21, thus completing the initial delivery of all GFE.

P-3 sensor head was returned to JPL July 14 to be used for a dry run of flight source loading at the Air Force Eastern Test Range (AFETR). The dry run was conducted in July, and the results were used for a second dry run conducted August 7. P-3 is to be returned to HAC for use as a spare to support SC-6 and -7 while F-3 has flight sources installed.

P-4 sensor head was removed from SC-5 August 11 to have flight sources installed. The unit will be returned to the spacecraft August 31. Flight source installation is presently under way.

F-3 sensor head was returned to JPL at AFETR August 11 to have flight sources installed. After the flight sources are installed, the unit will remain in a vacuum until SC-5 is launched and will serve as a spare. After launch, the sources will be removed from F-3, and the unit will be returned to HAC bonded stores at AFETR and remain there to support SC-6.

A series of anomalies has occurred with F-1 sensor on SC-6 since the beginning of systems tests. All were related to the sensitivity of the instrument to noise and RF interference.

The first anomaly occurred during SC-6 mission sequence/electromagnetic interference (MS/EMI) phase-2 testing, wherein considerable noise events were recorded in the lower alpha data channels. This condition indicated a possible detector failure, and the sensor head was returned to the payload systems laboratory. Subsequent testing showed the detectors had not failed and the unit was returned to SC-6. Data taken during the MS/EMI tests were analyzed and the presence of a definite 103 pulse/min noise pattern was detected. Further investigation located the source of the noise to be an applications technology satellite (ATS), which was being tested in the vicinity of SC-6. The ATS satellite has an electronically despun VHF antenna which operates at about 100 rpm and at a frequency which is within the range of frequencies known to affect the alpha scattering instrument. The effect has been noted on the spacecraft signature list.

The proton channel showed a high rate of events in all detectors while in solar thermal vacuum (STV) dry run. All possible sources of noise were investigated before the problem was found to be caused by radioactive material in a dew point meter. The meter had been installed in the chamber to measure the humidity near the sensor head.

Later, during STV tests, an event showed up in the data taken with no detectors on. By examining the computer data versus time and temperature, it was found to be due to the on and off cycling of the sensor head heater circuit.

During a special test after STV, considerable noise events again occurred in both alpha and proton channels, and the guard event monitor was activated, indicating

noise events in the guard detectors. An investigation of noise sources near the spacecraft showed that the ATS satellite, which had recently been moved into the environmental area near *Surveyor*, was the source. In this case, however, the VHF antenna was being operated in an omnidirectional mode and thus produced a different effect than previously.

e. Special studies and tests.

Television viewability. The deployment of various instruments, such as the alpha scattering device, on the surface of the moon by means of the SM/SS will undoubtedly require TV camera assistance in viewing the actual placement of the instrument. In support of this task, an analytical study[3] was conducted to determine the viewing capability of the *Surveyor*-type TV camera. In this study, mathematical relations have been derived which permit the determination of an exact contour of the photographed area on the surface of the moon, or at any level above the surface, if desired. The input data required are elevation and azimuth angles of the TV mirror, plane level to be viewed, and the optical field of view angle to be used. An effort is being made to generate a computer program for a scientific data systems computer for future use.

Humidity control equipment. The humidity control equipment to provide continuous dry nitrogen purging of the sensor head after flight sources are loaded were successfully tested during SC-5 combined systems tests at San Diego. Changes resulting from the experience gained were as follows:

(1) All purge system lines will be capped and kept under 2-lb pressure when not in use, to ensure best dew point measurements.

(2) The fitting for the empline tube that mates with sensor connections has been improved.

(3) The installation procedure to provide for flushing the JPL nosecone purge line and to make dew point measurements of line prior to encapsulation has been modified.

(4) All future JPL-supplied lines will be delivered to provide approximately 4 in. extra slack to avoid cutting of the line at AFETR.

The humidity control equipment and procedures, as modified above, were successfully used during joint flight acceptance tests at AFETR during July and August.

[3]HAC Interdepartmental Correspondence 2209.03/193, June 30, 1967.

The alpha scattering sensor head dry nitrogen purging operations were initiated on July 27 at 1310 h GMT for the SC-5 joint flight acceptance program and completed on August 1 at 420 h GMT. The total time "off purge" for the various switching operations reported by quality control was 6 min 27 s. There were no equipment failures, and the nitrogen bottles were replaced on schedule.

When the radioactive flight sources are installed in the sensor head by JPL and the unit is delivered back to the spacecraft area August 31, continuous dry nitrogen purging will be performed until launch. A master log for total time "off purge" will be established by quality control and will start in the JPL alpha scattering facility at the time the flight sources are installed. The total cumulative "off purge" time allowed is 3 h.

M. Flight Spacecraft Testing

1. *Surveyor IV* Flight Acceptance Testing

During this reporting period, *Surveyor IV* was at the Air Force Eastern Test Range (AFETR), where prelaunch preparations and tests were accomplished. The spacecraft was launched at 04:53 h PDT July 14, 1967.

Postjoint flight acceptance composite test (J-FACT) operations were performed in the explosive safe facility and were completed June 11. These activities included depressurization of the helium and nitrogen systems with transducer calibration, removal of J-FACT items, installation of the flight thrust chamber assemblies (TCAs), and initial alignment.

Retests on radar altimeter and doppler velocity sensor (RADVS) were successfully completed June 14 and a TCA spacecraft functional test of two spare engines was performed. The final comprehensive spacecraft test, (PVT)-5 began June 14 and was successfully completed June 17. The spacecraft was moved to the propellant loading building June 19.

Overdeviation of the transmitter due to nonlimiting vidicon hard saturation was discovered during testing at AFETR. Since this condition would affect picture quality only on a small percentage of pictures taken, it was decided not to make any hardware changes.

High-pressure leak and decay tests of the vernier propulsion system were completed during the week ending June 23. A bladder leak test was also performed. Oxidizer

and fuel pressure decay and composite bladder leaks were all within specification.

Final fuel and oxidizer loading was completed June 23. The spacecraft was moved to the explosive safe facility (ESF) assembly building and thermal finish touchup and cleaning operations were completed. Final spacecraft assembly, and weight balance and alignment were completed and pyrotechnic devices were installed. The spacecraft was moved to the north bay of the ESF July 3 and mated to the *Centaur* forward adapter. Final verification of spacecraft performance, PVT-6, was completed July 5. The spacecraft was encapsulated and mated to the *Atlas/Centaur* launch vehicle July 8 and a system readiness test and a HAC-only countdown were performed and launch readiness was thus achieved on schedule, July 8.

Launch was delayed from July 13 because of a problem in the fuel/oxidizer control system of the *Centaur* and occurred at 04:53 h PDT July 14, 1967. A midcourse maneuver was successfully performed July 15 and brought the projected landing point to within an estimated 4.2 km southwest of the target site. During the terminal descent July 16, however, total loss of data from the spacecraft was experienced approximately 2 s before the planned burnout of the main retrorocket. At the time of signal loss the spacecraft was stable and apparently functioning normally.

2. SC-5 Flight Acceptance Testing

During this report period, SC-5 was at both General Dynamics/Convair (GD/C) and AFETR facilities undergoing combined system test operations and prelaunch preparations. Joint flight acceptance composite testing (J-FACT), PVT-5, and spacecraft alignment were major milestones accomplished. The test chronology for SC-5 flight acceptance testing is given in Table 12.

a. Combined systems test, GD/C. The spacecraft arrived at GD/C June 17 and power was applied to the spacecraft June 19. A special TV test, relating to the anomaly observed on *Surveyor IV*, was conducted. Following this and the preencapsulation system readiness test, the SC-5 camera was removed and returned to HAC El Segundo in order to be available for potential modification.

b. Air Force eastern test range operations. SC-5 and its associated hardware arrived at AFETR June 28. The spacecraft was placed in the high bay area of the A0 building, where receiving, inspection, and reassembly operations began in preparation for PVT-1.

Table 12. SC-5 test chronology

Location	Event	Date
GD/C	Arrival at GD/C	June 17
	Power applied to spacecraft	June 19
	Mated to *Centaur*	June 21
	Combined system test	June 23
AFETR	Arrival at AFETR	June 28
	PVT-1, -2 completed	July 8
	PVT-3 completed	July 15
	PVT-4 completed	July 20
	Spacecraft mated to *Centaur* adapter	July 25
	Encapsulated	July 27
	Moved to launch pad and mated to *Centaur*	July 28
	J-FACT completed	July 31
	Alignment and weighing of flight retrorocket	July 31
	Spacecraft alignment completed	August 3
	PVT-5 completed	August 10

Further investigation of the TV camera white saturation problem indicated that a severe breakup of oversaturated pictures could occur in the TV ground data processing system. Alternative fixes were evaluated, and it was decided to install the SP-1 camera.

PVT-1 and -2 were completed July 8. The compartment A thermal control and heating assembly unit failed to return on each of 11 times attempted, duplicating a problem observed during combined systems test operations. The unit was replaced with a spare unit and operation was normal.

A RADVS ranging test performed July 12 revealed that the range tracker would not maintain lock in the vicinity of 1750 ft external range when in high deviation. This occurred despite the fact that adequate signal strength was finally obtained by removing the 10-dB pad from the feedhorn adapter, resulting in a strong signal and in a gain state 2 operation. The klystron power supply modulator (KPSM) was removed from the spacecraft and returned to Ryan Aeronautical Company for additional troubleshooting, verification of spectrum characteristics, and performance of ranging tests. The KPSM was returned to the spacecraft July 20; however, the klystron exhibited a wide return frequency spectrum and will be returned to Ryan Aeronautical Company for klystron retuning; KPSM serial number (SN) 11, which indicates a narrower frequency spectrum, will be installed as the flight unit.

A bladder leak check performed on all flight tanks July 11 revealed that fuel tank 1 had an excessive leak rate. It was replaced with a spare unit. The oxidizer check valve also exhibited an excessive leak rate and was replaced with a spare. A TCA "long lines" test on TCA 560 in engine position 1 was completed the weekend of July 22.

Preparation of the flight retrorocket (A21-28), including X-rays was completed, and the spacecraft was moved to the ESF. On July 25 it was mated to the *Centaur* adapter. Preencapsulation preparations, including configuration verification, were completed July 26, the spacecraft was encapsulated, and a systems readiness test (SRT) begun July 27. The spacecraft was moved to the launch pad and mated to the *Centaur*, and an SRT and countdown were performed July 28.

Joint flight acceptance composite test was completed July 31. During the test, phase jitter experienced on transmitter A resulted in break locks while DSIF and system test equipment assembly (STEA) receivers were operating at threshold. This condition was observed in both transponder and narrow-band modes when the traveling-wave tube temperature reached 140°F. A switch was made to transmitter B, and the test was completed. The spacecraft was demated from the *Centaur*, moved to the ESF, and decapsulated July 31. Removal of J-FACT items and initial spacecraft alignment were completed August 3, and the next report period will include final spacecraft preparations for launch, PVT-6, and the launch. Spacecraft was returned to building A0. Radar altimeter and doppler velocity sensor retests were performed using KPSM SN 11, and PVT-5 was completed August 12. The spacecraft was moved to the propellant loading building in preparation for high pressure leak tests and propellant loading.

3. SC-6 Flight Acceptance Testing

During this report period, SC-6 was at the El Segundo facility, where the mission sequence/electromagnetic interference (MS/EMI) test phase was completed, along with missions A, B, and 2A of the solar thermal vacuum (STV) test phase.

a. The mission sequence/electromagnetic interference test phase. Mission sequence/electromagnetic interference run 2 began June 2 and was aborted the same day because of failure of the flight control system to receive magnitude commands. The flight control sensor group was returned to the unit area, where the problem was found to be in the programmer unit. The SC-7 flight control sensor group was installed and flight control testing was completed June 16. The flight antenna solar panel positioner (ASPP) was also installed June 16, and ASPP testing was completed the next day.

Mission sequence/electromagnetic interference run 2 was again initiated and completed June 20. During this run, excessive noise was observed on the lower channels of the alpha data. Analysis of payload systems laboratory troubleshooting efforts and data recorded during MS/EMI run-2 indicated that the problem may have been due to an external radiation source. Run 3 was initiated June 23 and completed June 26, and the spacecraft moved to the STV facility.

b. Solar thermal vacuum test phase. A dry-run mission sequence was initiated July 8 and aborted that same day because of yaw gyro caging loop problems. The flight control sensor group was returned to the unit area, repaired, and returned to the spacecraft July 11. The dry-run mission sequence was successfully completed July 12.

The STV phase A mission began July 14. During the terminal descent portion of this mission, the timer on the RADVS STEA timed out and shut off the RADVS at an indicated range of 1700 ft. Subsequent analysis indicated a faulty adjustment in the range indicator in the flight control closed loop STEA, which caused a longer descent time. Following this aborted terminal descent, transmitter-B high power went off without command while low power remained on. During the second terminal descent, receiver A AGC indicated an 11 dB signal input change for approximately 50 s. The decoders indexed to receiver A; however, the uplink modulation was apparently not being seen by the receiver even though the signal level appeared to be strong. Receiver B telemetry did not indicate any anomalous operation. Special tests could not duplicate either of these problems.

The STV phase A mission was completed July 18 and the STV phase B mission was subsequently initiated. The mission proceeded normally except for a pressure increase in the C-4 chamber. This anomaly was traced to a speed control failure in one of the roughing pumps of the chamber. Phase B mission was successfully completed and the spacecraft was removed from the chamber July 23.

Because of the receiver and transmitter problems experienced during the STV phase A mission, a decision was made to rerun the phase A mission. This additional STV mission will slip the arrival date of the spacecraft at AFETR by 5 days and will also necessitate the elimination of combined system test operations in order to meet the present launch schedule.

Receiver A and transmitter B were replaced and STV phase 2A retest mission began July 29. This mission was subsequently aborted July 30 because of a phase jitter problem in transmitter B and spectrum spurs on transmitter A. The latter problem duplicates the receiver problem that occurred during the initial STV phase A terminal descent.

Transmitter A was replaced with the original transmitter B, which was removed after phase A/B. An exhaustive investigation of the phase jitter on transmitter B was conducted; however, no definite causes were determined. Although two slightly loose coaxial connectors were found, it is not known if this was the cause of the problem.

Upon completion of the phase jitter investigation and the retest, repeat of STV phase 2A was initiated. Launch occurred early August 3 and the mission was completed August 6.

Present planning indicates that vibration, including a plugs-out/mission sequence, will be completed by August 22, and the September 4 shipping date to AFETR can be met.

4. SC-7 Flight Acceptance Testing

During this report period, SC-7 was at the HAC El Segundo facility, where the initial system checkout (ISCO) and MS/EMI test run numbers 1 and 2 were partially completed. The test chronology for SC-7 flight acceptance testing is given in Table 13. A complete summary of the problems encountered during the MS/EMI test phase is given in Table 14.

Table 13. SC-7 test chronology

ISCO test phase	Date
SM/SS retrofit completed	June 12
TV testing completed	June 15
Alpha scattering experiment ISCO testing completed	June 20
RADVS antenna alignment and waveguide fitting completed	June 27
ASPP installed	June 30
Flight control/telecommunications testing completed	July 12
ISCO testing completed (except RADVS)	July 30
MS/EMI test phase	
MS/EMI run 1 completed	July 27

Table 14. SC-7 problem summary

Problem	Solution
Klystron power supply monitor ran hot.	Unit returned to Ryan Aeronautical Co. for investigation.
Transmitter SN 18 had low power output.	Replaced with SN 16.
Momentary short occurred on reference voltage as leg position potentiometer was being adjusted.	Engineering signal processor replaced because of suspected overstress. Terminals on leg potentiometers were coated.
Unlock elevation axis (lunar) squib firing pulse polarity was reversed.	Corrected spacecraft wiring error.
With omnidirectional antenna A extended, telemetry indicated not extended.	Replaced defective switch.
Phasing of gas jet 3 was incorrect.	Corrected spacecraft wiring error.
No SM/SS squib firing pulse.	Unit functioned normally after removal of ground wire to SM/SS auxiliary radiator plate. Auxiliary is presently in unit area for investigation.
Temperature sensors for SM/SS drive motors could not be installed because radius of curvature on sensors is different from radius of the motors.	Engineering has been released and adapter plates are being fabricated.
TV camera shutter did not open when camera was initially operated in "open shutter" mode, when starting TV tests.	Believed to be logic malfunction within the camera. Unit area will investigate when camera is returned for vidicon change.
Signal data converter low voltage power supply became intermittent.	Unit returned to Ryan Aeronautical Co. for investigation.

5. AGE Support

With completion of SC-6 MS/EMI testing, aerospace ground equipment (AGE) set 4 was no longer required to support spacecraft testing. The portions of this set required to upgrade AGE set 6 for complete hardline monitoring were removed and sent to AFETR. Certain units in the remaining racks were retained as spares for the operating AGE sets.

AGE set 1 has supported SC-6 solar thermal vacuum testing (STV) during this report period with only minor problems. Mandatory modifications required on this set for SC-7 STV were minor and have been incorporated and confirmed. Quality control history record squawks

against AGE set 1 have been greatly reduced in number with very few outstanding.

SC-6 STV retest required setting up AGE set 3 to support SC-6 vibration so that SC-7 STV preparations would not be delayed. Set 3 was set up and checked out for support of SC-6 vibration with no major problems being encountered.

6. Environmental Facilities

During SC-6 STV phase B, a malfunction of the speed control switch on the roughing pump caused a vent valve to open, resulting in a chamber pressure rise to 14 μm. Besides replacement of the speed control switch, a time delay has been added to ensure that an upstream valve is closed before the vent valve that protects the roughing pump opens. Malfunction of the speed control switch cannot explain the *Surveyor III* pressure rise during STV test, since a different method was utilized at that time to back the diffusion pumps.

A change to be incorporated for SC-6 vibration is a multipoint power averaging technique, which will be used for level control during random vibration. Acceptance of equalization runs from the M.B. Electronics equalizer/analyzer scope display should be valid and will save several hours of test time.

N. Space Flight Operations Facility Support Equipment

1. Trouble and Failure Reports

A review of trouble and failure report (TFR) statistics for this period reveals the following:

(1) One hundred twenty-five new TFRs were received during this 2-mo period, bringing the total to 2675.

(2) Operational support equipment engineering action completed 255 TFRs, leaving 70 to be completed. Engineering completions to date total 2595.

(3) Two hundred thirty TFRs were closed out during this period by project reliability, leaving 132 to be closed. A total of 2533 TFRs have been closed by project reliability to date.

No new TFRs were classified as critical during this period, and the four existing critical TFRs were closed. No command and data handling consoles critical TFRs remain in the system at this time.

a. Modification kits. Fifty-three modification kits were assembled and shipped for incorporation prior to mission D. Forty-two of these were approved for installation during the lunar night periods after mission C. Deep space instrumentation facility workloads precluded installation of the 11 remaining on-site kits. Six of these remaining kits have been approved for installation prior to mission E. Additional kits are being prepared and will be on-site for mission E installation. The total number of kits for mission E effectivity is not expected to exceed 20.

b. Engineering change request and change orders. Figure 27 shows the status and trends of engineering change requests (ECRs) and engineering change analyses (ECAs) for this and past report periods. The average ECR and ECA work loads have declined to about 20 and 7 per month, respectively.

2. New Work

Continued surveillance and expedited equipment and kit shipments made it possible for the three affected deep space stations to complete and check out the alpha scattering additions by the mission D freeze date. On-site spares were received from the vendor and shipped to the sites. Command and data handling console operations and maintenance manual technical data were received, processed through edit and production, and change notice packages were distributed to manual users.

O. Special Deep Space Station Test, Operations, and Training

1. *Surveyor IV* Operations

a. Robledo deep space station (DSS 61). Madrid support for the mission included commanding and monitoring of the initial star acquisition maneuver beginning at L+5^{h}49^m and ending with a confirmation of Canopus lock approximately 30 min later.

b. Cape Kennedy deep space station (DSS 71). The Air Force Eastern Test Range provided support for the prelaunch and launch portions of the mission. This support included the processing of telemetry data from the station and from various downrange stations via TEL-2. The data were processed by the CDC-11/SOCP (command and data handling console/*Surveyor* on-site computer program) and sent to the space flight operations facility via the high-speed data line. By switching in the various downrange data sources, the decommutator was kept in lock until approximately L+38^m. Utilization of the command transmitting capability was not required. No anomalies were detected during the mission.

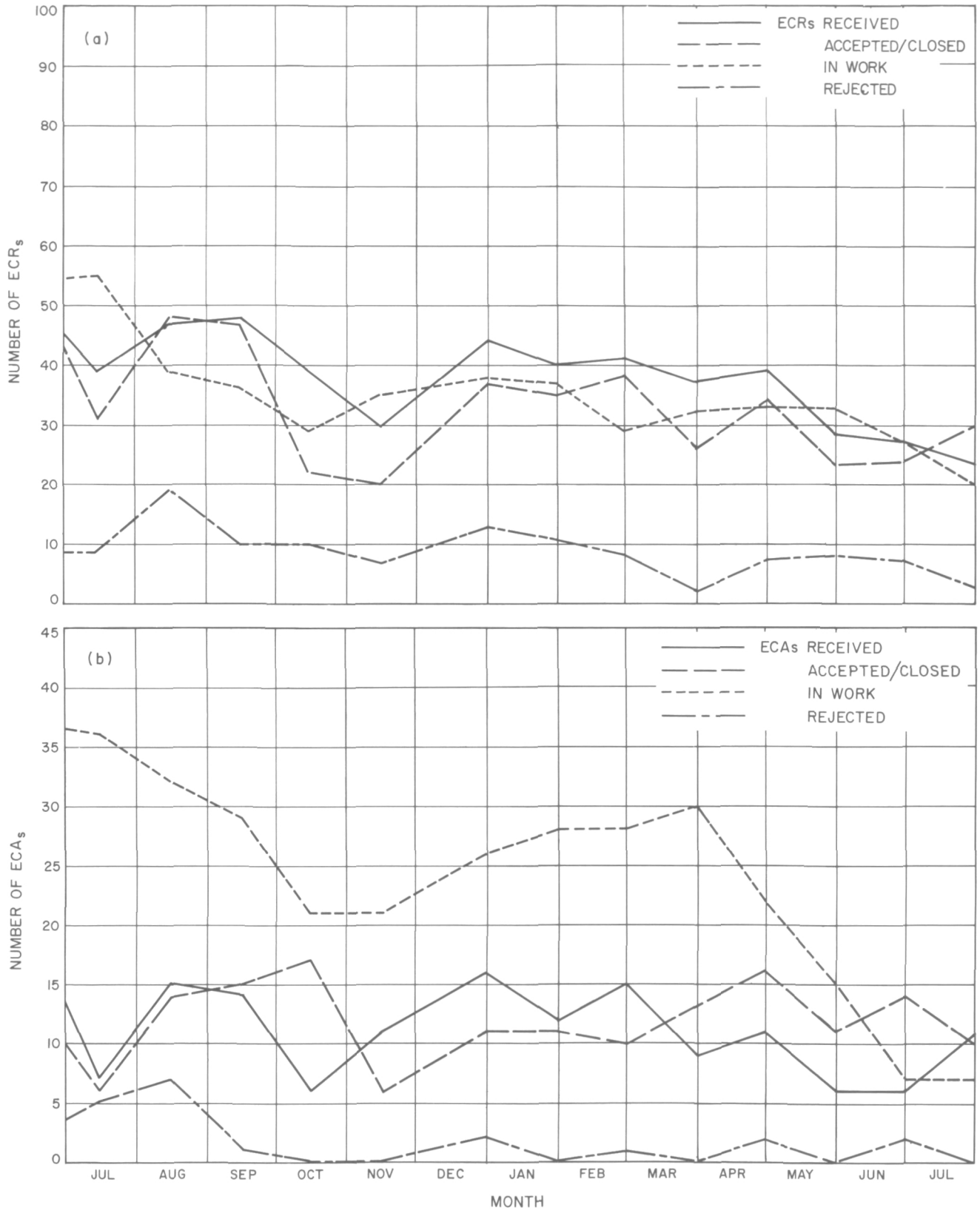

Fig. 27. Operational support equipment status and trends: (a) engineering change requests; (b) engineering change analyses

c. Ascension Island deep space station (DSS 72). Ascension was committed as the initial acquisition station for the mission and obtained decommutator lock at about L+17^{m}. The initial commanding was done from the station and marked the first time that the station commanded a *Surveyor*. There were no spacecraft or CDC anomalies during the mission.

2. Modification Kit Installations

Modifications on CDCs were completed at DSSs 61, 71, and 72. Modifications included those that satisfy the ground rule of keeping all DSIF CDC units as interchangeable as practicable.

P. Ground Support Equipment

1. Design

a. Alpha scattering instrument purge equipment. Use of alpha scattering instrument (ASI) purge equipment with SC-5 during combined systems test (CST) operations resulted in a few minor changes in the released engineering drawings. These changes had very little effect on the hardware but were mostly of a procedural nature. No drawing changes were made as a result of installing the purge equipment on pad 36B at the Air Force Eastern Test Range (AFETR). Except for possible changes that may occur after full operational use at AFETR, engineering on this equipment is considered complete.

b. Static charge elimination equipment. Considerable concern exists over possible control item damage and personnel hazards caused by the presence of electrostatic forces on the spacecraft and its components. This applies to cleanroom garments, thermal surface protective wrapping, packaging, containers, and assembled spacecraft in the systems test and prelaunch phases of operation. The aerospace ground equipment (AGE) department issued a change action plan to solve this problem on an accelerated basis for SC-6 and -7 and has coordinated the proper use of the equipment furnished. The solution to the problem is detection of the presence of an electrostatic charge and neutralization of that charge.

It was decided to use commercial static meters to accomplish the detection and to use the principle of ionization to perform the neutralization. Existing commercial equipment is capable of blowing air across units that ionize the air, i.e., breaks air atoms into free electrons (negative ions) and free positive nuclei (positive ions). When this air is directed over surfaces containing an electrostatic charge, ions of the opposite sign will combine with the charge on the surface until it is electrically neutral. The equipment selected, similar to that in use at HAC-AFETR, has an effective range up to 100 in. This permits adequate coverage when used in pairs around the spacecraft.

2. Equipment

a. ASI purge equipment. Initial delivery of hardware was made 4 days ahead of schedule to ensure ample time for installation and checkout at CST, San Diego, prior to SC-5 arrival. The filter package and the special Q-bottle installations on the *Centaur* torus ring were accomplished with no problems. The filter package was placed as close as possible to the purge outlet location in the *Centaur* nose fairing. The Q-bottle installation was made on the opposite side of the ring to minimize any effect on the balance of the encapsulated assembly during hoisting and mating to the *Centaur*. A fit-and-function of these units, the portable purge equipment (PPE), was successfully performed during SC-5 CST operations. An identical filter package from the on-pad purge equipment (OPPE) was also used during part of the ASI purge operation.

A partial shipment of OPPE was made to AFETR June 16 for the pad 36B umbilical tower installation. The balance of the OPPE and all of the PPE were shipped from El Segundo June 30, 1967. Support from the AGE department engineering was supplied to coordinate installation and checkout at AFETR, so as not to impact the SC-5 schedule. The OPPE installation on the pad 36A umbilical tower will occur after pad cleanup from the *Surveyor IV* launch.

The first fully operational use of all the purge equipment occurred during the SC-5 point flight acceptance composite test.

b. Static charge elimination equipment. The equipment for neutralizing static charges consists of a Simco Aerostat Ionizing Blower, type AS-20 with a D168R power supply, all mounted on a Davis Sanford tripod. Also separately supplied are the blower and power supply for portable use, as required.

Q. Operational Ground Equipment

1. Design

a. Modification of squib simulator adapters. The gold plating has been flaking from the connector pins in the new squib simulator adapters. To correct the problem, the adapters will be modified by adding a new cannon con-

nector to the assembly. Several adapters have been modified and tested to confirm the effectiveness of the change. Modification of the adapters will begin in early August.

b. Solar panel simulator. The new solar panel simulator for the launch complex equipment was put into use for the first time during tests of SC-5 at combined systems test (CST). The simulator design utilizes the same constant current/constant voltage power supply and diode shaping circuits as the simulator in the STEA power rack. Differences in output characteristics at the spacecraft interface and in control circuitry exist because of line length from equipment to spacecraft and because of the requirements for remote control from the *Surveyor* operations console.

c. Aerospace ground equipment 3 modification for SC-5 and subsequent spacecraft. Part of the aerospace ground equipment (AGE) modification for SC-5 and subsequent spacecraft incorporated filter capacitors across the Christie input lines in a box at the end of the 90-ft cable near the spacecraft. The capacitors were installed at this point with the intent of reducing the possibility of a Christie dump caused by transients at the remote sense points within the spacecraft. When the capacitors were used at CST, oscillations developed on the Christie output lines. They were caused by the combination of long output lines and filter capacitors. Moving the capacitors from the end of the line to the junction box in the AGE 3 trailer corrected the problem.

d. Christie power switching and sense circuit test modifications. Modifications to move the Christie power switching relay from the power rack to the junction box and to provide a self-test circuit for the Christie internal sense circuit are being incorporated into the AGE sets. Relocation of the switching relay eliminates the requirement to increase the Christie overcurrent shutoff setting when first applying power to the spacecraft. The increase in the setting had been necessary to prevent the large surge current used to charge the capacitors in the junction box from causing Christie shutoff. By placing the switching relay on the spacecraft side of the capacitors, the capacitors charge up during Christie turn-on rather than when the spacecraft power is applied; then shutoff does not occur. The Christie sense circuit test modification provides a self-test switch and a panel meter to test the Christie internal sense zener diodes and to read the Christie output voltages. The self-test switch opens the supply external sense lines. If the internal sense diodes are good, a known increase in output voltage will be observed on the panel meter. If one or both diodes are open, an abnormal indication will be observed.

e. RF STEA phase jitter test. During *Surveyor* spacecraft testing, several cases of system test equipment assembly (STEA) receiver phase jitter were observed. In order to evaluate the problem, the STEA receiver, transmitter, and power supply were subjected to a special test. The test results indicated a phase jitter susceptibility due to power line transients. An ac power line isolation transformer has proved to be effective in minimizing the jitter. Isolation transformers are currently being installed in the RF AGE racks.

f. AGE set 1 layout. The east wall of the screen room has been removed to obtain the new configuration, making it possible to duplicate the layout of AGE sets 2, 4, and 5. Set 1 no longer includes a system test stand or a screen room for electromagnetic interference (EMI) testing. All spacecraft EMI testing is now accomplished in the new screen room in building 350, which is associated with set 5.

g. Science rack in AGE 1. This rack is used in testing the alpha scattering experiment.

h. Closed-loop and flight control racks in AGE 1. These racks were redesigned under change order 127 and have proven to be superior to their predecessors in every respect. In brief, the closed loop rack was expanded into a double-bay rack to relieve congestion, and equipment was added to enhance its operability. The flight control rack was reduced to a single-bay configuration by removing equipment which was no longer used. As of this writing, all AGE sets, except AGE 2, have received their new racks and are operational.

i. New system test junction box in AGE set 1. A new junction box has been installed at AGE set 1. The design incorporates patch blocks, for ease of troubleshooting and modification, and isolation amplifiers for hardline power and signal lines from the spacecraft. Switching and filtering for AGE-supplied spacecraft power are also included in the box. Mounted on either side of the junction box are cable supports to ease cable strain. The AGE set 1 junction box was first put into use during SC-5 solar thermal vacuum (STV) testing.

j. New STV control rack in AGE set 1. The new STV control rack was first used for SC-5 STV tests. This rack contains unique STV equipment. Included in the category are the following:

(1) The vidicon survival heater emergency power supply provides power for the vidicon survival heater in case of loss of heater power from the spacecraft.

(2) The squib muffler monitor panel provides a visual indication that a squib has been fired.

(3) The line driver assembly provides isolation amplifiers for STV unique hardline power and signal lines from the spacecraft.

(4) The separation sensing and arming (SS and A) and plugs-out control panel provides enable-disable switches and various relays in the plugs-out relay box and the SS and A devices.

(5) The heater override panel switches can be used to override the spacecraft heater command and thermal switches.

(6) The SS and A actuator panel provides controls to actuate and reset the SS and A devices at the three spacecraft legs.

k. RF STEA load panel. During PVT-1 and -2 testing of spacecraft previous to SC-5, it was not possible to easily set the RF STEA power level to the spacecraft. To resolve the problem, the resistive type attenuator on the RF load panel was replaced with a more accurate waveguide cutoff attenuator. All RF load panels are being reworked to include this attenuator. Results of this change have proved very satisfactory.

l. Time code distribution panel. The time code distribution panel has been completed and installed on the west wall of building 365, where it supplies all AGE sets and computers with independent, noninteracting NASA time code.

m. RADVS AGE.

Blitz wheel. Arrangements were made with Ryan Aeronautical Company, San Diego, to provide a Blitz wheel on a loan basis for radar altimeter and doppler velocity sensor (RADVS) testing at AFETR through completion of the *Surveyor* program. The Blitz wheel is a rotating device which, when brought in proximity with an RADVS antenna, will appear as a moving target to the doppler radar, causing it to lock on. The apparent doppler frequency is directly proportional to the speed of rotation of the Blitz wheel. In its application to *Surveyor* testing, the Blitz wheel is an air-driven device supplied with calibration tables showing doppler frequency versus rpm versus air pressure at its input.

Single sideband modulators and crystals. It was discovered that the difficulty experienced by calibration personnel when trying to adjust the single sideband modulators (SSBM) in the RADVS rack was due primarily to a mechanical interference between the crystal and the cap, which locks it in place. As soon as the crystal cap was tightened to lock the crystal in place, the adjustment was lost. It was noticed that the crystal moved axially in the holder; this was caused by the end of the crystal bottoming in the cap. To avoid this problem, the cap was drilled with a hole large enough to clear the crystal. Using the drilled caps, the block was adjusted in a few minutes. Six blocks were adjusted in this manner. This method has improved the ease of adjustment and drastically reduced the number of damaged crystal caps and modulator blocks. By cementing to each crystal an extension which extends through the cap, it is possible to adjust the modulators without removing them from the racks.

Single sideband modulator tests. A test was performed on an RADVS SSBM to determine the effects on upper sideband output power of various modulation and carrier frequencies. The SSBM used was one of three previously calibrated by the calibration laboratory and met all required specifications for signal purity, lower sideband, and harmonic suppression. A Quantech model 303 wave analyzer was used to measure the upper sideband (USB) voltage. For initial calibration, the amplifier gain control preceding the Quantech analyzer was set for a reading of 300 mV on the Quantech at a carrier frequency of 13.3 GHz and a modulation of 20.83 kHz. This control was then left in the same position for all subsequent readings. Table 15 gives a maximum USB reading of 320 mV and a minimum of 240 mV. This difference in range is the greatest encountered in the test and amounts to less than 2.5 dB. However, to obtain this magnitude of change, the carrier frequency had to be shifted from 13.3075 to 12.290 GHz, a change of 17.5 MHz.

It can then be concluded that, if the power delivered to the STEA from the spacecraft is constant, the maximum loss incurred in the SSBM is 2.5 dB or less and would be incurred only for a carrier frequency shift of 17.5 MHz. The average drift encountered in the radar altimeter transmitter was 4 MHz and in the doppler velocity sensor transmitter, 6.4 MHz. With this amount of drift, the SSBM loss would be much less. It has been concluded from test data that the SSBM does not contribute to any apparent loss of power to the RADVS receivers.

n. Altitude marking radar AGE. During altitude marking radar (AMR) testing, it was noted that the carrier power being supplied to the AMR antenna from the AMR rack was fluctuating, making testing very difficult

Table 15. Upper sideband power with changes in carrier frequency

Modulator frequency, kHz	f_c = 13.305 GHz			+2.5 MHz			−2.5 MHz			+5 MHz			−5 MHz		
	USB	Second harmonic	Third harmonic	USB	Second harmonic	Third harmonic	USB	Second harmonic	Third harmonic	USB	Second harmonic	Third harmonic	USB	Second harmonic	Third harmonic
20.83	282	5.0	14.1	274	3.7	12.1	278	5.9	15.4	275	2.6	9.2	300	6.5	16.2
1.64	281	5.6	15.3	271	5.2	12.9	289	5.2	16.3	272	4.4	9.5	300	4.1	17.3
0.93	278	5.9	15.6	268	6.3	13.3	286	4.7	16.8	268	6.2	10.1	300	2.8	17.8
0.53	270	6.5	13.7	258	5.1	12.2	282	7.7	15.1	258	4.8	8.9	298	8.7	16.2
0.12	245	9.7	13.7	240	10.8	12.2	254	6.9	14.2	253	11.3	10.1	274	5.5	14.6
	f_c = 13.295 GHz														
20.83	305	4.5	13.1	305	5.1	4.5	310	3.4	10.8	300	6.3	15.8	315	2.0	7.6
1.64	307	0.3	14.2	305	1.9	15.4	312	1.7	11.2	301	4.0	16.8	315	3.6	7.7
0.93	309	4.0	15.0	307	2.7	16.1	315	5.6	11.8	301	2.6	17.2	315	8.1	8.0
0.53	310	7.5	13.0	310	7.9	13.6	317	7.0	10.5	298	8.6	15.4	316	5.4	6.5
0.12	300	7.1	11.7	293	5.4	12.8	315	10.0	8.5	273	5.3	14.2	320	13.1	5.3
	f_c = 13.310 GHz														
20.83	284	2.6	9.1	277	2.4	6.7	278	4.2	12.5	280	2.6	4.3	286	5.3	14.0
1.64	283	4.3	9.2	273	3.0	6.9	273	5.0	12.5	277	1.2	4.1	282	5.6	14.0
0.93	280	6.3	9.3	270	5.5	6.4	271	6.5	13.5	273	4.2	4.4	281	5.9	14.1
0.53	260	4.3	11.7	261	5.0	6.3	262	5.5	12.4	270	6.1	2.9	273	6.7	13.8
0.12	274	11.2	9.2	262	11.2	7.5	242	10.7	10.3	276	10.8	4.8	245	9.5	13.2
	f_c = 13.290 GHz														
20.83	315	1.8	7.0	315	2.3	10.5	310	0.9	4.8	315	4.3	13.0	301	1.3	
1.64	315	3.7	7.2	316	3.1	10.3	309	4.5	5.0	315	0.4	13.5	298	4.3	
0.93	315	8.3	7.5	317	8.0	10.8	307	8.5	5.1	315	4.4	4.4	295	7.8	
0.53	315	5.1	5.9	318	5.8	8.8	305	3.7	3.2	317	7.5	12.0	292	2.8	
0.12	318	13.7	4.7	320	13.2	8.5	306	14.5	3.9	313	8.6	—	301	14.0	

All readings are in mV.
USB level set at 300 mV at f_c = 13.3 GHz.
Conversion loss is 17.7 dB.
Carrier suppression >25 dB.
Lower sideband (LSB) suppression >28 dB.
Power input to SSBM equals 1.8 mW.

and, in some cases, impossible. The problem was located in a section of coax cable from the super high frequency generator to the waveguide coupler. The attenuation and voltage standing-wave ratio characteristics of this cable changed appreciably whenever the cable was flexed. To correct this problem, the flexible coax was replaced with rigid coax. The rigid coax is preformed to fit in place and has virtually eliminated the problem of power fluctuations.

o. AGE for vibration testing of spacecraft. The vibration AGE is located, when in use, just to the southeast of AGE 1 in building 365, near the vibration shakers. The new vibration junction box, related cables, and radar have resulted in a rather flexible vibration test capacity. In the event of interfering spacecraft test schedules, the vibration test setup can now be accomplished with use of equipment from AGE 1, 3, 4 (AGE 4 is now inactive), or 5, or a combination of these sets. Only some minor changes in AGE 3 were made to allow this trailer-mounted AGE set to be used as the vibration supporting AGE set.

2. Product Design

Recent innovations in thermal vacuum test hardware. When the vehicle is installed, its predrilled retroengine mounting holes will line up precisely with corresponding holes on the retroengine, when the spacecraft is aligned with its mounting holes centered on the support columns. This prepositioning operation saves valuable test time.

A design improvement has been effected for SC-6 and -7 testing by replacing the female halves with the connector blocks. This makes a much neater arrangement

for that portion of the thermocouple interconnections complex, which remains on the end bell more or less permanently. Reductions in setup time have also been realized by the improvement in visibility. The numerals stencilled at each connector identify the Kintel channel number. The use of channel numbers, rather than specific signal nomenclature, has been adopted in the interest of system flexibility and versatility.

Reference

1. *Lunar Night Survival Study Report,* SSD 78119R, Hughes Aircraft Co., El Segundo, Calif., July 17, 1967.